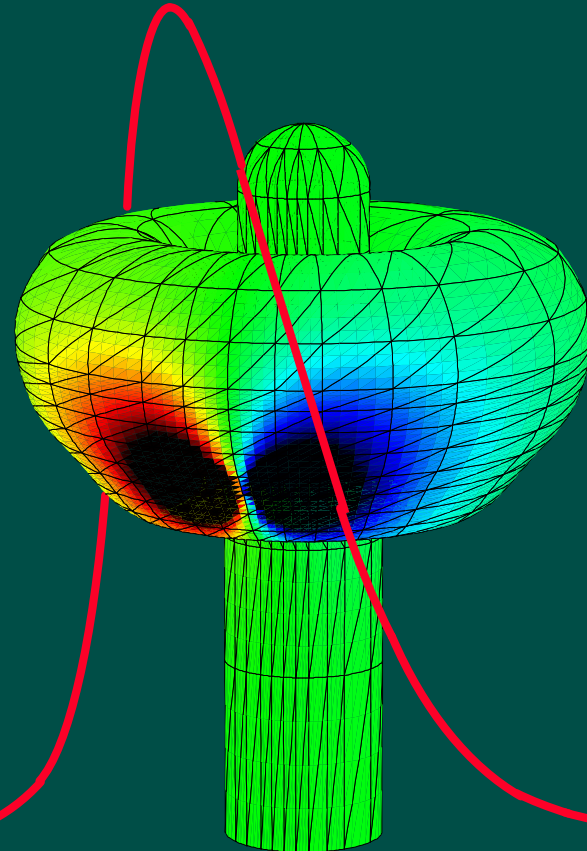


# Cochlear Implants

## A Modelling Approach

Cochlear Implants - A Modelling Approach

J.H.M. Frijns



J.H.M. Frijns

# **Cochlear Implants**

## **A Modelling Approach**

CIP-DATA KONINKLIJKE BIBLIOTHEEK, DEN HAAG

Frijns, Johannes Hubertus Maria

Cochlear implants : A modelling approach /  
Johannes Hubertus Maria Frijns. - [S.l. : s.n.] (Eindhoven : Lecturis). Ill.  
Thesis Rijksuniversiteit Leiden. - With ref. - With summary in Dutch.  
ISBN 90-9008221-2

NUGI 743

Subject heading: Auditory prostheses / Computational modelling /  
Electrical stimulation.

© 1995 J.H.M. Frijns

# Cochlear Implants

## A Modelling Approach

PROEFSCHRIFT

ter verkrijging van de graad van Doctor  
aan de Rijksuniversiteit te Leiden,  
op gezag van de Rector Magnificus Dr. L. Leertouwer,  
hoogleraar in de Faculteit der Godgeleerdheid,  
volgens besluit van het College van Dekanen  
te verdedigen op woensdag 24 mei 1995  
te klokke 15.15 uur

door

**Johannes Hubertus Maria Frijs**

geboren te 's-Gravenhage in 1961

Drukkerij Lecturis B.V., Eindhoven

## **PROMOTIECOMMISSIE:**

Promotor: Prof. Dr. J.J. Grote

Co-Promotor: Dr. J.H. ten Kate (Technische Universiteit Delft)

Referenten: Prof. Dr. Ir. H.P. Wit (Rijksuniversiteit Groningen)  
Prof. Dr. P.H. Schmidt

Lid: Dr. J.G. van Dijk

Deze promotie is mede mogelijk gemaakt door:

Abbott B.V., A.C.M. Ooms Allergie B.V., Astra Pharmaceutica B.V., Cendata (OPUS<sup>®</sup>), Dennis Mulder Hearing B.V., Electro Medical Instruments B.V., Entemed B.V., Glaxo B.V., GN Danavox Nederland B.V., het Heinsius-Houbolt fonds, JW Systems, Kuykhoven Adviesgroep Vrije Beroepen, Oticon Nederland B.V., Pfizer B.V. Bartlett Divisie, producent van o.a. Zithromax<sup>®</sup>, Polymed Electronic Instruments B.V., ReSound B.V., Roussel B.V., Siemens Audiologische Techniek, Soft Ear B.V., Syntex B.V., Schering-Plough B.V., SmithKline Beecham Farma B.V. (Augmentin<sup>®</sup>), UCB Pharma B.V., Veenhuis Medical Audio B.V., Yamanouchi Pharma B.V.

*Aan Antoinette*  
*Aan mijn ouders*



# Contents

---

I	General Introduction .....	9
II	A Model of Myelinated Nerve Fibres for Electrical Prosthesis Design .....	23
III	A Quantitative Approach to Modeling Mammalian Myelinated Nerve Fibers for Electrical Prosthesis Design .....	43
IV	Have Mammalian Myelinated Nerve Fibres Diameter Dependent Nodal Properties? A Model Study .....	69
V	Potential Distributions and Neural Excitation Patterns in a Rotationally Symmetric Model of the Electrically Stimulated Cochlea .....	93
VI	Spatial Selectivity in a Rotationally Symmetric Model of the Electrically Stimulated Cochlea .....	125
VII	A Multi-Channel Simultaneous Data Acquisition and Waveform Generator System Designed for Medical Applications .....	151
VIII	General Discussion .....	165
	Summary .....	173
	Samenvatting .....	177
	Curriculum Vitae .....	183



# *Chapter I*

---

## **GENERAL INTRODUCTION**

Profoundly deaf people experience a severe handicap in their social life. For that reason researchers all over the world are engaged in the development of cochlear implants that can offer these patients a sense of hearing by electrically stimulating the auditory nerve. At the moment approximately 10000 cochlear prostheses of several types have been implanted with varying success (Van Olphen, 1995): Currently available devices generally succeed in getting the deaf patient out of his/her acoustic isolation, but the ideal result, i.e. good open-set speech discrimination without the help of lip-reading, is still achieved in a minority of patients ( Gantz et al., 1988). Moreover, it is very difficult to identify the parameters that are crucial to predict the clinical outcome pre-operatively, as this appears to be the result of a complex interplay between various patient and device related factors ( Brokx et al., 1988; Blamey et al., 1992; Van Dijk et al., 1993; Gantz et al., 1993).

Initial research in this field was primarily defined in terms of clinical concerns. It established the feasibility of the approach and documented the beneficial effects and possible risks (House, 1994). However, in order to achieve a further improvement of the clinical results by more sophisticated implant designs, more information from basic research is needed to identify the key factors that need optimisation.

This thesis focuses on the development of a computational model of the implanted cochlea, which is intended to provide more insight in the fundamentals of functional electrical stimulation of the auditory nerve. Therefore, this introduction will not give a complete review of the literature on cochlear implants but highlight some topics that are relevant for the design of this study. This will lead to the identification of some unresolved issues in the field of modelling the response of mammalian myelinated nerve fibres to functional electrical stimulation in general and of auditory nerve fibres to cochlear prostheses in particular. This problem not only involves simulating the response of a nerve fibre to an externally applied potential field, but also the calculation of this potential distribution from the currents on the stimulating electrodes, which is especially intricate in the case of cochlear implants due to the complex geometry of the inner ear ( Fig. 1).

## **Cochlear implants**

More than 35 years ago the first patient underwent the surgical insertion of what would be called now a cochlear implant (Djourno and Eyries, 1957). In the next years a few humans were implanted experimentally with electrodes in the scala tympani (House and Urban, 1973) or in the modiolus (Simmons, 1966), but it lasted until the mid-seventies until the principle of direct electrical stimulation of the auditory nerve was applied systematically in a clinical setting. From then on dozens of different cochlear implant designs have been developed for the purpose of bringing profoundly deaf patients into auditory contact with the hearing environment ( Loeb, 1990). All these designs have some basic features

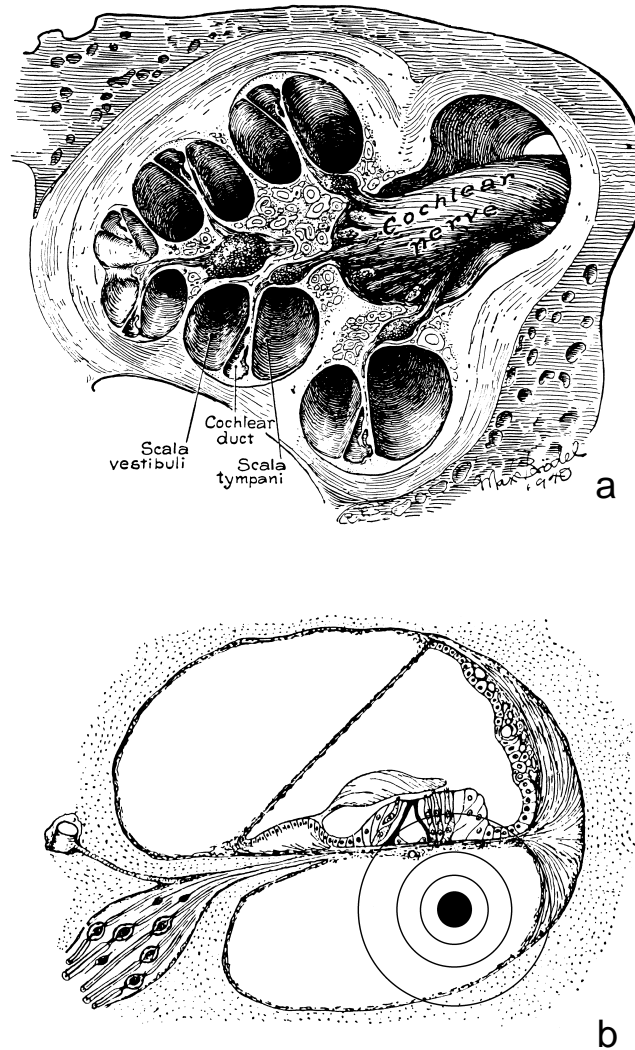


Fig. 1 a. Schematic cross section through the human cochlea or inner ear. The auditory or cochlear nerve in the modiolus forms the central core. Its fibres radiate to the hair cells distributed along the spiralling membranous labyrinth. This is deeply embedded in the petrous bone and consists of three fluid-filled chambers (scala tympani, scala media or cochlear duct and scala vestibuli), separated by thin membranes. (From: Jahn and Santos-Sacchi, 1988)

b. A more detailed cross section of the cochlear canal illustrating the electrical volume conduction problem addressed in this thesis. The black circle in the scala tympani represents an intracochlear electrode, the concentric circles the potential field that would result if the electrical properties of all cochlear tissues were identical. Since this is not the case, it is not trivial to calculate the potential distribution in the vicinity of the auditory nerve fibres that extend from their cell bodies in the spiral ganglion in the lower left corner of the figure. (Adapted from: Jahn and Santos-Sacchi, 1988)

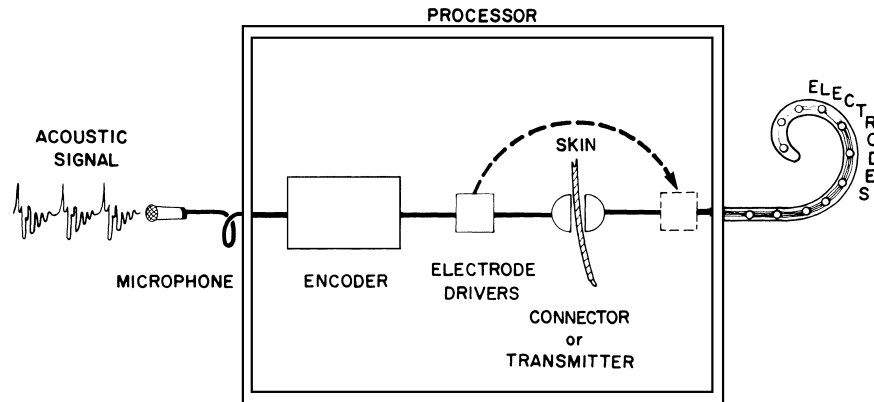


Fig. 2 The basic components of a cochlear implant (From: Pfingst, 1986)

in common: the incoming sounds are captured with a microphone, processed in a speech processor, which encodes the information in signals on an electrode or electrode array that is implanted in or near the cochlea ( Fig. 2). The precise implementation of these basic functions, however, varies widely amongst the various implant types. A gross classification of the different designs can be achieved on the basis of the number of electrodes (commonly called 'channels') and the location of these electrodes (Pfingst, 1986) as indicated in Table I.

In the physiological situation more basal cochlear nerve fibres (i.e. closer to the round window) encode for higher frequencies while more apical ones transmit low-frequency information. Multichannel implants are designed to make use of

Table I The classification of some well-known cochlear implant types on the basis of the number of channels available for stimulation and the site of electrode implantation.

	EXTRA-COCHLEAR	INTRA-COCHLEAR	MODIOLUS
SINGLE-CHANNEL	Vienna/3M (Burian et al., 1986)	House/3M (House and Berliner, 1986)	
MULTICHANNEL	Ann Arbor (Niparko et al., 1993)  Banfai/Hortmann (Banfai et al., 1986)	Clark/Nucleus (Clark et al., 1987) Ineraid/Symbion (Parkin and Steward, 1988)  LAURA/ABS (Peeters et al., 1993)	Simmons (Simmons, 1966)

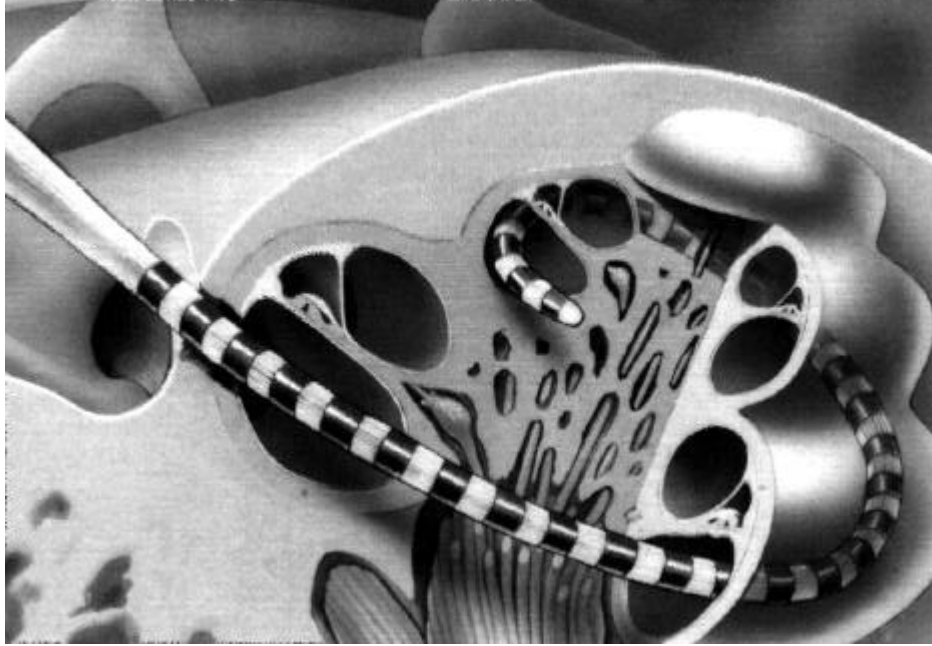


**Fig. 3** An artist's impression of the Clark/Nucleus multichannel intracochlear implant (Clark et al., 1987) showing the banded electrode array, containing 22 platinum electrodes, which is inserted into the scala tympani (Courtesy of Cochlear (UK) Ltd.).

this tonotopic organisation of the auditory nerve. These devices apply multiple electrodes to elicit different auditory sensations by stimulating discrete sub-populations of auditory nerve fibres, while single-channel implants make use of a single electrode in or near the cochlea.

Most currently used cochlear implants utilise intracochlear electrodes that are inserted into the scala tympani through the round window membrane or a drilled cochleostomy in its vicinity ( Fig. 3). Extracochlear devices use an electrode in the round window niche, which can be combined with electrodes in or against the otic capsule. Some experimental devices combine intra- and extracochlear electrode sites (Banfai et al., 1992).

Apart from the electrode configuration used, auditory prostheses differ also in the way the sound signals are converted into electrical stimuli on the electrodes. Two basic types of speech decoding strategies can be distinguished. The first type is based on feature extraction, which means that e.g., information regarding the frequency and amplitude of spectral peaks is used to encode formant information in vowels ( Clark et al., 1987). The other type of strategies is essentially based on conveying time information of the filtered incoming signal. This can be done by using either analog stimuli (i.e., the waveform of the electrode current is a transformed representation of the incoming signal) or by pulse sequences (Lawson et al., 1993). Since it is still subject of debate which type of encoding scheme is superior, some cochlear

implants are not restricted to a fixed processing strategy but have a programmable speech processor (Peeters et al., 1993).

Of course, the most important parameter for deciding between different cochlear implant designs is the benefit the patient experiences from it. Four levels of clinical performance can be distinguished:

1. *The prosthesis has a signal function*

The patient can detect and recognise common sounds, e.g., when someone enters the room behind his back, or when someone starts speaking.

2. *The prosthesis provides an aid in lip-reading*

Auditory information on rhythm and intonation helps the patient to understand spoken language, but he must heavily rely on lip-reading.

3. *The patient's speech production is improved*

The auditory feedback of the patient's own speech leads to an increased quality of his voice and speech production ( Leder and Spitzer, 1990).

4. *The patient can understand speech without the help of lip-reading*

This is the ideal result, which is achieved by a small, although important, minority of patients. An important distinction in this context is the one between so-called 'open set' and 'closed set' speech recognition, for in the latter case a restricted vocabulary is used to alleviate the task.

It is, however, important to notice that the subjective benefits reported by implant users, seem to depend primarily on the feeling of independence and confidence that is gained by wearing the implant rather than on objective measures of performance (Kou et al., 1994). Nevertheless, such objective methods for the evaluation of the auditory capabilities of severely hearing impaired patients with and without the use of visual information are important guides, both for therapeutic evaluation of individual patients and for the comparison of the results obtained with different implant designs. Such tests include supra-segmental items (such as detecting rhythm information and distinguishing between questions and affirmative sentences) and segmental ones (e.g., the recognition of short vowels). Well-known examples of English tests are the MAC test battery (Owens et al., 1985) and the Iowa Cochlear Implant Tests (Tyler et al., 1983), while the Antwerpen/Nijmegen test (Beijnon et al., 1990) was developed for the Dutch language domain.

Using such tests, several comparative studies involving groups of patients wearing different prostheses were performed (Cohen et al., 1993; Gantz et al., 1993). The general conclusion of most of such studies is that multichannel devices are superior to single-channel ones, but that the final clinical outcome depends complexly on many other factors, related to the individual patient and the kind of signal processing applied (Wilson et al., 1993).

Whereas the initial cochlear implant candidates were primarily post-lingually deafened adults, current implantation programs involve increasing numbers of pre- or perilingually deafened children (Soulière et al., 1994; Van Den Broek et al., 1995), for which very favourable results with respect to the development of language skills are reported. Initially children were not implanted, because of uncertainties regarding the potential damage to a developing auditory system due to the electrical fields generated by the implant. Animal experiments,

however have revealed that even the converse may be true: Early electrical stimulation at moderate intensity levels can induce a better development of the auditory nervous system when compared to unstimulated deafened cases (Snyder et al., 1990; Leake et al., 1990). Other safety issues still remain to be resolved. Although several successful reimplantations of scala tympani electrodes have been reported in adults (Lindeman et al., 1987) and in children (Miyamoto et al., 1994), there is certainly an insertion trauma associated with intracochlear electrodes, especially when long ones are inserted to reach more apical fibres (Kennedy, 1987; Linthicum et al., 1991; Welling et al., 1993). This can lead to fibrosis or ossification in the cochlear duct with the possible consequence of increased retrograde neuronal degeneration (Schuknecht, 1993).

In view of the ongoing improvements of cochlear implant designs and the inevitable failure of implanted hardware in time, it is wise to take maximum care that children that are implanted now will still be able to profit from future implant designs. Extracochlear devices may provide a solution to this problem, as they do not disturb the integrity of the cochlea. Therefore, further loss of residual hearing can be prevented, as contrasted with intracochlear electrode insertion (Bogess et al., 1989). This is particularly important in the light of recent findings that indicate the feasibility of electrical stimulation of residual hearing (McAnally and Clark, 1994). Extracochlear electrodes have the additional advantage that they can also be placed over the cochlear apex (Franz and Clark, 1988), which is inaccessible for intracochlear electrodes (cf. Fig. 3). This is especially interesting in the light of the fact that many patients suffering from severe sensorineural hearing loss have relatively many intact auditory nerve fibres in this region (Hinojosa and Marion, 1983). In addition, it are these low and middle frequency nerve fibres that are important for the understanding of speech in normally hearing subjects (Pfungst et al., 1987), while these fibres also play an important role in directional hearing by detection of interaural time differences (Von Békésy, 1930). It is therefore not surprising that the binaural interaction with bilateral intracochlear electrodes, i.e. in the high-frequency region of the cochlea, was found to depend solely on interaural intensity differences (Van Hoesel et al., 1993). Finally, the insertion of extracochlear electrodes suffers less than that of intracochlear ones from intrascalar ossification, which is known to occur frequently in cases of deafness due to meningitis (Jackler et al., 1987). An important drawback of the extracochlear location of electrodes is the fact that the distance between the stimulating electrodes and the excitable neural elements is relatively large. This is expected to result in higher stimulation thresholds and less selective stimulation, i.e. less groups of auditory nerve fibres that can be stimulated independently. The higher stimulus currents involved may also impose limitations on the dynamic range, e.g., due to stimulation of the facial nerve.

### **The Leiden University cochlear implant project**

In spite of the limitations inherent to the use of extracochlear electrodes we feel that the above-mentioned advantages of an extracochlear approach make it

worth-while to investigate the feasibility of a multichannel extracochlear implant with optimised electrode positions and stimulus patterns.

Unlike previous designs that required major surgical intervention in the middle ear and even the Eustachian tube (Banfai et al., 1986), the device should not disturb the integrity of the middle ear. For the fixation of the electrodes in the otic capsule and an adequate sealing of the inner ear these electrodes will be coated with Polyactive<sup>®</sup>, a degradable bio-active material, that was shown to induce active bone bonding (Bakker et al., 1990). Histological studies of the behaviour of this electrode coating on the guinea pig cochlea, with and without electrical stimulation, are currently going on in our laboratory (Kingma et al., unpublished results).

The electrophysiological part of the project focuses on identifying the stimulus parameters that are crucial for selective stimulation of small sub-populations of auditory nerve fibres. For this purpose electrophysiological measurements in guinea pigs, implanted with extracochlear electrodes are performed. The initial experiments involve normally hearing animals, since this allows the application of acoustical stimuli to measure the excitation patterns due to electrical stimulation (Charlet de Sauvage et al., 1983; Black et al., 1983; Van Den Honert and Stypulkowski, 1987), while later studies will use deafened animals. For these animal experiments we needed a multichannel programmable stimulus generator with current outputs and with at least 5  $\mu$ s time resolution per channel. To prevent current glitches due to asynchronous switching of electrodes we desired to refrain from using a multiplexer. We also wanted to be able to perform simultaneous data acquisition (e.g., measure electrophysiological responses) while stimulating both acoustically and electrically with the device. Since it did not appear feasible to fulfil the speed and timing requirements with commercially available equipment, we decided to develop the flexible, multichannel data acquisition and waveform generator system which is described in chapter VII of this thesis.

### **Aim and overview of the present study**

In order to guide these experiments and to get more insight in the fundamental processes involved in electrically stimulating the inner ear we felt the need to develop a computational model of the electrically implanted inner ear. This model had to combine a calculation of electrical fields due to the stimulating electrodes with the prediction of resulting neural responses ( Fig. 4).

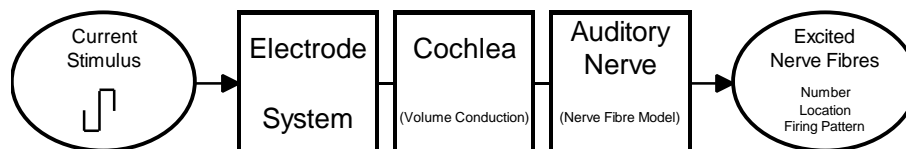
In order to be able to investigate the influence of different stimulus waveforms on the neural excitation, nerve fibre model should give a sufficiently accurate description of the response of the auditory nerve fibres to time-varying, externally applied electrical fields. This means that passive estimators of neural reactivity such as the activation function ( Rattay, 1989) or the total equivalent driving function ( Warman et al., 1992) cannot be applied, since their use is limited to predicting the response of a nerve fibre in its resting state to a single, monophasic stimulus. Also, single-node models with non-linear kinetics (Motz and Rattay, 1986) are not applicable for this purpose since they do not take the spatial distribution of the stimulating potential into account. On the other hand, the neural model should not be so intricate that it would cost too

much computational effort to simulate the overall response of the population of auditory nerve fibres present in the cochlear turns. This means that models that incorporate detailed anatomical information (Halter and Clark, 1991) also do not fulfil our aims.

Colombo and Parkins (1987) presented a more simplified non-linear model of the mammalian auditory nerve fibre based on the classical work on amphibian neurons of Frankenhäuser and Huxley (1964), as used by Reilly et al. (1985) in their so-called Spatially Extended Non-linear Node (SENN) model. However, they had to adapt the anatomy of the modelled nerve fibre significantly to represent physiological data obtained from single auditory nerve fibre experiments in squirrel monkeys. Furthermore, simulations we performed using their model parameters revealed that the duration of their simulated action potentials was about 1.3 ms, which is more than twice the spike duration observed *in vivo* (Kiang et al., 1976). Furthermore, the simulated spike conduction velocity was much lower than it is in real nerve fibres.

We concluded that a major factor causing the discrepancy between experimental and simulation data consisted of the difference between mammalian body temperature and the temperature at which Frankenhäuser and Huxley (1964) performed their voltage-clamp measurements (20 °C). Chapter II of this thesis investigates whether correcting this and a couple of other model assumptions results in a model that - although still based on amphibian data - can give an adequate description of the neural properties that are relevant for the design of electrical prostheses. Chapter III addresses the question whether a better description of the behaviour of large mammalian myelinated nerve fibres is obtained if nodal kinetics are used that are based upon voltage-clamp measurements in mammalian nerve fibres at body temperature (Schwarz and Eikhof, 1987).

Fig. 4 The conceptual framework behind the model of the electrically stimulated ear. The input signal is the current stimulus on the left, which is delivered by the speech processor (Fig. 2). This current induces a potential field in the cochlea via the electrode system. This potential field, as computed by the volume conduction model, forms the input of the nerve fibre model that predicts which auditory nerve fibres will be excited. The information conveyed to the brain is characterised by the number, location and firing pattern of these fibres, the model's output.



Both the MSENN model and the SEF model (as the models described in chapter II and III respectively, are called) describe the behaviour of large mammalian motor neurons with diameters of 10  $\mu\text{m}$  or above, which have action potential durations around 0.3 ms and maximum steady-state firing rates above 1 kHz. The auditory nerve fibres which are the target of stimulation for cochlear implants, however, possess axon diameters below 3  $\mu\text{m}$ , have spike durations of circa 0.5 ms (Kiang et al., 1976) and cannot sustain firing at spike

rates above 600 Hz (Moxon, 1968). This is consistent with the findings of Paintal (1966), who showed that both the spike duration and the length of the absolute refractory period (i.e. the period after the initiation of an action potential in which it is impossible to elicit a second propagated action potential) increases gradually with diminishing fibre diameter. Chapter IV of this thesis deals with the question how the SEF model can be generalised to simulate the behaviour of fibres of different sizes, including auditory spiral ganglion cells.

As stated above, the full mathematical model of the electrically implanted cochlea consists of two sub-models, the first of which is the nerve fibre model. This neural excitation model receives its input from the other sub-model that calculates the potential distribution in the cochlea from the stimulating electrode currents. Since the cochlear geometry is complex and the various cochlear structures have electrical conductivities that differ several orders of magnitude (Suesserman, 1992), it is impossible to derive an analytic solution to this three-dimensional volume conduction problem. Most previous studies unrolled the cochlear duct to simplify the geometry and used discrete resistive and capacitive components (Suesserman and Spelman, 1993) or applied numerical methods to solve this problem (Finley et al., 1990). We also did not model the cochlear duct as the tapered spiral it is in reality, but we solved the problem for a field model that is symmetric about a common mid-modiolar axis and features three tiers of neural loci, representing spiral ganglion cells from turns II, III and IV of the guinea pig cochlea. Chapter V describes this combined neural and volume conductor model and compares the resultant model predictions for several longitudinal bipolar electrode sites against experimental electrically evoked auditory brainstem response (EABR) data from the cat.

In chapter VI the model is applied to investigate the influence of temporal stimulus parameters and electrode configurations on the spatial selectivity of electrical stimulation by cochlear implants. In this chapter it is also studied to what extent the physiological variation in axon diameter or the loss of peripheral processes of the auditory nerve fibres is expected to influence these effects.

Chapter VII, which was outlined above when describing the Leiden cochlear implant project, describes the development of the multichannel data acquisition and waveform generator system used in the experimental part of the project. Finally, Chapter VIII discusses the overall results of the study and outlines some directions for future research.

## References

- Bakker, D., Blitterswijk, C.A. van, Hesseling, S.C., Daems, W.T. and Grote, J.J. (1990) Tissue/biomaterial interface characteristics of four elastomers. A transmission electron microscopical study. *J Biomed Mater Res* **24**, 277-293.
- Banfai, P., Karczag, A., Kubik, S., Lüers, P. and Sürth, W. (1986) Extracochlear sixteen-channel electrode system. *Otolaryngol Clin North Am* **19**, 371-408.
- Banfai et al. (1992) First results with a combined intra- and extracochlear implant. *Cochlear Implants - New Perspectives*, Toulouse.
- Beijnon, A.J., Brokx, P.P.L., Mens, L.H.M. and Broek, P. van den (1990) De eerste resultaten bereikt met een elektrische binnenoorprothese. *Logopedie en Foniatrie* **62**, 113-116.
- Békésy, G. von (1930) Zur Theorie des Hörens: Über das Richtungshören bei einer Zeitdifferenz oder Lautstärkeungleichheit der beiderseitigen Schalleinwirkungen. *Physik Zeits* **31**, 824-835, 857-868.
- Black, R.C., Clark, G.M., O'Leary, S.J. and Walters, C. (1983) Intracochlear electrical stimulation of normal and deaf cats investigated using brainstem response audiometry. *Acta Otolaryngol Suppl* **399**, 5-17.
- Blamey, P.J., Pyman, B.C., Gordon, M., Clark, G.M., Brown, A.M., Dowell, R.C. and Hollow, R.D. (1992) Factors predicting postoperative sentence scores in postlinguistically deaf adult cochlear implant patients. *Ann Otol Rhinol Laryngol* **101**, 342-348.
- Bogges, W.J., Baker, J.E. and Balkany, T.J. (1989) Loss of residual hearing after cochlear implantation. *Laryngoscope* **99**, 1002-1005.
- Broek, P. van den, Borne, S.C.F. van den and Brokx, J.P.L. (1995) Cochleaire implantatie bij kinderen. *Ned Tijdschr KNO-Heelkunde* **1**, 12-15.
- Brokx, J.P., Hombergen, G. and Coninx, F. (1988) Relations between audiometrical thresholds of potential cochlear implant patients and their performance in preoperative psycho-physical tests with electrical stimulation. *Scand Audiol* **17**, 217-222.
- Burian, K.; Hochmair-Desoyer, I. J. and Eisenwort, B. (1986) The Vienna Cochlear Implant Program. *Otolaryngol Clin North Am* **19**, 313-328.
- Charlet de Sauvage, R., Cazals, Y, Erre, J.-P. and Aran, J.M. (1983) Acoustically derived auditory nerve action potential evoked by electrical stimulation: An estimation of the waveform of single unit contribution. *J Acoust Soc Am* **73**, 616-627.
- Clark, G.M., Blamey, P.J., Brown, A.M., Gusby, P.A., Dowell, R.C., Franz, B.K., Pyman, B.C., Shepherd, R.K., Tong, Y.C., Webb, R.L. and et a (1987) The University of Melbourne-nucleus multi-electrode cochlear implant. [Review]. *Adv Otorhinolaryngol* **38**, 1-181.
- Cohen, N.L., Waltzman, S.B. and Fisher, S.G. (1993) A prospective, randomized study of cochlear implants. *N Engl J Med* **328**, 233-237.
- Colombo, J. and Parkins, J.W. (1987) A model of electrical excitation of the mammalian auditory-nerve neuron. *Hear Res* **31**, 287-312.
- Dijk, J.E. van, Olphen, A.F. van and Smoorenburg, G.F. (1993) Preoperative electrical nerve stimulation as one of the criteria for selection. *Adv Otorhinolaryngol* **48**, 103-107.
- Djourno, A. and Eyries, C. (1957) Prothèse auditive par exitation électrique à distance du nerf sensoriel à l'aide d'un bobinage inclus à demeure. *La Presse Médicale* **65**, 1417.

- Finley, C.C., Wilson, B.S. and White, M.W. (1990) Models of Neural Responsiveness to Electrical Stimulation. In: J.M. Miller and F.A. Spelman (Eds.) *Cochlear Implants: Models of the Electrically Stimulated Ear*. Springer-Verlag, New York, pp 55-96.
- Frankenhäuser, B. and Huxley, A.F. (1964) The action potential in the myelinated nerve fiber of *Xenopus Laevis* as computed on the basis of voltage clamp data. *J Physiol (London)* **171**, 302-315.
- Franz, B.K. and Clark, G.M. (1988) The surgical anatomy for multiple-electrode extracochlear implant operations. *J Laryngol Otol* **102**, 685-688.
- Gantz, B.J., Tyler, R.S., Knutson, J.F., Woodworth, G., Abbas, P., McCabe, B.F., Hinrichs, J., Tye-Murray, N., Lansing, C., Kuk, F. and et a (1988) Evaluation of five different cochlear implant designs: audiologic assessment and predictors of performance. *Laryngoscope* **98**, 1100-1106.
- Gantz, B.J., Woodworth, G.G., Knutson, J.F., Abbas, P.J. and Tyler, R.S. (1993) Multivariate predictors of audiological success with multichannel cochlear implants. *Ann Otol Rhinol Laryngol* **102**, 909-916.
- Halter, J.A. and Clark, J.W, Jr. (1991) A distributed-parameter model of the myelinated nerve fibre. *J Theor Biol* **148**, 345-382.
- Hinderink, J.B., Snik, A.F., Mens, L.H., Brokx, J.P. and Broek, P. van den (1994) Performance of prelingually or postlingually deafened adults who were using a single or multichannel cochlear implant. *Ear Nose Throat J* **73**, 180-183.
- Hinojosa, R. and Marion, M. (1983) Histopathology of profound sensorineural deafness. *Ann N Y Acad Sci* **405**; Cochlear Prosthesis - An International Symposium, 459-484.
- Hoesel, R.J. van, Tong, Y.C., Hollow, R.D. and Clark, G.M. (1993) Psychophysical and speech perception studies: a case report on a binaural cochlear implant subject. *J Acoust Soc Am* **94**, 3178-3189.
- Honert, C. van den and Stypulkowski, P.H. (1987) Single fiber mapping of spatial excitation patterns in the electrically stimulated auditory nerve. *Hear Res* **29**, 195-206.
- House, W.F. (1994) Cochlear implants: It's time to rethink. *Am J Otol* **15**, 573-587.
- House, W.F. and Berliner, K.I. (1986) Safety and efficacy of the House/3M cochlear implant in profoundly deaf adults. *Otolaryngol Clin North Am* **19**, 275-286.
- House, W.F. and Urban, J. (1973) Long term results of electrode implantation and electronic stimulation of the cochlea in man. *Ann Otol* **82**, 504-517.
- Jackler, R.K., Luxford, W.M., Schindler, R.A. and McKerrow, W.S. (1987) Cochlear patency problems in cochlear implantation. *Laryngoscope* **97**, 801-805.
- Jahn, A.F. and Santos-Sacchi, J. (Eds.) (1988) *Physiology of the ear*. Raven Press, New York.
- Kennedy, D.W. (1987) Multichannel intracochlear electrodes: mechanism of insertion trauma. *Laryngoscope* **97**, 42-49.
- Kiang, N.Y.S., Moxon, E.C. and Kahn, A.R. (1976) The relationship of gross potentials recorded from the cochlea to single unit activity in the auditory nerve In: R.J. Ruben, C. Elberling, and C. Salomon (Eds.) *Electrocochleography*. University Park Press, Baltimore. 95-115.
- Kou, B.S., Shipp, D.B. and Nedzelski, J.M. (1994) Subjective benefits reported by adult Nucleus 22-channel cochlear implant users. *J Otolaryngol* **23**, 8-14.
- McAnally, K.I. and Clark, G.M. (1994) Stimulation of residual hearing in the cat by pulsatile electrical stimulation of the cochlea. *Acta Otolaryngol (Stockh)* **114**, 366-372.

- Lawson, D.T., Wilson, B.S. and Finley, C.C. (1993) New processing strategies for multichannel cochlear prostheses. *Prog Brain Res* **97**, 313-321.
- Leake, P.A., Hradek, G.T., Rebscher, S.J. and Snyder, R.L. (1991) Chronic intracochlear electrical stimulation induces selective survival of spiral ganglion neurons in neonatally deafened cats. *Hear Res* **54**, 251-271.
- Leder, S.B. and Spitzer, J.B. (1990) Longitudinal effects of single-channel cochlear implantation on voice quality. *Laryngoscope* **100**, 395-398.
- Lindeman, R.C., Mangham, C.A. and Kuprenas, S.V. (1987) Single-channel and multichannel performance for reimplanted cochlear prosthesis patient. *Ann Otol Rhinol Laryngol Suppl.* 128, **96**, 1, Part 2, 150-151.
- Linthicum, F.H., Jr., Fayad, J., Otto, S.R., Gale, F.R. and House, W.F. (1991) Cochlear implant histopathology. *Am J Otol* **12**, 245-311.
- Loeb, G.E. (1990) Cochlear prosthetics. [Review]. *Annu Rev Neurosci* **13**, 357-371.
- Miyamoto, R.T., Osberger, M.J., Cunningham, L., Kirk, K.I., Myres, W.A., Robbins, A.M. and Kessler, K. (1994) Single-channel to multichannel conversions in pediatric cochlear implant recipients. *Am J Otol* **15**, 40-45.
- Motz, H. and Rattay, F. (1986) A Study of the Application of the Hodgkin-Huxley and the Frankenhaeuser-Huxley model for Electrostimulation of the Acoustic Nerve. *Neuroscience* **18**, 699-712.
- Moxon, E.C. (1968) Auditory nerve responses to electric stimuli. *MIT Quart Prog Rpt* **90**, 270-275.
- Niparko, J.K., Pflugst, B.E., Johansson, C., Kileny, P.R., Kemink, J.L. and Tjellstrom, A. (1993) Cochlear wall titanium implants for auditory nerve stimulation. *Ann Otol Rhinol Laryngol* **102**, 447-454.
- Olphen, A.F. van (1995) Cochleaire implantatie bij volwassenen. *Ned Tijdschr KNO-Heelkunde*, **1**, 6-11.
- Owens, E., Kessler, D.K., Raggio, M.W. et al. (1985) Analysis and revision of the Minimal Auditory Capabilities (MAC) Battery. *Ear Hear* **6**, 280-290.
- Paintal, A.S. (1966) The influence of diameter of medullated nerve fibers of cat on the rising and falling phases of the spike and its recovery. *J Physiol (London)* **184**, 791-811.
- Parkin, J.L. and Stewart, B.E. (1988) Multichannel cochlear implantation: Utah-design. *Laryngoscope* **98**, 262-265.
- Peeters, S., Offeciers, E., Kinsbergen, J., Van Durme, M., van Enis, P., Dijkmans, P. and Bouchataoui, I. (1993) A digital speech processor and various speech encoding strategies for cochlear implants. *Prog Brain Res* **97**, 283-289.
- Pflugst, B.E. (1986) Stimulation and encoding strategies for cochlear prostheses. *Otolaryngol Clin North Am* **19**, 219-236.
- Pflugst, B. E., Tjellström, A., Miller, J. M., Graham, M. D. & Brånemark, P. I. (1987) Multichannel implants in the cochlear wall. *Ann Otol Rhinol Laryngol Suppl.* 128, **96**, 1, Part 2, 56-57.
- Rattay, F. (1989) Analysis of Models for Extracellular Fiber Stimulation. *IEEE Trans Biomed Eng* **36**, 676-692.
- Reilly, J.P., Freeman, V.T. and Larkin, W.D. (1985) Sensory Effects of Transient Electrical Stimulation: Evaluation with a Neuroelectrical Model. *IEEE Trans Biomed Eng* **32**, 1001-1011.
- Schuknecht, H.F. (1993) *Pathology of the ear*. 2<sup>nd</sup> Ed. Philadelphia, Lea & Febiger, 319.
- Schwarz, J.R., and Eikhof, G. (1987) Na current and action potentials in rat myelinated nerve fibres at 20 and 37°C. *Pflügers Arch* **409**, 569-577.

- Simmons, F.B. (1966) Electrical stimulation of the auditory nerve in man. *Arch Otolaryngol* **84**, 2-54.
- Snyder, R.L., Rebscher, S.J., Cao, K.L., Leake, P.A. and Kelly, K. (1990) Chronic intracochlear electrical stimulation in the neonatally deafened cat. I: Expansion of central representation. *Hear Res* **50**, 7-33.
- Soulière, C.R., Jr., Quigley, S.M. and Langman, A.W. (1994) Cochlear implants in children. [Review]. *Otolaryngol Clin North Am* **27**, 533-556.
- Suesserman, M.F. (1992) Noninvasive Microelectrode Measurement Technique for Performing Quantitative, in Vivo Measurements of Inner Ear Tissue Impedances, Ph.D. Thesis, University of Washington.
- Suesserman, M.F. and Spelman, F.A. (1993) Lumped-parameter model for in vivo cochlear stimulation. *IEEE Trans Biomed Eng* **40**, 237-245.
- Tyler, R.S., Preece, J. and Lowder, M. (1983) *The Iowa Cochlear Implant Tests*. The University of Iowa, Iowa City.
- Warman, E.N., Grill, W.M. and Durand, D. (1992) Modeling the Effects of Electric Fields on Nerve Fibers: Determination of Excitation Thresholds. *IEEE Trans Biomed Eng* **39**, 1244-1254.
- Welling, D.B., Hinojosa, R., Gantz, B.J. and Lee, J.T. (1993) Insertional trauma of multichannel cochlear implants. *Laryngoscope* **103**, 995-1001.
- Wilson, B.S., Lawson, D.T., Finley, C.C. and Wolford, R.D. (1993) Importance of patient and processor variables in determining outcomes with cochlear implants. *J Speech Hear Res* **36**, 373-379.

# Chapter II

---

## **A MODEL OF MYELINATED NERVE FIBRES FOR ELECTRICAL PROSTHESIS DESIGN**

*J.H.M. Frijns and J.H. ten Kate (1994)  
Med.Biol.Eng.Comput., 32 (4), 391-398.*

## ABSTRACT

Starting with the spatially extended non-linear node model (REILLY *et al.*, 1985), which incorporates Frankenhaeuser-Huxley non-linearities at each of several nodes in a row, a model is developed to describe many aspects of the behaviour of mammalian nerve fibres in a quantitative way. By taking into account the effects of temperature and by introducing a realistic nerve morphology, a good fit is obtained between the shape, duration and conduction velocity of simulated and *in vivo* action potentials in mammals. The resulting model correctly predicts the influence of physiological variations of body temperature on various aspects of nerve behaviour. It is shown that the absolute refractory period predicted by the model is within physiological ranges. Both *in vivo* and in the model, the spike amplitude and the spike conduction velocity are reduced in the relative refractory period. It is concluded that single-node models (although widely used) cannot replace this multiple non-linear node model, as the stimulus repetition rates that can be followed by the simulated nerve fibre are limited by impulse conduction properties, rather than by the frequency following behaviour of a single node.

## 1 INTRODUCTION

In recent years, interest in the modelling of the generation and propagation of nerve impulses has increased as electrical nerve stimulation is more widely used in clinical practice, e.g., in hearing prostheses for the profoundly deaf (TYLER *et al.*, 1989) and in external control of the neuromuscular system (VELTINK *et al.*, 1989). REILLY *et al.* (1985; 1987; 1989) describe an elaboration of the McNeal (MCNEAL, 1976) model of a myelinated nerve fibre in an extracellularly applied field. Their spatially extended non-linear node model (SENN model) assumes the myelin sheath is a perfect insulator, and it incorporates Frankenhaeuser and Huxley (FH) (FRANKENHAEUSER and HUXLEY, 1964) non-linearities at each of several adjacent nodes of Ranvier. With this model, it is possible to simulate the behaviour of myelinated nerve fibres under varying extracellular electrode configurations and stimulus patterns. The models are mostly used to describe nerve behaviour in mammals, although they are derived from amphibian data (GORMAN and MORTIMER, 1983; MEIER *et al.*, 1992).

In the field of cochlear prostheses, Colombo and Parkins (COLOMBO and PARKINS, 1987) applied the SENN model to explain the response to electrical stimulation of the auditory nerve (fibre diameter 0.5 - 1  $\mu\text{m}$ ) in deafened squirrel monkeys. Sweeney *et al.* (SWEENEY *et al.*, 1987) proposed a non-linear cable model that uses the equations of Chiu *et al.* (CHIU *et al.*, 1979), which are based on measurements in a rabbit. Recently, Struijk *et al.* (STRUJK *et al.*, 1992) used these equations in modelling recruitment of dorsal column fibres in spinal cord stimulation. In Table 1, some properties of large mammalian myelinated nerve fibres are summarised and compared to the predictions of the SENN and Sweeney model. From this Table, it is clear that, although the SENN model can provide a good qualitative description of many aspects of nerve behaviour, it falls short quantitatively in several respects when

Table 1 - Summary of model results for the present model (MSENN) of a 10  $\mu\text{m}$  nerve fibre, compared to in vivo measurements by Paintal (P AINTAL, 1973) in the cat for A fibres of 10  $\mu\text{m}$  and 20  $\mu\text{m}$  outer diameter; to the original SENN model of a 20  $\mu\text{m}$  nerve fibre (REILLY *et al.*, 1985); and to our 10  $\mu\text{m}$  fibre model computations after Sweeney *et al.*'s model (SWEENEY *et al.*, 1987), with parameters based on the measurements of Chiu *et al.* (CHIU *et al.*, 1979); if the original FH kinetics are applied to the 10  $\mu\text{m}$  fibre under standard conditons (Table 2), the conduction velocity  $v$  changes to  $35.1 \text{ ms}^{-1}$ , but other results are the same as shown for the SENN model; the experimental value of the chronaxy  $t_{chr}$  was taken from work by Ranck (RANCK, 1975).

		MSENN 10 $\mu\text{m}$	10 $\mu\text{m}$ A Fibre	20 $\mu\text{m}$ A Fibre	SENN (REILLY <i>et al.</i> , 1985)	Chiu <i>et al.</i> , (CHIU <i>et al.</i> , 1979) 10 $\mu\text{m}$
$v$	( $\text{ms}^{-1}$ )	59.4	60	120	42.8 (20 $\mu\text{m}$ ) 35.1 (10 $\mu\text{m}$ )	57.2
$Q_{10,v}$	27°-37°C 18°-28°C	1.4 1.4	1.6 2.5	1.6 2.5	1.0 1.0	
$t_{rise}$	(ms)	0.07	0.08	0.07	0.19	0.06
$Q_{10,t_{rise}}$	27°-37°C 18°-28°C	(1.5) <sup>-1</sup> (1.6) <sup>-1</sup>	(2.5) <sup>-1</sup>	(2.5) <sup>-1</sup>	1.0 1.0	
$t_{fall}$	(ms)	0.26	0.29	0.23	1.05	0.26
$Q_{10,t_{fall}}$	27°-37°C 18°-28°C	(2.2) <sup>-1</sup> (2.6) <sup>-1</sup>	(3.5) <sup>-1</sup>	(3.5) <sup>-1</sup>	1.0 1.0	
ARP	(ms)	0.50	0.55	0.45	1.69	0.37
$Q_{10,ARP}$	27°-37°C	(2.0) <sup>-1</sup>	(3.2) <sup>-1</sup>	(3.2) <sup>-1</sup>	1.0	
$t_{chr}$	( $\mu\text{s}$ )	45	29-59	29-59	80	21

\*= computed with unmodified FH equations in a fibre with standard morphology (Table 2)

stimulation of mammalian nerve fibres is considered. As the FH equations were derived for a *Xenopus Laevis* (a cold-blooded animal) at 20°C, this could be expected beforehand. Similar observations can be made for the model proposed by Sweeney *et al.*.

In this paper, we present a modified SENN (MSENN) model (Fig. 1), which has been adapted to fit mammalian nerve fibre data from the literature. This was mainly done by taking into account the influence of body temperature on nerve kinetics. The spike shape, conduction velocity and strength/duration curves generated with the model at different temperatures are compared to physiological data. A detailed study of the behaviour of the modelled nerve fibre in the (relative) refractory period is carried out. Special attention is paid to the phenomenon of abortive spikes, the spike propagation and the repetitive firing abilities. We show how the spike amplitude and the spike conduction velocity depend on the stimulation frequency. The implications of the results for the use of nerve fibre models when designing electrical prostheses are also discussed.

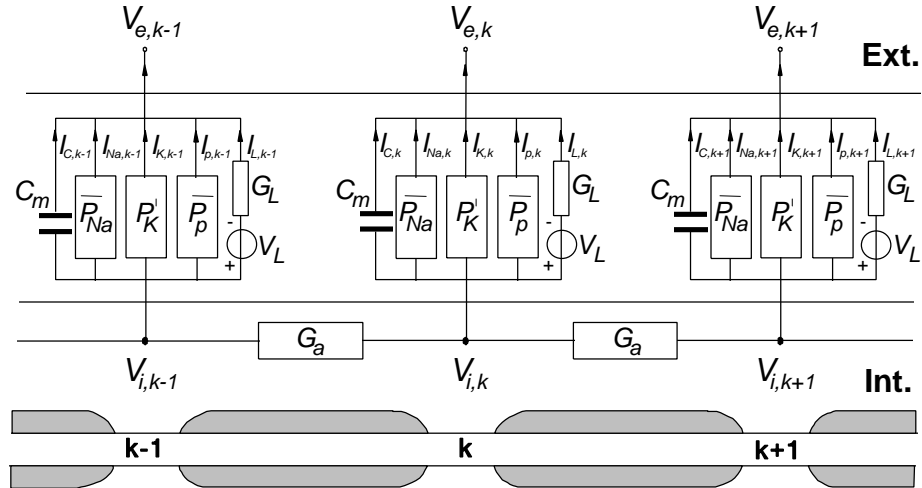


Fig. 1 - MSENN model representation of a myelinated nerve fibre; three nodes  $k - 1$ ,  $k$  and  $k + 1$  are connected by an internodal conductance  $G_a$ ; nodal membrane is shown between the dashed lines; it possesses a permeability for sodium ( $P_{Na}$ ), potassium ( $P_K$ ), non-specific ions ( $P_p$ ), a leak conductance ( $G_L$ ) and potential ( $V_L$ ) and a membrane capacitance ( $C_m$ ); currents through the various channels are labeled correspondingly;  $V_{i,k-1}$ ,  $V_{i,k}$ , and  $V_{i,k+1}$  are intracellular potentials at the nodes, and  $V_{e,k-1}$ ,  $V_{e,k}$ , and  $V_{e,k+1}$  are corresponding extracellular potentials; in the lower part, the axon with its myelin sheath of Schwann cells (shaded area) is displayed with each node immediately below its model representation.

## 2 MODEL DESCRIPTION

It was observed in an early stage of neurophysiological studies that the behaviour of nerve fibres is influenced strongly by temperature (SCHOEPPLE and ERLANGER, 1941). With rising temperature, the impulse conduction velocity in a nerve fibre increases and its action potentials last for a shorter time. However, increasing temperature  $T$  in the SENN model to mammalian body temperature ( $310.65 \text{ K} = 37.5^\circ\text{C}$ ), as done by Colombo and Parkins (COLOMBO and PARKINS, 1987), does not change conduction velocity or the duration of the action potential significantly. This is because the FH equations incorporate temperature in the so-called constant field (Goldman) term of the ionic currents only (see below for an explanation of these terms). For *Xenopus*, Frankenhaeuser and Moore (FRANKENHAEUSER and MOORE, 1963) reported that the  $Q_{10}$  values for sodium activation ( $a_m 1.7$ ,  $\beta_m 1.8$ ) were much smaller than those for sodium inactivation ( $a_h 2.8$ ,  $\beta_h 2.9$ ) and potassium ( $a_n 2.8$ ,  $\beta_n 3.2$ ). In the model equations, this can be described by multiplication of all these activation and inactivation rate constants with a factor  $f$  of the form

$$f = Q_{10}^{\frac{(T-T_0)}{10}}. \quad (1)$$

The first step to arrive at the MSEN model was to introduce this type of temperature dependence in the FH non-linearities at the active nodes in the SENN model, with  $T_0=293.15$  K (20°C). As a next step, the size and shape of the modelled nerve fibre were adapted to represent a 10  $\mu$ m diameter motor fibre, which is more in the middle range of physiological sizes than the 20  $\mu$ m used by McNeal (MCNEAL, 1976) and Reilly *et al.* (REILLY *et al.*, 1985) (see Table 2). The internodal resistivity  $r_i$  strongly influences the impulse conduction velocity, but unfortunately it has not yet been measured reliably. As it presumably depends on temperature, in the present model a  $Q_{10}$  value of  $(1.3)^{-1}$  (MOORE *et al.*, 1978) is incorporated if temperatures below mammalian body temperature are considered.

Unlike in the original SENN model, the resting membrane potential  $V_r$  was computed with the Goldman equation (constant field equation, TAsAKI, 1982, p.139). In this way, variations in the ionic content of the extracellular medium can be accounted for. If it is assumed that the so-called non-specific permeability  $P_p$  is working on sodium (FRANKENHAEUSER and HUXLEY, 1964, p.303), the Goldman equation reads as follows:

$$V_r = \frac{RT}{F} \cdot \text{Ln} \left( \frac{P_K n_0^2 [K^+]_o + (P_{Na} h_0 m_0^2 + P_p p_0^2) [Na^+]_o}{P_K n_0^2 [K^+]_i + (P_{Na} h_0 m_0^2 + P_p p_0^2) [Na^+]_i} \right). \quad (2)$$

For an explanation of the symbols used in eqn. 2 and other symbols introduced below without definition, readers should refer to work by McNeal (MCNEAL, 1976), Reilly *et al.* (REILLY *et al.*, 1985) and to Table 2, which defines the so-called standard conditions. All computations were performed for nerve fibres in an infinite linear isotropic homogeneous medium using these standard conditions, unless stated otherwise.

The differential equations were integrated with a fourth-order Runge-Kutta method with adaptive step-size control (PRESS *et al.*, 1988), adapted for systems of coupled differential equations. The resulting step sizes varied between 0.01  $\mu$ s and 10  $\mu$ s. For all tested stimulus strengths and wave forms, the rise of the  $m$  parameter (describing the sodium channel activation) above 0.7 proved a new, simple and robust threshold criterion for the occurrence of the first spike. To determine the absolute and relative refractory period, we added the criterion that the action potential must be conducted along the nerve fibre to be able to recognise abortive spikes (Fig. 7). To standardise the measurement of the rise and fall times  $t_{rise}$  and  $t_{fall}$  of the simulated transmembrane action potential, its shape was simplified to a triangle with its top at the maximum of the original spike. The rising and falling edges of this triangular action potential were defined to cross the simulated spike at 10% of spike height. This procedure is illustrated in Fig. 2a.

Table 2 - Set of parameters defining the standard conditions for the MSEN model; the ionic concentrations are chosen in accordance with mammalian data (GUYTON, 1981); the nodal gap width is based on data from work by Waxman (WAXMAN, 1978); the values of  $r_i$  and  $r_e$ , the ratios  $d/D$  and  $L/D$  and the nodal parameters are adopted from the SENN model (REILLY *et al.*, 1985); the  $Q_{10}$  values for  $r_i$  and  $r_e$  are based on work by Moore *et al.* (MOORE *et al.*, 1978)

parameter	unit	symbol	standard value
axoplasm resistivity	$\Omega \cdot m$	$r_i$	1.1 (37.5°C) $Q_{10} = (1.3)^{-1}$
external resistivity	$\Omega \cdot m$	$r_e$	3.0 (37.5°C) $Q_{10} = (1.3)^{-1}$
membrane capacitance/ unit area	$F m^{-2}$	$c_m$	0.02
leak conductance/ unit area	$\Omega^{-1} m^{-2}$	$g_L$	303
sodium permeability constant	$\mu m s^{-1}$	$\bar{P}_{Na}$	80.0
potassium permeability constant	$\mu m s^{-1}$	$\bar{P}_K$	12.0
nonspecific permeability constant	$\mu m s^{-1}$	$\bar{P}_p$	5.4
intracellular sodium concentration	$mol m^{-3}$	$[Na^+]_i$	10
extracellular sodium concentrations	$mol m^{-3}$	$[Na^+]_o$	142
intracellular potassium concentration	$mol m^{-3}$	$[K^+]_i$	141
intracellular potassium concentration	$mol m^{-3}$	$[K^+]_o$	4.2
fibre diameter	$\mu m$	$D$	10
axonal diameter	$\mu m$	$d$	7
nodal gap width	$\mu m$	$l$	1
internodal distance	$\mu m$	$L$	1000
temperature	K	$T$	310.65 (= 37.5°C)

### 3 RESULTS

In Figs. 2 - 9 the properties of the MSENN model (standard conditions unless stated otherwise) are demonstrated. Table 1 summarises these data and compares them with the corresponding values for real 10  $\mu\text{m}$  nerve fibres at mammalian body temperature. The corresponding values of a nerve fibre of the same geometry but with nodes obeying the original FH kinetics (SENN), in addition to data regarding the model described by Sweeney *et al.* (SWEENEY *et al.*, 1987) are added for comparison. It is clear that the behaviour of the present model resembles the *in vivo* situation more than the other models. The various aspects of model behaviour are discussed in detail below.

#### 3.1 Shape of the action potential

Fig. 2<sup>c</sup> shows the shape of the transmembrane action potential generated by the MSENN model. The rise time  $t_{rise}$  of the resulting action potential is 0.07 ms, while  $t_{fall}$  is 0.26 ms. Spike duration thus amounts to 0.33 ms. The spike height  $V_p$  is 111 mV and  $V_r$  is -83 mV (eqn. 2), which results in +28 mV as the maximum intracellular potential. The potassium and sodium equilibrium potentials are -94 mV and +71 mV, respectively.

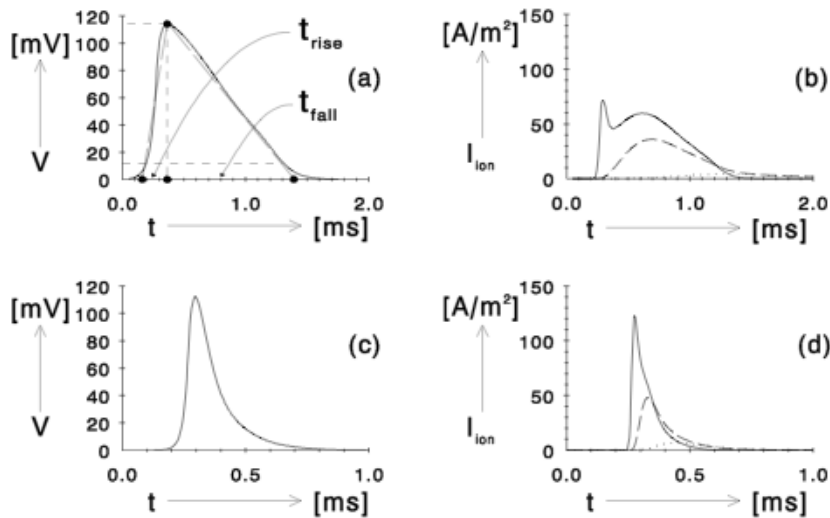


Fig. 2 - (a) Time course of the nodal potential  $V$  (i.e. the deviation of the transmembrane potential from its resting value) for an action potential simulated with the original SENN model; dashed lines illustrate the procedure used to approximate this action potential with a triangle and the definition of its rise time  $t_{rise}$  and its fall time  $t_{fall}$ ; (b) transmembrane ionic currents  $I_{ion}$  during the action potential in (a); solid line represents the sodium current  $I_{Na}$ , dashed line the potassium current  $I_K$ , the dotted line the non-specific current  $I_P$ ; (c) action potential generated by the MSENN model at 37.5°C; note that the time axis differs from that in (a); (d) as (b) but for the spike in (c).

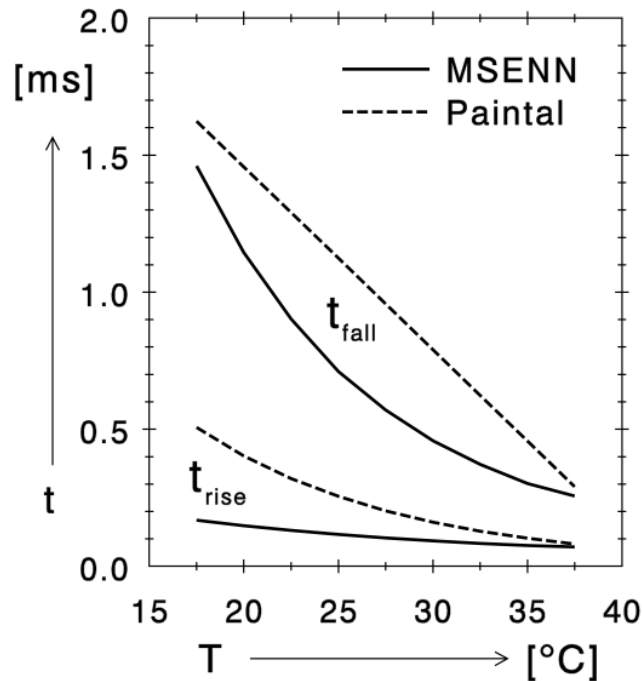


Fig. 3 - Rise time  $t_{rise}$  and fall time  $t_{fall}$  of the action potential generated by the MSENN model (solid lines) at temperatures between 17.5°C and 37.5°C, compared to measurements in the cat by Paintal (PAINTAL, 1966) (dashed curves).

For comparison, the action potential generated by the original SENN model is displayed in Fig. 2a. Obviously, the spike duration is much longer (1.24 ms), with a relatively short rise time of 0.19 ms. Figs. 2b and d show that the time course of the sodium current is also quite different in both models. This is mainly a temperature effect, reflecting the different  $Q_{10}$  values for the sodium activation and inactivation processes (Section 2).

In Fig. 3, the influence of temperature variations on  $t_{rise}$  and  $t_{fall}$  in the present model (solid curves) and *in vivo* in the cat (dashed lines; PAINTAL, 1966) is shown. As expected, both slopes of the spike decrease with increasing temperature, but the effect on the rising phase is smaller than it is on the falling one. For the temperature range between 27°C and 37°C, the model's  $Q_{10}$  is  $(1.48)^{-1}$  for  $t_{rise}$  and it is  $(2.22)^{-1}$  for  $t_{fall}$ . In lower temperature ranges, these effects are slightly stronger (Table 1).

### 3.2 Impulse conduction velocity

The conduction velocity  $v$  is  $59.4 \text{ ms}^{-1}$  in this  $10\mu$  fibre at 37.5°C. For lower temperatures,  $v$  is appreciably lower, with a  $Q_{10}$  value of 1.4 for the temperature range 17° - 37°C (Fig. 4). Although threshold currents increase when lower temperatures are simulated, the model does not exhibit a so-called blocking temperature below which impulses do not travel along the fibre. When the unmodified FH equations (as used in the SENN model) are applied

in a 10  $\mu\text{m}$  nerve fibre with the standard morphology,  $v$  is  $35.1 \text{ ms}^{-1}$ , a strongly incorrect value which expectedly hardly depends on temperature. The dashed curves in Fig. 4 show that the parameters which the largest influence on the temperature dependence of  $v$  are the temperature dependences of the FH parameters  $m$ ,  $h$ ,  $p$  and  $n$  and the temperature dependence of  $r_i$ . The introduction of the Goldman equation and the change in ionic content of the intra- and extracellular medium are minor alterations as far as spike conduction is considered. The Goldman equation does, however, make the nerve fibre sensitive to changes in the sodium and potassium concentrations; doubling the extracellular potassium concentration changes  $V_r$  from  $-83$  to  $-69 \text{ mV}$  and  $v$  is reduced from  $59.4$  to  $52.9 \text{ ms}^{-1}$ . On the other hand, if the extracellular sodium concentration is increased to  $200 \text{ mmol l}^{-1}$ ,  $V_r$  becomes  $-79 \text{ mV}$  and  $v$  increases to  $65.9 \text{ ms}^{-1}$ .

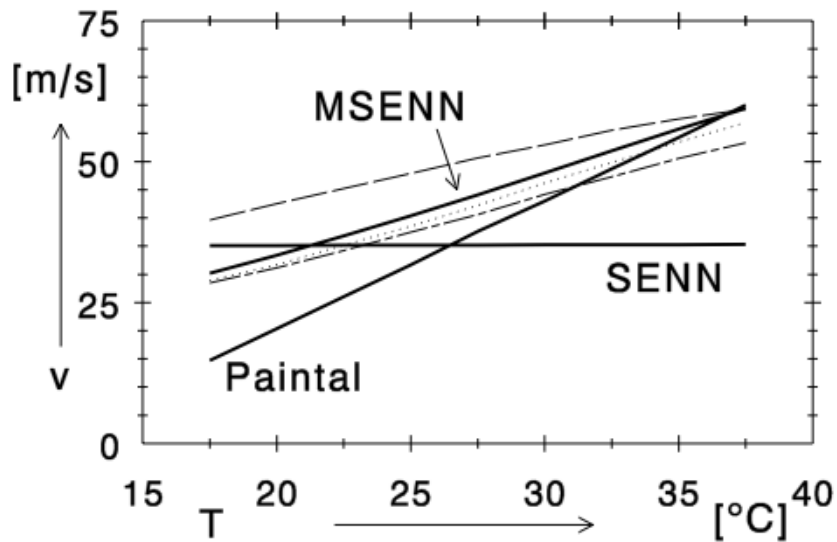


Fig. 4 - Spike conduction velocity  $v$  as a function of temperature  $T$ ; lines representing the MSENN model (standard conditions, Table 2), the SENN model (REILLY, *et al.*, 1985) with standard nerve morphology and *in vivo* measurements in the cat (PAINTAL, 1973) are labelled correspondingly; other curves demonstrate the relative importance of some parameters in the MSENN model; dashed line was computed with the MSENN model, with  $r_i = 1.1 \Omega\text{m}$  for all temperatures (otherwise standard conditions), dashed-dotted line was generated with MSENN model with  $V_r = -70\text{mV}$  (otherwise standard conditions), the dotted line with the MSENN model with amphibian sodium and potassium concentrations (otherwise standard conditions).

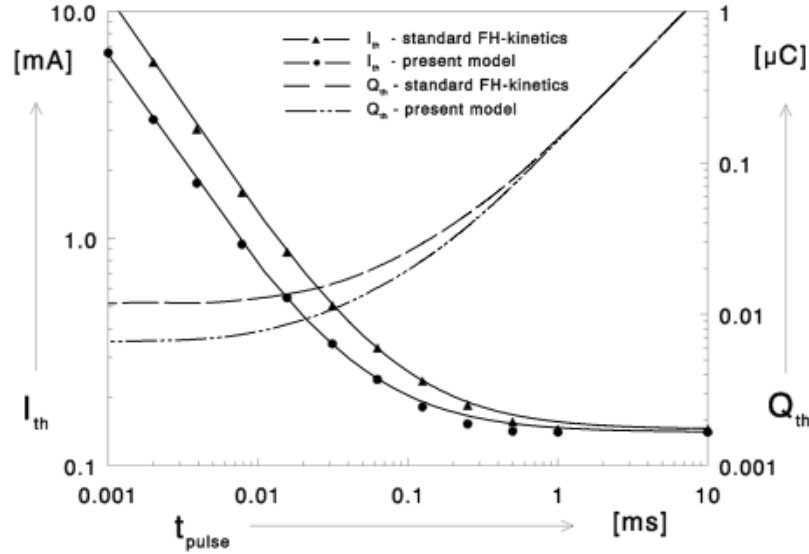


Fig.5 - Strength/duration curves for monophasic cathodal pulses for an electrode 1 internodal distance away from a nerve fibre under standard conditions; both the threshold currents  $I_{th}$  for pulses with duration  $t_{pulse}$  and the charge injected  $Q_{th} (= I_{th} \cdot t_{pulse})$  are shown for the MSENN model and for a nerve fibre with unmodified FH kinetics; continuous lines were drawn from the measured rheobase and chronaxy (eqn. 3); symbols represent measured points.

### 3.3 Strength/duration (SD) curves

Fig. 5 shows the relationship between the duration of monophasic cathodal pulses and the corresponding threshold current (SD curve) for a monopolar electrode one internodal distance away from the nerve fibre under standard conditions. The charge needed to produce an action potential (i.e. the product of pulse height  $I$  and pulse duration  $t_{pulse}$ ) is also displayed in this curve. The rheobase  $I_{rheo}$  (the threshold current for a pulse of infinite duration) is almost equal for both kinetics if the same model parameters are used otherwise, but the chronaxy  $t_{chr}$  (the threshold duration of a pulse twice as strong as the rheobase) is much shorter in the MSENN model (45  $\mu$ s vs. 80  $\mu$ s), as expected. Note that the points plotted in the SD curves in Fig. 5 were obtained by determining the threshold for pulses of the corresponding length, but that the curves between the points were computed from the measured rheobase and chronaxy with eqn. 3. This equation describes the classical hyperbolic relationship between  $I$  and  $t_{pulse}$ .

$$I = \left( 1 + \frac{t_{chr}}{t_{pulse}} \right) * I_{rheo} \quad (3)$$

Apparently, the simplified concepts of rheobase and chronaxy make sense in the context of both the original and the modified SENN model.

Additionally, Reilly *et al.* (REILLY *et al.*, 1985) interpret the strength/duration properties of their model in terms of an *equivalent strength/duration time constant*  $t_e$ , which they define as the *RC* time constant of a linear *RC* network model of a single node with an *SD* curve shape that best matches the shape of a given empirical curve. The value of  $t_e$  for the MSENN model is 55  $\mu\text{s}$ , whereas it is 100  $\mu\text{s}$  for the SENN model.

### 3.4 Refractory period

The absolute refractory period (ARP) is defined as the period after the initiation of an action potential in which it is impossible to elicit a second *propagated* action potential as a response to a second stimulus even if its strength is unlimited. The period thereafter is characterised by a state of reduced excitability, resulting in elevated thresholds for the generation of spikes. It is called the relative refractory period (RRP).

In the model described here, the ARP is 0.50 ms, as shown in Fig. 6. This figure was computed using 100  $\mu\text{s}$  cathodal current pulses (the first being 150% of threshold) from a monopolar electrode 1 mm (=1 internodal distance) away from the middle of a nerve fibre segment. The zero point of the time axis was chosen

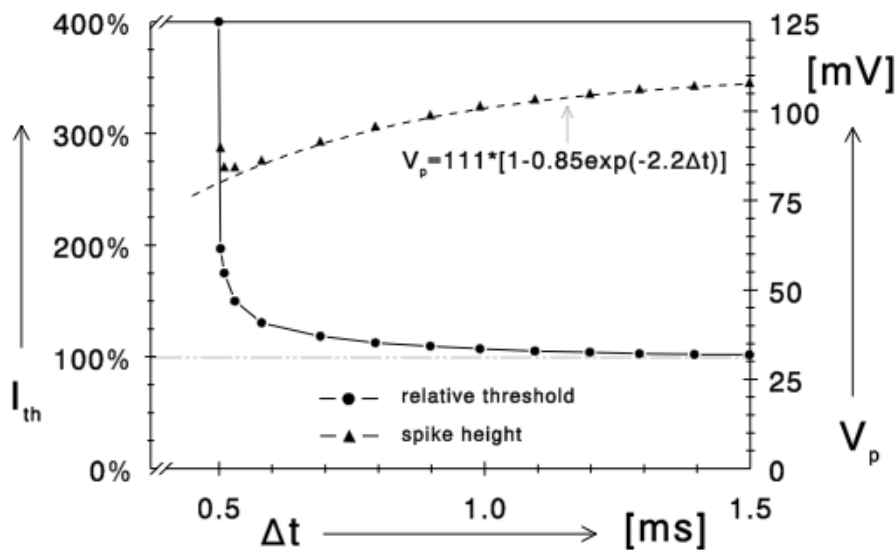
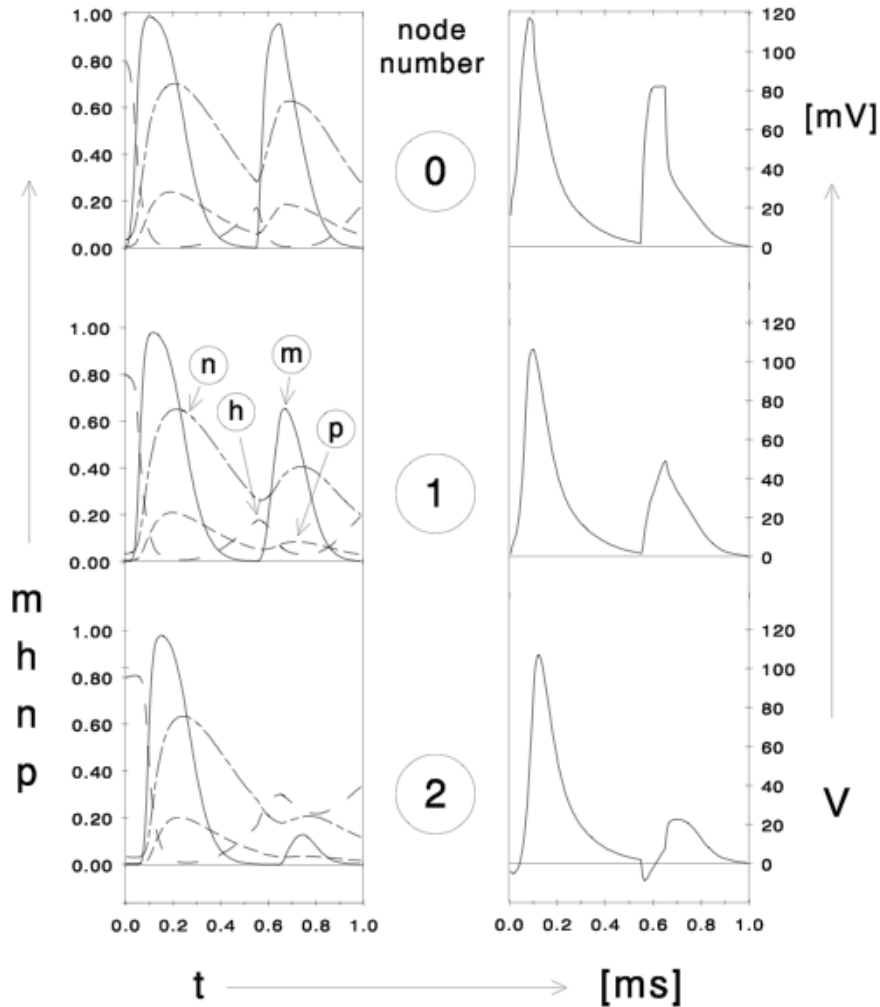


Fig. 6 - Threshold current  $I_{th}$  for eliciting an action potential (and its amplitude  $V_p$ ) in the relative refractory period of the MSENN model as a function of the time interval  $\Delta t$  elapsed since the initiation of the first spike; thresholds are measured relative to the threshold for the initiation of the first spike; dashed line through the triangles representing  $V_p$  is the exponential curve that fits these data optimal in a least squares sense; stimuli are cathodal pulses of 100  $\mu\text{s}$  duration.

at the beginning of the first spike (i.e. the moment  $m$  crosses the level 0.7) to reduce the influence of stimulus conditions on the calculated ARP. With the

stimulus used, this threshold is reached 92  $\mu$ s after the start of the stimulus. The  $Q_{10}$  of the ARP is  $(2.0)^{-1}$  in the temperature range 27°C–37°C. In the RRP, the threshold currents return quickly to almost pre-stimulus levels; at 1.0 ms after the beginning of the first spike, the threshold is just 7% elevated and the 1% level is reached at  $t = 1.85$  ms. The 'refractoriness' of the nerve fibre is also reflected in the height of the second action potential. It is as small as 70% of the height of the first spike in the early stages of the RRP, and it increases gradually to regain 99% of its original value at  $t = 2.00$  ms. A remarkable property of the model is the occurrence of local, abortive spikes at the end of the ARP. In a single node, these spikes are not distinguishable



the FH parameters  $m$ ,  $h$ ,  $n$  and  $p$ , and on the right the corresponding membrane potential  $V$ ; curves are shown for node 0, where the spike is initiated, and the adjacent nodes 1 and 2.

from normal spikes (e.g. by the transmembrane sodium or potassium currents, or the time course of the FH parameters  $m$ ,  $h$ ,  $p$  and  $n$ ), but they are not conducted to the end of the nerve fibre. The second action potential shown in Fig. 7 is such an abortive one. It is initiated in node 0, the node closest to the stimulating electrode. It travels to node 1 and 2 consecutively, but the traces for these adjacent nodes show that it is rapidly extinguished when it is conducted along the nerve fibre.

Owing to the strong stimulus required to elicit the phenomenon, a large stimulus artifact is discernible in the transmembrane potential, but the behaviour of the FH parameters shown on the left is similar for the first and the second spike, at least for node 0, and we cannot tell from the behaviour in node 0 that the spike is abortive.

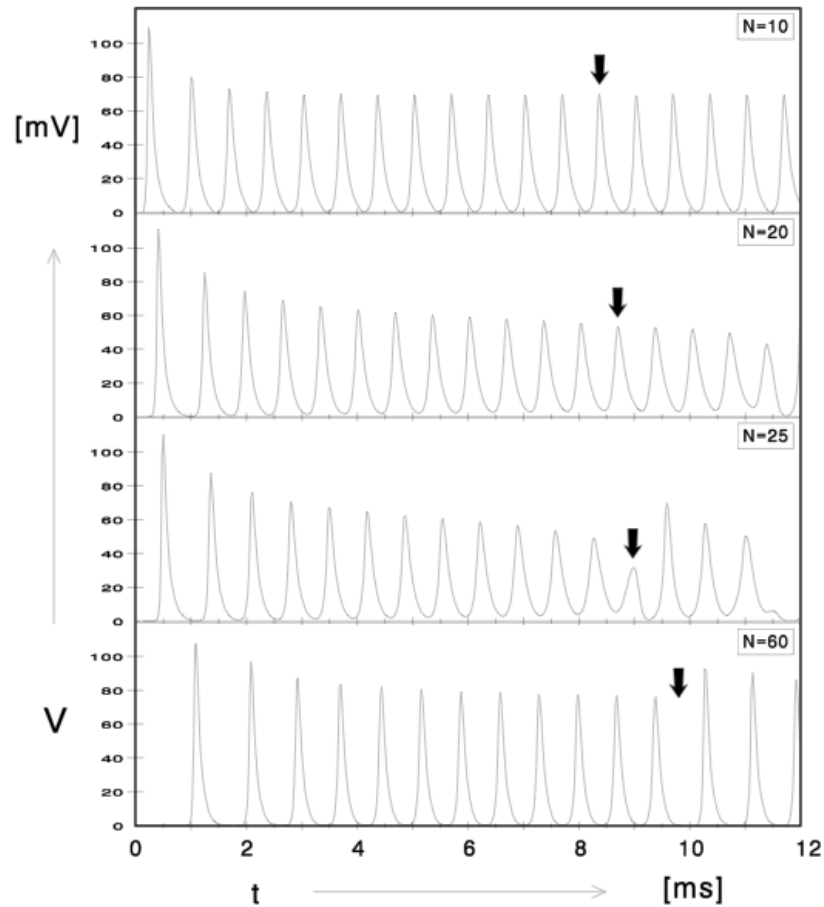


Fig. 8 - Spike abortion phenomenon demonstrated in a MSENN nerve fibre, stimulated at node 0 with cathodal pulses (1500 Hz repetition rate, first pulse at  $t = 0$ ); four simultaneous time traces are shown of the membrane potential  $V$  at node number  $N = 10, 20, 25$  and  $60$ ; arrows indicate the 13th action potential, which disappears before it reaches node 60 (reproduced with permission from FRIJNS and SCHOONHOVEN, 1992).

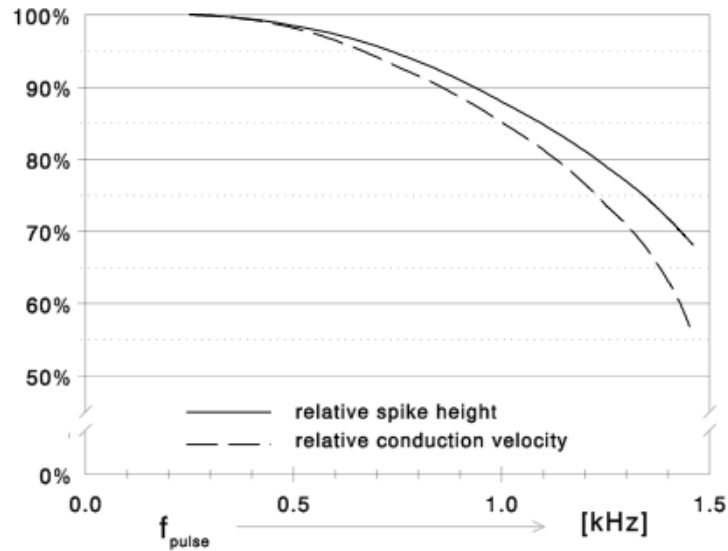


Fig. 9 - Relative spike height and conduction velocity as a function of stimulus rate  $f_{pulse}$  in the present model (standard conditions).

### 3.5 Frequency following

When fast repetitive stimuli are used, abortive spikes can also occur after several firings. This is illustrated in Fig. 8 for 100  $\mu$ s pulses with a repetition rate of 1500 Hz (at 200% of the threshold for the first spike). In this Figure, four time traces of the transmembrane potential  $V$  are shown for active nodes 10, 20, 25 and 60 internodal distances away from the node where the action potentials are elicited. In this case, consecutive spikes show decreasing amplitudes, and the average spike conduction velocity between the 20th and 60th node gradually decreases from its initial value of 59  $\text{m s}^{-1}$  for the first spike to 30  $\text{m s}^{-1}$  for the 12th spike. Finally, the 13th action potential (marked by an arrow in Fig. 8) is initiated and reaches node 20 like the previous ones, but it fails to travel further more than a couple of nodes and it never reaches node 60. A similar observation holds for the 17th spike, which does not even reach the 25th node. Thus, this spike abortion phenomenon induces a lower maximum discharge rate than the 2 kHz we might expect from the ARP value. Another interesting phenomenon illustrated by Fig. 8 is the changing height of a single action potential during its course along the nerve fibre. It gradually decreases initially but grows again later on. The spike conduction velocity also shows a minimum when a spike has travelled several internodal distances. Fig. 9 shows the dependence on firing frequency of the steady-state conduction velocity (again between nodes 20 and 60) and spike height (in node 60). Both  $v$  and  $V_p$  decrease gradually with increasing stimulus frequency, conduction velocity faster than spike height. The maximum steady-state discharge rate is slightly less than 1.5 kHz, when spike height is approximately 50% of its initial value.

## 4 DISCUSSION

The purpose of our MSEN model is to upgrade previous electrical nerve stimulation models for a realistic description of the behaviour of mammalian myelinated nerve fibres. It was developed from the SENN model (REILLY *et al.*, 1985), to which several modifications were introduced to adapt the originally amphibian data for warm-blooded animals.

The Goldman equation (eqn. 2) is used throughout to compute the resting membrane potential  $V_r$ . Under so-called standard conditions (Table 2),  $V_r$  is -83 mV, which is comparable with  $V_r = -80$  mV reported experimentally (BRISMAR, 1980).

When compared to the action potential generated by the original FH equations, the spike produced by the new model is significantly shorter and has a relatively large ratio of  $t_{rise}$  to  $t_{fall}$ . This is in accordance with the spike shape and duration reported by Paintal (PAINTAL, 1966), who extensively studied  $t_{rise}$  and  $t_{fall}$  in myelinated fibres in the cat (Table 1). When comparing data from different authors, we should bear in mind that the exact figures reported depend on the definition of spike duration used. Despite this, it is clear that the shape of the newly modelled action potential approximates the *in vivo* situation in mammals for more than the original SENN model, for which the spike duration is 1.24 ms.

As may be expected from the introduction of  $Q_{10}$  values for the FH parameters  $m$ ,  $h$ ,  $p$  and  $n$ , temperature does influence the shape of the action potential and the time course of the ionic currents in the MSEN model. However, the effect of large temperature variations on the spike shape is described only qualitatively by the present model, as the simulated  $Q_{10}$ s of  $t_{rise}$  and  $t_{fall}$  are relatively low (Table 1), and  $t_{fall}$  does not depend linearly on temperature as it does *in vivo* in the cat (Fig. 3). This discrepancy between the model and experimental data could be expected beforehand, as the model was developed using kinetics originally determined for amphibian nerve fibres at 20°C, with spike durations around 1.3 ms (FRANKENHAEUSER and HUXLEY, 1964). These spikes are significantly shorter than in the cat, for which Paintal (PAINTAL, 1966) recorded spike durations around 2 ms at 21.5°C in nerve fibres with normal conduction velocities around 60 m s<sup>-1</sup>. From this point of view, it is more surprising to note that the model fits mammalian data at normal body temperature in a quantitative manner.

Table 1 shows that the spike conduction velocity of the original SENN model is low when compared to measurements in mammalian nerve fibres. The ratio between conduction velocity  $v$  (in m s<sup>-1</sup>) and total fibre diameter  $D$  (in  $\mu\text{m}$ , axon and myelin sheath) was shown by Hirsch (HIRSCH, 1939) to be 6.0 for large fibres in the cat at 37.5°C. Boyd and Kalu (BOYD and KALU, 1979) reinvestigated this relation and found a mean ratio of 5.7 for the largest diameter fibres at temperatures between 35 and 37.5°C. At 37.5°C, the MSEN model gives a  $v/D$  ratio of 5.94, which is thus well within physiological ranges. In this model,  $v$  varies nearly linearly with temperature  $T$  as it does *in vivo*, but its  $Q_{10}$  is 1.4, a relatively low value. However, if the model is applied to electrical stimulation in mammals (body temperatures above 36°C), this difference between the model and experimental data is of little importance, as can be concluded from Fig. 4.

A comparison between the strength/duration (SD) curves of the SENN model and the MSENN model (Fig. 5) shows that the chronaxy, or alternatively the SD time constant  $t_e$ , is significantly shorter in the present model and that threshold charges for short pulses are lower. Reilly *et al.* (REILLY *et al.*, 1985) argue that sensory experiments by several investigators yield experimental values of  $t_e$  that are at least twice the value of 100  $\mu\text{s}$  computed with their model. This means that the lower  $t_e$  value of the present model is a shift in the wrong direction as far as sensory stimulation is concerned. On the other hand, Ranck (RANCK, 1975) reports a chronaxy of 29 - 59  $\mu\text{s}$  for extracellular stimulation of myelinated cat sural A fibres. The chronaxy value of 45  $\mu\text{s}$  of the MSENN model fits neatly in this range. This also means that the SD behaviour of the model is applicable in the field of functional electrical stimulation, i.e. neural prostheses for selective neuromuscular control (MEIER *et al.*, 1992).

The results in this paper also show that the refractory properties of the MSENN model resemble those of actual nerve fibres in many respects. In accordance with Paintal's work (PAINTAL, 1973), the absolute refractory period in the modelled fibre is about 1.5 times spike duration. If we define its end as the point where the threshold has returned to within 1% of its original value, the model's ratio RRP/ARP is 2.7, whereas it is about 4 *in vivo*. Thus, the model's relative refractory period is about one-third too short.

Regarding the occurrence of abortive spikes *in vivo*, Paintal (PAINTAL, 1973) reports that impulses can be initiated after the end of a spike; in fact, these are abortive because they are unable to propagate until they attain the so-called propagating amplitude, which is approximately 40% of the spike height. Fig. 7 shows that the MSENN model produces such abortive spikes, whereas Figs. 6 and 9 show that in this model the propagation amplitude is 55% - 70%, depending on stimulus conditions.

The maximum transmissible frequency is just below 1.5 kHz in the model situation (Figs. 8 and 9). As explained in Section 3.5, this is clearly lower than we would expect from the ARP but definitely higher than in real fibres. For fibres conducting at 60  $\text{m s}^{-1}$ , this peak frequency of discharge is about 800 Hz, which Paintal (PAINTAL, 1973) explains is due to spike abortion as every spike is travelling in the relative refractory phase of the preceding one and has a lower conduction velocity. From Figs. 8 and 9, it can be concluded that the model behaves similarly when repetitive firing is induced. This result stresses the fact that single-node models (MOTZ and RATTAY, 1986) should not be used for this purpose, even if only time aspects of nerve behaviour are considered.

In this context, it is worthwhile to reconsider Fig. 6, where the relation between 'refractoriness' and spike amplitude is shown. This gradual increase of spike amplitude with an increasing inter-stimulus interval was observed in cat peripheral nerve fibres by Paintal (PAINTAL, 1966) and in cat cochlear nerve fibres by Gaumond *et al.* (GAUMOND *et al.*, 1982). It has also been inferred from human compound action potentials by Stegeman *et al.* (STEGEMAN *et al.*, 1983), who described single-fibre action potential amplitude recovery with an exponential recovery function

$$V_p = \left[1 - \delta e^{-\gamma t}\right] * V_n \quad (4)$$

where  $V_n$  is the normal spike amplitude and  $V_p$  the actual spike amplitude. They deduced from the literature a 'rate of recovery'  $\gamma$  of  $2.5 \text{ (ms)}^{-1}$ . In Fig. 6, our simulation data shows that such an exponential curve, with  $\delta = 0.85$  and  $\gamma = 2.2 \text{ (ms)}^{-1}$  could be accommodated.

As the MSEN model shows a linear relationship between the diameter of a nerve fibre and its spike conduction velocity, changing the diameter influences this velocity in a realistic way, but there is no influence of the fibre diameter on spike duration and refractory behaviour. However, *in vivo* both the spike duration and the absolute refractory period vary inversely with fibre diameter (PAINTAL, 1966), effects which are not yet fully understood.

An explanation for quantitative discrepancies between the model and experimental data may be given by observations that mammalian nerve fibre kinetics is governed by different rules to those describing amphibian fibres (BRISMAR, 1980). Essentially, the difference is that mammalian fibres have far less active potassium channels and that repolarisation of the nerve fibre's membrane is mainly due to a relatively large leak conductance. The equations of Chiu *et al.* (CHIU *et al.*, 1979), as used by Sweeney *et al.* (SWEENEY *et al.*, 1987), do not incorporate any active potassium channels.

We have simulated a  $10 \text{ }\mu\text{m}$  fibre with these equations, using the parameter values given by Warman *et al.* (WARMAN *et al.*, 1992), and found that the spike shape and conduction velocity are comparable with those in the MSEN model (Table 1). However, the ARP is only slightly longer than the spike duration and, as a consequence, the fibre is able to transmit spike rates above  $2.1 \text{ kHz}$ , which is definitely too high. In addition, the chronaxy (determined with the method in Section 3.3) is less than half the value of the MSEN model. This means that, for relevant aspects of electrical stimulation models, the MSEN model yields a better fit of experimental data in mammals than Sweeney's model which uses mammalian data directly.

At present, we are studying a model based on voltage clamp data in the rat by Schwarz and Eikhof (SCHWARZ and EIKHOF, 1987). The results indicate, however, that the overall shape of the action potential and the time course of the sodium current are again not essentially different from those in the MSEN model.

Warman *et al.* (WARMAN *et al.*, 1992) introduced the total equivalent driving function, which eliminates the need to solve the full system of non-linear differential equations for the purpose of determining the excitation threshold for the first spike. This reduces the number of computations required for all nodal kinetics, including that presented in this paper. However, the full model is still required if an analysis of the response to repetitive stimuli, as used in neural prostheses, is desired in order to deal with abortive spikes (Figs. 7 and 8).

Another explanation for quantitative mismatches between the model and experimental results may be the obvious fact that the electrical characteristics of the internodal myelin sheath are deliberately neglected in the model. Halter and Clark (HALTER and CLARK, 1991) proposed a multi-axial cable model, in

which detailed anatomical data regarding the myelin sheath were incorporated. They found a spike conduction velocity of  $57.6 \text{ m s}^{-1}$  in a simulated  $17.5 \text{ }\mu\text{m}$  mammalian myelinated nerve fibre, which is obviously too low. Future research will have to clarify the exact role of the myelin sheath in nerve conduction.

A further serious drawback of an application of this kind of model for the design of electrical prostheses is the large amount of computing power required to solve the equations. The MSEN model, on the other hand, can be implemented on a simple personal computer and can describe many properties of mammalian nerve fibres adequately. Its spike shape, conduction velocity and absolute refractory period are well in agreement with experimental data. In addition, the model can describe the influence of temperature on various aspects of nerve behaviour and the consequences of repetitive firing. Examples of its application include motor nerve and auditory nerve stimulation, as repetitive stimulation is obligatory in these fields .

### **ACKNOWLEDGEMENTS**

The authors would like to thank Prof. Dr. J. J. Grote for continuous support throughout this work; J. Mooij for his assistance in developing the program; and to Dr. R. Schoonhoven for valuable comments on the first draft of the manuscript.

Part of this material was presented at the 14th Annual International Conference of the IEEE-EMBS, Paris, France, October 1992 (Frijns and Schoonhoven, 1992).

## REFERENCES

- BOYD, I. A., and KALU, K. U. (1979): 'Scaling factor relating conduction velocity and diameter for myelinated afferent nerve fibres in the cat hind limb,' *J. Physiol., Lond.*, **289**, pp. 277-297
- BRISMAR, T. (1980): 'Potential clamp analysis of membrane currents in rat myelinated nerve fibres,' *ibid.*, **298**, pp. 171-184
- CHIU, S. Y., RITCHIE, J. M., ROGART, R. B., and STAGG, D. (1979): 'A quantitative description of membrane currents in rabbit myelinated nerve. *ibid.*, **292**, pp. 149-166
- COLOMBO, J., and PARKINS, C. W. (1987): 'A model of electrical excitation of the mammalian auditory-nerve neuron,' *Hear. Res.*, **31**, pp. 287-312
- FRANKENHAEUSER, B., and MOORE, L. E., (1963): 'The effect of temperature on sodium and potassium permeability changes in myelinated nerve fibres of *Xenopus laevis*,' *J. Physiol. Lond.*, **169**, pp. 431-437
- FRANKENHAEUSER, B., and HUXLEY, A. F. (1964): 'The action potential in the myelinated nerve fibre of *Xenopus laevis* as computed on the basis of voltage clamp data,' *ibid.*, **171**, pp. 302-315
- FRIJNS, J. H. M., and SCHOONHOVEN, R., (1992): 'Refractoriness and Frequency Following Behavior in a Model of Electrical Stimulation of Mammalian Myelinated Nerve Fibres.' *Proc. Ann. Conf. IEEE-EMBS*, **14**, pp. 1372-1373
- GAUMOND, R. P., MOLNAR, C. E., and KIM, D. O. (1982): 'Stimulus and recovery dependence of cat cochlear nerve fibre spike discharge probability,' *J. Neurophysiol.*, **48**, pp. 856-873
- GORMAN, P. H., and MORTIMER, J. T. (1983): 'The effect of stimulus parameters on the recruitment characteristics of direct nerve stimulation,' *IEEE Trans.*, **BME-60**, pp. 407-414
- GUYTON, A. C. (1981): 'Textbook of medical physiology' (W. B. Saunders Company, Philadelphia) pp. 41-54
- HALTER, J. A., and CLARK, J. W. JR. (1991): 'A distributed-parameter model of the myelinated nerve fibre. *J. Theor. Biol.*, **148**, pp. 345-382
- HESS, A., and YOUNG, J. Z. (1949): 'Correlation of internodal length and fibre diameter in the central nervous system,' *Nature*, **164**, pp. 490-491
- HURSH, J. B. (1939): 'Conduction velocity and diameter of nerve fibres,' *Am. J. Physiol.*, **127**, pp. 131-139
- MCNEAL, D. R. (1976): 'Analysis of a model for excitation of myelinated nerve,' *IEEE Trans.* **BME-23**, pp. 329-337
- MEIER, J. H., RUTTEN, W. L. C., ZOUTMAN, A. E., BOOM, H. B. K., and BERGVELD, P. (1992): 'Simulation of multipolar fibre selective neural stimulation using intrafascicular electrodes,' *IEEE Trans.* **BME-39**, pp. 122-134
- MOORE, J. W., JOYNER, R. W., BRILL, M. H., WAXMAN, S. D., and NAJAR-JOA, M. (1978): 'Simulations of conduction in uniform myelinated fibres: relative sensitivity to changes in nodal and internodal parameters. *Biophys. J.*, **21**, pp. 147-160
- MOTZ, H., and RATTAY, F. (1986): 'A study of the application of the Hodgkin-Huxley and the Frankenhaeuser-Huxley model for electrostimulation of the acoustic nerve,' *Neurosci.*, **18**, pp. 699-712
- PAINTAL, A. S. (1966): 'The influence of diameter of medullated nerve fibres of cat on the rising and falling phases of the spike and its recovery,' *J. Physiol., Lond.*, **184**, pp. 791-811

- PAIN TAL, A. S. (1973): 'Conduction in mammalian nerve fibres' in DESMEDT, J. E. (Ed.): 'New developments in electromyography and clinical neurophysiology' (Karger, Basel) pp. 19-41
- PRESS, W. H., FLANNERY, B. P., TEUKOLSKY, S. A., and VETTERLING, W. T. (1988): 'Numerical recipes: the art of scientific computing' (Cambridge University Press, Cambridge) pp. 547-560
- RANCK, J. B. JR. (1975): 'Which elements are excited in electrical stimulation of mammalian central nervous system: a review,' *Brain Res.*, **98**, pp. 417-440
- REILLY, J. P., FREEMAN, V. T. and LARKIN, W. D. (1985): 'Sensory effects of transient electrical stimulation: evaluation with a neuroelectrical model,' *IEEE Trans.*, **BME-32**, pp. 1001-1011
- REILLY, J. P., and BAUER, R. H. (1987): 'Application of a neuroelectric model to electrocutaneous sensory sensitivity: parameter variation study,' *IEEE Trans.*, **BME-34**, pp. 752-754
- REILLY, J. P. (1989): 'Peripheral nerve stimulation by induced electric currents: exposure to time-varying magnetic fields,' *Med. Biol. Eng. Comput.*, **27**, (2), pp. 101-110
- SCHOEPFLE, G. M., and ERLANGER, J. (1941): 'The action of temperature on the excitability, spike height and configuration, and the refractory period observed in the responses of single medullated nerve fibers,' *Am. J. Physiol.*, **134**, pp. 694-704
- SCHWARZ, J. R., and EIKHOF, G. (1987): 'Na currents and action potentials in rat myelinated nerve fibres at 20 and 37°C,' *Pflügers Arch.*, **409**, pp. 569-577
- STEGEMAN, D. F., DE WEERD, J. P. C. and NOTERMANS, S. L. H. (1983): 'Modelling compound action potentials of peripheral nerves in situ. III: nerve propagation in the refractory period,' *Electroenceph. Clin. Neurophysiol.*, **55**, pp. 668-679
- STRUJIK, J. J., HOLSHEIMER, J., VAN DER HEIDE, G. G. and BOOM, H. B. K. (1992): 'Recruitment of dorsal column fibers in spinal cord stimulation: influence of collateral branching,' *IEEE Trans.*, **BME-9**, pp. 903-912
- SWEENEY, J. D., MORTIMER, J. T., and DURAND, D. (1987): 'Modelling of mammalian myelinated nerve for functional neuromuscular stimulation.' *Proc. Ann. Conf. IEEE-EMBS*, **9**, pp. 1577-1578
- TASAKI, I. (1982): 'Physiology and electro chemistry of nerve fibres'. (Academic Press, New York)
- TYLER, R. S., MOORE, B. C. J., and KUK, F. K. (1989): 'Performance of some of the better cochlear-implant patients,' *J. Speech Hear. Res.*, **32**, pp. 887-911
- VELTINK, P. H., VAN ALSTE, J. A., and BOOM, H. B. K. (1989): 'Multielectrode intrafascicular and extraneural stimulation,' *Med. Biol. Eng. Comput.*, **27**, (1), pp. 19-24
- WARMAN, E. N., GRILL, W. M., and DURAND, D. (1992): 'Modeling the effects of electric fields on nerve fibers: determination of excitation thresholds,' *IEEE Trans.*, **BME-39**, pp. 1244-1254
- WAXMAN, S. G. (1978): 'Variations in axonal morphology and their functional significance' in WAXMAN, S. G. (Ed.): 'Physiology and pathobiology of axons,' (Raven Press, New York) pp. 169-174

# Chapter III

---

## **A QUANTITATIVE APPROACH TO MODELING MAMMALIAN MYELINATED NERVE FIBERS FOR ELECTRICAL PROSTHESIS DESIGN**

*Johan H. M. Frijns, Member, IEEE, Jaap Mooij and Jaap H. ten Kate (1994)  
IEEE Trans. Biomed. Eng. 41 (6), 556-566.*

## Abstract

This paper presents an upgraded cable model of mammalian myelinated nerve fibers in an extracellularly applied field. The kinetics of the nodes is based upon voltage clamp data in rat motor fibers at 37°C [18], while the resting membrane potential is computed with the Goldman equation. The resulting spike shape, conduction velocity, strength/duration behavior, and absolute and relative refractory period are in good quantitative agreement with published experimental data in mammals at normal body temperature and at 20 °C. Results at intermediate temperatures however, suggest that the widely used concept of a constant  $Q_{10}$  for the rate constants is invalid. In addition, the model generates realistic abortive spikes towards the end of the absolute refractory period and it can describe the consequences of repetitive firing. The results stress the advantages of a multiple nonlinear node model even if only time aspects of nerve behavior are under study. It turned out, that the model presented here describes *in vivo* neural properties relevant for electrical prosthesis design better than previous models in literature.

## I. Introduction

Until the early eighties the insights into the physiology of single nerve fibers were predominantly based on measurements with the voltage clamp technique in unmyelinated [1] and myelinated [2] nerve fibers of cold blooded animals. Although there were indications that the situation is different [3] in mammals, it was generally assumed that mammalian nerve fibers are not essentially different from their cold blooded counterparts, although functioning at higher temperatures.

Using these data, several authors published models describing spike conduction and electric excitation in myelinated nerve fibers. Fitzhugh [4] assumed each node of Ranvier to obey the Hodgkin and Huxley equations and described the internodal myelin sheath as a distributed leaky capacitance. Goldman and Albus [5] used a similar model with nodes obeying the nonlinear Frankenhaeuser and Huxley [2] equations (further referred to as FH equations) to demonstrate a linear relationship between axon diameter and conduction velocity, which is in agreement with experimental data [6]. For purposes of functional electrical stimulation McNeal [7] developed the first model of a myelinated nerve fiber in an extracellularly applied field. In this model the myelin sheath is assumed to be a perfect insulator. All nodes of Ranvier are represented by a linear electrical circuit, except the so-called excitation node for which the FH equations are used. A further elaboration of the model was given by Reilly *et al.* [8] - [10]. His spatially extended nonlinear node model (SENN model) incorporates FH nonlinearities at each of several adjacent nodes. With the SENN model it is possible to simulate the behavior of myelinated nerve fibers under varying extracellular electrode configurations and stimulus patterns. The model is mostly used to describe nerve behavior in mammals, although it is derived from amphibian data [11], [12]. In the field of cochlear prostheses Colombo and Parkins [13] applied it to explain the strength/duration response to electrical stimulation of the auditory nerve (fiber

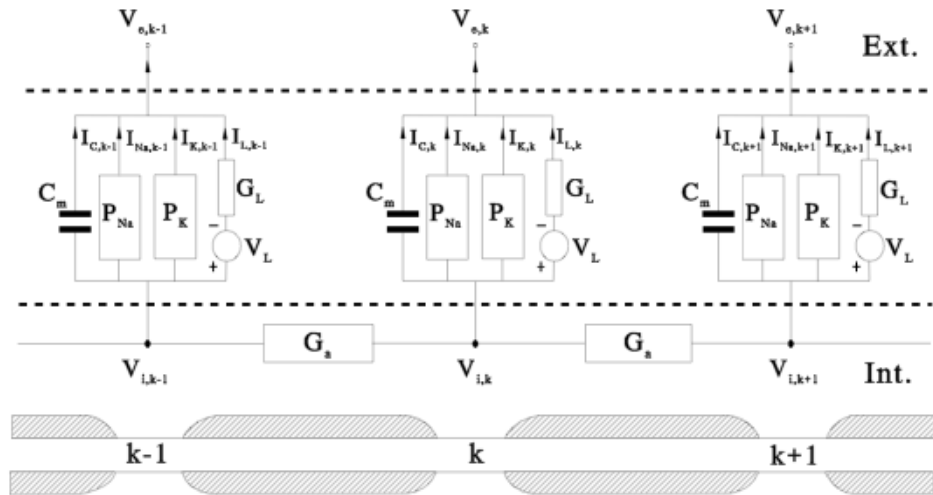


Fig. 1. Schematic representation of three nodes  $k-1$ ,  $k$  and  $k+1$  in the SEF model of a myelinated nerve fiber. In the lower part of the figure, the axon with its sheath of Schwann cells (shaded area) is displayed, with the model representation immediately above it. The nodal membrane with its permeability for Sodium ( $P_{Na}$ ) and Potassium ( $P_K$ ), its leak conductance ( $G_L$ ) and leak potential ( $V_L$ ), and its membrane capacitance ( $C_m$ ), is shown between the dashed lines. The currents flowing through the various channels are labeled correspondingly.  $V_{i,k-1}$ ,  $V_{i,k}$  and  $V_{i,k+1}$  are the intracellular potentials at the nodes, whereas  $V_{e,k-1}$ ,  $V_{e,k}$  and  $V_{e,k+1}$  are the corresponding extracellular potentials.  $G_a$  is the internodal conductance.

diameter 0.5 - 1  $\mu\text{m}$ ) in deafened squirrel monkeys. Unfortunately, their model cannot quantitatively describe the refractory and repetitive firing properties, which are essential in cochlear prostheses. We showed that a SENN model with adapted FH kinetics (further referred to as the MSENN model) can describe many aspects of the behavior of mammalian nerve fibers in a quantitative way [14]

In the last decades, there was growing evidence that mammalian nerve fiber kinetics is governed by rules that differ from those describing amphibian fibers [15], [16]. However, the overall shape of the action potentials is not essentially different from the ones generated by amphibian nerve fibers [17]. Essentially, the difference is that mammalian fibers have far less active potassium channels in the nodal area and that repolarization of the nerve fiber's membrane is mainly due to a relatively large leak conductance. Schwarz and Eikhof [18] (further referred to as SE) were the first to measure and describe quantitatively action potentials and membrane currents in single myelinated rat (and cat) fibers at 20 and 37  $^{\circ}\text{C}$ .

Sweeney *et al.* [19] incorporated the equations given by Chiu *et al.* [15] in the so-called CRRSS model, which is currently the most cited nerve fiber model in the context of functional electrical stimulation. In a previous paper [20] we showed, however, that the amphibian-based MSENN model is remarkably superior to the mammalian-based CRRSS model in its description of nerve

fiber properties that are essential for electrical prosthesis design, such as the frequency following behavior. A comparison of the properties of several single-node models for mammalian nodal membranes (including modified FH and SE equations) is also found in Rattay [21]. In the present paper, we will introduce a multiple nonlinear node model of myelinated motor fibers with nodes obeying the (mammalian) SE equations (see Fig. 1). This SEF model is tested by comparing its spike shape, its conduction velocity and its strength/duration curves at different temperatures to physiological data. A detailed study of the behavior of the modeled nerve fiber in the (relative) refractory period is carried out. Special attention is paid to the phenomenon of abortive spikes, the spike propagation and the repetitive firing abilities. Finally, the implications of the results for modeling mammalian myelinated nerve fibers will be discussed.

## II. Description of the Model

The set of parameters defining the so-called standard conditions is presented in the Appendix. These standard conditions are used for the computations throughout this paper unless explicitly stated otherwise. Here we give some specific considerations about the choice of these parameters. For the mathematical details of the model equations the reader is referred to the Appendix.

As stated above, the model presented here is based upon the measurements of Schwarz and Eikhof [18], who used motor fibers which were taken from rat and cat sciatic nerves. In order to be able to validate this so-called SEF model using experimental data from other authors, we first have to estimate the diameter and other relevant parameters of the modeled nerve fiber that were not extensively documented by SE.

It is well known that the duration and shape of action potentials depend on fiber diameter, e.g., from measurements of Paintal [22], who extensively studied rise time  $t_{rise}$  and fall time  $t_{fall}$  in myelinated fibers in the cat. At 37 °C the duration of the spikes recorded and simulated by SE is about 0.3 ms with  $t_{fall} \approx 0.23$  ms. Comparison of this spike shape with Paintal's data leads to the conclusion that SE must have used fibers with an action potential conduction velocity  $v$  of approximately 85 m/s. Then, the total fiber diameter  $D$  of the average neuron Schwarz and Eikhof most likely used can be estimated by application of the relation  $v = D \cdot 5.7 \times 10^6 \text{ s}^{-1}$  as experimentally observed by Boyd and Kalu [23]. This gives  $D = 15 \mu\text{m}$ , which is well within the range of large motor fibers (also called A-fibers). This estimated value of the total fiber diameter was used for all computations in the present paper, while the axon diameter  $d$  was 70% of this value. The length  $l$  of the nodes of Ranvier used in the computations is  $1 \mu\text{m}$  and the internodal distance  $L$  is 1.5 mm, i.e.,  $100 D$ .

This fiber geometry was used to convert the total nodal sodium and potassium permeability  $P_{Na}$  and  $P_K$  and the total nodal leak conductance  $G_L$  as used by Schwarz and Eikhof to the corresponding quantities per unit area, which will be relevant in forthcoming adaptations of the model to thin fibers as present in the auditory nerve. The sodium and potassium concentrations inside and outside the nerve cell were changed from those in Ringer's solution to mammalian

values according to Guyton [24]. All computations in this paper were performed for nerve fibers in an infinite linear isotropic homogeneous medium. The temperature dependence (expressed as  $Q_{10}$ 's) of the rate constants for  $m$  (sodium activation),  $h$  (sodium inactivation) and  $n$  (potassium activation) was taken from the SE paper. The internodal resistivity  $r_i$  was adopted from the original SENN model to be  $1.1 \Omega \cdot m$  at  $20^\circ C$ . In fact, this parameter, which strongly influences the impulse conduction velocity, has not been measured reliably yet. However, it presumably does depend on temperature; Moore *et al.* [25] argue that  $r_i$  has a  $Q_{10}$  value of  $(1.3)^{-1}$  (or  $-1.3$  in a notation frequently used in physiological literature). In the present model this value was incorporated, giving  $r_i = 0.7 \Omega \cdot m$  at  $37^\circ C$ .

In the SE equations, the resting membrane potential  $V_r$  was fixed at  $-78$  mV, rather than computed from the ionic contents and membrane properties as one might expect. We have followed a different approach and use the Goldman equation (constant field equation [26, p. 139])

$$V_r = \frac{RT}{F} \ln \left( \frac{P_K n_0^2 [K^+]_o + \overline{P_{Na}} h_0 m_0^3 [Na^+]_o}{P_K [K^+]_i + \overline{P_{Na}} h_0 m_0^3 [Na^+]_i} \right). \quad (1)$$

In this way, variations in the ionic content of the extracellular medium can be accounted for. For an explanation of the symbols used in (1) and other symbols introduced below without definition, the reader is referred again to the Appendix.

### III. Computational Aspects

The model equations were integrated with a fourth order Runge-Kutta method with adaptive stepsize control [27], adapted for systems of coupled differential equations. The resulting stepsizes varied between  $0.01 \mu s$  and  $10 \mu s$  and computing speed was comparable with the conventional Runge-Kutta method and a stepsize of  $1 \mu s$ . The former method is superior in maintaining numerical stability if large stimuli of short duration, applied in the relative refractory period, are to be simulated.

The membrane equations were dynamically initialized by requiring that the membrane is stable in each node  $k$  at rest, i.e.,  $dm_k/dt = dh_k/dt = dn_k/dt = 0$  for  $V_k = 0$  (See (A.4)). As a consequence of the use of (1), the leak potential  $V_L$ , which is computed from the requirement that the net transmembrane current must be zero under resting conditions, becomes zero and can be eliminated from the equations.

Reilly *et al.* [8] used as a threshold criterion the occurrence of an  $80$  mV depolarization in response to monophasic stimuli. For biphasic stimuli they required unambiguous propagation of an action potential. In the present study a more robust threshold criterion was used that allowed computer-controlled iterative determination of threshold currents irrespective of the stimulus wave form or electrode configuration. For all tested stimulus strengths and wave forms the rise of the  $m$  parameter (describing the sodium channel activation)

above 0.7 proved adequate for this purpose. Using this criterion, the program allowed the automatic determination of strength/duration curves, impulse conduction velocity  $v$  and absolute and relative refractory period. In our study of the refractory period, we added the criterion that the action potential must be conducted along the nerve fiber, to deal with abortive spikes which occur towards the end of the absolute refractory period. To standardize the measurement of the rise and fall times  $t_{rise}$  and  $t_{fall}$  of the simulated transmembrane action potential its shape was simplified to a triangle with its top at the maximum of the original spike. The rising and falling edges of this triangular action potential were defined to cross the simulated spike at 10% of spike height. To assess  $t_{fall}$  reliably it is essential that the length of the actively modeled segment is at least as large as the spatial extent of the spike. In the present study we used 25 nodes to determine spike shape and conduction velocity, which amply fulfilled this criterion.

## IV. Results

In Figs. 2 - 8 the properties of the present SEF model (standard conditions unless stated otherwise, see Appendix) are demonstrated. Table I summarizes these data and compares them with the corresponding values for real mammalian 15  $\mu\text{m}$  nerve fibers at body temperature. The corresponding values of a nerve fiber of the same geometry but with nodes obeying temperature dependent FH equations (MSENN, [20]) and the CRRSS model [19] respectively, are added in this table for comparison. The various aspects of the model behavior will be discussed in detail below.

### A. The Shape of the Action Potential

The action potential generated by the SEF model at 37 °C is shown in Fig. 2 (a). To avoid a stimulus artifact in this figure, a nerve fiber with 25 nonlinear nodes was depolarized at its first node and the spike was recorded after traveling 12 nodes along. The rise time  $t_{rise}$  of the action potential is 0.083 ms and  $t_{fall}$  is 0.243 ms. Spike duration thus amounts to 0.33 ms. The spike height  $V_p$  is 108 mV and  $V_r$  is -85 mV (1), which results in +23 mV as the maximum intracellular potential. The potassium and sodium equilibrium potentials are -94 mV and +71 mV respectively.  $V_r$  is -80 mV when the original ionic concentrations from the SE paper are used to compute  $V_r$  with (1), which is only slightly more negative than the fixed value of -78 mV as used in that paper.

In Fig. 2(c) the spike computed with modified FH kinetics is shown for comparison. Although the underlying spike generating mechanism is essentially different (see Section I) and the potassium currents are much larger (Fig. 2(b) versus (d)), the overall spike shape and the time course of the sodium current are comparable to the spike in Fig. 2 (a).

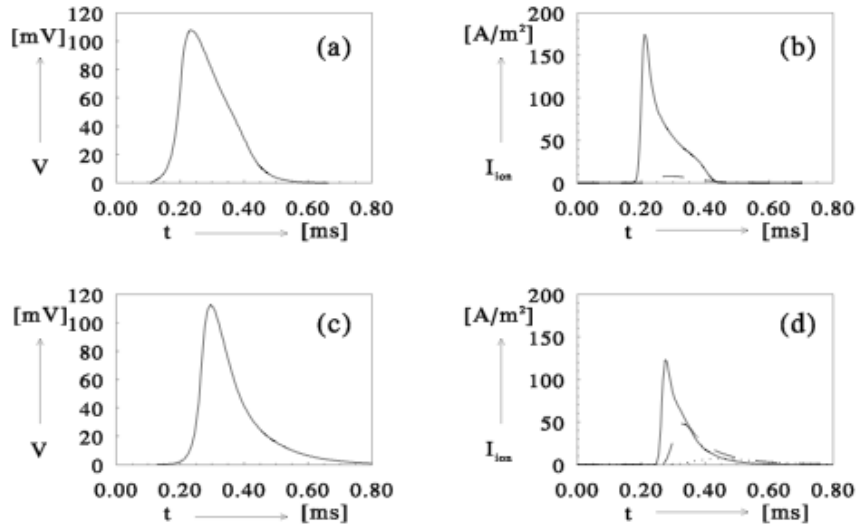


Fig. 2. (a) The time course of the nodal potential  $V$  (see (A.4) for its definition) for an action potential simulated with the SEF model. (b) The transmembrane ionic currents  $I_{ion}$  during the action potential in (a). The solid line represents the sodium current, the dashed one the potassium current. (c) The action potential generated by the MSEN model at 37°C. (d) As (b), now for the spike in (c). The short-dashed line represents the nonspecific current.

The amplitude of the action potential increases if the temperature  $T$  is lowered: it is 115 mV at 27°C and 117 mV at 20°C. With falling temperature  $t_{rise}$  increases with  $Q_{10} = (1.9)^{-1}$  as does  $t_{fall}$  with a  $Q_{10}$  value of  $(2.4)^{-1}$  for the temperature range between 27°C and 37°C. In the temperature range between 18 and 28°C these effects are slightly stronger ( $Q_{10} = (2.1)^{-1}$  and  $(2.7)^{-1}$  respectively). In Fig. 2(a), the influence of these temperature variations on the duration of the rising and the falling phase of the spike is shown for the present model and in Fig. 3(b) for *in vivo* measurements in the cat [22].

### B. Impulse Conduction Velocity

The spike conduction velocity  $v$  was measured simultaneously with the determination of the shape of the action potential. For the simulated 15  $\mu\text{m}$  nerve fiber under standard conditions  $v$  was 84.2 m/s, giving  $Y = 5.61 \cdot 10^6 \text{s}^{-1}$ . As shown in curve 1 in Fig. 4,  $v$  strongly depends on  $T$  with  $Q_{10} = 1.8$  for the temperature range between 27 and 37°C, while  $Q_{10} = 2.0$  when measured between 18 and 28°C. If the temperature dependence of  $r_i$  is omitted,  $Q_{10}$  for  $v$  is 1.5 (27 - 37°C, see Fig. 4, curve 5). The model does not exhibit a so-called blocking temperature below which impulses do not travel along the fiber.

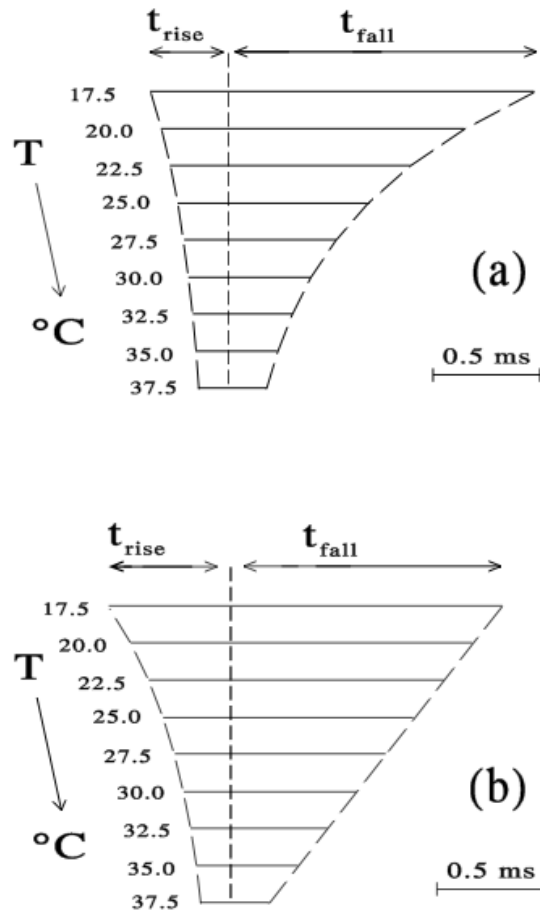


Fig. 3. (a) The rise time  $t_{\text{rise}}$  and the fall time  $t_{\text{fall}}$  of the single-fiber action potential generated by the SEF model at temperatures between 17.5 $^{\circ}\text{C}$  and 37.5 $^{\circ}\text{C}$ . (b) As (a), now for action potentials recorded in the cat [22].

In the FH based MSEN model with temperature dependent rate constants,  $Q_{10}$  is 1.2 for  $v$  in the range 27 - 37 $^{\circ}\text{C}$ . It increases to 1.4 if a  $Q_{10}$  value of  $(1.3)^{-1}$  is used for  $r_i$  (Fig. 4, curve 3). In the original (FH based) SENN model,  $Y$  is  $2.15 \cdot 10^6 \text{s}^{-1}$ . Using its FH kinetics in a 15  $\mu\text{m}$  fiber with the standard morphology gives  $Y = 3.51 \cdot 10^6 \text{s}^{-1}$ . This value is of course fairly independent of temperature (Fig. 4, curve 4), since  $T$  is only substituted in the constant field terms of the ionic currents. The introduction of the Goldman equation and the change in ionic content of the intra- and extracellular medium are minor alterations as far as spike conduction is considered. In other words, the parameters which have the largest influence on the temperature dependency of  $v$  are the temperature dependencies of the rate constants  $m$ ,  $h$  and  $n$  and the temperature dependency of  $r_i$ .

### C. Strength/Duration (SD) Curves

When stimulating current is being passed in constant current pulses, the relation between the amount of current  $I$  and the duration of the pulse  $t_{pulse}$  which just gives rise to an action potential yields the well known strength/duration curves. The current threshold of a long duration pulse is called the rheobase  $I_{rh}$ , whereas the chronaxy  $t_{chr}$  is defined as the time on the SD curve corresponding to twice  $I_{rh}$ . Many SD curves (including those derived with the model) fit the empirical equation

$$I = I_{rh} * \left( 1 + \frac{t_{chr}}{t_{pulse}} \right). \quad (2)$$

As can be seen in Fig. 5, in the SEF model both  $I_{rheo}$  and  $t_{chr}$  depend strongly on the position of the stimulating (current-driven) electrode relative to the nerve fiber and the polarity of the stimulus. For cathodal stimulation, chronaxy values between 28  $\mu$ s and 45  $\mu$ s are found, with the smallest values for the current source positioned very close to the nerve fiber. Anodal stimulation results in smaller chronaxies (between 17  $\mu$ s and 39  $\mu$ s) and higher thresholds, but the difference between the chronaxy for the two stimulus modalities decreases with increasing distance. The polarity selectivity ratio (defined as

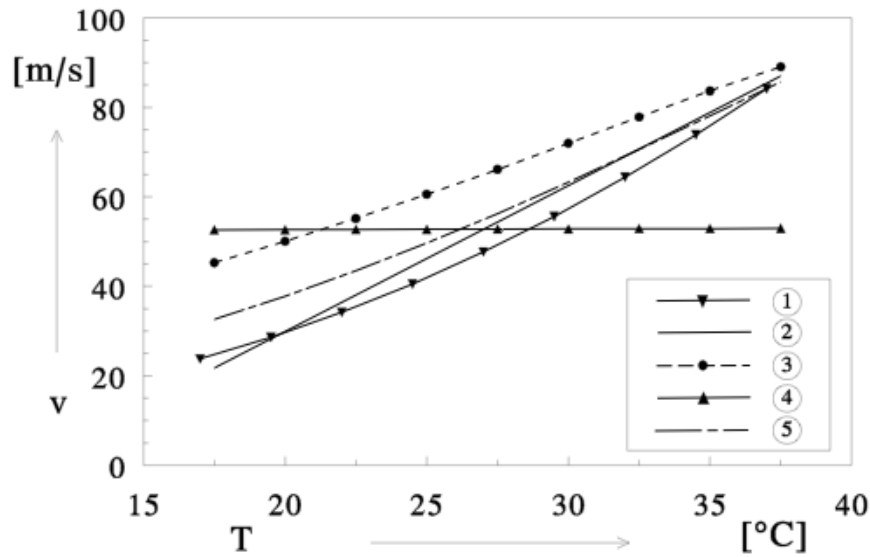


Fig. 4. The dependence of impulse conduction velocity  $v$  on temperature  $T$ :  
 1) The SEF model presented in this paper (standard conditions, Appendix).  
 2) *In vivo* measurements in the cat after Paintal [35].  
 3) The MSENN model (Frijns and Schoonhoven [14]), with standard nerve morphology and temperature dependency.  
 4) The SENN model [8], standard nerve morphology.  
 5) The SEF model with  $r_1 = 0.7 \Omega \cdot m$ , otherwise standard conditions.

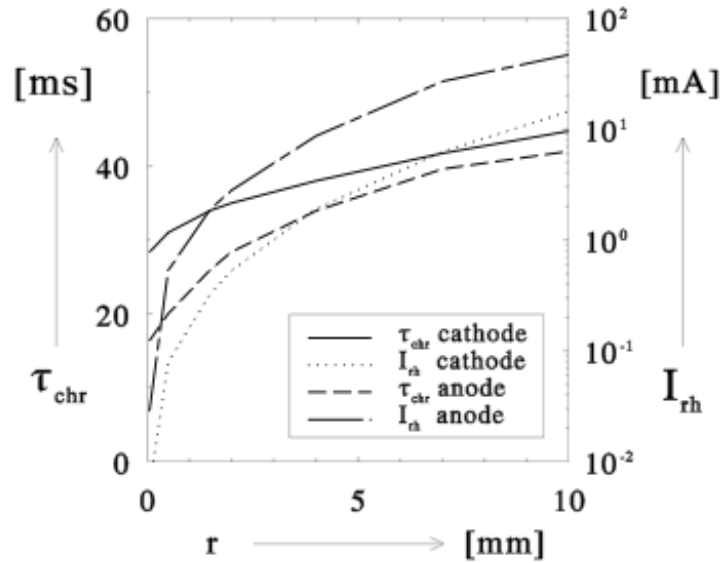


Fig. 5. The chronaxy  $t_{chr}$  (left axis) and the rheobase current  $I_{rh}$  (right axis) of the SEF model as a function of the distance  $r$  to the nerve fiber (standard conditions, Appendix) for monopolar anodal and cathodal stimulation.

the ratio between thresholds for anodal and cathodal stimulation) varies between 4.2 and 6.6, depending on electrode position and pulse duration, with lower values for shorter pulses and more distant electrodes. For the purpose of comparison of model results with other temperatures, a monopolar electrode, one internodal distance radially away from a node of Ranvier was used. Under these circumstances  $t_{chr}$  is 34  $\mu$ s at 37°C and 56  $\mu$ s at 27°C for cathodal pulses and 26  $\mu$ s and 43  $\mu$ s for anodal stimuli at 37 and 27°C respectively.

#### D. Refractory Period

The absolute refractory period (ARP) is defined as the period after the initiation of an action potential in which it is impossible to elicit a second *propagated* action potential as a response to a second stimulus even if its strength is unlimited. The period thereafter is called the relative refractory period (RRP). It is characterized by a state of reduced excitability, resulting in elevated thresholds for the generation of spikes.

In the model described here, the ARP is 0.60 ms and its  $Q_{10}$  is  $(2.0)^{-1}$  in the temperature range from 27°C to 37°C. These values were determined using 100  $\mu$ s cathodal pulses from a monopolar electrode one internodal distance (1.5 mm) away from the middle of a nerve fiber segment with 25 active nodes and 10 passive nodes at both ends. The first spike was elicited with a stimulus current 150% of threshold. The zero point of the time axis was chosen at the

beginning of the first spike (i.e., the moment  $m$  crosses the level 0.7, see Section III) to reduce the influence of stimulus conditions on the calculated ARP. With the 100  $\mu$ s pulse used this level is reached 49  $\mu$ s after the start of the stimulus.

In Fig. 6, the behavior of the nerve fiber model in the RRP is shown. The threshold currents return quickly to almost pre-stimulus levels: at 1.25 ms after the beginning of the first spike the threshold is just 10% elevated and the 1% level is reached at  $t = 3.0$  ms. The refractoriness of the nerve fiber also influences the height of the second action potential. Ten nodes from the excitation point it is as small as 70% of the height of the first spike in the early stages of the RRP and it increases gradually to regain 90% of its original value at  $t = 3.0$  ms.

A remarkable property of the model is the occurrence of local, abortive spikes at the end of the ARP. In a single node near the point of excitation these spikes are not distinguishable from normal spikes (e.g., by the transmembrane sodium or potassium currents or the time course of  $m$ ,  $h$  and  $n$ ), but they are not conducted to the end of the nerve fiber. Expectedly, the time interval in which such abortive spikes are elicitable increases with falling temperature.

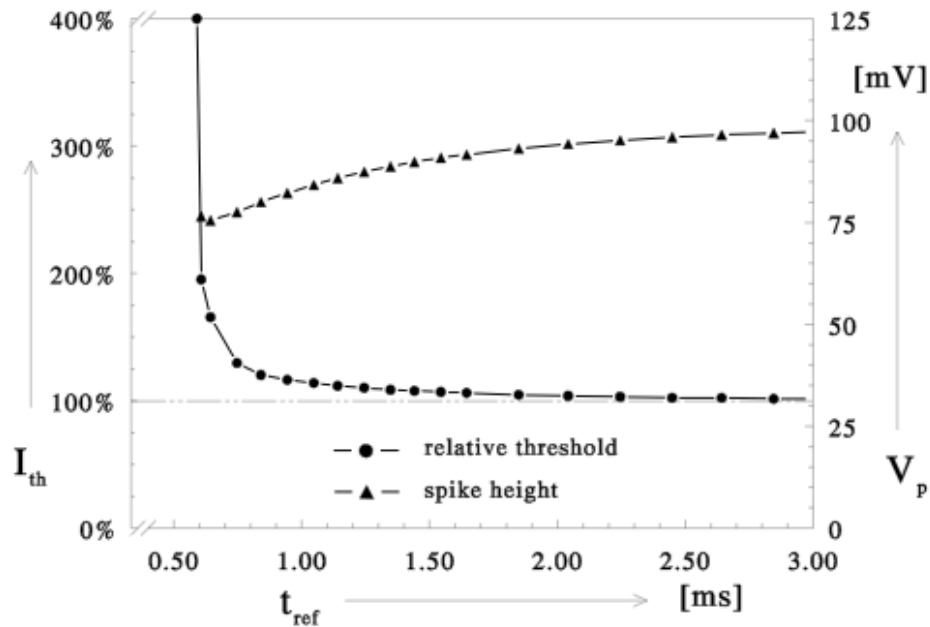


Fig. 6. The threshold current  $I_{th}$  for eliciting a second action potential in the refractory period,  $t_{ref}$  after the initiation of the first one. The stimuli are cathodal pulses of 100  $\mu$ s duration. Thresholds are measured relative to the threshold for the initiation of the first spike. The triangles represent the amplitude  $V_p$  of the second action potential.

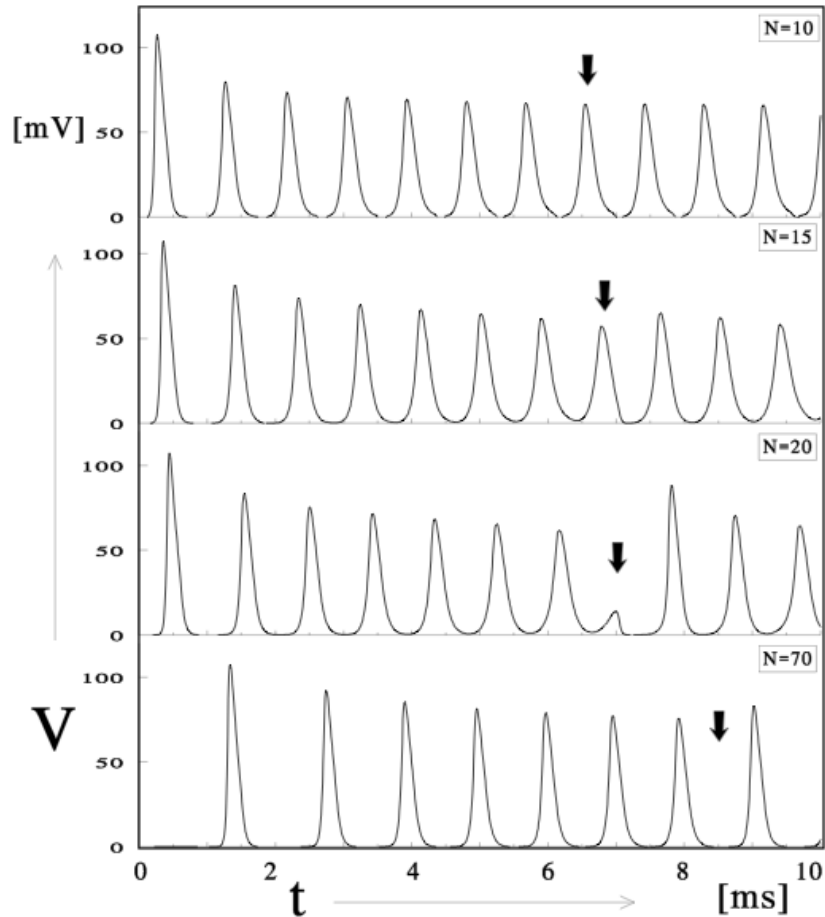


Fig. 7. Time traces of membrane potential  $V$  at node number  $N = 10, 15, 20$  and  $70$  of a nerve fiber stimulated at node  $0$  with cathodal pulses at a  $1150$  Hz rate, starting at  $t = 0$ . The arrows indicate the eighth action potential, which disappears before it reaches node  $60$  (standard conditions).

#### E. Frequency Following Behavior

Abortive spikes can also occur after several firings when fast repetitive stimuli are used. This is illustrated in Fig. 7 for  $100 \mu\text{s}$  pulses with a repetition rate of  $1150$  Hz (at  $200\%$  of the threshold for the first spike). In this figure, four time traces of the transmembrane potential  $V$  are shown for active nodes,  $10, 15, 20,$  and  $70$  internodal distances away from the point where the action potentials are elicited. In that case each consecutive spike is somewhat smaller than the previous one and the spike conduction velocity at the  $70$ th node gradually decreases from its initial value of  $84$  m/s for the first spike to  $47$  m/s for the seventh spike. Finally, the eighth action potential (marked by an arrow in Fig. 7) is initiated and reaches node  $15$  like the previous ones but it fails to travel further more than a couple of nodes and it never reaches node  $70$ . A similar observation holds for the  $12$ th spike. Thus, although one might expect from the refractory curve that the modeled nerve fiber can fire at rates above  $1.6$  kHz (i.e., signal periods above ARP), this spike abortion phenomenon results in a lower maximum discharge rate.

An interesting phenomenon that is illustrated by Fig. 8(a) is the changing height of a single action potential during its course along the nerve fiber. It gradually decreases initially but later on it is growing again. A similar observation holds for the spike conduction velocity (Fig. 8(b)), which also shows a minimum when a spike has traveled several internodal distances. After the abortion of a spike the next one has a larger amplitude and is initially conducted with an elevated conduction velocity, but eventually its amplitude decreases and it slows down to reach the same velocity as the previous one. The net effect at node 70 is that the spikes arrive almost regularly spaced in time with a 950 Hz repetition frequency. The steady state conduction velocity and spike height decrease gradually with increasing stimulus frequency, conduction velocity faster than spike height. The maximum steady state discharge rate  $f_{max}$  is approximately 1.1 kHz, when  $v$  (at node 70) is 50% of its initial value and  $V_p$  65%.

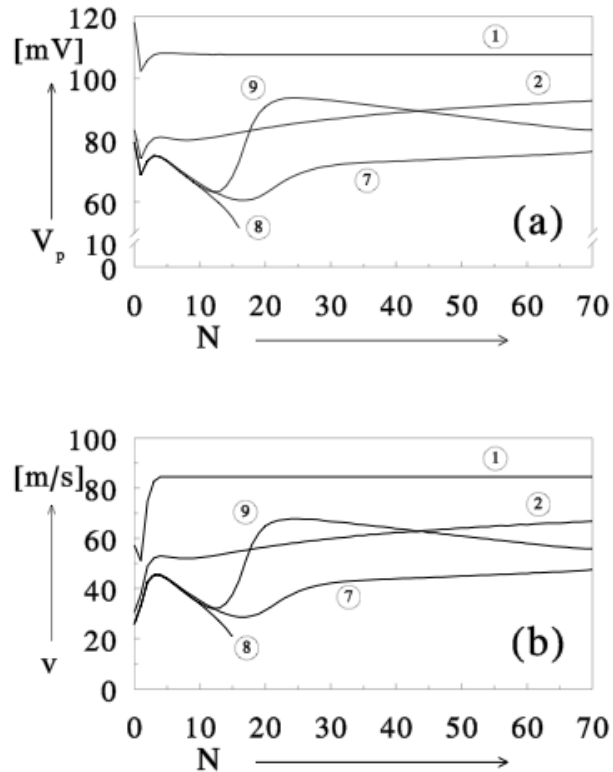


Fig.8. (a) The spike height  $V_p$  of the first, second, seventh, eighth (abortive), and ninth spike as measured at node number  $N$  in a nerve fiber stimulated with 100  $\mu$ s cathodal pulses at a rate of 1150 HZ. (i.e. the situation of Fig. 7). The numbers in circles represent the spike number. (b) The conduction velocity  $v$  along the nerve fiber of the five spikes of which the height is shown in (a). Clearly, the time course of  $v$  closely resembles the one of  $V_p$ .

Table I - Summary of model results for the present model (SEF) of a 15  $\mu\text{m}$  myelinated nerve fiber, compared to *in vivo* measurements by Paintal in the cat [35], to the original SENN model [8], the CRRSS model [19] and to the SENN model with temperature dependent FH kinetics (MSENN, [20]). The model values for the chronaxy  $t_{chr}$  were computed for extracellular cathodes at distances between 50  $\mu\text{m}$  and 10 mm to the fiber. The experimental value of the chronaxy  $t_{chr}$  was taken from Ranck [33] (see text), the one for the  $v/D$  ratio  $Y$ , from Boyd and Kalu [23]. All SEF model results were computed for standard conditions (Appendix). See the text for an explanation of symbols.

		15 $\mu\text{m}$ A fiber	SENN (1985)	CRRSS (1987)	MSENN (1992)	SEF
$Y$	( $10^6\text{s}^{-1}$ )	5.7	2.15	5.72	5.94	5.61
$Q_{10,v}$	27°-37°C	1.6	1.0	1.7	1.4	1.8
	18°-28°C	2.5	1.0	2.1	1.4	2.0
$t_{rise}$	(ms)	0.08	0.19	0.06	0.07	0.08
$Q_{10,t_{rise}}$	27°-37°C	(2.5) <sup>-1</sup>	1.0	(2.3) <sup>-1</sup>	(1.5) <sup>-1</sup>	(1.9) <sup>-1</sup>
	18°-28°C	(2.5) <sup>-1</sup>	1.0	(2.5) <sup>-1</sup>	(1.6) <sup>-1</sup>	(2.1) <sup>-1</sup>
$t_{fall}$	(ms)	0.23	1.05	0.26	0.26	0.24
$Q_{10,t_{fall}}$	27°-37°C	(3.5) <sup>-1</sup>	1.0	(2.8) <sup>-1</sup>	(2.2) <sup>-1</sup>	(2.4) <sup>-1</sup>
	18°-28°C	(1.7) <sup>-1</sup>	1.0	(2.9) <sup>-1</sup>	(2.6) <sup>-1</sup>	(2.7) <sup>-1</sup>
$ARP$	(ms)	0.50	1.69	0.37	0.50	0.60
$Q_{10,AR}$ $P$	27°-37°C	(3.2) <sup>-1</sup>	1.0	(2.5) <sup>-1</sup>	(2.0) <sup>-1</sup>	(2.0) <sup>-1</sup>
$f_{max}$	(kHz)	1.0-1.1	0.5	2.1	1.5	1.1
$t_{chr}$	( $\mu\text{s}$ )	29-59	67-117	17-32	34-78	28-45

## V. Discussion

The purpose of the model presented in this paper is to give a better description than previous models of those aspects of the behavior of mammalian myelinated nerve fibers, that are most relevant for the design of electrical prostheses. It was developed from the SENN model [8] to which several modifications were introduced to adapt it for warm-blooded animals.

The main modification is the use of the Schwarz and Eikhof equations [18], which were derived from voltage clamp data in mammals, instead of the amphibian-based Frankenhaeuser and Huxley [2] equations. Additionally, the various ionic concentrations were chosen in physiological ranges and the Goldman equation (1) was used to compute the resting membrane potential  $V_r$  to reflect the fact that *in vivo* the sodium and potassium concentrations are kept within narrow limits by the physiological system itself to

prevent disregulation of the nervous system due to a changed resting membrane potential [28]. Doubling the extracellular potassium concentration changes  $V_r$  from -85 to -70 mV and  $v$  is reduced from 84.2 to 71.5 m/s. Contrarily, if the extracellular sodium concentration is increased to 200 mmol/l  $V_r$  becomes -82 mV and  $v$  increases to 96.5 m/s. Clearly, the direction of the change in  $V_r$  does not predict the corresponding change in impulse conduction properties.

We have chosen to start from a linear cable model rather than from a more complex structure like the multi-axial cable proposed by Halter and Clark [29] for a number of reasons. Although the latter model is theoretically able to incorporate detailed anatomical and physiological data, there are several uncertainties regarding the choice of parameters in that model. A further serious drawback of such a multi-axial cable model is the amount of computing power required to solve the equations. To determine excitation thresholds, calculations based on a total equivalent driving function as proposed by Warman *et al.* [30] save time, but a full model is required when repetitive stimulation is considered. The fact that the SEF model can be implemented on a simple personal computer greatly enhances its applicability for the design of functional electrical stimulation devices.

When compared to the single node action potentials generated by the original SE equations a slightly prolonged rise and fall time are observed in the SEF model due to current flow along the cable. The increase in spike duration is much more pronounced in the model published by Halter and Clark [29], which generates spike durations above 0.4 ms in a fiber with a diameter of 17.5  $\mu\text{m}$ . Halter and Clark report a conduction velocity of 57.6 m/s in their simulated fiber. This means a ratio  $Y$  between conduction velocity  $v$  and total fiber diameter  $D$  (axon and myelin sheath) of  $3.29 \cdot 10^6 \text{s}^{-1}$ , which is well below the value of  $5.61 \cdot 10^6 \text{s}^{-1}$  found in the present paper. Hursh [6] showed that  $Y = 6.0 \cdot 10^6 \text{s}^{-1}$  for large fibers in the cat at 37.5  $^\circ\text{C}$ . Boyd and Kalu [23] reinvestigated this relation and found a mean ratio of  $5.7 \cdot 10^6 \text{s}^{-1}$  for the largest diameter fibers (10 to 21  $\mu\text{m}$ ) at temperatures between 35 and 37.5 $^\circ\text{C}$ . At mammalian body temperature, the value of  $Y$  in the present model is thus well in physiological ranges. Additionally, Fig. 4 (curve 1) shows that  $v$  varies nearly linearly with temperature  $T$  as it does *in vivo* (Fig. 4, curve 2), with  $Q_{10}$  values that are comparable to those measured experimentally.

We have investigated the dependence of various aspects of model behavior on fiber diameter  $D$  and found that  $Y$ , the spike duration and the refractory behavior do not depend on  $D$  provided that  $L/D$  is unchanged. This is not a surprising result, since the model obeys the same two of the three main conditions necessary for Rushton's "corresponding states" rule [31] as does the model of Goldman and Albus [5] which also has these properties. A linear relationship between  $v$  and  $D$  is acceptable in view of the available experimental data [23]. However, *in vivo* both the spike duration and the absolute refractory period vary inversely with fiber diameter [22]. This points to a shortcoming of model behavior which is not yet fully understood.

Both at 37 $^\circ\text{C}$  and at temperatures just below 20 $^\circ\text{C}$  (the other temperature for which Schwarz and Eikhof performed their voltage clamp measurements) the action potential in the simulated 15  $\mu\text{m}$  fiber is in good agreement with Paintal's data [22] for similar fibers. However, there is a definite mismatch between the simulated and measured spike shapes for intermediate temperatures as can be seen in Fig. 3. Apparently, the concept of a constant  $Q_{10}$  for the rate constants,

as used in the present paper and by previous authors, including Schwarz and Eikhof, is not a valid one.

If temperature dependent rate constants according to Frankenhaeuser and Moore [38] are introduced in the original SENN model, an acceptable spike shape is obtained at 37°C (see Fig. 2). In a previous paper [20] we showed that such a model can also describe other aspects of mammalian nerve behavior quantitatively, although the maximum attainable discharge frequency (1.5 kHz for a fiber with  $D = 10 \mu\text{m}$ ) is too high. However, the underlying mechanism is essentially different, since mammalian fibers have far less active potassium channels and a larger leak conductance (see Fig. 2). In the CRRSS model [19] which is based on the measurements of Chiu *et al.* [15] in the rabbit, no active potassium channels are incorporated at all. We have also implemented that model (see Table I) and found that the total spike duration is comparable with the one in the present model again, but that the action potential has a relatively short rise time of 0.06 ms, exhibits even shorter chronaxies and the maximum firing rate exceeds 2 kHz, a conclusion which is in agreement with Rattay's [21] analysis of single node behavior. Furthermore, the simplification to omit an active potassium conductance precludes the use of the Goldman equation.

In his review article, Ranck [33] mentions a chronaxy of 29 - 59  $\mu\text{s}$  for extracellular stimulation of myelinated cat sural A fibers. The chronaxies (28 - 45  $\mu\text{s}$ ) and polarity selectivity ratios found for the present model for cathodal stimulation of a large myelinated nerve fiber are in accordance with this reference. However, experimental data on  $t_{chr}$  in mammals span a large range and include values well in excess of 100  $\mu\text{s}$  [34]. For instance, single neuron data regarding auditory nerve fibers indicate chronaxies as large as 350  $\mu\text{s}$  [13]. At present, only part of this variation in experimental data can be explained by differences in the method of stimulation, e.g., small values are found for intracellular electrodes and  $t_{chr}$  increases with increasing distance between the electrode and the nerve fiber, both *in vivo* and in the present model. For a discussion on the different potential distribution along the nerve fiber for anodal and cathodal stimulation and, as a consequence, the different site of excitation for the two stimulus modalities, the reader is referred to the literature [33], [21].

In this paper, special attention has been paid to the refractory period and repetitive firing properties of the model, since these subjects are of utmost importance in the field of auditory prostheses which we are interested in. It was shown that this model behaves like actual nerve fibers in many respects. According to Paintal [35] the absolute refractory period in a large fiber is about 1.5 times the spike duration  $t_{spike}$  and the ratio of the RRP to the ARP is approximately 4. In the present model the ARP is 0.60 ms, which is 1.8 times  $t_{spike}$ . The situation with the relative refractory period is more complicated since its definition is less strict. We have defined its end as the point where the threshold has returned to within 1% of its original value, and the model's RRP is 2.4 ms which is exactly four times the ARP.

In Fig. 6, the relation between refractoriness and spike amplitude is shown. This gradual increase of spike amplitude with an increasing interstimulus

interval was observed in cat peripheral nerve fibers by Paintal [22], in cat cochlear nerve fibers by Gaumond *et al.* [36] and our laboratory in guinea pigs [37]. Stegeman *et al.* [38] inferred a similar relation from human compound action potentials.

The occurrence of abortive spikes at the end of the ARP and during repetitive stimulation *in vivo* is discussed in detail by Paintal [35]. Both in his data and in the SEF model the occurrence of abortive spikes is enhanced at lower temperatures. Paintal explains that "although an impulse can be initiated after the end of the spike, such impulses are in fact abortive because they are unable to propagate until they attain propagating amplitude, which is approximately 40% of spike height". Our simulations (Figs. 6 and 8(a)) suggest that in our model this propagating spike height is of the order 55 - 70%. It is unlikely that the minimum in spike amplitude and conduction velocity which occurs several nodes away from the excitation node (see Fig. 8) is related to the "anodal surround" that typically occurs adjacent to the site of highest depolarization under an extracellular cathode [33, p.423], since the site of maximum hyperpolarization appears to be just three nodes away from the excitation node and moreover, the minimum moves to larger distances with decreasing pulse frequency. In fact, the initial dip in spike velocity for the first spike and in spike height for all spikes (Fig. 8) is due to the anodal surround.

The maximum transmissible frequency is just above 1.1 kHz in the model situation, which is comparable to frequencies observed in real fibers of this diameter. As *in vivo*, this frequency is less than the frequency that would be expected from the ARP of the fibers. Figs. 7 and 8 are in agreement with Paintal's [35] observation that this is due to the reduced conduction velocity of spikes traveling in the relative refractory period of previous ones. These results stress the fact that single-node models (e.g., [39]) are less suited for this purpose, even if only time aspects of nerve behavior are considered.

Following McNeal [7], the internodal myelin has been treated as a perfect insulator in the SEF model. To test the influence of this simplifying assumption, we have performed a series of simulations with the internode represented by a passive node (see Appendix) with a time constant of 334.4  $\mu\text{s}$  ( $R = 139.3 \text{ M}\Omega$ ,  $C = 2.4 \text{ pF}$ ) according to Rubinstein [40], a value that is in accordance with Tasaki [26]. Virtually all model results are significantly affected: the spike duration increases to 0.42 ms, excitation thresholds almost double and the chronaxy increases. This increase of  $t_{chr}$  was predicted by Rubinstein, who states that "a nonlinear model assuming that myelin is a perfect insulator will ... underestimate the strength/duration time constant." However, the effect is relatively limited, since for a point cathode 1.5 mm radially away from the fiber  $t_{chr}$  increases from 34  $\mu\text{s}$  to 47  $\mu\text{s}$ , whereas the time constant for the node-internode unit, computed with Rubinstein's theory, increases from 27.5  $\mu\text{s}$  to 98  $\mu\text{s}$ . The introduction of the internodal time constant has a more pronounced effect on the spike conduction velocity. It decreases from 84.2 m/s to 33.5 m/s (i.e.,  $Y = 2.23 \cdot 10^6 \text{ s}^{-1}$ ). The maximum steady-state firing frequency  $f_{max}$  is reduced to 825 Hz. Subdivision of each internode in more segments did not further change the model's behavior very much, which is in accordance with Blight's [41] observations. If the nodal ionic

permeability constants are multiplied by a factor 4.7 and the nodal leak conductance is divided by a factor 1.2 as did Halter and Clark [29],  $v$  increases to 60.2 m/s ( $Y = 4.01 \cdot 10^6 \text{s}^{-1}$ ) and spike duration reduces to 0.36 ms with a very short rise time ( $t_{rise} = 51 \mu\text{s}$ ), but  $t_{chr}$  remains unchanged. Thus, the introduction of the internodal time constant gives a shift of most model results away from experimental values and we decided not to incorporate it in the present model, for the purpose of the SEF model is not to study nerve fiber behavior in each and every detail but to give a quantitative description of those aspects of nerve fiber behavior that are relevant in the context of functional electrical stimulation. Future research on the internode, *in vivo* and with e.g., multiaxial models [29], has to answer the questions like why real nerve fibers can conduct at such high velocities in spite of the large internodal time constants. Summarizing, it can be stated that the model presented in this paper can describe many properties of mammalian nerve fibers better than amphibian based SENN models do, even if the temperature dependence of the rate constants is accounted for (see Table I). In many respects, the model is also superior to previous models based on mammalian kinetics. Its spike shape, conduction velocity and (absolute and relative) refractory period are in good agreement with experimental data. In addition, the model can describe the influence of temperature on various aspects of nerve behavior, as well as the consequences of repetitive firing. Examples of its application include electrical control of the neuromuscular system, since in this field the use of repetitive stimuli is obligatory. In a forthcoming paper, we will show how an extended version of the model can be used in conjunction with a volume conduction model of the cochlea to simulate the behavior of small, bipolar auditory nerve fibers when stimulated by a cochlear implant.

## Appendix Model Equations and Standard Conditions

In this paper, the neural response to an extracellular current stimulus is modeled with the equivalent circuit model shown in Fig. 1. The nerve fiber is represented as an electrical cable of  $N$  nodes of Ranvier.

In each node of Ranvier, a membrane capacitance  $C_m$  and leak conductance  $G_L$  are present which can be calculated from

$$C_m = c_m p d l \quad (\text{A.1})$$

and

$$G_L = g_L p d l \quad (\text{A.2})$$

in which  $c_m$  = the membrane capacitance per unit area  
 $g_L$  = the leak conductance per unit area  
 $l$  = the length of the nodal membrane.

The nodes are interconnected by an axoplasmic conductance  $G_a$  formed by the conductive intracellular axoplasm

$$G_a = \frac{p d^2}{4 r_i L} \quad (\text{A.3})$$

in which  $d$  = the axonal diameter  
 $L$  = the internodal distance  
 $r_i$  = the axoplasm resistivity.

It is assumed that the passive electrical properties of the myelin sheath surrounding the extranodal membrane can be ignored. The validity of this assumption is discussed in Section V of this paper.

In the present paper, the resting membrane potential  $V_r$  (defined as the voltage drop experienced when going from extracellular to intracellular in a nerve fiber in its resting state) is computed from the ionic contents of the intracellular and extracellular fluid with the Goldman equation (1), whereas the original SE-equations used a fixed value.

The so-called active nodes are governed by the equations formulated by Schwarz and Eikhof (SE) [18] and the resulting model is described by a system of coupled nonlinear first order differential equations. This set of equations can be written in a convenient notation using (nontime dependent) matrices and so-called state vectors that fully describe the state of the nerve fiber.

First, consider the  $k$ th node of Ranvier. The time course of the transmembrane potential in this node ( $E_k$ ) is described in terms of its deviation  $V_k$  from  $V_r$

$$V_k = E_k - V_r = (V_{i,k} - V_{e,k}) - V_r \quad (\text{A.4})$$

where

$V_{i,k}$  = the internal potential at node  $k$   
 $V_{e,k}$  = the external potential at node  $k$

In this paper, all computations are performed for a fiber lying in an infinite linear isotropic homogeneous environment with resistivity  $r_e$ . We assume that the influence of the fiber itself on the potential field may be neglected. Then,  $V_{e,k}$  due to  $M$  electrodes with respective stimulating current  $I_j$  is given by

$$V_{e,k} = \frac{r_e}{4p} \sum_{j=1}^M \frac{I_j}{r_{j,k}} \quad (\text{A.5})$$

where  $r_{j,k}$  is the distance between electrode  $j$  and node  $k$ .

According to the SE-equations, the leak current  $I_L$  across the leak conductance in this  $k^{\text{th}}$  node can be computed as follows

$$I_{L,k} = G_L(V_k - V_L) \quad (\text{A.6})$$

in which  $V_L$  is the leak current equilibrium potential. For an active node,  $V_L$  is computed from the criterion that the net transmembrane current must be zero if the nerve fiber is in its resting state. In such a node, two additional ionic currents are involved, the sodium ( $i_{Na,k}$ ) and potassium ( $i_{K,k}$ ) current *per unit area*, which together constitute  $I_{act,k}$ , the so-called total active current in node  $k$

$$I_{act,k} = pdI(i_{Na,k} + i_{K,k}). \quad (\text{A.7})$$

On the other hand, if node  $k$  ( $k \notin \{1\}$  and  $k \notin \{N\}$ ) is modeled passively this can be formulated by simultaneously stating that  $V_{L,k}$  and  $I_{act,k}$  are zero. In other words, no nonlinearities are incorporated (see [2]).

Application of Kirchhoff's law at the internal point of (either active or passive) node  $k$ , i.e., requesting that the sum of the incoming currents at this point is zero, gives, with substitution of (A.4)

$$\begin{aligned} \frac{dV_k}{dt} = \frac{1}{C_m} \{ & [G_a(V_{k-1} - 2V_k + V_{k+1}) - pdI g_L V_k] + \\ & [G_a(V_{e,k-1} - 2V_{e,k} + V_{e,k+1}) - (I_{act,k} - G_L V_L)] \}. \end{aligned} \quad (\text{A.8})$$

If the boundary conditions in node 1 and node  $N$  are chosen in such a way that no axial current can flow past the nerve fiber's endings, the  $N$  coupled differential equations describing the simulated nerve fiber's behavior under an applied electrical field can be written in a convenient matrix-vector notation

$$\frac{d\vec{V}}{dt} = A\vec{V} + B\vec{V}_e + C[\vec{I}_{act} + \vec{I}_L] \quad (\text{A.9})$$

where

$$\begin{aligned} \vec{V} &= (V_1, \dots, V_N)1 \\ \vec{V}_e &= (V_{e,1}, \dots, V_{e,N}) \\ \vec{I}_{act} &= (I_{act,1}, \dots, I_{act,N})2 \\ \vec{I}_L &= (-G_L V_L, \dots, -G_L V_L) \end{aligned}$$

are vectors of length  $N$  and the time-independent matrices  $A$ ,  $B$ , and  $C$  (size  $N \times N$ ) are given by

$$A = \frac{1}{C_m} \begin{pmatrix} -(G_a + pdlg_L) & G_a & & & 0 \\ & \ddots & \ddots & \ddots & \\ & & G_a & -(2G_a + pdlg_L) & G_a \\ & & & \ddots & \ddots \\ 0 & & & & G_a & -(G_a + pdlg_L) \end{pmatrix} \quad (A.10)$$

$$B = \frac{G_a}{C_m} \begin{pmatrix} -1 & 1 & & 0 \\ & \ddots & \ddots & \ddots \\ & & 1 & -2 & 1 \\ & & & \ddots & \ddots & \ddots \\ 0 & & & & 1 & -1 \end{pmatrix} \quad (A.11)$$

$$C = \frac{1}{C_m} \begin{pmatrix} 1 & & & 0 \\ & \dots & & \\ & & 1 & \\ & & & \dots \\ 0 & & & & 1 \end{pmatrix} \quad (A.12)$$

The equations governing the ionic currents in the (active) node  $k$ , i.e., the  $k$ th component of  $I_{act}$  (see (A.6)), are adopted from Schwarz and Eikhof

$$i_{Na,k} = \bar{P}_{Na} h_k m_k^3 \cdot \frac{E_k F^2}{RT} \cdot \frac{[Na^+]_o - [Na^+]_i \cdot \exp\{E_k F/RT\}}{1 - \exp\{E_k F/RT\}} \quad (A.13)$$

$$i_{K,k} = P_{K'} n_k^2 \cdot \frac{E_k F^2}{RT} \cdot \frac{[K^+]_o - [K^+]_i \cdot \exp\{E_k F/RT\}}{1 - \exp\{E_k F/RT\}} \quad (A.14)$$

- where
- $T$  = the absolute temperature
  - $F$  = Faraday's constant
  - $R$  = the gas constant
  - $[Na^+]_o$  = the extracellular sodium concentration
  - $[Na^+]_i$  = the intracellular sodium concentration
  - $[K^+]_o$  = the extracellular potassium concentration
  - $[K^+]_i$  = the intracellular potassium concentration
  - $\bar{P}_{Na}$  = the sodium permeability constant
  - $P_{K'}$  = the potassium permeability constant

and  $m_k$ ,  $h_k$  and  $n_k$  are dimensionless variables describing the function of the various ionic channels of node  $k$ .

If we define the vectors

$$\vec{m} = (m_1, \dots, m_N) \quad 6$$

$$\vec{h} = (h_1, \dots, h_N) \quad 7$$

$$\vec{n} = (n_1, \dots, n_N) \quad 8$$

the set of first order differential equations governing these variables can be written in matrix-vector notation. For  $\vec{m}$  9 this equation reads as follows

$$\frac{d\vec{m}}{dt} = \begin{pmatrix} \mathbf{a}_{m,1} \\ \dots \\ \mathbf{a}_{m,N} \end{pmatrix} + \begin{pmatrix} \mathbf{a}_{m,1} + \mathbf{b}_{m,1} & & 0 \\ & \dots & \\ 0 & & \mathbf{a}_{m,N} + \mathbf{b}_{m,N} \end{pmatrix} \cdot \vec{m}. \quad (\text{A.15})$$

Similar equations can be derived for  $\vec{h}$  and  $\vec{n}$  10. These equations are initialized with starting values  $m_0$ ,  $h_0$ ,  $n_0$  respectively for all active nodes, in such a way that the nerve fiber is at rest at its resting potential computed with

(1), i.e.,  $\frac{d\vec{m}}{dt} = \frac{d\vec{h}}{dt} = \frac{d\vec{n}}{dt} = \vec{0}$  11 at  $\vec{V} = \vec{0}$  12. The  $\mathbf{a}$  and  $\mathbf{b}$  coefficients in (A.15) -

(A.17) are voltage dependent and depend on temperature  $T$  with  $Q_{10}$  values of 2.2, 2.9, and 3.0, respectively [18].

$$\mathbf{a}_{m,k} = \frac{A_{a_m}(V_k - B_{a_m})}{1 - \exp\left[\frac{B_{a_m} - V_k}{C_{a_m}}\right]} \cdot Q_{10,a_m}^{\frac{(T-T_0)}{10}}, \quad \mathbf{b}_{m,k} = \frac{A_{b_m}(B_{b_m} - V_k)}{1 - \exp\left[\frac{V_k - B_{b_m}}{C_{b_m}}\right]} \cdot Q_{10,b_m}^{\frac{(T-T_0)}{10}} \quad (\text{A.16})$$

$$\mathbf{a}_{h,k} = \frac{A_{a_h}(B_{a_h} - V_k)}{1 - \exp\left[\frac{V_k - B_{a_h}}{C_{a_h}}\right]} \cdot Q_{10,a_h}^{\frac{(T-T_0)}{10}}, \quad \mathbf{b}_{h,k} = \frac{A_{b_h}}{1 + \exp\left[\frac{B_{b_h} - V_k}{C_{b_h}}\right]} \cdot Q_{10,b_h}^{\frac{(T-T_0)}{10}} \quad (\text{A.17})$$

$$\mathbf{a}_{n,k} = \frac{A_{a_n}(V_k - B_{a_n})}{1 - \exp\left[\frac{B_{a_n} - V_k}{C_{a_n}}\right]} \cdot Q_{10,a_n}^{\frac{(T-T_0)}{10}}, \quad \mathbf{b}_{n,k} = \frac{A_{b_n}(B_{b_n} - V_k)}{1 - \exp\left[\frac{V_k - B_{b_n}}{C_{b_n}}\right]} \cdot Q_{10,b_n}^{\frac{(T-T_0)}{10}} \quad (\text{A.18})$$

in which  $T_0 = 293.15$  K (20°C). For the values of the other constants in these equations, the reader is referred to [18, Table I].

Table II defines the so-called standard conditions which were used for the computations in this paper, unless explicitly stated otherwise.

## Acknowledgment

The authors wish to express their thanks to Prof.Dr. J.J. Grote for continuous support throughout this work, and to Dr. R. Schoonhoven for valuable comments on the first draft of the manuscript.

Table II - The set of parameters defining the standard conditions

Parameter	Unit	Symbol	Standard Value
axoplasm resistivity	$\Omega \cdot m$	$r_i$	0.7 (37°C) $Q_{10} = (1.3)^{-1}$
external resistivity	$\Omega \cdot m$	$r_u$	3.0 (37°C) $Q_{10} = (1.3)^{-1}$
membrane capacitance /unit area	F/m <sup>2</sup>	$c_m$	0.02
leak conductance /unit area	$\Omega^{-1}/m^2$	$g_L$	728
sodium permeability constant	$\mu m/s$	$\bar{P}_{Na}$	51.5
potassium permeability constant	$\mu m/s$	$P_K$	2.0
intracellular sodium concentration	mol/m <sup>3</sup>	$[Na^+]_i$	10
extracellular sodium concentration	mol/m <sup>3</sup>	$[Na^+]_o$	142
intracellular potassium concentration	mol/m <sup>3</sup>	$[K^+]_i$	141
extracellular potassium concentration	mol/m <sup>3</sup>	$[K^+]_o$	4.2
fiber diameter	$\mu m$	$D$	15
axonal diameter	$\mu m$	$d$	10.5
nodal gap width	$\mu m$	$l$	1
internodal distance	$\mu m$	$L$	1500
temperature	K	$T$	310.15 (= 37°C)

**REFERENCES**

- [1] A. L. Hodgkin and A. F. Huxley, "A quantitative description of membrane current and its application to conduction and excitation in nerve," *J. Physiol. (London)*, vol. 117, pp. 500-544, 1952.
- [2] B. Frankenhaeuser and A. F. Huxley, "The action potential in the myelinated nerve fibre of *Xenopus laevis* as computed on the basis of voltage clamp data," *J. Physiol. (London)*, vol. 171, pp. 302-315, 1964.
- [3] M. Horáckova, W. Nonner and R. Stämpfli, "Action potentials and voltage clamp currents of single rat Ranvier nodes," *XXIV Int. Cong. Physiol. Sci.*, 1968, p. 198.
- [4] R. Fitzhugh, "Computation of impulse initiation and saltatory conduction in a myelinated nerve fibre," *Biophys. J.*, vol. 2, pp. 11-21, 1962.
- [5] L. Goldman and J. S. Albus, "Computation of impulse conduction in myelinated fibres; theoretical basis of the velocity-diameter relation," *Biophys. J.*, vol. 8, pp. 596-607, 1968.
- [6] J. B. Hursh, "Conduction velocity and diameter of nerve fibres," *Am. J. Physiol.*, vol. 127, pp. 131-139, 1939.
- [7] D. R. McNeal, "Analysis of a model for excitation of myelinated nerve," *IEEE Trans. Biomed. Eng.*, vol. BME-23, pp. 329-337, 1976.
- [8] J. P. Reilly, V. T. Freeman, and W. D. Larkin, "Sensory effects of transient electrical stimulation: Evaluation with a neuroelectrical model," *IEEE Trans. Biomed. Eng.*, vol. BME-32, pp. 1001-1011, 1985.
- [9] J. P. Reilly and R. H. Bauer, "Application of a neuroelectric model to electrocutaneous sensory sensitivity: Parameter variation study", *IEEE Trans. Biomed. Eng.*, vol. BME-34, pp. 752-754, 1987.
- [10] J. P. Reilly, "Peripheral nerve stimulation by induced electric currents: exposure to time-varying magnetic fields," *Med. Biol. Eng. Comput.*, vol. 27, pp. 101-110, 1989.
- [11] P. H. Gorman and J. T. Mortimer, "The effect of stimulus parameters on the recruitment characteristics of direct nerve stimulation," *IEEE Trans. Biomed. Eng.*, vol. BME-30, pp. 407-414, 1983.
- [12] J. H. Meier, W. L. C. Rutten, A. E. Zoutman, H. B. K. Boom, and P. Bergveld, "Simulation of multipolar fibre selective neural stimulation using intrafascicular electrodes," *IEEE Trans. Biomed. Eng.*, vol. 39, 1992
- [13] J. Colombo and C. W. Parkins, "A model of electrical excitation of the mammalian auditory-nerve neuron," *Hear. Res.*, vol. 31, pp. 287-312, 1987.
- [14] J. H. M. Frijns and R. Schoonhoven, "Refractoriness and frequency following behavior in a model of electrical stimulation of mammalian myelinated nerve fibers," *IEEE 14<sup>th</sup> Ann. Int. Conf. Eng. Med. and Biol. Soc.*, 1992, pp. 1372-1373.
- [15] S. Y. Chiu, J. M. Ritchie, R. B. Rogart, and D. Stagg, "A quantitative description of membrane currents in rabbit myelinated nerve," *J. Physiol. (London)*, vol. 292, pp. 149-166, 1978.
- [16] T. Brismar, "Potential clamp analysis of membrane currents in rat myelinated nerve fibres," *J. Physiol. (London)*, vol. 298, pp. 171-184, 1980.
- [17] B. Neumcke, J. R. Schwarz and R. Stämpfli, "A comparison of sodium currents in rat and frog myelinated nerve: Normal and modified sodium inactivation," *J. Physiol. (London)*, vol. 382, pp. 175-191, 1987.
- [18] J. R. Schwarz and G. Eikhof, "Na currents and action potentials in rat myelinated nerve fibres at 20 and 37 °C," *Pflügers Arch*, vol. 409, pp. 569-577, 1987.

- [19] J. D. Sweeney, J. T. Mortimer, and D. Durand, "Modelling of mammalian myelinated nerve for functional neuromuscular stimulation," in *IEEE 9th Ann. Int. Conf. Eng. Med. and Biol. Soc.*, 1987, pp. 1577-1578.
- [20] J. H. M. Frijns and J. H. ten Kate, "A Model of myelinated nerve fibres of electrical prosthesis design," *Med. Biol. Eng. Comput.*, vol. 32, 1994.
- [21] F. Rattay, *Electrical Nerve Stimulation: Theory, Experiments and Applications*. New York & Wien, Austria: Springer Verlag, 1990.
- [22] A. S. Paintal, "The influence of diameter of medullated nerve fibres of cat on the rising and falling phases of the spike and its recovery," *J. Physiol. (London)*, vol. 184, pp. 791-811, 1966.
- [23] I. A. Boyd and K. U. Kalu, "Scaling factor relating conduction velocity and diameter for myelinated afferent nerve fibres in the cat hind limb," *J. Physiol. (London)*, vol. 289, pp. 277-297, 1979.
- [24] A. C. Guyton, *Textbook of Medical Physiology*. Philadelphia, PA: W. B. Saunders, 1981, ch. 4, pp. 41-54.
- [25] J. W. Moore, R. W. Joyner, M. H. Brill, S. D. Waxman and M. Najjar-Joa, "Simulations of conduction in uniform myelinated fibers: relative sensitivity to changes in nodal and internodal parameters," *Biophys. J.*, vol. 21, pp. 147-160, 1978.
- [26] I. Tasaki, *Physiology and Electrochemistry of Nerve Fibres*. New York: Academic Press, 1982.
- [27] W. H. Press, B. P. Flannery, S. A. Teukolsky, and W. T. Vetterling, *Numerical Recipes; The Art of Scientific Computing*. Cambridge, MA: Cambridge Univ. Press, 1988, ch. 15, pp. 547-560.
- [28] A. M. Harvey, R. J. Johns, V. A. McKusick, A. H. Owens, Jr., and R. S. Ross, *The Principles and Practice of Medicine*. New York: Appleton-Century-Crofts, 1984, ch. 6-7, pp. 59-74.
- [29] J. A. Halter and J. W. Clark Jr., "A distributed-parameter model of the myelinated nerve fiber," *J. Theor. Biol.*, vol. 148, pp. 345-382, 1991.
- [30] E. N. Warman, W. M. Grill and D. Durand, "Modeling the effects of electric fields on nerve fibers: Determination of excitation thresholds," *IEEE Trans. Biomed. Eng.*, vol. 39, pp. 1244-1254, 1992.
- [31] W. A. H. Rushton, "A Theory of the effects of fibre size in medullated nerve," *J. Physiol. (London)*, vol. 115, pp. 101-122, 1951.
- [32] B. Frankenhaeuser and L. E. Moore, "The effect of temperature on sodium and potassium permeability changes in myelinated nerve fibres of *Xenopus Laevis*," *J. Physiol. (London)*, vol. 169, pp. 431-437, 1963.
- [33] J. B. Ranck, Jr., "Which elements are excited in electrical stimulation of mammalian central nervous system: a review," *Brain Research*, vol. 98, pp. 417-440, 1975.
- [34] J. P. Reilly, *Electrical Stimulation and Electropathology*. Cambridge, MA: Cambridge Univ. Press, 1992.
- [35] A. S. Paintal, "Conduction properties of normal peripheral mammalian axons," in *Physiology and Pathobiology of Axons*, S. G. Waxman, Ed. New York; Raven Press, 1978, pp. 131-144.
- [36] R. P. Gaumond, C. E. Molnar, and D. O. Kim, "Stimulus and recovery dependence of cat cochlear nerve fiber spike discharge probability," *J. Neurophysiol.*, vol. 48, no 3, 1982.
- [37] H. Versnel, R. Schoonhoven and V. F. Prijs, "Single-fibre and whole-nerve responses to clicks as a function of sound intensity in the guinea pig," *Hear. Res.*, vol. 59, pp. 138-156, 1992.

- [38] D. F. Stegeman, J. P. C. de Weerd, and S. L. H. Notermans, "Modeling compound action potentials of peripheral nerves in situ. III. Nerve propagation in the refractory period," *Electroenceph. clin. Neurophysiol*, vol. 55, pp. 668-679, 1983.
- [39] H. Motz and F. Rattay, "A study of the application of the Hodgkin-Huxley and the Frankenhaeuser-Huxley model for electrostimulation of the acoustic nerve," *Neuroscience*, vol. 18, no 3, pp. 699-712, 1986.
- [40] J. T. Rubinstein, "Analytical theory for extracellular electrical stimulation of nerve with focal electrodes. II. Passive myelinated axon," *Biophys.J.*, vol. 60, pp.538-555, 1991.
- [41] A. R. Blight, "Computer simulation of action potentials and afterpotentials in mammalian myelinated axons: The case for a lower resistance myelin sheath," *Neuroscience*, vol. 15, pp.13-31, 1985.

# *Chapter IV*

---

***HAVE MAMMALIAN MYELINATED NERVE FIBERS  
DIAMETER DEPENDENT NODAL PROPERTIES?  
A MODEL STUDY***

*J.H.M. Frijns, J. Mooij and R. Schoonhoven  
Submitted for Publication.*

## Summary

It has been known for several years that the duration of a nerve fiber's action potential depends on its diameter, but there is still no firm explanation for this phenomenon. This paper addresses this issue by means of a non-linear cable model of a large mammalian myelinated nerve fiber that is known to give a quantitative description of many aspects of actual neural behavior. A variation of parameters identifies the systematic variation with fiber diameter of the nodal leak conductance and the active permeabilities (by the same multiplication factor per unit area of membrane) as the most likely hypothesis. It turns out that this hypothesis allows to match the model's relation between the conduction velocity of a spike and its fall time with Paintal's experimental data (Paintal, 1966) for any physiologically realistic value of the  $g$ -ratio. The resulting generalized model yields a reduced velocity-diameter ratio for thinner fibers, which conforms with physiological data. Moreover, the model simulates many auditory nerve fiber properties correctly, including the maximum firing rate. It is concluded that the results support the hypothesis that the dependence of the spike shape on fiber size is due to a systematic variation of the active and passive nodal conductances.

## I. Introduction

The generation and propagation of action potentials in myelinated nerve fibers has been studied extensively, experimentally, by analytic theory, as well as in computer simulations. Early experiments showed that there is an approximate proportionality between fiber size and the distance between adjacent nodes of Ranvier and that there exists an almost linear relationship between the velocity  $v$  with which action potentials are conducted along a fiber and the outer diameter  $D$  of the fiber (Hursh, 1939). This linear relation between  $v$  and  $D$  has been accepted as an established fact, despite the finding of Gasser and Grundfest (1939) that a slightly S-shaped curve had to be used to obtain a good reconstruction of their measured compound action potentials (cf. Stegeman and De Weerd, 1982).

The proportional relation between fiber diameter and spike conduction velocity was given a theoretical basis by Rushton's 'corresponding states' theory (Rushton, 1951). A central role in this elegant theory is played by the notion that each point in a nerve fiber has a 'corresponding point' in a fiber of different size, that is defined by geometric scaling, and that each point has always the same potential as its corresponding point. The three main conditions necessary for this assumption to be valid are that the specific properties, both of the nodal membranes and of the myelin (which Rushton treated as a passive, leaky cable) are identical for all fibers, that the area of the excitable nodal membrane is proportional to the square of the axon diameter  $d$  divided by the internodal length  $L$  and that the following relation between  $L$ ,  $d$ , and  $D$  is fulfilled:

$$L \propto d \cdot [\ln(D/d)]^{1/2} \quad \text{or} \quad L/D \propto g(-\ln g)^{1/2} \quad (1)$$

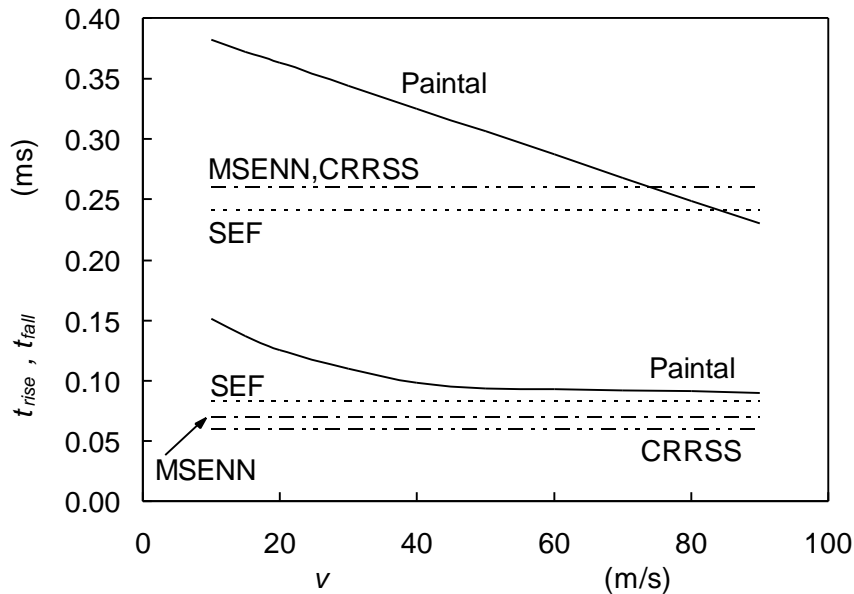


Fig. 1 The diameter dependence of the rise time  $t_{rise}$  (lower solid curve) and the fall time  $t_{fall}$  (upper solid line) of the transmembrane action potential as measured in the cat (Paintal, 1966). For comparison the values of  $t_{rise}$  and  $t_{fall}$  as simulated by the CRRSS (Sweeney et al., 1987), MSEN (Frijns and Ten Kate, 1994a) and SEF (Frijns et al., 1994b) models (which do not depend on fiber diameter) are displayed also.

where:  $g = d/D$ , which is fixed as a consequence of geometric scaling.

Rushton also deduced that the proportionality between  $v$  and  $D$  still may be roughly obeyed if  $g$  is not quite constant for different fibers, and that the ratio  $Y$  between  $v$  and  $D$  has a maximum for  $g = 0.6$ .

Paintal, who studied experimentally myelinated (Paintal, 1966) and unmyelinated (Paintal, 1967) single fibers in the cat, showed that more neural properties depend on fiber diameter than the conduction velocity alone: Both the rise time  $t_{rise}$  and the fall time  $t_{fall}$  of the action potential and thus the spike duration  $t_{spike}$  increase with decreasing fiber diameter (Fig. 1), results which were confirmed by Coppin (1973). Also the absolute refractory period (ARP), which is the period after the initiation of a spike in which it is impossible to induce another propagated action potential, increases with decreasing fiber diameter, while the maximum transmissible frequency diminishes correspondingly (Paintal, 1978).

Insight into the active processes responsible for the generation of action potentials was gained by voltage-clamp measurements in unmyelinated (Hodgkin and Huxley, 1952) and myelinated (Frankenhaeuser and Huxley, 1964) amphibian nerve fibers. These measurements showed that in the initial depolarization phase of the action potential an inward sodium current occurs, while an outflow of potassium ions is the main factor responsible for the repolarization during the falling phase of the spike. These processes can be

described by a set of coupled non-linear differential equations governing the time behavior of the voltage-dependent ion channels involved.

More recently, reliable voltage-clamp data for mammalian nerve fibers became available. Then it became clear that the mechanism behind the generation and propagation of action potentials in the case of mammalian fibers is somewhat different from the amphibian situation. Essentially, the difference is that the potassium conductance in the nodal membrane is only about one fifth of the amphibian value and that repolarisation of the membrane is largely due to a much larger leak conductance (Horáckova et al., 1968; Chiu et al., 1978; Brismar, 1980) rather than due to an outward potassium current.

Schwarz and Eikhof (1987) were the first to perform a full Hodgkin-Huxley analysis for large rat myelinated nerve fibers at body temperature, for which they recorded and simulated intracellular action potentials with durations around 0.3 ms, which is a realistic value in the light of Paintal's (1966) data. To our knowledge such experimental data are not available for mammalian myelinated fibers with diameters below 10  $\mu\text{m}$ .

Several authors developed cable models of myelinated nerve fibers with nodal kinetics based on such voltage-clamp data in cold-blooded animals (Fitzhugh, 1962; Goldman and Albus, 1968; McNeal, 1976; Reilly et al., 1985; Frijns and Ten Kate, 1994a) and in mammals (Sweeney et al., 1987; Halter and Clark, 1991; Frijns et al., 1994b). If these models are used to simulate smaller nerve fibers by proportionally changing the geometry of the fiber while keeping the length  $l$  of the nodes of Ranvier fixed, they obey the above-mentioned conditions necessary for Rushton's 'corresponding states rule' (Rushton, 1951), and as a consequence (see also Goldman and Albus, 1968) the spike conduction velocity  $v$  varies linearly with the fiber diameter. This is roughly in accordance with the *in vivo* situation, although there are indications that smaller fibers conduct less fast relative to their fiber diameter than larger ones (Gasser and Grundfest, 1939; Boyd and Kalu, 1979).

However, these models are conflicting with Paintal's observations, since the simulated spike durations do not depend on the fiber diameter. Jack (1975) discussed the problem of the dependence of spike shapes on fiber diameter in detail and arrived at the conclusion that there is experimental evidence that at least part of this discrepancy may be due to a systematic variation in the size of the conductances (per unit area of membrane) responsible for generating the action potential in myelinated and unmyelinated amphibian nerve fibers. The findings of Smith and Schauf (1981) regarding a decrease of the potassium conductivity with fiber diameter in *R. Pipiens* further corroborated this conclusion. Since no reliable voltage-clamp data for mammals were available at that time Jack (1975) had to be more speculative about the situation in mammals.

For our research program on electrical stimulation of the auditory nerve as a method for rehabilitating the profoundly deaf we are interested in a model of auditory nerve fibers. These are bipolar nerve fibers, i.e. they consist of a peripheral and a central axon with diameters between 2 and 3  $\mu\text{m}$ , interconnected by a cell body, with a typical diameter between 10 and 20  $\mu\text{m}$ .

Only for the cell body voltage clamp data are currently available ( Santos-Sacchi, 1993). In accordance with the notion that smaller nerve fibers have longer action potentials, single fiber recordings from such auditory fibers indicate spike durations around 0.5 ms (Kiang et al., 1976) and absolute refractory periods above 1 ms (Moxon, 1968).

Recently, we developed the so-called SEF model (Frijns et al., 1994b), which is a non-linear cable model of a 15  $\mu\text{m}$  A-fiber, based on the Schwarz and Eikhof (1987) data. This model gives a good quantitative description of many properties (including spike shape ( $t_{\text{spike}} = 0.32$  ms), spike conduction velocity-to-diameter-ratio ( $Y = 5.6 \cdot 10^6 \text{s}^{-1}$ ) and refractoriness (ARP = 0.60 ms)) of large myelinated mammalian fibers, but as discussed above, simple geometric scaling does not result in the experimentally observed longer spike durations and refractory periods for smaller diameters. In this study we will investigate to what extent this model can be generalized to describe the spike shape, spike conduction velocity  $v$  and firing properties of neurons of different sizes, including auditory nerve fibers. First, we will investigate the effect on simulated neural behavior of varying individual parameters of the model. Then we will reconsider Jack's hypothesis that all nodal permeabilities vary with fiber diameter  $D$  in terms of a single multiplication factor  $h$ . It will be shown how a form of this hypothesis that is adapted for mammalian fibers allows one to fit the simulated spike shapes of the SEF model to Paintal's experimentally observed relation between spike shape and conduction velocity of cat myelinated fibers (Paintal, 1966). Next, we will consider how the model can be extended further to include also fibers which have a ratio  $g$  between  $d$  and  $D$  that deviates from the value of 0.7 used in the SEF model thus far. The predictions of the resulting generalized SEF model (e.g., the dependence of spike conduction velocity  $v$  on  $D$ ) will be compared to experimental and simulated data in literature. Finally, we will discuss the extent to which the findings support the hypothesis that a size-dependent variation of nodal properties is responsible for the systematic dependence on fiber diameter of physiological properties of mammalian myelinated nerve fibers, such as action potential duration.

## II. The influence of parameter variations on simulated spike shape and conduction velocity in the SEF model

The SEF model (Frijns et al., 1994b) is a linear cable model of a 15  $\mu\text{m}$  mammalian myelinated nerve fiber with nodal kinetics based upon the measurements of Schwarz and Eikhof (1987) in rat and cat sciatic nerve fibers at 37°C. As in the SENN model (Reilly et al., 1985), the myelin sheath is considered to be a perfect insulator. To account for variations in the ionic content of the intracellular and extra-cellular fluids the Goldman equation (Frijns et al., 1994b) is used to compute the resting membrane potential. The model parameters defining so-called standard conditions were chosen to be physiologically realistic and are summarized in Table I. The model equations themselves are not reproduced here, since they can be found in the literature cited above. Also for computational details regarding the integration of the model equations and the method used to determine the spike shape we refer to our previous paper (Frijns et al., 1994b).

Table I The set of parameters defining the standard conditions for the SEF model.

Parameter	Unit	Symbol	Standard Value
axoplasm resistivity	$\Omega \cdot m$	$r_i$	0.7 (37°C)
external resistivity	$\Omega \cdot m$	$r_e$	3.0 (37°C)
membrane capacitance /unit area	F/m <sup>2</sup>	$c_m$	0.02
leak conductance /unit area	$\Omega^{-1}/m^2$	$g_L$	728
sodium permeability constant	$\mu m/s$	$\bar{P}_{Na}$	51.5
potassium permeability constant	$\mu m/s$	$P'_K$	2.0
intracellular sodium concentration	mol/m <sup>3</sup>	$[Na^+]_i$	10
extracellular sodium concentration	mol/m <sup>3</sup>	$[Na^+]_o$	142
intracellular potassium concentration	mol/m <sup>3</sup>	$[K^+]_i$	141
extracellular potassium concentration	mol/m <sup>3</sup>	$[K^+]_o$	4.2
fiber diameter	$\mu m$	$D$	15
axonal diameter	$\mu m$	$d$	10.5
nodal gap width	$\mu m$	$l$	1
internodal distance	$\mu m$	$L$	1500
temperature	K	$T$	310.15 (= 37°C)

In that paper we showed that this model gives a quantitative description of many properties of large mammalian neurons, including the spike shape, conduction velocity, strength/duration behavior and absolute and relative refractory period, both at normal mammalian body temperature and below. In search for a way to generalize the SEF model to fibers of different sizes, i.e. to account for the longer spike durations in smaller fibers while maintaining a realistic ratio  $Y$  between  $v$  and  $D$ , a parameter variation study was performed by applying a multiplication factor  $f$  ( $= 0.5$  or  $2$ ) to the nodal parameters (Table II). Some important effects were observed. Changing  $l$ , the nodal gap width, without any change of the specific membrane properties does virtually not influence the spike shape, while  $v$  decreases significantly with increasing  $l$ . A similar observation holds for the axoplasmic resistivity  $r_i$ . Increasing the specific nodal capacity  $c_m$  results in prolonged action potentials, but a 25%

increase of  $t_{spike}$  is associated with a reduction of  $Y$  by approximately one-third. Another way the prolonged action potentials in thinner nerve fibers can be explained, is by the hypothesis that the time constants  $t_m$ ,  $t_h$ , and  $t_n$  of the sodium activation, sodium inactivation, and the potassium activation, respectively, depend on fiber diameter. The data in Table II regarding simulations in which these time constants have been varied individually, indicate that such a variation of a single time constant cannot account for the effects observed experimentally:  $t_m$  and  $t_h$  each influence only one phase of the action potential and have a strong influence on  $Y$ , while changes of  $t_n$  have little bearing on the model's behavior as a consequence of the small potassium permeability in mammals. If, however,  $t_m$ ,  $t_h$ , and  $t_n$  are varied simultaneously and by the same factor, this induces a change of both phases of the action potential that is proportionate in the light of Paintal's observations (cf. Fig. 1), although this is accompanied by a relatively large effect on  $Y$  (see Section VI for a discussion on this subject).

Similarly, variation of the ionic permeabilities  $\bar{P}_{Na}$  and  $P_K'$  and of  $g_L$ , the leak conductance per unit area, leads to changes in the spike duration. Again, individual changes of a single ionic permeability or the leak conductance can also not explain the effect of the fiber diameter on the spike shape: A decrease of the sodium permeability per unit area  $\bar{P}_{Na}$  increases  $t_{rise}$  and reduces  $Y$ , but has hardly any influence on  $t_{fall}$ . On the other hand, a decrease in the leak conductance per unit area  $g_L$  will result in a prolonged fall time with little

**Table II** The effect of variations of the parameters in the SEF model on the ratio  $Y$  between spike conduction velocity  $v$  and fiber diameter  $D$ , on rise time  $t_{rise}$ , fall time  $t_{fall}$  and spike amplitude  $A$ . The values computed with the standard parameter set (Table I) are given in the top row.  $t_m$ ,  $t_h$ , and  $t_n$  designate the time constants for sodium activation, inactivation and potassium activation respectively. The label ' $f = 0.5$ ' means that the parameter value in the first column was divided by 2, while the label ' $f = 2$ ' means that it is multiplied by 2. The other symbols are explained in Table I.

	$Y = 5.61 \cdot 10^{-6} s^{-1}$		$t_{rise} = 84 \mu s$		$t_{fall} = 241 \mu s$		$A = 107.5 mV$	
	$f = 0.5$	$f = 2$	$f = 0.5$	$f = 2$	$f = 0.5$	$f = 2$	$f = 0.5$	$f = 2$
$f * I$	8.14	3.78	83	92	240	239	107.9	106.4
$f * C_m$	7.75	3.76	70	111	213	304	112.5	99.9
$f * r_i$	8.19	3.78	83	92	240	238	107.9	106.4
$f * \bar{P}_{Na}$	3.78	7.03	128	67	249	260	84.2	121.4
$f * P_K'$	5.22	5.85	91	80	248	234	101.8	110.6
$f * g_L$	7.21	3.17	77	123	292	214	121.7	84.9
$f * (\bar{P}_{Na}, P_K', g_L)$	5.42	5.26	105	73	302	213	100.3	112.1
$f * t_m$	3.23	8.17	154	56	297	224	89.9	115.6
$f * t_h$	6.01	4.60	87	96	389	195	119.8	83.2
$f * t_n$	5.62	5.59	85	84	248	238	108.1	106.3
$f * (t_m, t_h, t_n)$	3.88	7.52	140	55	427	151	112.5	99.9

influence on  $t_{rise}$ , while it causes a significant increase of the conduction velocity-to-diameter-ratio (Table II). However, if  $g_L$ ,  $P_{Na}$  and  $P_K$  are changed simultaneously and by the same proportion, this leads to a variation of  $t_{fall}$  that is in the same direction as (but larger than) the variation of  $t_{rise}$ , while it has only a limited effect on  $Y$ .

This led us to hypothesize that in mammals the fact that the spike duration increases with decreasing fiber diameter is caused by a concomitant variation of  $g_L$ ,  $P_{Na}$  and  $P_K$  by the same diameter dependent multiplication factor  $h(D)$ . In fact, this hypothesis is identical to the one formulated by Jack (1975) for amphibian fibers with the modification that  $g_L$  obeys the same diameter dependence as the active ionic permeabilities.

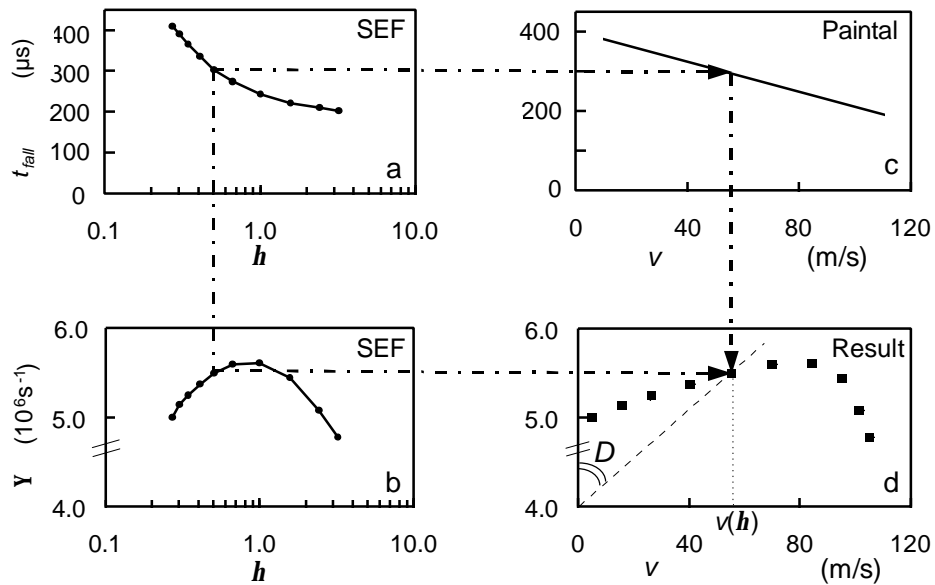


Fig. 2 Graphical representation of the procedure used to arrive at the diameter dependence of the multiplication factor  $h$ . The dash-dotted lines and arrows connecting the different parts of the figure indicate the individual steps of this procedure (see text).

- a. The dependence of the simulated action potential fall time  $t_{fall}$  on  $h$ .
- b. The dependence on  $h$  of the ratio  $Y$  of simulated spike conduction velocity  $v$  and fiber diameter  $D$ .
- c. The experimental dependence of  $t_{fall}$  on  $v$  in cats at 37°C (Paintal, 1966). The vertical axis is identical to the corresponding one in (a).
- d. The diameter  $D$  corresponding with each value of  $h$  is found as the quotient of the values of  $v(h)$  determined in (c) and  $Y(h)$  as found in (b). The vertical axis is identical to the corresponding one in b.

### III. Extension of the SEF model to include variation of spike shape with fiber diameter

As a next step to test the hypothesis that the diameter dependent changes in action potential duration can be explained by a simultaneous variation of PNa, PK' and gL with the same diameter dependent multiplication factor  $\eta(D)$ , we decided to explore whether there exists function  $h(D)$  that makes the SEF model produce the same relationship between spike shape and conduction velocity as measured by Paintal (1966).

#### a. Relating multiplication factor $h$ to fiber diameter

To arrive at this generalized form of the SEF model we made use of the observations that for any fixed value of  $h$  both the simulated spike shape and  $Y$  are not influenced by geometric scaling, provided that the nodal gap width  $l$  -which is generally considered to be independent of fiber diameter ( Hildebrand et al., 1993)- is left unchanged.

These observations implied that we did not need to know beforehand to which fiber diameter  $D$  a given value of  $h$  would be related in the final model, but that it made sense to perform repeated simulations with the standard SEF model ( $D = 15 \mu\text{m}$ ) for a wide range of  $h$  values, record the resulting spike shape and  $Y(h)$ , and determine the geometrical scaling factor corresponding with each  $h$  afterwards. To accomplish the latter step, Paintal's ( 1966) data on the relation between spike shapes and spike conduction velocity served to relate each simulated fall time (and by that  $h$ ) to the conduction velocity  $v(h)$  that the simulated fiber with this fall time should have. Finally, the diameter  $D(h)$  of the modeled fiber that produces these desired conduction velocity  $v(h)$  and fall time  $t_{fall}(h)$  could be determined unambiguously by application of the definition of  $Y$  to the recorded value of  $Y(h)$ :

$$D(h) = v(h)/Y(h) . \quad (2)$$

This procedure, which will be described in detail now, is illustrated in Fig. 2. Fig. 2<sup>a</sup> shows the dependence of  $t_{fall}$  on  $h$ , as determined by varying  $h$  in an otherwise standard SEF neuron, while Fig. 2<sup>b</sup> displays the simultaneously recorded  $Y$  as a function of  $h$ . To link these simulated curves to experimental data, Paintal's observation that  $t_{fall}$  depends linearly on  $v$  (Paintal, 1966), was applied. Using his data set for 32.9°C and his Q<sub>10</sub>-value of  $(3.5)^{-1}$  for  $t_{fall}$  we derived for nerve fibers at mammalian body temperature (37°C):

$$t_{fall} = 401 - 1.9 \cdot v \Leftrightarrow v = (401 - t_{fall}) / 1.9 \quad (3)$$

where  $t_{fall}$  is expressed in  $\mu\text{s}$  and  $v$  in m/s. This experimentally determined relation, plotted in Fig. 2<sup>c</sup>, was combined with the simulation data in Fig. 2<sup>a</sup> by substituting each simulated  $t_{fall}(h)$  in Eq. 3. This procedure is symbolized by the horizontal arrow that points from a simulation data point in Fig. 2<sup>a</sup> to the line representing Eq. 3 in Fig. 2<sup>c</sup>. This yields  $v(h)$ , which is the spike conduction velocity to be associated with the value of  $t_{fall}(h)$  (and thus  $h$ ) in the generalized SEF model. Finally, the  $Y$  value for each  $h$  in Fig. 2<sup>b</sup> was used in conjunction with Eq. 2 to determine unambiguously the diameter  $D(h)$  that corresponds to :

velocity to be associated with the value of  $t_{fall}$  (and thus  $h$ ) in the generalized SEF model. Finally, the  $Y$  value for each  $h$  in Fig. 2<sup>b</sup> was used in conjunction with Eq. 2 to determine unambiguously the diameter  $D(h)$  that corresponds to  $h$ :

$$D(h) = v(h) / Y(h) = [401 - t_{fall}(h)] / [1.9 \cdot Y(h)]. \quad (4)$$

This procedure is illustrated in Fig. 2d, where  $D(h)$  is represented by the tangent of the angle between the  $\Psi$  axis and the line through the origin and the intersection of the dotted lines coming from Figs. 2<sup>a</sup> and 2<sup>c</sup>. Theoretically, performing this procedure for all values of  $h$  will completely determine the unique function  $D(h)$  that relates the multiplication factor  $h$  for the nodal parameters to fiber size, provided that the SEF model produces values of  $t_{fall}(h)$  and  $Y(h)$  that allow  $D(h)$  to cover the full range of nerve fiber diameters between 0.5 and 24  $\mu\text{m}$ .

#### *b. Consequences of generalizing the SEF model*

We performed the procedure described in Section III.a for the SEF model and it turned out that variations of  $h$  between approximately 0.3 and 4.0 sufficed to identify  $D(h)$  for fiber diameters between 0.5 and 24  $\mu\text{m}$ . Therefore we could proceed with the next step, i.e. determining its inverse relation  $h(D)$ , which gives the value of  $h$  that should be applied to the nodal parameters to simulate a fiber with arbitrary diameter  $D$ . Only for descriptive purposes we have fitted a polynomial function through the data points using a linear least squares estimation (Press et al., 1988) and requiring that  $h = 1$  for  $D = 15 \mu\text{m}$  in order to keep the generalized model representation for this diameter identical to the original SEF model. We found that a polynomial of order of six in  $D$  had to be taken to give also sufficiently accurate values of  $h$  for the smallest fibers. The resulting function is plotted in Fig. 3<sup>a</sup> in conjunction with the data points used in the analysis. It is of practical importance in defining the set of nodal parameters for a simulated neuron of any diameter, in such a way that Eq. 3 which is based on experimental data, is satisfied. This is demonstrated in Fig. 3<sup>b</sup>, where both the resulting rise time  $t_{rise}$  and the fall time  $t_{fall}$  are plotted as a function of simulated conduction velocity. There is a negligible deviation of the simulated fall time from the straight line representing Paintal's data (Eq. 3) due to the use of the polynomial fit for  $h$ , while also the fall time is within physiological ranges. As is shown in Fig. 3<sup>c</sup> spike height gradually diminishes with conduction velocity in the generalized SEF model, a phenomenon that is absent if the original model is scaled down in the classical way. The implications of this finding will be discussed in Section V.

When discussing the data in Table II (Section II) we already observed that the hypothesis that the nodal permeabilities  $P_{Na}$  and  $P_K$  and leak conductance  $g_L$  are size-dependent, does slightly influence the ratio  $Y$  between  $v$  and  $D$ . Therefore this hypothesis must have an effect on the dependence of the simulated spike conduction velocity on fiber diameter, which will no longer be a linear function.

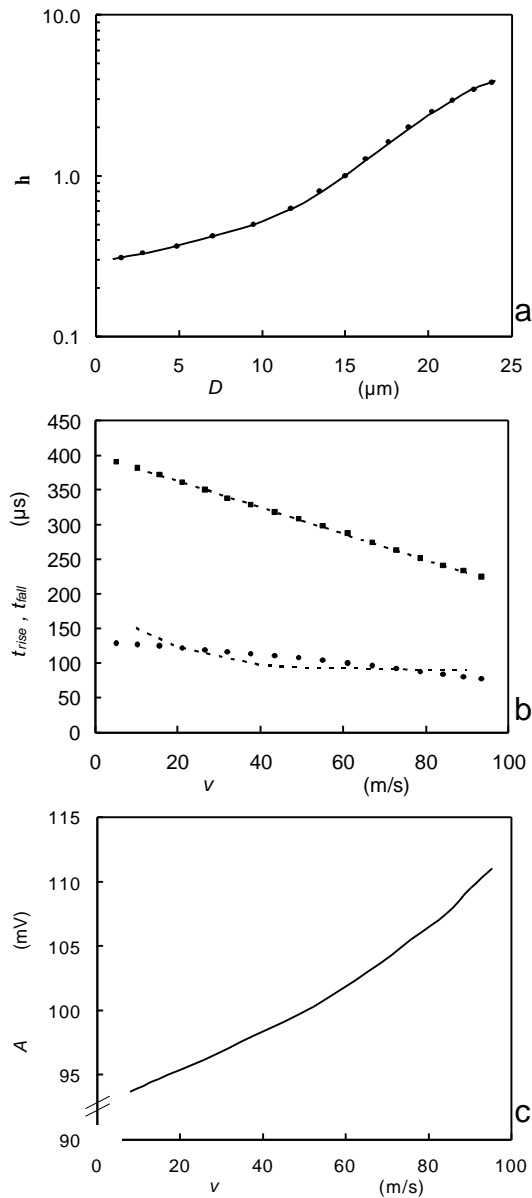


Fig. 3 a. The dependence of  $h$  on diameter  $D$ . The data points represent values that were obtained by direct simulation, the curve was computed with a polynomial, fitted to the data.  
 b. The simulated dependence of  $t_{\text{rise}}$  (filled circles) and  $t_{\text{fall}}$  (filled squares) on conduction velocity  $v$  when  $h(D)$  as shown in (a), is applied to the nodal parameters of the SEF model, compared with experimental values in the cat (dashed lines; Paintal, 1966).  
 c. The simulated dependence of spike amplitude  $A$  on spike conduction velocity  $v$  if  $P_{\text{Na}}, \overline{P_K}$  and  $g_L$  depend on  $D$  by multiplication factor  $h(D)$  (see (a)).

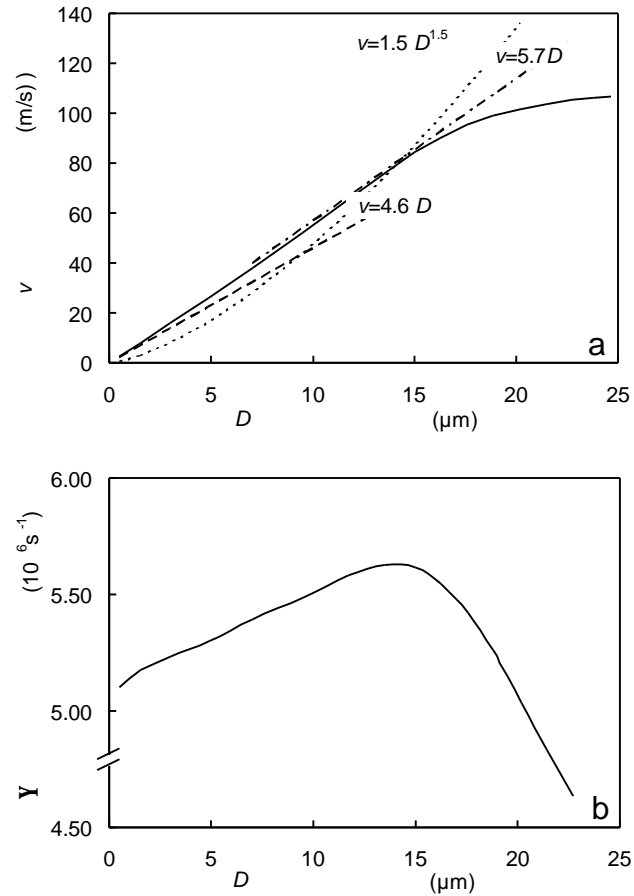


Fig. 4 a. The simulated relationship between spike conduction velocity  $v$  and fiber diameter  $D$  when  $h(D)$  (Fig. 3<sup>a</sup>) is used (solid curve). The dashed lines represent this relationship according to Boyd and Kalu (1979), the dotted line the one according to Coppin and Jack (1972).  
 b. The ratio  $Y$  between simulated  $v$  and  $D$  for the same model as a function of the fiber diameter.

Fig. 4<sup>a</sup> shows that the generalized SEF model exhibits a non-linear relation between  $v$  and  $D$  indeed, and that the curve saturates for the largest fibers. The slope of the line connecting a point on this curve with the origin is  $Y$ , which gradually increases from  $5.1 \cdot 10^6 \text{ s}^{-1}$  at  $D = 0.5 \mu\text{m}$  to reach a plateau of about  $5.6 \cdot 10^6 \text{ s}^{-1}$  for  $D$  between 12 and 16  $\mu\text{m}$  (Fig. 4<sup>b</sup>). For larger fibers  $v$  continues to increase with fiber diameter, but  $Y$  gradually decreases to  $4.6 \cdot 10^6 \text{ s}^{-1}$  for the largest fibers with myelinated diameters around 23  $\mu\text{m}$ .

#### IV. Simulating the influence of the g-ratio on conduction velocity

While a ratio  $g$  between axon diameter and fiber diameter of 0.7 (as it is in the SEF model, Table I) is realistic for relatively large A I fibers, (Dyck et al., 1993), this ratio is known to vary with fiber type and diameter (Waxman and Bennett, 1972; Behse, 1990), which in turn is expected to influence the spike conduction velocity (Rushton, 1951; Goldman and Albus, 1968). In the present section we will first show how the procedure that related  $h$  to  $D$  by application of Paintal's experimental data can be extended to include different fiber morphologies, and then investigate the consequences of this extension for the simulated velocity-diameter relation for A<sub>II</sub> and A<sub>III</sub> fibers for which Behse (1990) measured the  $g$ -ratio.

##### a. Anatomical observations

There has been discussion on the subject whether the ratio  $g$  between axon diameter  $d$  and total fiber diameter  $D$  is fixed or depends systematically on fiber size (Waxman and Bennett, 1972; Hildebrand et al., 1993). At present, most evidence points into the direction that the number of myelin lamellae and therefore the total myelin thickness for a given axon diameter depends on both fiber type and animal species. Using light and electron microscopic techniques Behse (1990) showed that the relation between myelin thickness  $D_{my}$  and axon diameter  $d$  for A<sub>II</sub> and A<sub>III</sub> fibers in human sural nerves is best described by two different straight lines of the form:

$$D_{my} = a \cdot d + b \quad (5)$$

where  $a$  and  $b$  are constants that are different for each of these two fiber types. Application of the definition of the  $g$ -ratio and some straightforward mathematical manipulations to Eq. 5 yields the following dependence of  $g$  on  $D$ :

$$g = \left(1 - \frac{2 \cdot b}{D}\right) / (1 + 2 \cdot a). \quad (6)$$

This relation, with parameters  $a$  and  $b$  taken from Behse (Behse, 1990) has been plotted in Fig. 5 for both A<sub>II</sub> and A<sub>III</sub> fibers. It appears that in both cases  $g$  diminishes gradually with decreasing fiber size, but that there is a notable difference in the region of overlap for diameters around 6  $\mu\text{m}$ , where the A<sub>II</sub> fibers have much smaller  $g$ -ratios than A<sub>III</sub> fibers of the same outer diameter  $D$ .

##### b. Adjusting the model parameters to include different g-ratios

Like we did in Section III.a, we performed repeated simulations for a wide range of values of  $h$  for  $g$ -ratios between 0.40 and 0.80 with an otherwise standard 15  $\mu\text{m}$  SEF neuron. It appeared that the resulting fall time  $t_{fall}(h, g)$  (cf. Fig. 2<sup>a</sup>) did not depend on the  $g$ -ratio, i.e.  $t_{fall}(h, g) = t_{fall}(h)$ . Therefore, the spike conduction velocity to be associated with each value of  $t_{fall}$ , determined by application of Paintal's observations as formulated in Eq. 3, is also only a function of  $h$  and not of  $g$ , i.e.  $v(h, g) = v(h)$ .

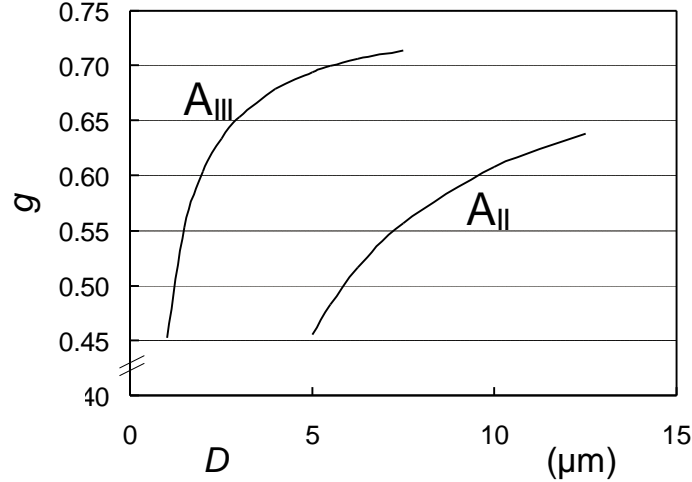


Fig. 5 The ratio  $g$  between axon diameter  $d$  and fiber diameter  $D$  for human sural A<sub>II</sub> and A<sub>III</sub> fibers as computed with Eq. 6 from Behse's data (Behse, 1990).

However, it turned out that the influence of the multiplication factor  $h$  on the ratio  $Y(h, g)$  between the simulated value of  $v$  and the fiber's diameter could not be described by simply scaling the original function  $\Psi(h)$ , determined in Section III and plotted in Fig. 2<sup>b</sup>, by a factor that is only a function of  $g$ . As a consequence, we were not able to find the diameter dependent nodal properties of the model with respect to different  $g$ -ratios by means of a simple transformation of the polynomial  $h(D)$  derived for  $g = 0.7$ .

Therefore, we had to resort to performing the analysis illustrated in Fig. 2 for each simulation in our data set. In this way  $D(h, g)$ , the outer diameter of a fiber with  $g$ -ratio  $g$  that is to be associated with multiplication factor  $h$  in the final model, is determined by the following equation, which is the generalized form of Eq. 4:

$$D(h, g) = v(h, g) / Y(h, g) = [401 - t_{fall}(h, g)] / [1.9 \cdot Y(h, g)]. \quad (7)$$

As the final step in the analysis we performed a two-dimensional linear least squares fit to find a bivariate polynomial that describes  $h(D, g)$  for fibers of all diameters with an arbitrary  $g$ -ratio, with the additional constraint that  $h(15, 0.7) = 1$  in order to include the original SEF model in its generalized formulation. This resulted in the following bivariate function of order 6 in  $D$  (expressed in  $\mu\text{m}$ ) and order 2 in  $g$ :

$$h(D, g) = \sum_{m=0}^6 \sum_{n=0}^2 a_{mn} D^m g^n. \quad (8)$$

For descriptive purposes the coefficients are given in Table III.

Table III The parameters  $a_{nm}$  of Eq. 8, the bivariate function of order 6 in  $D$  and order 2 in  $g$ , yielding the value of multiplication factor  $h(D,g)$ .

m \ n	0	1	2
0	$3.4106 \cdot 10^{-1}$	$-1.5311 \cdot 10^{-1}$	$1.1590 \cdot 10^{-1}$
1	$-5.4317 \cdot 10^{-2} \mu\text{m}^{-1}$	$2.0508 \cdot 10^{-1} \mu\text{m}^{-1}$	$-1.5961 \cdot 10^{-1} \mu\text{m}^{-1}$
2	$2.8972 \cdot 10^{-2} \mu\text{m}^{-2}$	$-0.9926 \cdot 10^{-1} \mu\text{m}^{-2}$	$8.0065 \cdot 10^{-2} \mu\text{m}^{-2}$
3	$-6.2567 \cdot 10^{-3} \mu\text{m}^{-3}$	$2.1838 \cdot 10^{-2} \mu\text{m}^{-3}$	$-1.6520 \cdot 10^{-2} \mu\text{m}^{-3}$
4	$5.8617 \cdot 10^{-4} \mu\text{m}^{-4}$	$-2.0009 \cdot 10^{-3} \mu\text{m}^{-4}$	$1.3836 \cdot 10^{-3} \mu\text{m}^{-4}$
5	$-2.3011 \cdot 10^{-5} \mu\text{m}^{-5}$	$7.4148 \cdot 10^{-5} \mu\text{m}^{-5}$	$-4.1686 \cdot 10^{-5} \mu\text{m}^{-5}$
6	$3.0626 \cdot 10^{-7} \mu\text{m}^{-6}$	$-8.9616 \cdot 10^{-7} \mu\text{m}^{-6}$	$3.2493 \cdot 10^{-7} \mu\text{m}^{-6}$

### c. Application of the generalized SEF model to different fiber morphologies

Simulations performed for values of  $g$  between 0.4 and 0.8 that used Eq. 8 to provide  $h(D,g)$  showed that the resulting generalized version of the SEF model obeyed Eq. 3 as neatly as the fit for  $g = 0.7$  (see Fig. 3<sup>b</sup>), indicating that the fit is sufficiently accurate in this respect. In fact, also the plot of  $t_{fall}$  as a function of simulated conduction velocity  $v$  does not depend on  $g$ . Therefore, it is not reproduced here as it is identical to the corresponding plot in Fig. 3<sup>b</sup>.

With this fit, the influence on neural behavior of the anatomical variations of the  $g$ -ratio with fiber diameter can be simulated. Fig. 6<sup>a</sup> displays the computed relation between spike conduction velocity and diameter for the morphology of A<sub>II</sub> and A<sub>III</sub> sural nerve fibers as reported by Behse (see Section IV.a) and for A<sub>I</sub> fibers with a fixed  $g$ -ratio of 0.7. The most striking observation in this figure is that the model predicts that, for diameters in regions of overlap between fiber classes, A<sub>II</sub> fibers conduct more slowly than both A<sub>I</sub> and A<sub>III</sub> fibers of the same outer diameter. The differences between the fiber types appear in a more prominent way in Fig. 6<sup>b</sup>, which displays  $Y$  as a function of  $D$  for these fiber classes. It appears that simulated values of  $Y$  range from approximately  $4.1 \cdot 10^6 \text{s}^{-1}$  for the smallest A<sub>II</sub> and A<sub>III</sub> fibers to  $5.6 \cdot 10^6 \text{s}^{-1}$  for A<sub>I</sub> fibers with diameters between 12 and 15  $\mu\text{m}$ . From comparison with Fig. 4<sup>b</sup>, which shows this relation for a constant ratio  $g = 0.7$ , it follows that the predicted influence of geometrical factors on the relative spike conduction velocity is somewhat larger than the introduction of the multiplication factor  $h$ , at least for the A<sub>II</sub> fibers and the smallest A<sub>III</sub> fibers.

## V. Physiological implications

It is expected that the introduction of a diameter dependent scaling factor  $h(D,g)$  for the nodal permeabilities and the introduction of variable  $g$ -ratios will not only modify the spike shape and spike conduction velocity but also other aspects of neural behavior. Here the influence of these factors on the strength/duration behavior and on the maximum firing rate will be studied.

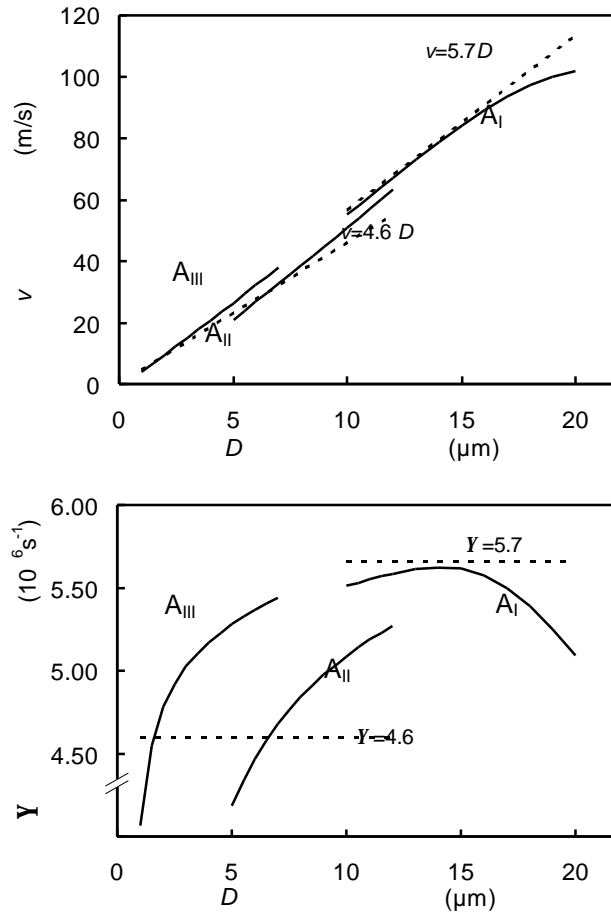


Fig. 6 As Fig. 4, now for  $A_I$  fibers with a constant  $g$ -ratio of 0.7, and  $A_{II}$  and  $A_{III}$  fibers with  $g$ -ratios according to Behse (1990). The dotted lines represent the relationship between  $v$  and  $D$  as reported by Boyd and Kalu (1979).

#### a. Rheobase and chronaxy

To investigate the influence of  $h(D, g)$  on the predicted strength/duration behavior we have computed the rheobase and chronaxy of fibers from the various fiber classes for cathodal stimulation. The rheobase  $I_{rh}$ , defined as the current threshold for a long duration pulse, was determined using a pulse width of 1 ms. The chronaxy  $t_{chr}$  is defined as the minimum duration of a pulse necessary to excite the fiber with a current strength twice  $I_{rh}$ . The simulations were performed for fibers that were modeled using 120 active nodes and a point source electrode, 1 mm radially away from the central node of these fibers.

It appears that  $I_{rh}$  increases gradually with decreasing fiber diameter in all cases (Fig. 7<sup>a</sup>). From comparison of the curve computed with the original SEF model

against the one computed with  $g = 0.7$  in the extended SEF model (labeled  $A_I$  in Fig. 7<sup>a</sup>) it follows that the introduction of  $h(D,g)$  diminishes this effect. The corresponding curves computed for  $A_{II}$  and  $A_{III}$  fibers indicate that a reduction of the  $g$ -ratio results in a minor increase of excitation thresholds, thus slightly counteracting the effect of  $h(D,g)$  on this aspect of model behavior. Fig. 7<sup>b</sup> displays the effect of fiber diameter on  $t_{chr}$  in the same model situations. It appears that for  $g = 0.7$  this chronaxy increases substantially more with decreasing fiber diameter in the generalized SEF model (curve labeled  $A_I$ ) than in the original model. This effect is enhanced to a minor extent by the varying  $g$ -ratios used in the simulations for  $A_{II}$  and  $A_{III}$  fibers.

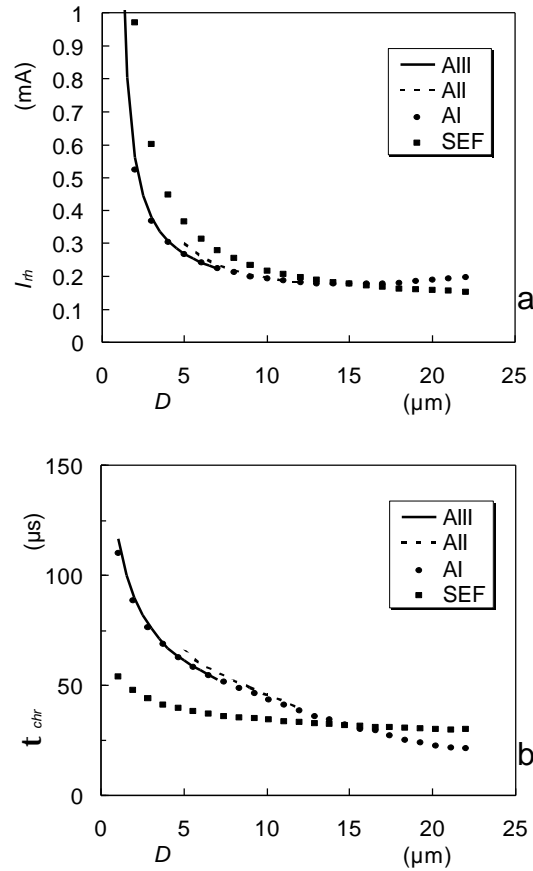


Fig. 7 a. The rheobase current  $I_{rh}$  as a function of fiber diameter  $D$  for the original SEF model ( $g = 0.7$ ), and the generalized SEF model for  $A_{II}$  and  $A_{III}$  fiber classes with  $g$ -ratios according to Behse (1990). The data points labelled  $A_I$  were computed with the generalized model and a constant  $g$ -ratio of 0.7, which is for  $D > 10 \mu\text{m}$  the generalized model representation of  $A_I$  fibers. The  $A_I$  data points for  $D < 10 \mu\text{m}$  were included to illustrate the predictions of the model described in Section III. Results were computed for a cathode, 1 mm radially away from the centre of a fiber consisting of 120 nodes.

b. The chronaxy  $t_{chr}$  as a function of diameter for the same fibers as used in (a).

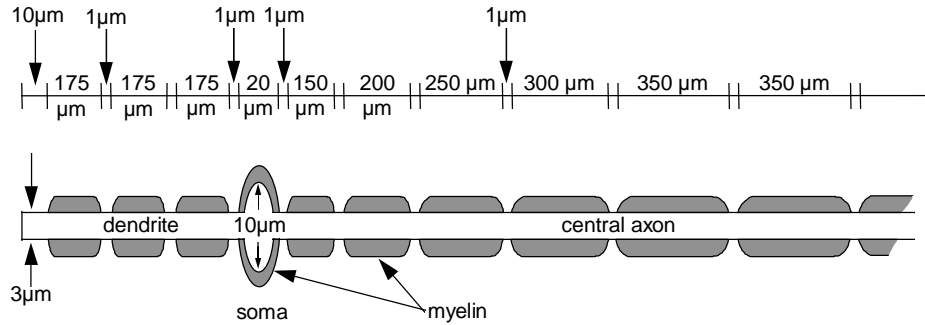


Fig. 8 The morphology of the auditory nerve fiber model used to test the influence of the application of  $h(D,g)$  as given by Eq. 8 on the frequency following behavior.

### b. Firing behavior of auditory nerve fibers during repetitive stimulation

An aspect of neural behavior that is important in neural prostheses in general and in auditory prostheses in particular is the frequency following behavior. From the fact that the introduction of  $h(g,D)$  results in prolonged action potentials for thinner fibers, it is expected that this will be accompanied by a prolonged refractory period, and as a consequence, by a reduction of the maximum steady-state firing rate. As stated in Section I these properties, which are well-documented for auditory nerve fibers, do not depend on fiber diameter if the specific nodal properties are fixed as in the original SEF model. To investigate the behavior of the extended model in this respect, an auditory nerve fiber model was constructed, based on the morphological findings reported by Liberman and Oliver (1984) in the cat and Brown (1987) and Gleich and Wilson (1993) in the guinea pig, taking into account a shrinkage of approximately 10% due to labeling with horseradish peroxidase, and assuming that the resultant fiber with an axon diameter of 3  $\mu\text{m}$  had a  $g$ -ratio of 0.685 like an A<sub>III</sub>-fiber of the same dimensions (Fig. 8). The rise time of the simulated action potential is 0.12 ms, while its fall time is 0.36 ms, resulting in a total spike duration of 0.48 ms. The absolute refractory period appeared to be 1.1 ms, while the maximum steady-state firing rate is approximately 650 Hz, which is indeed lower than the value of 1.1 kHz found with the original SEF kinetics (Frijns et al., 1994b).

## VI. Discussion

This paper aims at getting a better understanding of the mechanism behind the observation that the duration of the action potentials of mammalian myelinated nerve fibers decreases with increasing spike conduction velocity (Paintal, 1966; Coppin 1973), a phenomenon that is not explained by existing theoretical and computational models. Geometrical scaling of existing active cable models yields a linear relationship between fiber diameter and spike conduction velocity, which is in accordance with Rushton's corresponding state theory, and

acceptable in the light of experimental findings, but the simulated spike shapes are identical for all fiber diameters (Fig. 1). To account for this discrepancy, Jack (1975) hypothesized that the membrane properties of amphibian (and possibly also mammalian) peripheral nerve fibers are correlated with their size. He formulated this hypothesis on the basis of a model based on the Hodgkin and Huxley (1952) equations.

The present study addresses the subject by means of simulations with an active cable model of a 15  $\mu\text{m}$  mammalian myelinated nerve fiber with nodal kinetics based upon voltage-clamp data in large rat and cat fibers at mammalian body temperature (Schwarz and Eikhof, 1987). In our previous paper (Frijns et al., 1994b) it was demonstrated that this SEF model, which treats the internodal myelin as a perfect insulator, describes many neural properties, including the spike shape, spike conduction velocity and the maximum firing frequency in a quantitatively correct way. We also discussed that the classical way to represent the internodal myelin as a leaky capacitor or a series of leaky capacitors (cf. Fitzhugh, 1962; Goldman and Albus, 1968) causes a large increase in spike duration that is inconsistent with the measurements of Schwarz and Eikhof (1987), and also unrealistically reduces the spike conduction velocity by more than 60%. The latter findings conform with the results obtained with a multi-axial cable model that took into account many anatomical details of both the nodal and internodal areas (Halter and Clark, 1991). Furthermore, the inclusion of an internodal time constant in the SEF model would not only corrupt the simulated spike shape and the spike conduction velocity, but also relevant model properties such as the refractory behavior and the maximum steady-state firing rate. However, the effect of an internodal time constant on the chronaxy appeared to be limited: As contrasted with Rubinstein's (1991) theoretical predictions from the analysis of a passive cable, a more than three-fold increase of the time constant of the node-internode unit increased  $t_{chr}$  less than 40%. Therefore, we decided not to include such a capacitive internode, as our aim was to give a quantitatively correct description of at least the spike shape and conduction velocity.

The parameter variation study performed in Section II led to the conclusion that there are two ways to explain the phenomenon that a fiber's spike shape depends on its spike conduction velocity  $v$ . First, the rate constants  $t_m$ ,  $t_h$ , and  $t_n$  of the differential equations governing the activation and inactivation of the ion channels might depend on diameter, like they depend on temperature (Frijns et al., 1994b). An argument against this hypothesis is that such a variation has an unrealistically strong influence on the spike conduction velocity (Table II). This effect might be reduced by introducing a diameter dependence of  $t_m$  that is less pronounced than that for  $t_h$ . We did not further pursue this possibility, also because of the relatively large influence of the temperature on the spike conduction velocity when compared with its influence on the spike shape, despite the fact that the temperature dependence of  $t_m$  is less than that of  $t_h$  (cf. Figs. 3 and 4 in Frijns et al., 1994b).

The other hypothesis that can explain the relation between spike conduction velocity and spike shape is that there is a systematic variation in the active and passive ionic permeabilities (per unit area of membrane). Although the effect

of the active potassium channels on mammalian nerve fiber properties is very limited (Schwarz and Eikhof, 1987; Table II), we have assumed that the diameter dependence of  $P_{Na}$  and  $P_K$  is identical. This ensures that the resting membrane potential  $V_r$  as computed with the Goldman equation is independent of fiber diameter. Such a dependence is unlikely, since this would imply e.g., DC-currents to flow in the resting state along bipolar auditory neurons which can have different axon diameters on both sides of the cell body (Gleich and Wilson, 1993).

Therefore the hypothesis was elaborated that  $\bar{g}_L$ ,  $P_{Na}$  and  $P_K'$  vary systematically, and by the same multiplication factor  $h$ , with fiber diameter. It turned out that it is possible to match the model's spike fall time with Paintal's experimental data (Paintal, 1966) on the basis of this hypothesis, not only for fibers with a fixed ratio  $g = 0.7$  between axon diameter  $d$  and total fiber diameter  $D$  (Section III), but also for any other physiologically realistic value of this ratio (Section IV). It appeared that this scaling also results in values of  $t_{rise}$  that are roughly in accordance with Paintal's observations (Fig. 3<sup>b</sup>). As stated before, it is not pretended that the bivariate function used to describe the dependence of multiplication factor  $h$  on  $D$  and  $g$  (Eq. 8) has a physiological background, but it is of practical importance in defining the set of nodal parameters for simulating a neuron with an arbitrary geometry.

An interesting property of this generalized version of the SEF model is the fact that it predicts that the conduction velocity of thin fibers is lower relative to their diameter than that of larger ones (Fig. 4), resulting in a slightly non-linear, sigmoidal form of the diameter-velocity relationship. This finding is in accordance with physiological data regarding the analysis of compound action potentials, both in amphibia (Wijesinghe et al., 1991), and in mammals as first reported by Gasser and Grundfest (1939) and given renewed evidence by Stegeman and De Weerd (1982) (see Schoonhoven and Stegeman (1991) for a review of literature on this subject). This effect is further enhanced if allowance is made for the known physiological variation of the  $g$ -ratio with fiber size (Fig. 5; Eq. 6) as deduced from Behse (1990). Then, the model yields ratios  $Y$  between  $v$  and  $D$  that are close to the experimental values reported by Boyd and Kalu (1979) for various nerves, including the sural nerve, in the cat hind limb (Fig. 6), not only for large fibers like the original SEF model, but also for thinner A<sub>II</sub> and A<sub>III</sub> fibers. We conclude that the generalization introduced to correct the spike shape also results in a shift of the velocity diameter relation in a physiologically realistic direction.

The data regarding the excitation thresholds and chronaxy (Fig. 7) show that the occurrence of longer spikes due to the introduction of diameter dependent nodal properties is associated with an increased strength/duration time constant. This effect could be expected beforehand (cf. Rubinstein, 1991), since a reduction of  $\bar{g}_L$ ,  $P_{Na}$  and  $P_K'$  increases the nodal time constant and as a consequence the time constant of the node-internode unit. Changes of the  $g$ -ratio, however, do not notably influence the strength/duration behavior. The changed strength/duration properties, including a reduction relative to the SEF model of the predicted rheobase for small fibers, will have their bearing upon the predicted recruitment of fibers in a nerve bundle that is stimulated with

electrical pulses of varying width, as typically occurs in the field of functional electrical stimulation (Veltink et al., 1988; Rijkhoff et al., 1994). Therefore, comparison of the model predictions with and without the application of  $h(D,g)$  to the nodal parameters with experimental results from this field may yield further information regarding the physiological significance of the underlying hypothesis.

More direct evidence to decide between the two possible explanations of the dependence of spike shape on fiber diameter, i.e. a diameter dependence of either the rate constants or of the ionic conductances, may come from experiments that measure the height of the transmembrane action potential for fibers with different diameter. As is readily seen in Fig. 3<sup>c</sup>, a decrease of the conduction velocity due to a decrease of  $g_L$ ,  $P_{Na}$  and  $P_K$  is accompanied by a decrease of the amplitude of the action potential. If, on the other hand, the prolonged spike duration of fibers with lower conduction velocities results from a reduction of the rate constants  $t_m$ ,  $t_h$ , and  $t_n$ , this is associated with an increase of spike height for thinner fibers (see Table II). To our knowledge there are no reliable experimental data regarding this issue available in literature.

We conclude that the simulation results obtained with the generalized SEF model at least do not contradict the hypothesis that both the active and passive nodal conductances depend on fiber diameter, since fitting the fall time of the action potential to experimentally derived data resulted not only in a concomitant change of the rise time that is acceptable in the light of the same data, but also in a physiologically realistic non-linearity of the diameter-velocity relationship. Moreover, the spike shape and repetitive firing properties (Section V.b) of the auditory nerve fiber model that was constructed on the basis of this generalized SEF model are also in good agreement with the physiological data cited in Section I. This makes this auditory nerve fiber model applicable to study electrical stimulation of the deaf inner ear with cochlear implants (Frijns et al., 1995).

Of course, one should realize that the SEF model is a simplified representation of the *in vivo* situation, which cannot account for all known neural properties. Nevertheless, we feel that further experimental research is required in order to validate or falsify the hypothesis on which the present analysis is based. In addition, substantial modeling effort is still required since even today's most sophisticated models like the one presented by Halter and Clark (1991) fall short when quantitative aspects of neural behavior are considered.

## References

- Behse, F. 1990. Morphometric studies on the human sural nerve. *Acta Neurol. Scand.* 82, Suppl. 132; 1-38.
- Boyd, I.A., and K.U. Kalu. 1979. Scaling factor relating conduction velocity and diameter for myelinated afferent nerve fibers in the cat hind limb. *J. Physiol.* 289; 277-297.
- Brismar, T. 1980. Potential clamp analysis of membrane currents in rat myelinated nerve fibers. *J. Physiol. (London)* 298; 171-184.
- Brown, M.C. 1987. Morphology of labeled afferent fibers in the guinea pig cochlea. *J. Comp. Neurol.* 260; 591-604.
- Chiu, S.Y., J.M. Ritchie, R.B. Rogart, and D. Stagg. 1978. A quantitative description of membrane current in rabbit myelinated nerve. *J. Physiol. (London)* 292; 149-166.
- Coppin, C.M.L. 1973. A study of the properties of mammalian peripheral nerve fibres. D.Phil. thesis, University of Oxford.
- Coppin, C.M., and J.J.B. Jack. 1972. Internodal length and conduction velocity of cat muscle afferent fibres. *J. Physiol. (London)* 222; 91-93.
- Dyck, P.J., P.K. Thomas, J.W. Griffin, P.A. Low, and J.F. Poduslo. 1993. Peripheral neuropathy. Saunders, Philadelphia.
- Fitzhugh, R. 1962. Computation of impulse initiation and saltatory conduction in a myelinated nerve fibre. *Biophys. J.* 2:11-21.
- Frankenhaeuser, B., and A.F. Huxley. 1964. The action potential in the myelinated nerve fibre of *Xenopus laevis* as computed on the basis of voltage clamp data. *J. Physiol. (London)* 171; 302-315.
- Frijns, J.H.M., and J.H. ten Kate. 1994a. A model of myelinated nerve fibres for electrical prosthesis design. *Med. Biol. Eng. Comput.* 32; 391-398.
- Frijns, J.H.M., J. Mooij, and J.H. ten Kate. 1994b. A quantitative approach to modelling mammalian myelinated nerve fibers. *IEEE Trans. Biomed. Eng.* 41; 556-566.
- Frijns, J.H.M., S.L. de Snoo, and R. Schoonhoven. 1995. Potential distributions and neural excitation patterns in a rotationally symmetric model of the electrically stimulated cochlea. *Submitted for publication.*
- Gasser, H.S. and Grundfest, H. 1939. Axon diameters in relation to the spike dimensions and the conduction velocity in mammalian A fibers. *Am. J. Physiol.* 127, 393-414.
- Gleich, O. and S. Wilson. 1993. The diameters of guinea pig auditory nerve fibres: distribution and correlation with spontaneous rate. *Hear. Res.* 71; 69-79.
- Goldman, L., and J.S. Albus. 1968. Computation of impulse conduction in myelinated fibres; theoretical basis of the velocity-diameter relation. *Biophys. J.* 8; 596-607.
- Halter, J.A., and J.W. Clark Jr. 1991. A distributed-parameter model of the myelinated nerve fibre. *J. Theor. Biol.* 148; 345-382.
- Hildebrand, C., S.Remahl, H. Persson, and C. Bjartmar. 1993. Myelinated nerve fibres in the CNS. *Progress in Neurobiology* 40; 319-384.
- Hodgkin, A.L., and A.F. Huxley. 1952. A quantitative description of membrane current and its application to conduction and excitation in nerve. *J. Physiol.(London)* 117; 500-544.
- Horáckova, M., W. Nonner, and R. Stämpfli. 1968. Action potentials and voltage clamp currents of single rat Ranvier nodes. *XXIV Int. Cong. Physiol. Sci.*; 198.
- Hursh, J.B. 1939. Conduction velocity and diameter of nerve fibers. *Am. J. Physiol.* 127; 131-139.

- Jack, J.J.B. 1975. Physiology of peripheral nerve fibres in relation to their size. *Br. J. Anaesth.* 47; 173-182.
- Kiang, N.Y.S., E.C. Moxon, and A.R. Kahn. 1976. The relationship of gross potentials recorded from the cochlea to single unit activity in the auditory nerve. *In* *Electrocochleography*. R.J. Ruben, C. Elberling, and C. Salomon, editors. University Park Press, Baltimore. 95-115.
- Lieberman, M.C. and M.E. Oliver. 1984. Morphometry of intracellularly labeled neurons of the auditory-nerve: correlations with functional properties. *J.Comp.Neurol.* 223; 163-176.
- McNeal, D.R. 1976. Analysis of a model for excitation of myelinated nerve. *IEEE Trans. Biomed. Eng.* 23; 329-337.
- Moxon, E.C. 1968. Auditory nerve responses to electric stimuli. *M.I.T. Quart. Prog. Rpt.* 90; 270-275.
- Paintal, A.S. 1966. The influence of diameter of medullated nerve fibers of cat on the rising and falling phases of the spike and its recovery. *J. Physiol. (London)* 184; 791-811.
- Paintal, A.S. 1967. A comparison of the nerve impulses of mammalian non-medullated nerve fibres with those of the smallest diameter medullated fibres. *J. Physiol. (London)* 193; 523-533.
- Paintal, A.S. 1978. Conduction properties of normal peripheral mammalian axons. *In* *Pathology and Pathobiology of Axons*. S.G. Waxman, editor. Raven Press, New York. 131-144.
- Press, W.H., B.P. Flannery, S.A. Teukolsky, and W.T. Vetterling. 1988. *Numerical recipes; The art of scientific computing*. Cambridge Univ. Press, Cambridge, MA.
- Reilly, J.P., V.T. Freeman, and W.D. Larkin. 1985. Sensory effects of transient electrical stimulation: Evaluation with a neuroelectrical model. *IEEE Trans. Biomed. Eng.* 32; 1001-1011.
- Rijkhoff, N.J.M., J. Holsheimer, E.L. Koldewijn, J.J. Struijk, P.E.V. van Kerrebroeck, F.M.J. Debryne, and H. Wijkstra. 1994. Selective stimulation of sacral nerve roots for bladder control: A study by computer modeling. *IEEE Trans. Biomed. Eng.* 41; 413-424.
- Rubinstein, J.T. 1991. Analytical theory for extracellular electrical stimulation of nerve with focal electrodes: II. Passive myelinated axon. *Biophys. J.* 60; 538-555.
- Rushton, W.A.H. 1951. A theory of the effects of fibre size in medullated nerve. *J. Physiol. (London)* 115; 101-122.
- Santos-Sacchi, J. 1993. Voltage-dependent ionic conductances of type I spiral ganglion cells from the guinea pig inner ear. *J. Neurosci.* 13; 3599-3611.
- Schoonhoven, R., and D.F. Stegeman. 1991. Models and analysis of compound action potentials. *Crit. Rev. Biomed. Eng.* 19; 47-111.
- Schwarz, J.R., and G. Eikhof. 1987. Na current and action potentials in rat myelinated nerve fibres at 20 and 37°C. *Pflügers Arch.* 409; 569-577.
- Smith, K.J., and C.L. Schauf. 1981. Size-dependent variation of nodal properties in myelinated nerve. *Nature* 293; 297-299.
- Stegeman, D.F. and Weerd, J.P.C. de. 1982. Modelling compound action potentials of peripheral nerves *in situ*. I. Model description; evidence for a nonlinear relation between fibre diameter and velocity. *Electroenceph. Clin. Neurophysiol.*, 54, 436-448.
- Sweeney, J.D., J.T. Mortimer, and D. Durand. 1987. Modeling of mammalian myelinated nerve for functional neuromuscular stimulation. *Proc. IEEE 9th Ann. Int. Conf. EMBS*; 1577-1578.

- Veltink, P.H., J.A. van Alsté, and H.B.K. Boom. 1988 Influences of stimulation conditions on recruitment of myelinated nerve fibres: A model study. *IEEE Trans. Biomed. Eng.* 35; 917-924.
- Waxman, S.G., and M.V.L. Bennett. 1972. Relative conduction velocities of small myelinated and non-myelinated fibres in the central nervous system. *Nature New Biol.* 238; 217-219.
- Wijesinghe, R.S., F.L.H. Gielen, and J.P. Wikswo, Jr. 1991 A model for compound action potentials and currents in a nerve bundle III: A comparison of the conduction velocity distributions calculated from compound action currents and potentials. *Ann. Biomed. Eng.* 19; 97-121.

# Chapter V

---

**POTENTIAL DISTRIBUTIONS AND  
NEURAL EXCITATION PATTERNS IN A  
ROTATIONALLY SYMMETRIC MODEL OF THE  
ELECTRICALLY STIMULATED COCHLEA**

*J.H.M. Frijns, S.L. de Snoo and R. Schoonhoven  
Submitted for Publication.*

## Abstract

In spite of many satisfactory results, the clinical outcome of cochlear implantation is poorly predictable and further insight in the fundamentals of electrical nerve stimulation in this complex geometry is necessary. For this purpose we developed a rotationally symmetric volume conductor model of the implanted cochlea, using the Boundary Element Method (BEM). This configuration mimics the cochlear anatomy more closely than previous, unrolled models. The calculated potential distribution in the cochlea due to stimulating electrodes is combined with a multiple non-linear node model of auditory nerve fibres, which we developed recently. The combined model is used to compute excitation profiles of the auditory nerve for a variety of stimulus levels and electrode positions. The model predicts that the excitation threshold, the spatial selectivity and the dynamic range depend on the exact position of the electrode in the scala tympani. These results are in good agreement with recently published electrical ABR data. It is shown that the use of actively modelled nerve fibres is essential to obtain correct predictions for the biphasic stimuli typically used in cochlear implants and that unrolling the cochlear duct as done in previous models leads to erroneous predictions regarding modiolar stimulation.

## Introduction

The last decades several types of cochlear prostheses have been developed that can offer the profoundly deaf a sense of hearing (Balkany, 1986). These cochlear implants stimulate the auditory nerve electrically inside the inner ear, where the terminal parts of its nerve fibres diverge in a spiral-like manner. Multi-channel prostheses are equipped with multiple electrodes to take advantage of this spatial distribution and the tonotopic organisation of cochlear neurones, aiming at stimulation of a different neural population by each channel and thus providing a different psycho-acoustic percept. Although these multi-channel prostheses have proven to be superior to previous single-channel devices (Gantz and Tyler, 1990), the ideal result -i.e. the understanding of speech without the help of visual cues- is achieved in a minority of patients. Furthermore, it is still virtually impossible to predict pre-operatively which patient will benefit most of the implant (Gantz et al., 1993). In order to get more insight in the processes involved in this type of stimulation and to be able to identify which parameters of an electrical auditory prosthesis are crucial to realise selective stimulation of discrete sub-populations of the auditory nerve fibres, a model of the implanted cochlea would come in useful. Such a model should include two sub-models, the first one describing the electrical volume conduction process, i.e. computing the potential distribution in the cochlea due to the stimulating current sources, the other one simulating the behaviour of the auditory nerve fibres in response to this potential distribution. In an attempt to arrive at the latter sub-model Colombo and Parkins (1987) developed a model of the mammalian auditory-nerve neurone based on the classical work on amphibian nerve fibres of Frankenhaeuser and Huxley (1964), as used by Reilly et al. (1985) in their so-called Spatially

Extended Non-linear Node (SENN) model. In order to fine tune the model to represent physiological data obtained from single auditory-nerve fibre experiments in squirrel monkeys they had to adapt the modelled nerve fibre's anatomy significantly. Rattay and co-workers (Motz and Rattay, 1986; Rattay and Aberham, 1993) used a single-node model to investigate the time structure of the response of the auditory nerve to electrical stimuli and concluded that the Hodgkin and Huxley (1952) model of unmyelinated squid giant axon membrane simulates the electrically stimulated auditory nerve best in time behaviour. Recently we developed the so-called MSENN (Frijns et al., 1994a) and SEF (Frijns et al., 1994b) models which are non-linear cable models which represent essential mammalian nerve fibre properties, including spike conduction velocity, refractory behaviour and repetitive firing, better than previous models. The SEF model is based upon voltage clamp measurements in rat and cat motor nerve fibres at mammalian body temperature performed by Schwarz and Eikhof (1987). In this paper a generalised version of the SEF model is used, which has been extended to include nerve fibres of smaller diameter, details of which are to be published elsewhere.

Apart from the excitability properties of the nerve fibres, the neural excitation patterns are strongly determined by the three-dimensional potential pattern set up in the cochlea by the stimulating current sources. Measurements of the *in vivo* electrical properties of a cochlea implanted with an electrode array confirmed this strong influence of the cochlear electro-anatomy (Black et al., 1983; Iftukube and White, 1987). The first theoretical models on this point assumed an exponential decay of current from its source to the nerve fibres along the cochlea, modelled in one dimension (O'Leary et al., 1985). Sapozhnikov (1990) computed potential distributions with a finite difference method in a linear, unrolled cochlear geometry, incorporating two cochlear turns. Girzon (1987) also used a finite difference method to compute the potential distribution in an anatomically-based three-dimensional volume conductor that included a continuously spiralling cochlear duct, and showed that the scala tympani acts in part as a terminated leaky transmission line. The limited spatial resolution of his model, however, did not permit the computation of neural excitation functions. Finley et al. (1990) were the first to present an integrated three-dimensional neuron-field model of a segment of an unrolled cochlea, using the finite element method (FEM) and a passive nerve fibre model based upon activation functions (Rattay, 1989) for most of their computations. Suesserman and Spelman (1993) developed a so-called lumped-parameter model of the unrolled first turn of a guinea pig cochlea in which they incorporated resistive and capacitive components but did not include any neural element.

In this paper we will present a rotationally symmetric volume conduction model of the second turn of the guinea pig cochlea, coupled with an active nerve fibre model. Unlike previous models, this model preserves the contiguity in the modiolus of the auditory nerve fibres coming from different places in the cochlea (See Fig. 1). Therefore it is expected to give a more accurate description of the neural recruitment characteristics, especially for higher stimulus currents where

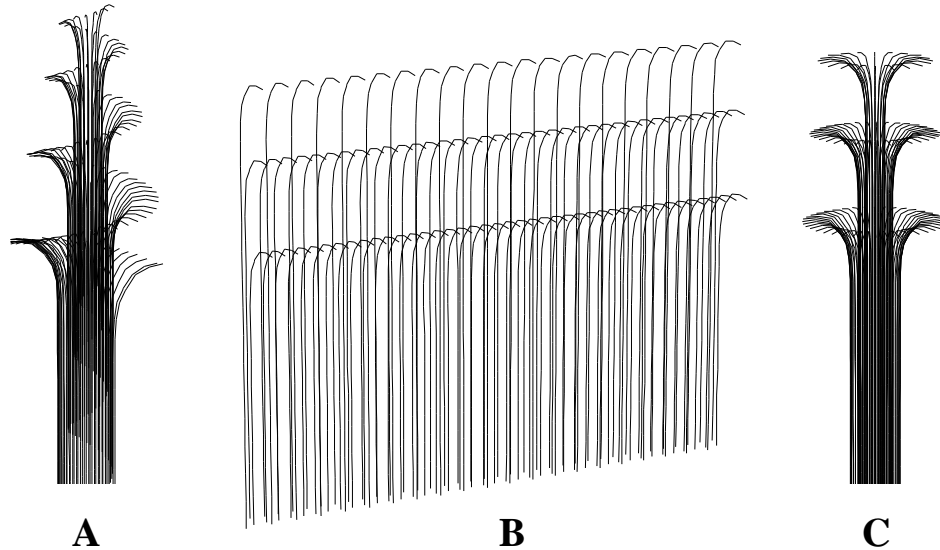


**Fig. 1** **A** Schematic representation of the way the auditory nerve fibres are distributed in the normal cochlea. The fibres are tonotopically organised in such a way that more apically ending fibres encode for lower frequencies and follow a more central course in the modiolus.  
**B** In an unrolled cochlea model especially the modiolar portion of the cochlea is heavily distorted. As a result, the central portions of the auditory nerve fibres are running more widely apart.  
**C** A rotation-symmetric geometry preserves the spatial relationship of the central axons in the modiolus.

excitation of nerve fibres in the modiolus is likely to take place. To validate this hypothesis we will use this integrated model to simulate neural responses as a function of electrode current for various electrode positions. First we will present the solution of the volume conduction problem for the rotationally symmetric cochlea, resulting in the potential distribution throughout the cochlea for any given set of electrodes. Then we will describe the way we modelled the neural responses to given potentials at the nodes of Ranvier. Finally, we will combine the two sub-models to compute spatial excitation patterns over the fibre population and the dependence of the number of activated fibres on the stimulus level as reflected in input-output curves of the auditory nerve. The latter results will be compared with electrically evoked auditory brainstem responses (EABR) that were measured *in vivo* in the cat (Shepherd et al., 1993). To assess the relevance of using our complex type of model rather than models based on simplified assumptions as reported before, we will also compare our results with a similar analysis based on either an unrolled cochlea model or on a passive nerve fibre model.

## Calculating potential fields in the cochlea

### *The Boundary Element Method*

There exist several computational methods to solve complex volume conduction problems in three dimensions (Binns et al., 1992). In the present study we will use the Boundary Element Method (BEM) (Meijs et al., 1989; Van Oosterom, 1991), also known as the Integral Equation Method. This method uses Green's second theorem to express the potential distribution due to a current source distribution in a piece-wise homogeneous volume conductor of arbitrary shape as the superposition of two components. The first component is identified as the potential distribution that would be induced by these current sources in a homogeneous medium of infinite extent, whereas the second component is a correction term that accounts for the inhomogeneities in the volume conductor in terms of imaginary secondary sources arising from the boundaries between the various media.

An advantage of the BEM for the complex geometry of the cochlea is the relative ease of mesh generation: It requires discretisation of the *boundaries* between volumes with different conductivity rather than discretisation of these volumes themselves. Another interesting property of the method results from the fact that it is a two-step procedure. The first of these steps accounts for the volume conduction properties of the specific geometry under study by computing the strength of the secondary sources. Once this first step has been performed, the potentials due to different current source configurations can be calculated rapidly in the second step without the need to repeat the much larger computational effort of the first step. In the present paper all current sources will be bipolar point sources directed longitudinally along the basilar membrane, but the method allows the future use of macro-electrodes in arbitrary configurations.

From the analysis of passive neural models it is known that the driving force for the excitation of a nerve fibre at a node far from its end points is roughly proportional to the second order difference quotient of the extracellular potential along the axon. For stimulation at the ends of a finite length fibre -which is frequently the case for an auditory nerve fibre when stimulated by a cochlear implant- the situation is different, and the driving force appears to be proportional to the first spatial difference quotient of the extracellular potential (Warman et al., 1992). From these observations it follows that the accuracy of the solution of the volume conduction problem is not only determined by the accuracy in the computed potential but also by the accuracy of its first and second derivative to the place. For this reason one should either use a mesh which is much finer than the internodal distance to solve the volume conduction problem, or use a coarser mesh in a method which applies at least second order interpolation functions for the potential. We decided for the second option and discretised all boundaries with quadratically curved triangular surface elements on which the potential was also interpolated quadratically. This did not only increase the numerical accuracy of the method

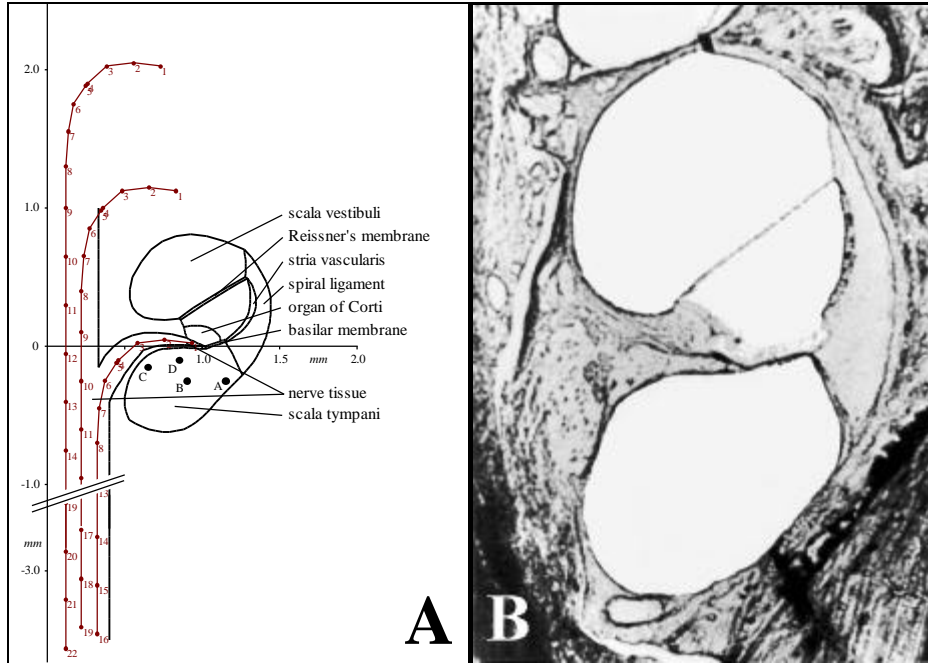


**Fig. 2** **A** The modelled cross-section of the second turn of the guinea pig cochlea. The various compartments with different conductivities (see Table I) are indicated as well as the four electrode sites (A = near the outer wall; B = central in the scala tympani; C = near the spiral ganglion; and D = underneath the dendrites). The course of three nerve fibres, one ending in the modelled second turn and two in more apical turns, is displayed. The numbered dots along these nerve fibres designate the location of the nodes of Ranvier.

**B** Photomicrograph of the cross-section at the beginning of the second turn of a left guinea pig cochlea that was used to construct the boundary element mesh in A.

but also resulted in a more realistic shape of the modelled cochlea (see Figs. 2 and 3; cf. De Munck (1992), Strang and Fix (1973)).

The application of second order interpolation functions implies that the error terms in the calculations are of order three and above, and therefore it is expected that the accuracy of the calculated potentials is inversely proportional to the third power of the length of the sides of the surface elements. This conclusion was confirmed by calculations we performed on configurations with concentric cylinders and spheres for which analytical solutions are available. Further details of the numerical method are beyond the scope of this paper and are to be published elsewhere.

#### *The rotationally symmetric model of one turn of the cochlea*

As our intention was to arrive at a model of the implanted cochlea that can be used in conjunction with our animal experiments on guinea pigs, a cross-section at the base of the second turn of the guinea pig cochlea was used to

construct the mesh of the present model. The contours of this cross-section were approximated by 41 quadratically curved elements through 72 mesh points (see Figure 2 for a comparison between the modelled and observed anatomy). This cross-section was rotated around the central modiolar axis and the created volume 'azimuthally' subdivided in sixteen segments, resulting in the toroidal structure shown in Figure 3. To optimise the numerical accuracy the segments in the vicinity of the electrodes were chosen to be smaller than the more distant ones. The final mesh consisted of 2240 elements and 4194 nodes. Although part of a real guinea pig cochlea projects into an air-containing bulla, the modelled cochlear turn was completely embedded in bone (like the cross-section in Fig 2<sup>B</sup>) for now. This increased the similarity with the human/feline situation, for which relevant experimental ABR data became available recently (Shepherd et al., 1993). Of course, other species-related differences in cochlear anatomy exist, e.g. the fact that the guinea pig cochlea is smaller than the feline one and that it has four instead of three turns. Similarly, the location of Rosenthal's canal in both the cat and guinea pig cochlea differs from the human situation (Shepherd et al., 1993). Such differences must be kept in mind when comparing experimental or simulation data across species.

Although the BEM can deal with the presence of capacitive effects, it is assumed throughout this paper that the impedances of all media in the cochlea are purely resistive, as this allows to evaluate time-varying stimuli without consideration of charge-storage effects in the tissue. This simplifying assumption is supported by the findings of Spelman et al. (1982), who showed that the potentials in the scala tympani are virtually frequency-independent for all frequencies tested (up to 12.5 kHz).

Table I The conductivities of the various cochlear tissues as used in the computations. The data were compiled from Finley et al. (1990), Suesserman (1992) and Strelhoff (1973). The values for the basilar membrane and Reissner's membrane are enlarged by a factor 5 and 10 respectively to correct for the geometric scaling applied to minimise computational errors (see text).

Tissue	Conductivity ( $\text{Wm}^{-1}$ )
Scala tympani	1.43
Scala vestibuli	1.43
Scala media	1.67
Stria vascularis	0.0053
Spiral ligament	1.67
Reissner's membrane	0.00098
Basilar membrane	0.0625
Organ of Corti	0.012
Bone	0.156
Nerve tissue	0.3

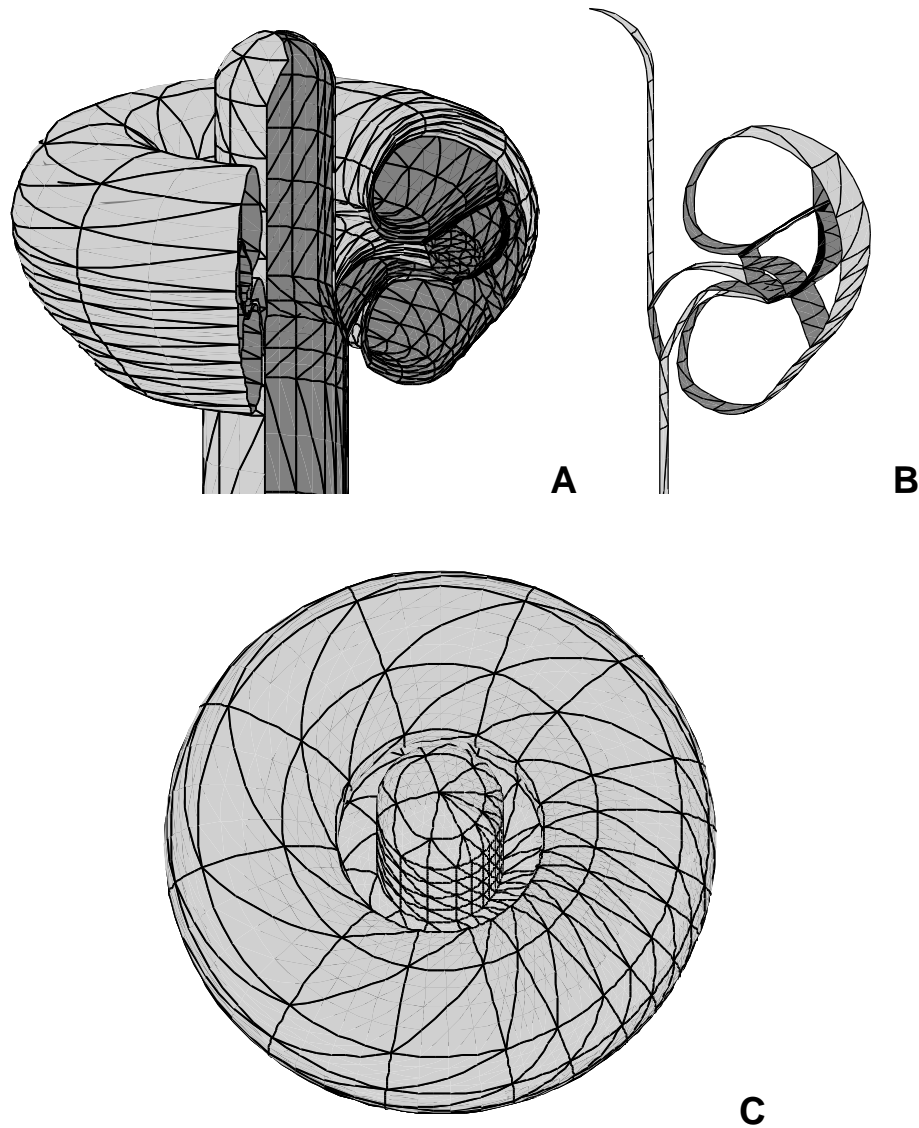


Fig. 3 A Three-dimensional view of the boundary element mesh of the rotationally symmetric cochlea model, with a part intentionally left out. The boundaries between the compartments with different conductivity are described by quadratically curved surfaces.  
B A slice of the mesh in A (cf. Fig. 2<sup>A</sup>)  
C Top view of the boundary element mesh of the rotationally symmetric cochlea, illustrating the smaller element size near the stimulating electrodes in order to reduce computational errors.

The conductivities of the various media in the cochlea as used in the computations are listed in Table I. Summarising these data, the scala tympani, vestibuli and media are well conducting media, separated by very thin, highly resistive membranes, which are embedded in poorly conducting bone. Many values in Table I were adopted from Finley et al. (1990), who compiled their parameter values from several authors. For the conductivity of the bony tissue more recent data from Suesserman (1992) were used. We computed the conductivity of the stria vascularis, the spiral ligament, the organ of Corti, Reissner's membrane and the basilar membrane from the resistance data of Strelhoff (1973), combined with morphologic data from Nijdam (1982) and Fernández (1952), using the dimensions in the second turn of the guinea pig cochlea at 10 mm from the stapes. The estimated *in vivo* thickness of Reissner's membrane, the basilar membrane and the stria vascularis is 1.7  $\mu\text{m}$ , 4  $\mu\text{m}$  and 40  $\mu\text{m}$  respectively. In the rotationally symmetric model of the cochlea however, we have enlarged the thickness of Reissner's membrane and of the basilar membrane (and consequently also enlarged their conductivities) by a factor 10 and 5 respectively, to prevent excessive numerical errors inherent to the BEM. From computations on geometries with known analytic solutions it followed that these errors occur when membranes are modelled with surface elements that are closer to one another than  $1/20^{\text{th}}$  of the side of the elements. With the above-mentioned adaptations to the membrane morphology this situation is avoided without the need to introduce additional mesh points.

*The computed potential distribution due to intracochlear electrodes.*

Figure 4 shows the potential distribution in a cross-section of the cochlea near the anodic part of a bipolar current source for the four electrode sites (A = near the outer wall, B = in the middle of scala tympani, C = adjacent to the modiolus and D = underneath the peripheral dendrites) that were adopted from Shepherd et al. (1993). From this figure it is clear that the scala media is electrically well insulated from its surroundings. Apparently, for scala tympani electrodes it serves with the osseous spiral lamina as a barrier for the excitation of the terminal ends of nerve fibres in more apical turns of the cochlea. It is also clear from this figure that the potential distribution in the neural compartment (i.e. the volume occupied by the auditory nerve fibres) is fairly different for the various electrode positions, so it is expected that neural responses to these fields will depend on the electrode site. These quantitative differences between the potential distributions are illustrated in more detail by Figure 5, which displays the course of the potential along nerve fibres located in the same cross-section (cf. Fig. 2<sup>A</sup>). In spite of these differences, the general course of the curves in Fig. 5 is similar for all four electrode sites (A - D). It turns out that the maximum potentials occur in the peripheral part of the nerve fibres originating from the modelled second turn, while the potential reaches its maximum in the modiolus for the fibres coming from more apical turns. This maximum value is, however, significantly lower than the one in the fibre coming from the second turn, and it is expected that this will result in higher excitation thresholds for these fibres. As shown in Fig. 5, the potential in

fibres originating from the third and fourth cochlear turn reaches also a maximum at the peripheral terminal, but due to the shielding effect of the scala media this maximum is even lower than the one in the modiolus.

The potential field in a 'horizontal' plane through the osseous spiral lamina (indicated by the line HH' in Fig. 4<sup>D</sup>) due to the current dipole underneath the peripheral dendrites (site D) is shown in Fig. 6. This figure shows that there exists a zero potential plane exactly midway between the electrodes. As this plane runs radially through the modiolus, i.e. in the direction of the peripheral dendrites of the auditory nerve fibres (cf. line AA' in Fig. 6), it is evident that nerve fibres in this region are not likely to respond to stimulation by this

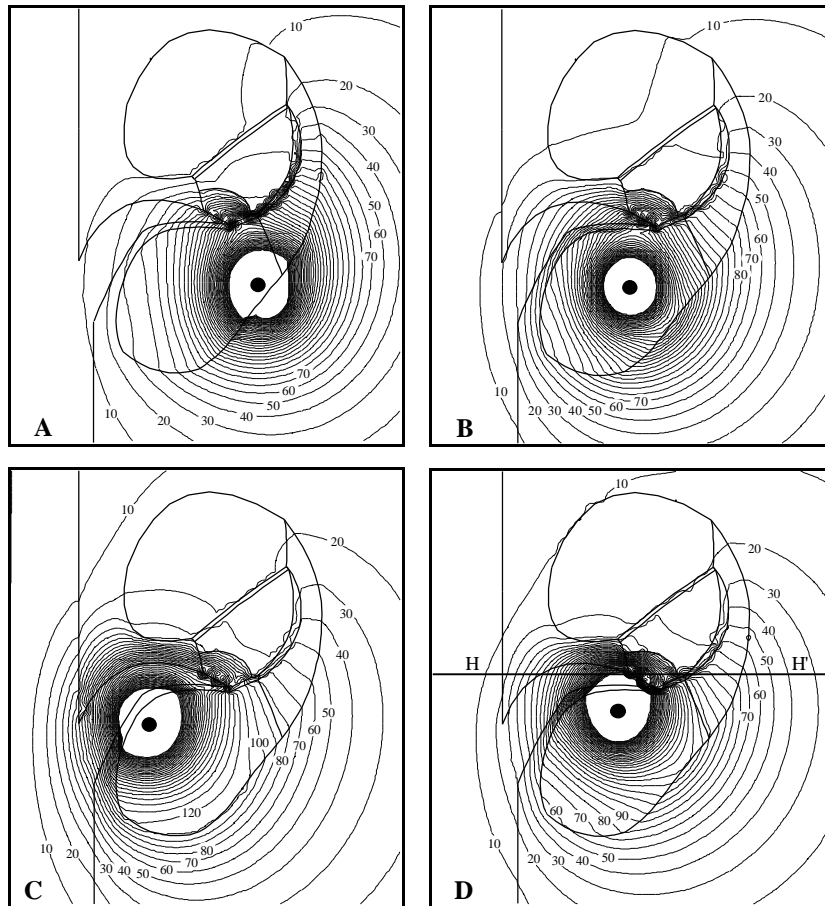


Fig. 4 Equipotential lines for bipolar current sources (strength 1 mA) in planes near the anode for the electrode sites A - D. The numbers on the equipotential lines indicate the potential in millivolts. The black circles represent the electrodes. The line HH' in D indicates the level of the cross-section used in Figure 6.

electrode pair. To understand however, from such a potential distribution which fibres will be excited for a given stimulus strength a neural excitation model is obligatory.

With the mesh used for the calculations, the equipotential lines in Figs. 4 and 6 in poorly conducting media as the stria vascularis have an irregular course due to a limited numerical accuracy. Yet, we refrained from a local refinement of the mesh, since we were mainly interested in the potentials in the relatively good conducting neural compartment, where the method apparently gives more accurate results (cf. Fig. 5). As a test for the accuracy of the calculated potentials on the nerve fibres we repeated the calculations while doubling the length of the sides of all surface elements, and computed for each electrode

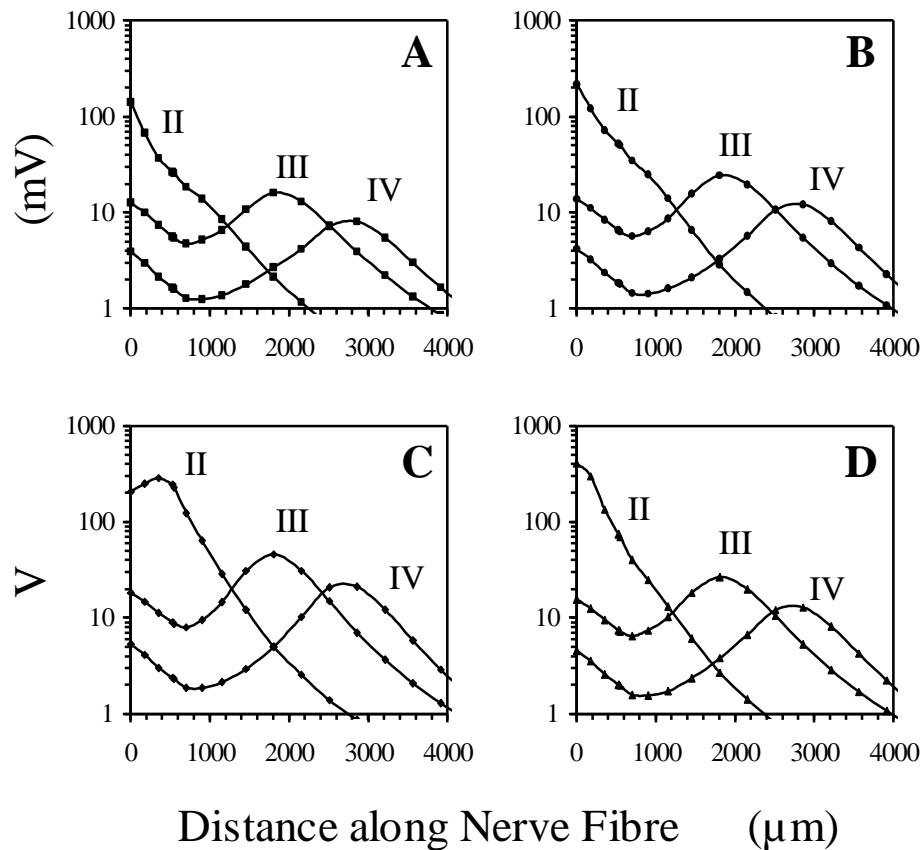


Fig. 5 The course of the potential along the nerve fibres for bipolar current sources (strength 1 mA) in planes near the anode for the electrode sites A - D. The numbers II - IV indicate the cochlear turn from which each nerve fibre originates. The zero point of the abscissa is located at the end of each fibre's unmyelinated terminal. The symbols on the lines represent the nodes of Ranvier (cf. Fig. 2<sup>A</sup>).

configuration used in this paper the root mean square error calculated over all nodes of Ranvier of all nerve fibres (see the next section for their exact location):

$$RMS \text{ error} = \sqrt{\frac{\sum_k (j_k - j_k^C)^2}{\sum_k j_k^2}} \quad (1)$$

where:  $j_k$  = the potential in node  $k$  computed with the fine mesh  
 and  $j_k^C$  = the potential in node  $k$  computed with the coarser mesh.

Typical RMS errors were approximately 0.1 (range from 0.03 to 0.40), the

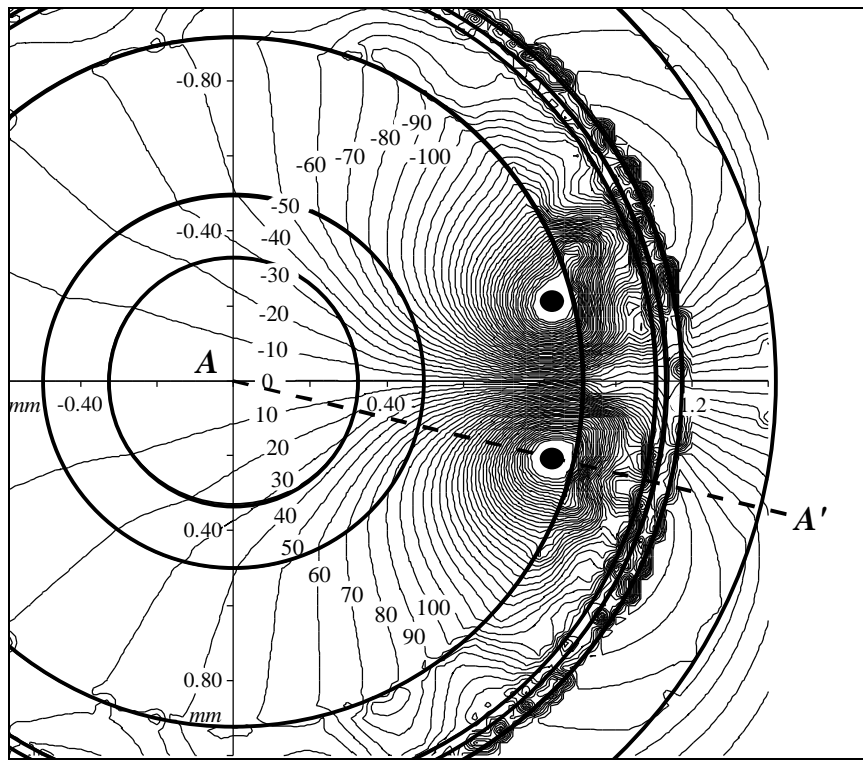


Fig. 6 Equipotential lines for the bipolar current source in site D (= below the dendrites) in a plane perpendicular to the modiolus at the level of the dendrites of the axons in the second turn (i.e. at 0.05 mm on the vertical axis in Fig. 2<sup>A</sup> as indicated by the line HH' in Fig. 4<sup>D</sup>). The numbers indicate the potential in millivolts if a 1 mA current source is used. The concentric circles represent the boundaries between the various media (from the inside out: modiolar nerve tissue; bone of the osseous spiral lamina; dendritic nerve tissue; organ of Corti; scala media; stria vascularis; spiral ligament; outer wall bone). The dashed line AA' illustrates the radial orientation of the nerve fibres.

largest error occurring for the configuration in electrode site C with the largest inter-electrode spacing ('bipolar+2', see below), where both the electrodes and some nerve fibres are close to the same surface elements (cf. Fig. 4). As explained when describing the BEM, the accuracy of the calculated potentials is roughly inversely proportional to the third power of the length of the sides of the surface elements and the RMS error in the final solution is expected to be less than 0.05 ( $= 0.40/2^3$ ), which is expected to be sufficient in the light of the inter-individual anatomical variability and other uncertainties in the model.

## Modelling the auditory nerve fibre responses

### *The kinetics, morphology and spatial distribution of the modelled auditory nerve fibres*

The nerve fibre responses in the present paper are calculated with a version of the SEF model (originally describing a 15  $\mu\text{m}$  motor fibre, see Frijns et al., 1994b) that has been extended to give a quantitatively correct description of many relevant properties (including spike duration, spike conduction velocity and frequency following behaviour) of mammalian nerve fibres with myelinated diameters in the range between 0.5 and 22  $\mu\text{m}$ . The kinetics of this extended model was used to construct an active cable model of a high spontaneous rate auditory nerve fibre with a morphology based upon the findings of Liberman and Oliver (1984) in the cat and Brown (1987) and Gleich and Wilson (1993) in the guinea pig, taking into account a shrinkage of approximately 10% due to labelling with horseradish peroxidase. This resulted in a bipolar fibre, consisting of a peripheral and a modiolar axon with a diameter  $d$  of 3  $\mu\text{m}$ , interconnected by a cell body (soma) with a length of 20  $\mu\text{m}$  and a diameter of 10  $\mu\text{m}$ . The nodal gap width is 1  $\mu\text{m}$  throughout the fibre, the length of the unmyelinated terminal was chosen to be 10  $\mu\text{m}$  (see Figure 7<sup>A</sup>). The internodal myelin sheath was considered to be a perfect insulator, as it was in the original SEF model. The internodal length varied along the nerve fibre as indicated in Fig. 7<sup>A</sup> (Liberman and Oliver, 1984). This nerve fibre morphology was used to represent both the fibres coming from hair cells in the modelled second turn of the cochlea as well as the fibres running down more centrally in the modiulus and originating from locations in the third and fourth turn. The positions of the nodes of Ranvier of these fibres relative to a transversal section through the modelled cochlea are indicated in Fig. 2<sup>A</sup>. For the computation of the excitation profiles of the fibres from the modelled turn, 40 fibres, uniformly distributed around the turn, were used to represent the approximately 10,000 fibres existing in the second turn *in vivo*. Thus, the computed response of each single nerve fibre in the model represents the behaviour of approximately 250 nerve fibres present in each real cochlear segment of 9 degrees ( $\approx 0.17$  mm along the basilar membrane). To account for the fibres from the more apical turns, another 55 fibres of the same morphology and kinetics (35 for the third turn and 20 for the fourth one) were embedded on two, more centrally located, concentric circles in the modiulus (Fig. 1<sup>C</sup>).

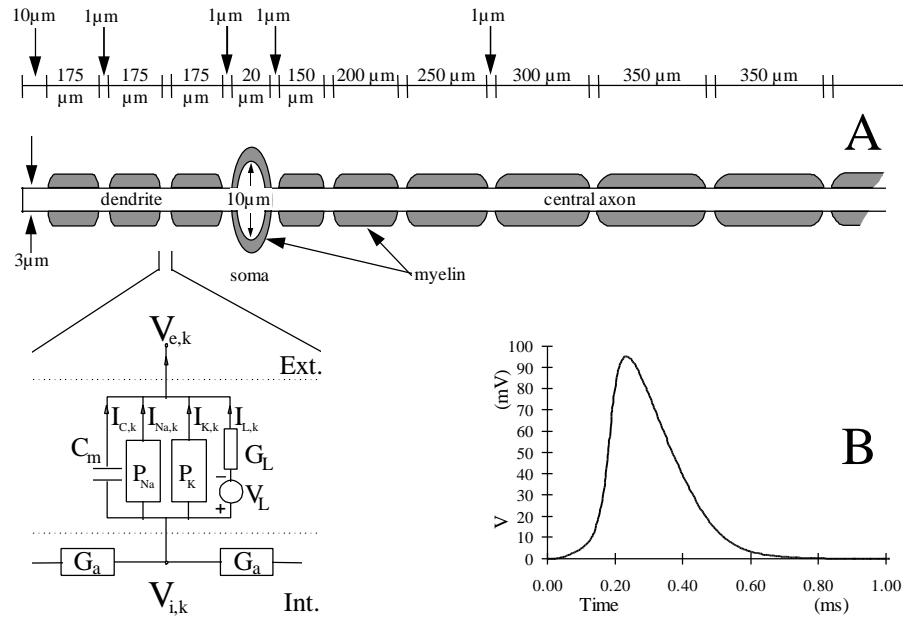


Fig. 7 A The morphology of the high spontaneous rate auditory nerve fibre model used (not to scale). The inset in the lower left part of the figure shows the non-linear electrical circuit used to simulate the nodal kinetics (see Appendix A).  
 B The action potential produced by the auditory nerve fibre model.

For each nerve fibre a system of 64 coupled non-linear differential equations (i.e. 4 equations for each of the 16 included active nodes of Ranvier) had to be solved. Appendix A summarises details of the associated equations and the parameters used in the computations. For further computational details (e.g., the threshold criterion) the reader is referred to previous papers (Frijns et al., 1994a; Frijns et al., 1994b). A detailed study of the time-dependent properties of the nerve fibre model is beyond the scope of the present paper. The results can be summarised as follows: the total spike duration amounts to 0.48 ms (see Figure 7<sup>B</sup>), the absolute refractory period is 1.1 ms and the maximum steady-state firing rate is approximately 650 Hz.

*Simulating excitation profiles of the auditory nerve*

Recently, it was shown experimentally in cats that both the threshold currents and the slope of the input-output curves of the electrically evoked auditory brainstem response (EABR) due to stimulation by bipolar scala tympani electrodes depend upon the exact location of these electrodes (Shepherd et al., 1993). As these differences must be reflected in the excitation patterns of the auditory nerve at the level of the cochlea, these data provide an opportunity to validate our model predictions with experimental results.

For this purpose we computed potential distributions in the rotationally symmetric cochlea model for longitudinally directed bipolar electrodes at four locations comparable to the ones used by Shepherd et al. (1993) (see Figs. 2 and 4). In the model situation also the stimuli used by these authors were applied, viz. biphasic current pulses with a pulse width of 200  $\mu$ s per phase, but all electrode spacings were scaled down by a factor 2 to account for the difference in size between the modelled guinea pig cochlea and the feline cochlea used in the experiments. For the so-called 'bipolar' stimulus mode this resulted in a 375  $\mu$ m inter-electrode distance, whereas it was 0.75 mm and 1.125 mm for the situations that will be referred to as 'bipolar+1' and 'bipolar+2' respectively (a terminology that was adopted from the Nucleus cochlear implant used by Shepherd et al., 1993).

Using the potential distributions computed this way, we stepped through a range of stimulus levels in 3 dB steps, and determined in which fibres a propagating action potential was generated and in which ones this was not the

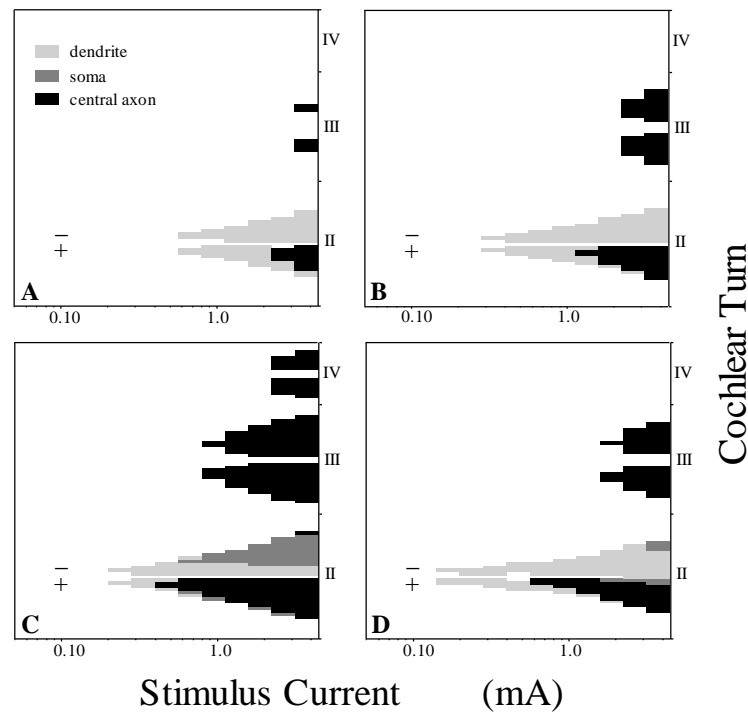


**Fig. 8** Excitation profiles of the three upper turns for the rotationally symmetric guinea pig cochlea computed with biphasic current pulses (200  $\mu$ s/phase, the apical electrode being cathodic-first as indicated by the '-' and '+' symbols denoting the location and initial polarity of the electrodes) for bipolar electrode configurations located in the modelled second turn in site A - D (see Fig. 2<sup>A</sup>). The roman numbers mark the various cochlear turns. The location of the node of Ranvier where the initial excitation of each nerve fibre takes place is indicated by a grey shading.

case. For the four 'bipolar' electrode configurations the results are presented as so-called excitation patterns in Fig. 8. For each nerve fibre in the modelled turn it is indicated in this figure whether the initial excitation occurred in the peripheral dendrite, the nodes surrounding the soma (i.e. in the spiral ganglion), or more centrally in the modiolar axon. Also stimulation of nerve fibres running down in the modiolus from more apical cochlear turns is shown. As expected from the potential field in Fig. 6, there exists a region of elevated thresholds for fibres located near the midplane between electrodes, resulting in a bi-modal distribution of excited fibres, which is most prominent for lower stimulus strengths. Simulations for 'bipolar+1' and 'bipolar+2' stimulus modes revealed that this bi-modality increases with the inter-electrode distance. For each electrode configuration the fibres near the stimulating electrodes appear to be stimulated most easily. Current thresholds differ however, significantly between the four electrode sites. The lowest thresholds are found for the dendritic position (D), where excitation occurs in the unmyelinated terminals of selected fibres for currents slightly above 0.1 mA. For the outer wall position (A) the highest thresholds (almost 0.5 mA) are predicted by the model (See also Table **Error! Unknown switch argument.**). The part of the nerve fibre that is excited first varies depending on the electrode configuration, the stimulus strength and the location of the nerve fibre itself. Some general observations can however, be formulated. Firstly, for all electrode sites except the one close to the spiral ganglion (C), stimulation takes place in the peripheral dendrite for fibres located near the part of the dipole that is cathodic during the first phase of the stimulus. For electrode site C these fibres are frequently excited in the 2 nodes surrounding the cell body in the spiral ganglion. Secondly, for fibres located near the initially anodic part of the dipole the place of excitation shifts with increasing stimulus intensity from the unmyelinated terminal to the modiolar part of the axon. Thirdly, fibres running down from more apical parts of the cochlea are excited in the modiolus at a node of Ranvier close to the stimulating electrodes rather than at their peripheral processes. This is consistent with the maximum in the potential distribution which occurs in or near this node (Fig. 5). We will use the term ectopic stimulation to denote such activation of fibres from turns not containing stimulated electrodes. This phenomenon occurs most easily for the electrode near the spiral ganglion (site C), while the thresholds are two to four times higher for stimulation by the other electrode positions.

#### *Computing input-output curves*

Counting the number of modelled nerve fibres that respond at each stimulus intensity for a given electrode configuration provides a way to summarise the data available in an excitation profile. This results in so-called input-output (I/O) curves that can be considered the modelled analogues of the EABR input-output curves measured experimentally, since the amplitude of the EABR is generally considered a measure of the number of excited nerve fibres in the cochlear partition. The upper pane of Fig. 9 displays such I/O-curves

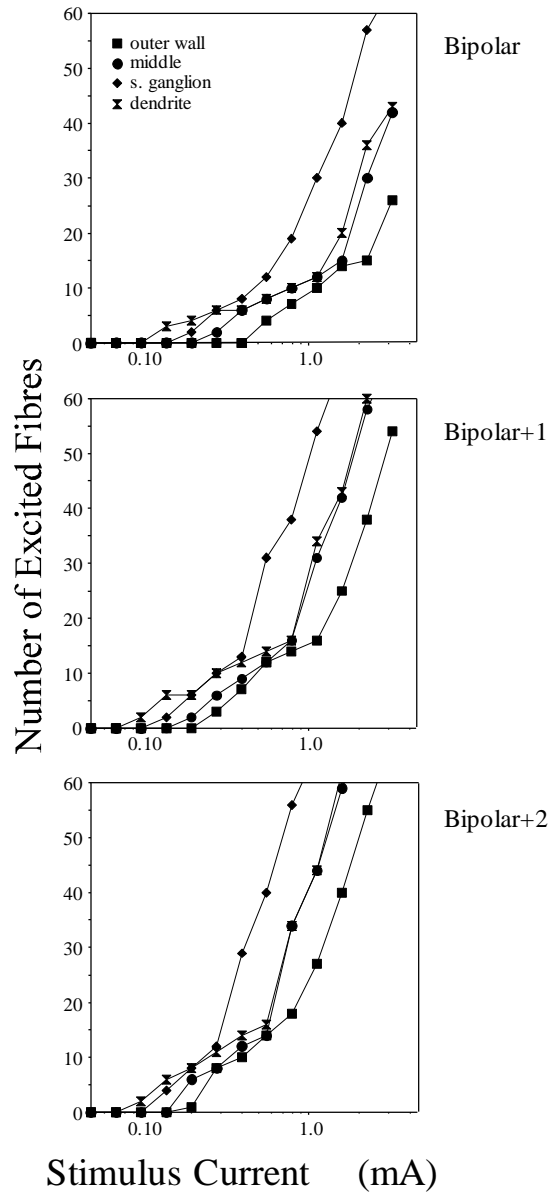


Fig. 9 Computed Input-output-curves for biphasic current pulses ( $200 \mu\text{s}/\text{phase}$ ) in the bipolar, bipolar+1 and bipolar+2 electrode configurations for the four electrode sites A - D in the second turn of the rotationally symmetric cochlea. The curves were constructed by counting the number of excited nerve fibres for each stimulus current in the corresponding excitation patterns.

computed from the excitation profiles from Fig. 8 for the bipolar stimulation mode, while the lower panes of Fig. 9 present the corresponding curves for the bipolar+1' and bipolar+2' configurations respectively. The excitation thresholds for all these electrode combinations are listed in Table II. Particularly for small inter-electrode spacings there are clear differences between the four electrode sites, amongst which the dendritic site (D) takes a special position. This site results in the lowest excitation thresholds and the largest range of stimulus intensities for which the I/O-curve has a shallow slope, corresponding with a large dynamic range. The electrode close to the spiral ganglion (site C) yields the next higher thresholds, but a much steeper I/O-curve. The highest thresholds were observed for the electrode site near the outer wall (site A). All thresholds tend to decrease with increasing inter-electrode spacing (Table II, column 2), but the initial slope of the curves increases, corresponding with a wider region of excitation and a smaller dynamic range (Table II, column 5). Another factor diminishing the dynamic range for large inter-electrode distances is the fact that the thresholds for ectopic excitation of apical nerve fibres in the modiolus are generally lowered more than the overall excitation thresholds. The spiral ganglion site (C) suffers most from this limitation.

## **Discussion**

In the present paper a rotationally symmetric model of the electrically implanted cochlea was described. It is a combination of two sub-models, the first one computing the potential distribution due to stimulating electrodes in the complex geometry of the cochlea, the other one simulating the neural reaction to this potential field. The model allows the computation of input-output curves and the corresponding neural excitation patterns for arbitrary stimuli and electrode configurations.

In order to test the validity of the model results, the circumstances (including electrode positions and stimulus wave forms) for the computation of Figs. 8 and 9 were chosen in such a way that they are comparable to the experimental conditions used by Shepherd et al. (1993), although geometric scaling can only partially eliminate the differences between the modelled guinea pig cochlea and the feline used in these experiments. Generally speaking, however, there is a great deal of similarity between the model and the experimental situation. If one assumes that the amplitude of wave IV in the EABR is a measure of the number of excited nerve fibres in the cochlea, it makes sense to compare the computed I/O-curves (Fig. 9) with the measured ones (Fig. 3 in Shepherd et al., 1993), which leads to the conclusion that the model's predictions are in good agreement with these experimental results. In both cases the neural response increases with stimulus current in the range between 0.1 and 2.5 mA, while excitation thresholds and gradients of the curves depend comparably on electrode site. Especially the favourable outcome for the dendritic position (D), with its lowest excitation thresholds and its largest current range with a low gradient of the I/O curve is apparent in both situations. In addition, the model correctly predicts the diminishing differences between the I/O-curves for the four

electrode sites with increasing inter-electrode distance. The main discrepancy between the model results and the experiments occurs for the higher stimulus levels, where the curves for the four electrode sites converge more to one another in the experimental situation than in the simulations. Table II gives a more quantitative comparison between simulation results and experimental data. It appears that the average ratio between the experimental and simulated current thresholds is approximately 2.8, rather than 1.0 (which would obviously have been the ideal result), but the fact that this ratio is fairly independent from electrode site and electrode spacing, implies that the model gives realistic predictions of the relative threshold shifts between the various electrode configurations. Possible explanations for this factor 2.8 include geometric differences between the modelled guinea pig cochlea and the (scaled) cat cochlea, threshold differences between the auditory nerve fibre

**Table Error! Unknown switch argument.** Comparison of the computed thresholds ( $I_{th}$ ) and I/O-curve gradients ( $G_{IO}$  and  $G'_{IO}$ , computed over turns II - IV and turn II respectively) with corresponding experimental EABR data (Shepherd et al., 1993),  $I_{th}^{exp}$  and  $G_{IO}^{exp}$  for all electrode spacings and electrode sites A - D.

Electrode site	$I_{th}$ (mA)	$I_{th}^{exp}$ (mA)	$I_{th}^{exp}/I_{th}$	$G_{IO}$ (fibres/dB)	$G'_{IO}$ (fibres/dB)	$G_{IO}^{ex}$ <sub>P</sub> ( $\mu$ V/dB)	$G_{IO}^{exp}/G_{IO}$ ( $\mu$ V/fibre)	$G_{IO}^{exp}/G'_{IO}$ ( $\mu$ V/fibre)
<b>Bipolar</b>								
A	0.497	1.100	2.21	1.33	1.33	0.423	3.15	3.15
B	0.278	0.990	3.56	1.00	1.00	0.476	2.10	2.10
C	0.177	0.660	3.73	1.00	1.00	0.331	3.02	3.02
D	0.124	0.320	2.58	0.58	0.58	0.193	3.02	3.02
Mean $\pm$ SD			3.02 $\pm$ 0.74				2.82 $\pm$ 0.49	2.82 $\pm$ 0.49
<b>Bipolar+1</b>								
A	0.269	0.590	2.19	1.33	1.33	0.470	2.84	2.84
B	0.183	0.550	3.01	1.17	1.17	0.455	2.56	2.56
C	0.135	0.340	2.52	2.50	1.50	0.377	6.63	3.98
D	0.089	0.260	2.92	0.83	0.83	0.307	2.71	2.71
Mean $\pm$ SD			2.66 $\pm$ 0.38				3.69 $\pm$ 1.97	3.02 $\pm$ 0.65
<b>Bipolar+2</b>								
A	0.202	0.470	2.33	1.50	1.50	0.503	2.98	2.98
B	0.154	0.410	2.66	1.50	1.33	0.459	3.27	2.90
C	0.107	0.310	2.90	2.67	1.50	0.451	5.91	3.33
D	0.088	0.240	2.73	1.00	1.00	0.350	2.86	2.86
Mean $\pm$ SD			2.65 $\pm$ 0.24				3.76 $\pm$ 1.45	3.02 $\pm$ 0.21
<b>All spacings</b>								
Mean $\pm$ SD			2.78 $\pm$ 0.49				3.42 $\pm$ 1.37	2.96 $\pm$ 0.45

model and real auditory nerve fibres. Table **Error! Unknown switch argument.** also contains data regarding the slope of the computed I/O-curves. These gradients were computed by counting the number of auditory nerve fibres that are excited by a biphasic stimulus that is 12 dB above the threshold for that electrode configuration. Again, the results were compared with Shepherd's data on EABR I/O-curves by computing the ratio between the experimental (Shepherd et al., 1993, Table V) and the simulated data. Ideally, this procedure would result in a fixed ratio relating the EABR amplitude to the number of excited nerve fibres in the model. With the responses of nerve fibres from all turns included in the computations, we found ratios around  $3.0 \mu\text{V}/\text{fibre}$  for all electrode configurations except for the 'bipolar+1' and 'bipolar+2' electrodes in site C (= near the spiral ganglion). In the latter two cases approximately twice this ratio was found. Table **Error! Unknown switch argument.** shows that this discrepancy disappears if the calculations are restricted to the responses of the fibres in the modelled second turn.

There are two major differences between the present model and previous ones (Sapozhnikov, 1990; Finley et al., 1990; Suesserman and Spelman, 1993). Firstly, the present rotationally symmetric model includes a more realistic geometry of the modiolus than models that incorporate an unrolled cochlear duct. Especially for larger inter-electrode separations and higher stimulus strengths this difference is expected to have a significant effect. To test this hypothesis, a boundary element mesh of an unrolled cochlear model was generated by translating the cochlear section from Fig. 2<sup>A</sup> along the length of the basilar membrane (Fig. 10<sup>A</sup>) rather than rotating it around the modiolus (Fig 3). The dimensions of this unrolled cochlea model were chosen in such a way that its basilar membrane length is equal to the rotationally symmetric counterpart. For this unrolled model, Fig 10<sup>B</sup> displays the potential field (cf. Fig. 6) for the dendritic electrode position in the 'bipolar' configuration (inter-electrode distance 0.375 mm). Fig. 10<sup>C</sup> shows the computed I/O-curves for this and the three other standard 'bipolar' electrode (sites A - D in Fig. 2). It is evident from Fig. 10 that unrolling the cochlea model influences the recruitment characteristics of the nerve fibres, reflected in the I/O-curves, which are initially more shallow due to a more gradual spread of excitation along the cochlear turn. For higher stimulus currents however, the curves are steeper due to the relatively easy excitation of fibres passing by from more apical turns. This results from the fact that unrolling causes many modiolar fibres to be moved away from the (zero potential) midplane between the electrodes. So, it turns out that ectopic stimulation takes place in an unrolled model more easily than in the equivalent rotationally symmetric case (Figs. 6 and 9). Future research will have to elucidate the consequences of using this rotationally symmetric structure instead of a continuous spiral, for which Girzon (1987) showed that the scala tympani acts more or less as a non-uniform, leaky transmission line of finite length.

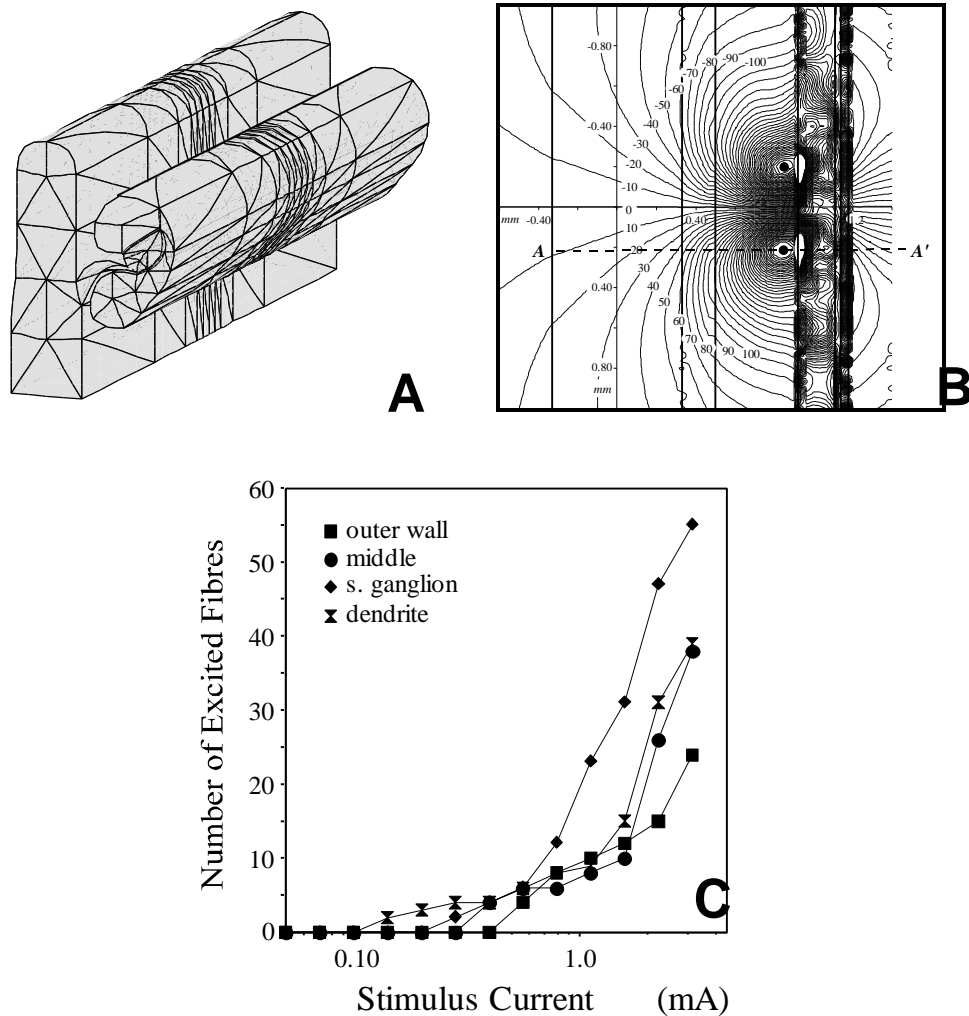


Fig. 10 A Three-dimensional view of the unrolled cochlea model, constructed by translation of the mesh in Fig. 2<sup>A</sup>. Note the smaller element size in the middle part of the mesh, i.e. around the electrodes.

B Equipotential lines for the bipolar current source in site D (= below the dendrites) in the unrolled cochlea model in a plane perpendicular to the modiolus at the level of the dendrites of the axons in the second turn (i.e. at 0.05 mm on the vertical axis in Fig. 2<sup>A</sup>). The numbers indicate the calculated potential in millivolts for a 1 mA current source. The thick vertical lines represent the boundaries between the various media (from left to right: bone; modiolar nerve tissue; bone of the osseous spiral lamina; dendritic nerve tissue; organ of Corti; scala media; stria vascularis; spiral ligament; outer wall bone). The dashed line AA' illustrates the orientation of the nerve fibres.

C Computed I/O-curves for biphasic current pulses in the bipolar stimulation mode for the four electrode sites A-D in the second turn of the unrolled cochlea model.

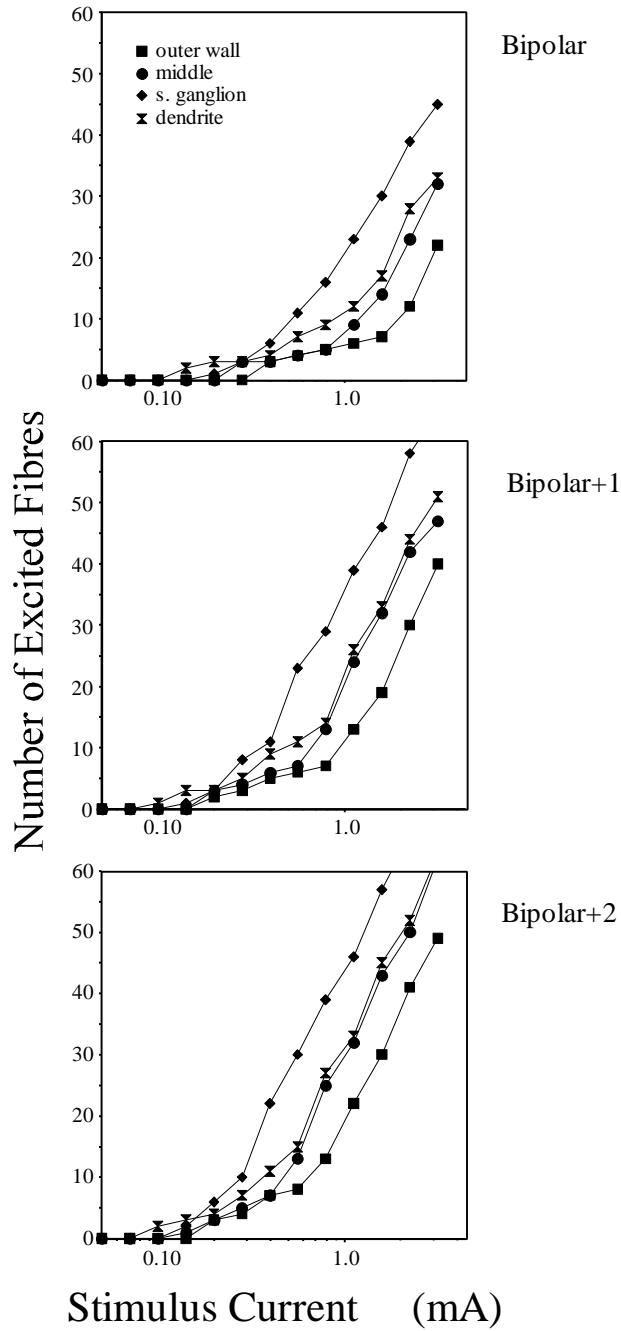


Fig. 11 Input-output-curves for the bipolar, bipolar+1 and bipolar+2 electrode configurations for the four electrode sites A - D in the second turn of the rotationally symmetric cochlea, computed for 200  $\mu$ s current pulses with a passive nerve fibre model. The curves were constructed by counting the number of excited nerve fibres for each stimulus current in the corresponding excitation patterns.

The second major difference between the present model and previous ones is the inclusion of an actively modelled auditory nerve fibre with mammalian nodal kinetics, where the previous models used either passive neural models or amphibian kinetics. This aspect of our model increases the time necessary to compute the excitation profiles, but it allows to include realistic *temporal* stimulus waveforms, such as biphasic pulses, in the study. At first sight, threshold estimates obtained with (computationally much less intensive) passive neural models based upon the activating function  $f_k^{act}$  (Rattay, 1989) and the total equivalent driving function  $T_k^{PW}$  (Warman et al., 1992) provide an attractive alternative. In fact, the latter is a generalised form of the activating function, which not only takes into account the stimulating influence of an extracellular potential field but also the current redistribution along the nerve fibre during the active phase (pulse width  $PW$ ) of monophasic stimuli. For the present paper it suffices to know that this method gives estimates of threshold currents for arbitrary extracellular electrode configurations near an infinite length fibre that are based upon the so-called critical voltage  $V_c(PW)$ . This is defined as the membrane depolarisation in an equivalent passive cable model at the end of a current pulse at threshold strength for the actively modelled counterpart. It is possible to perform a complete analysis of  $T_k^{PW}$  for the present (finite length!) auditory nerve fibre model, which will abolish the need to perform repeated computations with the SEF model for each fibre and each different electrode configuration. However, the same results will obviously be obtained with a simulation with the equivalent passive cable model in the same potential field, provided that the value of  $V_c(PW)$  has once been determined on beforehand for each node. For practical reasons we have decided to follow the latter approach to produce the input-output curves presented in Fig. 11. The most striking difference between these curves and those computed with the active model (Fig. 9) is the reduced gradient of all I/O-curves in the case of the passive fibre. Another important difference between Figures 9 and 11 is seen in the I/O-curves for the electrodes near the outer wall (A). The initial slope of this curve and the suggested dynamic range are comparable to the corresponding results for the dendrite position (D), although the predicted excitation thresholds are elevated. This would suggest that both electrode positions A and D are equally effective, which is contradictory to the experimental results currently available (Shepherd et al., 1993). Thus, the application of passive neural models, although computationally attractive, is a simplification yielding less reliable and sometimes misleading estimates of the response to the biphasic stimulation typically applied in cochlear implants. Unlike us, Finley et al. (1990) did not incorporate the stria vascularis, the spiral ligament and the organ of Corti in their model. This may be considered a minor anatomical detail, but in the present model this results in a scala media that is electrically well insulated from its surroundings as it is *in vivo*, where this is a prerequisite for maintaining the endocochlear potential. Histologically the lining of the scala media is characterised by tight junctions between neighbouring cells that prevent ion leakage into and from the scala media, and although these thin membranes are known to be both capacitive and resistive, the membrane capacitances are expected to have little effect on the fields in

the scala tympani or the nerve tissue during electrical stimulation with scala tympani electrodes due to their high resistivity, as discussed by Girzon (1987). The question of frequency dependence of fields in other parts of the cochlea, e.g. in the habenula perforata, is still open. Therefore the present approach with a purely resistive cochlea model should be considered as a first approximation of the *in vivo* situation. Future versions of the model should include capacitive elements in order to evaluate their potential influence on the calculated temporal responses.

That the insulating effect of the scala media has implications for cochlear implants with intra-scalar electrodes is illustrated by Figs. 4 and 5, where the scala media acts as a barrier between the electrodes and fibres in more apical segments of the cochlea. Similarly, the model predicts higher thresholds for extra-cochlear stimulation with electrodes located in the bone lateral from the stria vascularis than for electrodes lateral from the scala tympani.

The morphology of the auditory nerve fibres used in our computations differs in several respects from similar models found in the literature, although we also used the data provided by Liberman and Oliver (1984) as a starting point. Firstly, the central axon diameter of the modelled high spontaneous rate fibre is 3  $\mu\text{m}$  rather than 1  $\mu\text{m}$  as proposed by Colombo and Parkins (1987) or 2  $\mu\text{m}$  (Rattay, 1990). This relatively large diameter is based upon the measurements in guinea pigs performed by Brown (1987) and Gleich and Wilson (1993), taking into account the shrinkage factor demonstrated by the latter authors. The peripheral axon (i.e. the dendritic part of the fibre) was modelled to have the same diameter rather than a smaller one, making the fibre representative for high spontaneous rate fibres, which are known to exhibit lower electrical thresholds (Van Den Honert and Stypulkowski, 1987). Preliminary simulations with fibres with thinner peripheral processes resulted in slightly elevated thresholds indeed. Since Gleich and Wilson (1993) showed that there exists a wide variation in fibre diameter *in vivo*, this suggests that the inclusion of a more heterogeneous population of nerve fibres may be a meaningful future extension of the model. Calculations with nerve fibres with a constant rather than gradually increasing nodal spacing of 350  $\mu\text{m}$  for the part of the fibre proximal to the cell body (cf. Colombo and Parkins, 1987) did not give rise to significant changes in the simulated excitation profiles nor in the computed input-output curves and may therefore be considered to be of minor importance.

The boundary element method was used to solve the volume conduction problem for a number of reasons. One of the advantages of the method is the relative ease of mesh generation, which is of particular importance when a full three-dimensional model of the cochlea is to be constructed. Also the rapid calculation of the potential distribution due to varying current source distributions once the first step of the procedure has been performed (see the description of the method) is a favourable property. The use of second order interpolation functions resulted in a good approximation of the shape of the various structures in the cochlea (Fig. 2). We also concluded that the accuracy of the solution was sufficient despite the relatively small number of mesh points, not only because of the limited RMS errors as computed with eq. 1, but

also because we found that doubling the average size of the sides of the surface elements did only marginally affect the calculated neural responses. We tested the sensitivity of the model to uncertainties in the conductivity of the various media by systematically varying the individual conductivities up and down by a factor 2. It turned out that this induced surprisingly insignificant changes to the calculated neural excitation patterns for all media with exception of the perilymph and the bone. The main effect of doubling the conductivity of the bone was a reduction of the thresholds for ectopic stimulation by 1 - 3 dB depending on the electrode site, probably due to an increased radial current flow through the outer cochlear wall. An increased conductivity of the perilymph caused an approximately proportionate increase of the excitation thresholds, as well as a slight reduction of the gradient of the I/O-curves. As the conductivity of perilymph is known within a few percent, while the conductivity of cochlear bone has been measured with an accuracy of approximately 30% (Suesserman, 1992), we concluded that the model predictions are relatively insensitive to the uncertainties in all resistivities. Several extensions and refinements to the present model are still conceivable, some of which were already mentioned above. Future versions of the model will, for example, have to incorporate realistic electrode shapes instead of the point current sources used here, since larger electrode surfaces and the presence of an insulating electrode carrier in the scala tympani will influence the calculated potential distributions (Finley et al., 1987). We expect, however, that the effect on the simulations presented here will be limited, as Shepherd et al. (1993) used relatively small electrodes, occupying less than 4% of the cross-sectional area of the scala tympani (see their Fig. 1, which is to scale according to its caption). Theoretically, the BEM allows for the inclusion of an anisotropic conductivity in the modiolus (Van Der Weiden and De Hoop, 1989; Zhou, 1994), but we have not yet fully finished the implementation of this model extension. In addition, we intend to construct an anatomically-based, fully three-dimensional (i.e. spiralling) mesh of the implanted cochlea. This will allow the calculation of neural excitation patterns due to current injection by electrodes that are located in different cochlear turns. Furthermore, such a model will account for the electrical non-uniformity of the cochlea as a consequence of the tapering of the scalae from base to apex. As can also be inferred from Girzon's (1987) results, the influence of both this non-uniformity and of the fact that the cochlea is a spiralling structure rather than a rotationally symmetric one, is likely to increase with increasing inter-electrode spacing.

It is the subject of further research to find out to what extent the present rotationally symmetric model can deal with other experimental data, e.g., single fibre mappings of the spatial selectivity of various electrode configurations (Van Den Honert and Stypulkowski, 1987). The results obtained thus far make us confident that this modelling approach will help us in identifying the biophysical constraints imposed on restoring hearing by electrically stimulating the inner ear. This insight, in turn, will be useful to optimise stimulation strategies and electrode configurations in future cochlear implant designs.

Table A.I The parameters of the generalised SEF high spontaneous rate auditory nerve fibre model.

Parameter	Unit	Symbol	Value
axoplasm resistivity	$\Omega\text{m}$	$r_i$	0.7
nodal membrane capacitance	pF	$C_m$	0.189
nodal leak conductance	$\text{n}\Omega^{-1}$	$G_L$	2.43
nodal sodium permeability	$(\mu\text{m})^3\text{s}^{-1}$	$P_{Na}$	172
nodal potassium permeability	$(\mu\text{m})^3\text{s}^{-1}$	$P_K$	6.68
intracellular sodium concentration	$\text{mol m}^{-3}$	$[Na^+]_i$	10
extracellular sodium concentration	$\text{mol m}^{-3}$	$[Na^+]_o$	142
intracellular potassium concentration	$\text{mol m}^{-3}$	$[K^+]_i$	141
extracellular potassium concentration	$\text{mol m}^{-3}$	$[K^+]_o$	4.2
Temperature	K	$T$	310.15 (= 37°C)

## Appendix A. the generalised SEF auditory nerve fibre model

The auditory nerve fibre model used in the present paper (Fig. 7) is an active cable model of a guinea pig high spontaneous rate fibre, based on an extension of the SEF model (Frijns et al., 1994b) to fibres of smaller diameter. Here we will only summarise the model equations and parameters of this auditory nerve fibre model. For symbols that are not explained in the text Table A.I will provide additional information. For further details we refer to the literature (Schwarz and Eikhof, 1987; Frijns et al., 1994b). In the latter paper we showed that the model equations of a uniform finite-length active cable model with  $N$  nodes can be written as an equation with time-independent matrices **A**, **B** and **C** and time-dependent vectors describing the status of all nodes:

$$\frac{d\vec{V}}{dt} = \mathbf{A}\vec{V} + \mathbf{B}\vec{V}_e + \mathbf{C}[\vec{I}_{act} + \vec{I}_L] \quad (\text{A.1})$$

where:  $\vec{V} = (V_1, \dots, V_N)$  the deviation from the resting membrane potential,  
 $\vec{V}_e = (V_{e,1}, \dots, V_{e,N})$  the extracellular potentials due to the stimulating electrodes,  
 $\vec{I}_{act} = (I_{act,1}, \dots, I_{act,N})$  the sum of the active sodium and potassium current per node,  
 and  $\vec{I}_L = -G_L V_L \cdot (1, \dots, 1)$  with  $G_L$  = the nodal leak conductance, and  $V_L$  = the leak current equilibrium potential.

For non-uniform fibres like the present auditory nerve fibre the structure of the matrices **A**, **B** and **C** given in the previous paper (Frijns et al., 1994b) requires a slight modification, to account for the variation with segment number  $k$  of the nodal gap width  $l_k$ , the internodal length  $L_k$  and axon diameter  $d_k$ . This leads to the following dependence on  $k$  of the nodal membrane capacitance  $C_{m,k}$ , the nodal leak conductance and the axoplasmic conductance  $G_{a,k}$ :

$$C_{m,k} = c_m p d_k l_k \quad (\text{A.2})$$

$$G_L = p d_k l_k g_L \quad (\text{A.3})$$

and

$$G_{a,k} = \frac{p d_k^2}{4 r_i L_k} \quad (\text{A.4})$$

where  $c_m$  = the membrane capacitance per unit area  
 $g_L$  = the leak conductance per unit area  
 and  $r_i$  = the axoplasm resistivity.

This results in the following expressions for **A**, **B** and **C**:

$$\mathbf{A} = \begin{pmatrix} \frac{(G_{a,1}+G_{L,1})}{C_{m,1}} & \frac{G_{a,1}}{C_{m,1}} & & & \\ & \dots & & & \\ & & \frac{G_{a,k-1}}{C_{m,k}} & -\frac{(G_{a,k-1}+G_{L,k}+G_{a,k})}{C_{m,k}} & \frac{G_{a,k}}{C_{m,k}} \\ & & & \dots & \\ & & & & \frac{G_{a,N-1}}{C_{m,N}} & -\frac{(G_{a,N-1}+G_{L,N})}{C_{m,N}} \end{pmatrix} \quad (\text{A.5})$$

$$\mathbf{B} = \begin{pmatrix} \frac{G_{a,1}}{C_{m,1}} & \frac{G_{a,1}}{C_{m,1}} & & & \\ & \dots & & & \\ & & \frac{G_{a,k-1}}{C_{m,k}} & -\frac{(G_{a,k-1}+G_{a,k})}{C_{m,k}} & \frac{G_{a,k}}{C_{m,k}} \\ & & & \dots & \\ & & & & \frac{G_{a,N-1}}{C_{m,N}} & -\frac{G_{a,N-1}}{C_{m,N}} \end{pmatrix} \quad (\text{A.6})$$

$$\mathbf{C} = \frac{1}{C_m} \begin{pmatrix} 1 & & & 0 \\ & \dots & & \\ & & 1 & \\ & & & \dots \\ 0 & & & & 1 \end{pmatrix} \quad (\text{A.7})$$

In the high spontaneous rate auditory nerve fibre model used in the present paper (Fig. 7) the nodal gap width  $l$  is fixed throughout the fibre. Also the axonal diameter  $d$  is identical on both sides of the cell body. The cell body itself has a larger internal diameter (10  $\mu\text{m}$  instead of 3  $\mu\text{m}$ ). We could, however, not detect any influence of the soma thickness on the computed I/O-curves nor on the excitation profiles of the auditory nerve, but a large discontinuity in the axon diameter resulted in up to ten-fold increased computation times, due to the much smaller integration step-sizes required to maintain numerical stability. Therefore we decided to perform some of our computations with a 3  $\mu\text{m}$  soma thickness.

The generalised SEF model equations describing the active nodal sodium and potassium currents  $I_{Na,k}$  and  $I_{K,k}$  for each node  $k$  are:

$$I_{Na,k} = P_{Na,k} h_k m_k^3 \cdot \frac{E_k F^2}{RT} \cdot \frac{[Na^+]_o - [Na^+]_i \cdot \exp(E_k F/RT)}{1 - \exp(E_k F/RT)} \quad (\text{A.8})$$

$$I_{K,k} = P_{K,k} n_k^2 \cdot \frac{E_k F^2}{RT} \cdot \frac{[K^+]_o - [K^+]_i \cdot \exp(E_k F/RT)}{1 - \exp(E_k F/RT)} \quad (\text{A.9})$$

where

$T$	=	the absolute temperature
$F$	=	Faraday's constant
$R$	=	the gas constant
$E_k$	=	the transmembrane potential in node $k$

and  $m_k$ ,  $h_k$  and  $n_k$  are dimensionless variables describing the kinetics of the ionic channels of node  $k$ . For  $\vec{m} = (m_1, \dots, m_N)$  the matrix-vector equation describing the set of first order differential equations that controls its time course reads:

$$\frac{d\vec{m}}{dt} = \begin{pmatrix} \mathbf{a}_{m,1} \\ \dots \\ \mathbf{a}_{m,N} \end{pmatrix} + \begin{pmatrix} \mathbf{a}_{m,1} + \mathbf{b}_{m,1} & & 0 \\ & \dots & \\ 0 & & \mathbf{a}_{m,N} + \mathbf{b}_{m,N} \end{pmatrix} \cdot \vec{m}. \quad (\text{A.10})$$

Similar equations apply for  $\vec{h} = (h_1, \dots, h_N)$  and  $\vec{n} = (n_1, \dots, n_N)$ . The way the  $\alpha$  and  $\beta$  parameters in Eq. **Error! Picture string contains unmatched quotes.** depend on voltage and temperature is described in detail in our previous paper (Frijns et al., 1994b). The equations are initialised with starting values  $\vec{m}_0$ ,  $\vec{h}_0$  and  $\vec{n}_0$  respectively, that ensure that the nerve fibre is at rest at its resting potential  $V_r$ , i.e.  $d\vec{m}/dt = d\vec{h}/dt = d\vec{n}/dt = \vec{0}$  at  $\vec{V} = \vec{0}$ . The value of  $V_r$  is computed with the Goldman equation to account for variations in the ionic content of the extracellular medium:

$$V_r = \frac{RT}{F} \cdot \ln \left( \frac{P_K n_o^2 [K^+]_o + P_{Na} h_o m_o^3 [Na^+]_o}{P_K n_i^2 [K^+]_i + P_{Na} h_i m_i^3 [Na^+]_i} \right). \quad (\text{Error! Picture string contains unmatched q}$$

In summary, for the 16 nodes of Ranvier included in the auditory nerve fibre model a system of 64 coupled non-linear first order differential equations had to be solved (viz. Eqs. **Error! Picture string contains unmatched quotes.** and A.10 and the equivalent equations for  $\vec{h}$  and  $\vec{n}$ ). These equations were integrated by means of a fourth order Runge-Kutta algorithm with adaptive step-size control with step-sizes varying between 0.001  $\mu$ s and 1 $\mu$ s. These small integration steps were necessary because of the large range (over 40 dB) of stimulus strengths applied.

### Acknowledgement

We gratefully acknowledge the advice and assistance of Prof.J.J. Grote, MD PhD, head of our department, and of J.H. ten Kate, PhD from the Acoustic Perception Group, Applied Physics Department, Delft University of Technology. We would also like to thank J. Mooij, MSc for his help in developing the neural model and the Heinsius Houbolt Fund for its financial support. Finally, we wish to thank C.C. Finley, PhD and D.L. Jewett, MD for their valuable comments on an earlier version of the manuscript.

## References

- Balkany, Th.J., ed. (1986) Cochlear Implants, *Otolaryngol. Clin. North. Am.* **19** (2), 215-449.
- Binns, K.J., Lawrenson, P.J., Trowbridge, C.W. (1992) *The Analytical and Numerical Solution of Electric and Magnetic Fields*. Wiley & Sons New York, 486 pp..
- Black, R.C., Clark, G.M. & Patrick, J.F. (1983) Current distributions in cochlear stimulation. *Ann. N.Y. Acad. Sci.* 405, 137-145.
- Brown, M.C. (1987) Morphology of Labeled Afferent Fibers in the Guinea Pig Cochlea. *J. Comp. Neurol.* 260, 591-604.
- Colombo, J. and Parkins, J.W. (1987) A Model of Electrical Excitation of the Mammalian Auditory-Nerve Neuron. *Hear. Res.* 31, 287-312.
- Fernández, C. (1952) Dimensions of the Cochlea (Guinea Pig). *J. Acoust. Soc. Am.* 24, 519-523.
- Finley, C.C., Wilson, B.S., and White, M.W. (1987) A Finite-Element Model of Bipolar Field Patterns in the Electrically Stimulated Cochlea - A Two Dimensional Approximation. *IEEE Ninth Ann. Int. Conf. EMBS*, 1901-1903.
- Finley, C.C., Wilson, B.S. and White, M.W. (1990) Models of Neural Responsiveness to Electrical Stimulation. In: J.M. Miller and F.A. Spelman (Eds.), *Cochlear Implants: Models of the Electrically Stimulated Ear*. Springer-Verlag, New York, pp. 55-96.
- Frankenhaeuser, B. and Huxley, A.F. (1964) The Action Potential in the Myelinated Nerve Fiber of *Xenopus Laevis* as Computed on the Basis of Voltage Clamp Data. *J. Physiol. (London)* 171, 302-315.
- Frijns, J.H.M. and ten Kate, J.H. (1994a) A Model of Myelinated Nerve Fibres for Electrical Prosthesis Design. *Med. Biol. Eng. Comput.* 32, 391-398.
- Frijns, J.H.M., Mooij, J. and ten Kate, J.H. (1994b) A Quantitative Approach to Modelling Mammalian Myelinated Nerve Fibres for Electrical Prosthesis Design. *IEEE Trans. Biomed. Eng.* 41, 556-566.
- Gantz, B.J. and Tyler, R.S. (1990) Evaluation of Five Different Cochlear Implant Designs: Audiologic Assessment and Predictors of Performance. *Laryngoscope* 98, 1100-1106.
- Gantz, B.J., Woodworth, G.G., Knutson, J.F. et al. (1993) Multivariate predictors of audiological success with multichannel cochlear implants. *Ann. Otol. Rhinol. Laryngol.*, 102 (12), 909-916.
- Girzon, G. (1987) Investigation of Current Flow in the Inner Ear during Electrical Stimulation of Intracochlear Electrodes. MSc Thesis, Massachusetts Institute of Technology, 193 pp..
- Gleich, O. and Wilson, S. (1993) The Diameters of Guinea Pig Auditory Nerve Fibres: Distribution and Correlation with Spontaneous Rate. *Hear. Res.* 71, 69-79.
- Hodgkin, A.L. and Huxley, A.F. (1952) A Quantitative Description of Membrane Current and its Application to Conduction and Excitation in Nerve. *J. Physiol. (London)* 117, 500-544.
- Honert, C. van den and Stypulkowski, P.H. (1987) Single fiber mapping of spatial excitation patterns in the electrically stimulated auditory nerve. *Hear. Res.*, 29, 195-206.
- Ifukube, T. and White, R.L. (1987) Current distributions produced inside and outside the cochlea from a scala tympani electrode array. *IEEE Trans. Biomed. Eng.* 34, 883-890.
- Liberman, M.C. and Oliver, M.E. (1984) Morphometry of Intracellularly Labeled Neurons of the Auditory-Nerve: Correlations with Functional Properties. *J. Comp. Neurol.* 223, 163-176.

- Meijs, J., Weiers, O., Peters, M. and Oosterom, A van (1989) On the Numerical Accuracy of the Boundary Element Method. *IEEE Trans. Biomed. Eng.* 36, 1038-1049.
- Motz, H. and Rattay, F. (1986) A Study of the Application of the Hodgkin-Huxley and the Frankenhaeuser-Huxley model for Electrostimulation of the Acoustic Nerve. *Neuroscience* 18, 699-712.
- Munck, J.C. de (1992) A Linear Discretization of the Volume Conductor Boundary Integral Equation Using Analytically Integrated Elements. *IEEE Trans. Biomed. Eng.* 39, 986-990.
- Nijdam, H.F. (1982) Auditory Sensory Cell Pathology in the Waltzing Guinea Pig. Ph.D. Thesis, Groningen University.
- O'Leary, S.J., Black, R.C. and Clark, G.M. (1985) Current Distributions in the Cat Cochlea: A Modelling and Electrophysiological Study. *Hear. Res.* 18, 273-281.
- Oosterom, A. van (1991) Mathematical Aspects of Source Modeling. *Acta Otolaryngol. (Stockh.) Suppl* 491, 70-79.
- Rattay, F. (1989) Analysis of Models for Extracellular Fiber Stimulation. *IEEE Trans. Biomed. Eng.* 36, 676-692.
- Rattay, F. (1990) *Electrical Nerve Stimulation - Theory, Experiments and Applications*, Springer-Verlag, Wien, 255 pp.
- Rattay, F and Aberham, M (1993) Modeling Axon Membranes for Functional Electrical Stimulation. *IEEE Trans. Biomed. Eng.* 40, 1201-1209.
- Reilly, J.P., Freeman, V.T. and Larkin, W.D. (1985) Sensory Effects of Transient Electrical Stimulation: Evaluation with a Neuroelectrical Model. *IEEE Trans. Biomed. Eng.* 32, 1001-1011.
- Sapozhnikov, A. (1990) Computer Modelling of the Implanted Cochlea. BSc Thesis, University of Melbourne.
- Schwarz, J.R. and Eikhof, G. (1987) Na Currents and Action Potentials in Rat Myelinated Nerve Fibres at 20 and 37°C. *Pflügers Arch.* 409, 569-577.
- Shepherd, R.K., Hatsushika, S. and Clark, G.M. (1993) Electrical Stimulation of the Auditory Nerve: The Effect of Electrode Position on Neural Excitation. *Hear. Res.* 66, 108-120.
- Spelman, F.A., Clopton, B.M., and Pflingst, B.E. (1982) Tissue Impedance and Current Flow in the Implanted Ear. Implications for the Cochlear Prosthesis. *Ann. Otol. Rhinol. Laryngol., Suppl.* 98, 91, 3-8.
- Strang, G. and Fix, C.J. (1973) *An Analysis of the Finite Element Method*. Prentice Hall, Englewood, N.J..
- Strelhoff, D. (1973) A Computer Simulation of the Generation and Distribution of Cochlear Potentials, *J. Acoust. Soc. Am.* 54, 620-629.
- Suesserman, M.F. (1992) Noninvasive Microelectrode Measurement Technique for Performing Quantitative, in Vivo Measurements of Inner Ear Tissue Impedances. Ph.D. Thesis, University of Washington.
- Suesserman, M.F. and Spelman, F.A. (1993) Lumped-Parameter Model for In Vivo Cochlear Stimulation. *IEEE Trans. Biomed. Eng.* 40, 237-245.
- Warman, E.N., Grill, W.M. and Durand, D. (1992) Modeling the Effects of Electric Fields on Nerve Fibers: Determination of Excitation Thresholds. *IEEE Trans. Biomed. Eng.* 39, 1244-1254.
- Weiden, R.M. van der, and Hoop, A.T. de (1989) Boundary Integral Equations for the Computational Modeling of Three-Dimensional Groundwater Flow Problems. *Computational Mechanics* 4, 283-291.

# Chapter VI

---

## **SPATIAL SELECTIVITY IN A ROTATIONALLY SYMMETRIC MODEL OF THE ELECTRICALLY STIMULATED COCHLEA**

*J.H.M. Frijns, S.L. de Snoo and J.H. ten Kate  
Submitted for Publication.*

## Abstract

A rotationally symmetric model of electrical stimulation of the guinea pig cochlea with active neural elements is used to study the influence of temporal stimulus parameters and electrode configurations on the spatial selectivity of electrical stimulation by cochlear implants.  $Q_{10\text{ dB}}$  values of the excitation patterns are determined with respect to the position of the stimulating electrode pairs in the cochlea. The results are compared against single fibre data from the cat cochlear nerve as measured by Van den Honert and Stypulkowsky (1987). It turns out that the use of charge-balanced asymmetric rather than symmetric biphasic pulses approximately doubles the number of independent channels that can be applied in a cochlear implant with longitudinal bipolar electrodes, like a configuration with radial electrode pairs using symmetric biphasic pulse stimulation will also do. Finally, the influence on selectivity of the physiological variation in diameter of the cochlear nerve fibres and of a possible loss of their peripheral processes is studied.

## Introduction

The use of multi-electrode devices in electrical stimulation of the auditory nerve in deaf patients is based upon the concept that isolated sub-populations of surviving auditory nerve fibres can be stimulated by employing disparate electrode combinations. Since these nerve fibres are tonotopically arranged in the cochlea (i.e. the fibres encoding for the higher frequencies are located more basally and those encoding for lower frequencies more apically) such a selective excitation of discrete parts of the cochlea is expected to give rise to different psycho-acoustic percepts. The clinical outcome with currently available multi-channel implants is usually more favourable than that usually achieved with older single-channel devices (Gantz and Tyler, 1990). This suggests that it is worth-while to put further effort in optimising the spatial selectivity of future devices.

The number of independent channels that can be used for frequency coding depends on the interaction between separate electrodes. There have been several attempts to quantify this interaction, both psycho-acoustically (Eddington et al., 1978; Townsend et al., 1987) and electrophysiologically with evoked potentials (O'Leary et al., 1985). Recordings from central auditory structures (Black and Clark, 1980) and single fibre recordings from the auditory nerve (Van Den Honert and Stypulkowski, 1987) provided additional information on the subject.

The region of excitation is larger with monopolar than with bipolar stimulation (Shannon, 1983), while the observed interaction patterns for bipolar stimulation broaden with increasing inter-electrode distance. Non-simultaneous stimulation results in a weaker interaction between electrodes (Favre and Pelizzone, 1993), an effect that is successfully applied in the so-called continuous interleaved sampling (CIS) strategy (Wilson et al., 1991). Phase-locking the current pulses to the input signal adds temporal cues to this CIS-strategy and results in an even better open set speech recognition (Peeters et al., 1993). Other suggested ways to reduce channel interaction are to apply

multipolar electrical stimulation rather than monopolar or bipolar to sharpen the region of excitation (Townsend and White, 1987) or to use radially instead of longitudinally oriented electrode pairs (Van Den Honert and Stypulkowski, 1987).

Most authors interpret these results in terms of current spread along the scala tympani and some researchers tried to measure this spread experimentally (Black et al., 1981; Ifukube and White, 1987). In addition, several computational models were developed to describe and understand the potential distribution in the cochlea and the resulting neural excitation patterns. The simplest models assume an exponential decay of current from its source to the neural elements (O'Leary et al., 1985), whereas others consist of discrete resistive (Black and Clark, 1980) or resistive and capacitive (Suesserman and Spelman, 1993) elements. Finley et al. (1990) used the finite element method to solve the three-dimensional volume conduction problem for an unrolled cochlear turn and were able to explain the differences in excitation patterns observed between radial and longitudinal electrode configurations with a passive neural model. Colombo and Parkins (1987) arrived at similar conclusions regarding radial and longitudinal electrodes using an infinite, homogeneous volume conductor and an active neural model.

In a previous paper (Frijns et al., 1995a) we presented a rotationally symmetric model of the electrically stimulated guinea pig cochlea which incorporates active neural elements, and computed excitation profiles of the auditory nerve and their dependence on stimulus level and electrode position. In order to be able to compare these simulation data against available electrically evoked auditory brainstem (EABR) data of cats (Shepherd et al, 1993), we embedded this cochlea model in a bony outer medium and adapted the dimensions of the electrode configurations to account for the dimensional dissimilarities between the cochleae of both species. It turned out that the model predicted differences between the thresholds and gradients of the EABR input/output curves for the distinct electrode configurations that were in good agreement with the experimental data. We also showed that unrolling the cochlear duct (Finley et al., 1990) or the use of a passive neural model (Warman et al., 1992) will lead to erroneous conclusions. In this paper we will apply this model to study the influence of several relevant temporal stimulus parameters and electrode configurations on the spatial selectivity that can be achieved with cochlear implants. We will also study to what extent the simulated responses are influenced by physiological differences in diameter of the peripheral processes of the auditory nerve fibres (Gleich and Wilson, 1993) or by the total absence of these dendrites as is frequently observed in deaf ears (Johnsson, 1988; Schuknecht, 1993).

## Materials and Methods

In the present study we will use the computational model of the implanted guinea pig cochlea we described in a previous paper (Frijns et al., 1995a) as a starting point, including the adaptations described in the Introduction to allow for comparison with cat data. The model consists of two sub-models, the first one computing the potential distribution due to stimulating current sources in a rotationally symmetric cochlear geometry, the other one describing the neural responses to the calculated potential field. We will give a short description of both sub-models below. For further details we refer to the above-mentioned paper.

### *The rotationally symmetric volume conduction model of the second turn of the guinea pig cochlea*

For the purpose of simulating the neural responses to the focal injection of stimulus currents into the cochlea we were interested in calculating the potentials in the nodes of Ranvier of the auditory nerve fibres due to these current sources. As an analytic solution of such a three dimensional volume conduction problem is restricted to geometries that are much simpler than the cochlea, the problem had to be solved numerically. We applied the numerical method which is known as the Boundary Element Method or the Integral Equation Method (Meijs et al., 1989, Van Oosterom, 1991). This method offers the advantages of a relative ease of mesh generation and the opportunity to perform calculations with multiple current source configurations instead of one, with a limited additional amount of computational effort. It requires discretisation of the *boundaries* between volumes with different conductivity rather than discretisation of these volumes themselves, and uses Green's second theorem to express the potential distribution due to a current source distribution in a piece-wise homogeneous volume conductor of arbitrary shape as the superposition of two components. The first component is identified as the potential distribution that would be induced by these current sources in a homogeneous medium of infinite extent, whereas the second component is a correction term that accounts for the inhomogeneities in the volume conductor in terms of imaginary secondary sources arising from the boundaries between the various media. To increase the numerical accuracy and to obtain a more realistic shape of the modelled cochlea we discretised all boundaries with quadratically curved triangular surface elements on which the potential was also interpolated quadratically (Brebbia and Dominguez, 1992; Frijns and De Snoo, 1995).

We limited the number of surface elements and the complexity of the mesh generation by simplifying the spiralling cochlear anatomy to the rotationally symmetric structure shown in Fig. 1<sup>c</sup>, which consists of 2240 curved elements and 4194 nodes. This toroidal structure was created by rotating the cross-section shown in Fig. 1<sup>a</sup> around the modiolus and 'azimuthally' subdividing the created volume in sixteen segments in such a way, that the surface elements located in the vicinity of the electrodes were smaller than those further away

(Fig. 1<sup>b</sup>). The conductivities of the various media in the cochlea were derived from experimental data in literature as listed in Table I.

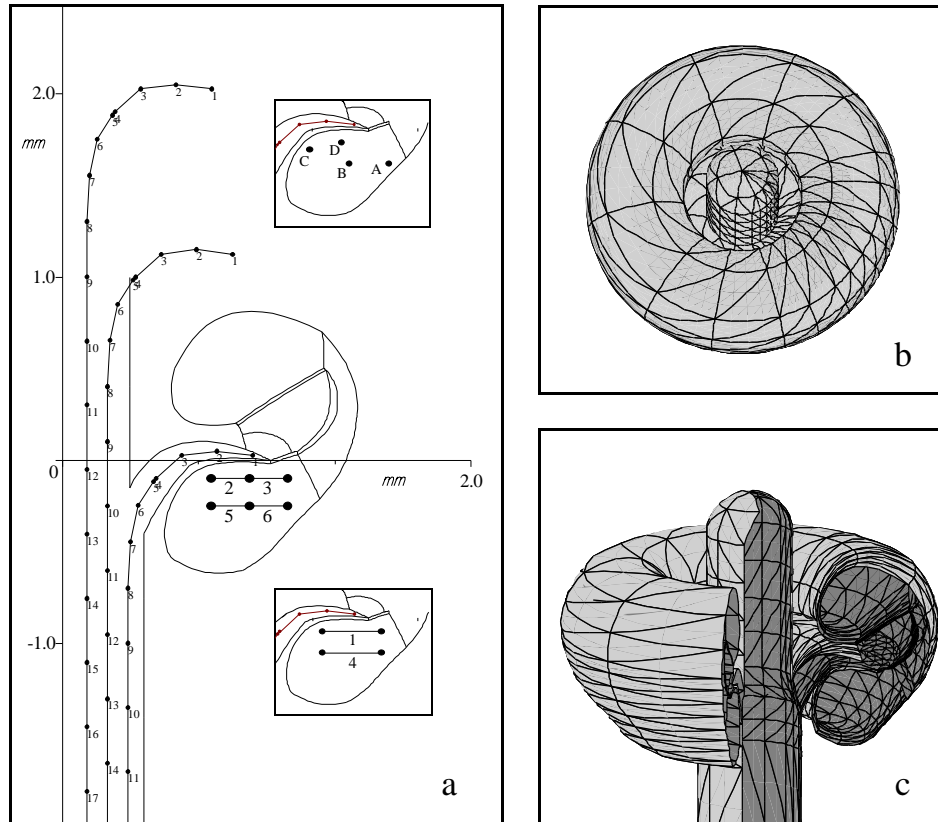


**Fig. 1** a The modelled cross-section of the cochlea, which is based upon a histologic section through the base of the second turn of a guinea pig cochlea. The course of three nerve fibres, one ending in the modelled second turn and two in more apical turns, is displayed. The numbered dots along these nerve fibres designate the location of the nodes of Ranvier. The numbers in the scala tympani designate the radial dipoles with electrode spacing 187.5 μm, while the lower inset shows the way these dipole locations are combined to obtain radial dipoles with electrode spacing 375 μm. The upper inset summarises the four longitudinal electrode sites (A = near the outer wall; B = central in the scala tympani; C = near the spiral ganglion; and D = underneath the dendrites).

b Top view of the boundary element mesh of the rotationally symmetric cochlea, illustrating the smaller element size near the stimulating electrodes in order to reduce computational errors.

c Three-dimensional view of the quadratically curved boundary element mesh of the rotationally symmetric cochlea model, with a part intentionally left out.

Table I The conductivities of the various cochlear tissues as used in the computations. The data were compiled from Finley et al. (1990), Suesserman (1992) and Strelieff (1973). The values for the basilar membrane and Reissner's membrane are enlarged by a factor 5 and 10 respectively to correct for the geometric scaling of these membranes, which was applied to minimise computational errors.

Tissue	Conductivity ( $\text{Wm}^{-1}$ )
Scala tympani	1.43
Scala vestibuli	1.43
Scala media	1.67
Stria vascularis	0.0053
Spiral ligament	1.67
Reissner's membrane	0.00098
Basilar membrane	0.0625
Organ of Corti	0.012
Bone	0.156
Nerve tissue	0.3

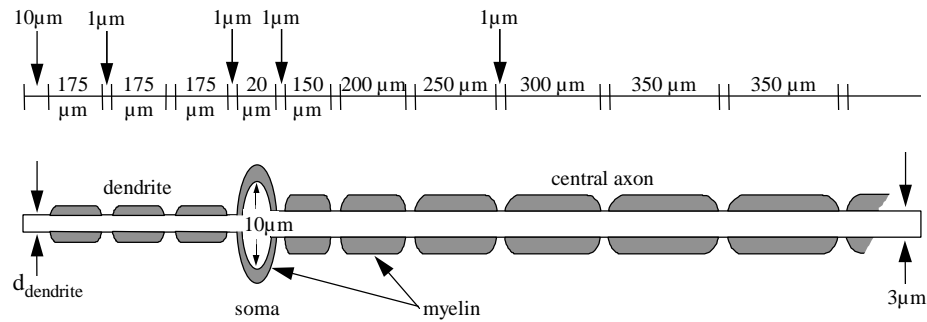


Fig. 2 The morphology of the auditory nerve fibre model that is used in the calculations. For high spontaneous rate (HSR) fibres the axonal diameter of the peripheral process  $d_{dendrite}$  is 3  $\mu\text{m}$ , while it is 2  $\mu\text{m}$  in simulations with low spontaneous rate (LSR) fibres.

*The auditory nerve fibre model*

In our previous paper (Frijns et al., 1995a) we demonstrated that an active, non-linear nerve fibre model produces more accurate predictions of the excitation patterns in the auditory nerve due to biphasic stimuli than passive estimators based upon the potential distribution in cochlea, such as the activating function (Rattay, 1989) or the total equivalent driving function (Warman et al., 1992). Therefore, also the present paper will use this model of guinea pig auditory nerve fibres, which can simulate the response to time-varying potential fields in the cochlea. The model equations of this auditory nerve fibre model, which has nodal kinetics based on voltage clamp data in the rat (Schwarz and Eikhof, 1987), are described in detail elsewhere (Frijns et al., 1994b, 1995a, 1995b) and will not be reproduced here. Fig. 2 shows the morphology of the bipolar auditory fibres used in the calculations. Most simulations in the present paper were performed for high spontaneous rate (HSR) nerve fibres. These fibres, which were also used in our previous paper (Frijns et al., 1995a), consist of a peripheral and a modiolar axon with a diameter of 3  $\mu\text{m}$ , interconnected by a cell body with a diameter of 10  $\mu\text{m}$ . The gap width of the nodes of Ranvier is 1  $\mu\text{m}$ , and the length of the unmyelinated terminal 10  $\mu\text{m}$ . Some calculations involved low spontaneous rate (LSR) fibres, which have a similar morphology but have a terminal axon diameter of 2  $\mu\text{m}$  (Gleich and Wilson, 1993).

Although the volume conduction part of the model represents the geometry of a single turn of the cochlea, it includes nerve fibres originating in three successive cochlear turns, viz. in the modelled turn and the two more apical ones. In the modiolus, where all fibres are coming closely together, the more apical fibres take a more central course to reflect the tonotopic organisation normally present in the auditory nerve (Fig. 1<sup>a</sup>). The modelled second turn accommodates 40 nerve fibres, the third and fourth turns 35 and 20, respectively. This means that the model incorporates approximately 15 fibres per octave, or equivalently, 50 fibres per decade and that each modelled nerve fibre represents about 250 real nerve fibres.

*Measures of spatial selectivity*

The model's results can be interpreted in terms of spatial selectivity in several ways. In our previous paper (Frijns et al., 1995a) we computed the average gradient for the first 12 dB of the calculated input/output curves for this purpose. Such I/O-curves (see Fig. 3<sup>b</sup> for an example) display the total number of excited nerve fibres as a function of stimulus intensity and can therefore be compared with experimental EABR data. A shallow slope of such a curve means a gradual recruitment of nerve fibres with increasing stimulus strengths, which corresponds with a restricted region of excitation. I/O-curves, however, do not provide information on the distribution of the excited fibres along the cochlear partition, which limits their value for the present study.

So-called excitation profiles (the rightmost four panels in Fig. 3) give more detailed information on this subject, as they show the position of the excited

fibres in the cochlea for a given stimulus level. In these figures the part of the nerve fibre (dendrite, soma or modiolar axon) where the initial excitation takes place is indicated by a grey shading. Such excitation profiles allow, e.g., the identification of stimulus conditions for which the model predicts so-called ectopic excitation of fibres from higher cochlear turns passing by in the modiolus, which imposes a limit on the usable range of stimulus levels. The excitation profiles also provide a way to quantify the spatial selectivity by measuring the sharpness of the peaks in the distribution of the excited fibres around the electrodes. We will express this sharpness in terms of a quality factor  $Q_{10\text{ dB}}$  in analogy with the practice for measuring frequency selectivity in hearing subjects (Evans, 1975). This  $Q_{10\text{ dB}}$  is defined as the centre frequency  $f_0$  of the region of excitation due to an electrode configuration, divided by the bandwidth  $Df$ , 10 dB above the best threshold. It is important to bear in mind that this definition does neither imply that this threshold is reached at  $f_0$ , nor that the fibres corresponding with  $f_0$  are excited at all. This applies, e.g., to the bimodal excitation profiles in Fig. 3, which will be described in detail in the next section. Taking into account the fact that the model incorporates 50 nerve fibres per decade (see the previous section), and assuming that a region with a width of  $n$  simulated nerve fibres, centred around  $f_0$ , is excited by a stimulus 10 dB above threshold, the corresponding  $Q_{10\text{ dB}}$  can be computed as follows:

$$Q_{10\text{ dB}} = \frac{f_0}{Df} = \frac{f_0}{f_0 10^{\frac{1}{2}n/50} - f_0 10^{-\frac{1}{2}n/50}} = \frac{1}{10^{n/100} - 10^{-n/100}}. \quad (1)$$

A high value of  $Q_{10\text{ dB}}$ , which, according to Eq. 1, depends only on the width of the excited region and not on the place of excitation, corresponds to a small region of excitation and thus to a high spatial selectivity.

## Results

### *Influencing neural recruitment by stimulus parameters*

In our previous study (Frijns et al., 1995a) we calculated neural excitation profiles and input/output (I/O) curves for longitudinal bipolar electrodes at positions, comparable to those used experimentally by Shepherd et al. (1993). These four positions (A = near the outer wall, B = in the middle of scala tympani, C = adjacent to the modiolus and D = underneath the peripheral dendrites) are illustrated in the inset in Fig. 1<sup>a</sup>. We demonstrated that the model's results for all three tested inter-electrode spacings ('bipolar' = 375  $\mu\text{m}$ , 'bipolar+1' = 750  $\mu\text{m}$  and 'bipolar+2' = 1125  $\mu\text{m}$ ) were in good agreement with available electrical ABR data in cats (Shepherd et al, 1993) if the calculations were performed for the same symmetric biphasic pulses (pulse width 200  $\mu\text{s}$ /phase, the most apical electrode becoming cathodic first) as applied in the experiments. Fig. 3 displays this stimulus waveform and summarises the results for the four 'bipolar' electrode configurations. From the I/O-curve in Fig. 3<sup>b</sup> it is clear that the excitation threshold greatly depends on the electrode site: the electrode in the dendritic position (site D) has the lowest excitation threshold, while the threshold for the electrode near the outer wall (site A) is

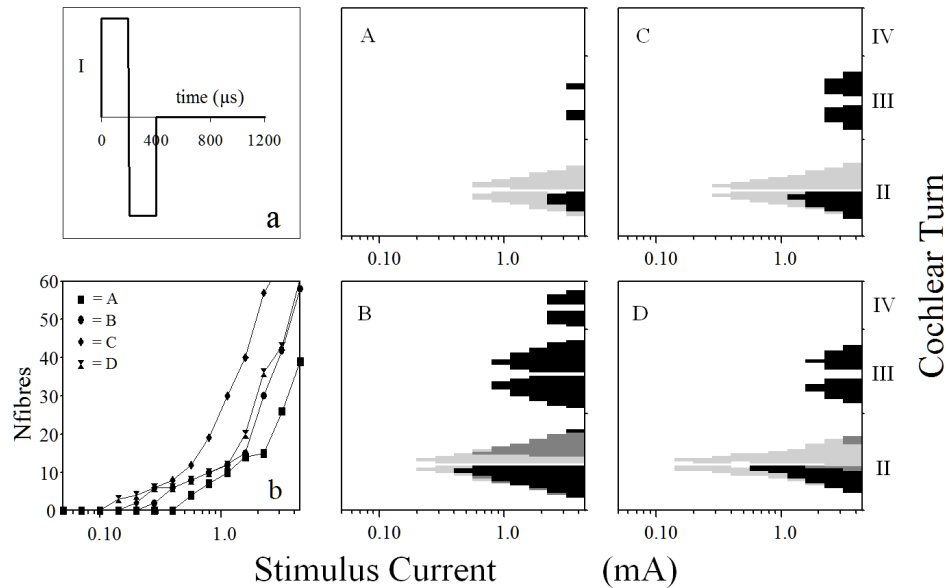


**Fig. 3** a The symmetric biphasic current pulse ( $I$ ) applied to the basal electrode of the bipolar pair used in the simulations presented in this figure. The apical electrode has the opposite polarity, i.e. it is cathodic first.  
 b The number of excited nerve fibres ( $N_{fibres}$ ) as a function of the stimulus current (input/output curves) for the HSR auditory nerve fibre model ( Fig. 2) and the stimulus waveform in (a) with 'bipolar' electrodes at the four electrode sites A, B, C and D (see legend and the upper inset in Fig. 1<sup>a</sup>).  
 The rightmost four panels show the location along the cochlear turns of the excited nerve fibres at a given stimulus strength for each of the four electrode configurations tested. The location of the node of Ranvier where the initial excitation takes place is indicated by a grey shading (dendrite = lightest, central axon = black, around the soma = intermediate).

approximately four times that value. The underlying excitation profiles ( Fig. 3) demonstrate that also the dynamic range as determined by ectopic stimulation as well as the spatial selectivity vary with the exact position in the scala tympani of the stimulating dipole.

The  $Q_{10\text{ dB}}$ -values (computed with Eq. 1) for the four 'bipolar' electrode configurations from Fig. 3 are listed in Table II together with similar data for the corresponding 'bipolar+1' and 'bipolar+2' electrode configurations. Evidently, electrodes in the dendritic position (site D), which we showed to have the lowest excitation threshold for all electrode spacings (Frijns et al., 1995a), also exhibit the highest  $Q_{10\text{ dB}}$ , indicating that these electrodes allow the most localised excitation, while the outer wall position (site A) is the least favourable in both respects. On the other hand, the spatial selectivity in the excitation profiles of all electrode sites deteriorates with increasing inter-electrode distance: the average  $Q_{10\text{ dB}}$  for the 'bipolar' electrodes is 1.89, while it is 1.28 for the 'bipolar+2' configuration. Also the differences between the excitation

profiles for the four electrode sites diminish with increasing inter-electrode spacing; electrodes in sites C and D are slightly more sensitive to this parameter than those in sites A and B.

All excitation profiles in Fig. 3 show a bimodal distribution of excited fibres, which is centred around the mid-plane between the electrodes constituting the bipolar pair. The central region of high excitation thresholds is an inevitable consequence of the existence of a zero-potential plane in the centre of any current dipole (cf. Fig. 6<sup>a</sup>), but close observation of the simulations suggested that the almost symmetric bimodal distribution of excitation is caused by the fact that symmetric biphasic pulses were used: It appeared that the excitation of nerve fibres near the most apical electrode of the current dipole took place during the initial phase of the stimulus, whereas fibres close the other electrode depolarised during the second stimulus phase. In fact, most fibres appeared to respond when the nearest part of the current dipole acted as the cathode, especially for lower stimulus intensities. From this observation we expected that the use of monophasic stimuli would result in a unimodal distribution of excited nerve fibres around the cathode, offering the opportunity to achieve more localised stimulation. Fig. 4 shows the excitation profiles and the resulting I/O-curves for the case of monophasic pulses of 200  $\mu$ s duration and the same four longitudinal 'bipolar' electrode configurations as used for Fig. 3, with the more apical electrode acting as the cathode. As argued above, there exists a region of elevated thresholds near the mid-plane between the electrodes, and the region with the lowest thresholds is located around the cathode indeed. Thresholds around the anode tend to be 6 dB to 12 dB higher, resulting in a range of stimulus intensities for which the slope of the I/O-curves in Fig. 4<sup>b</sup> is approximately half that of the equivalent curve in Fig. 3<sup>b</sup>. This is also reflected in the  $Q_{10\text{ dB}}$ -values in Table II, which are evidently higher than in the case of symmetric biphasic pulses. Now, the average  $Q_{10\text{ dB}}$  is 5.02, while it was 1.89 for symmetric biphasic pulses. For electrode site D the  $Q_{10\text{ dB}}$  is even raised from 2.40 to 10.85. On the contrary, the  $Q_{10\text{ dB}}$  for electrode site C remains unchanged, as a consequence of the fact that this electrode site exhibits a threshold difference between anodal and cathodal stimulation of just 6 dB (see Fig. 4<sup>e</sup>). Table II shows that similar observations hold for the 'bipolar+1' and 'bipolar+2' electrode spacings, although the relative advantage of monophasic pulses over symmetric biphasic ones is less for larger inter-electrode distances. The excitation profiles in Fig. 4 demonstrate another interesting phenomenon: at stimulus strengths 2 to 8 times threshold for each individual fibre, nerve fibres located near the cathode failed to generate action potentials that propagated through the modiolus. This so-called cathodal block resulted in a gradual shift of the centre of excitation caused by the cathode away from the mid-plane between the electrodes towards the apex. Such an effect is not discernible around the anode.

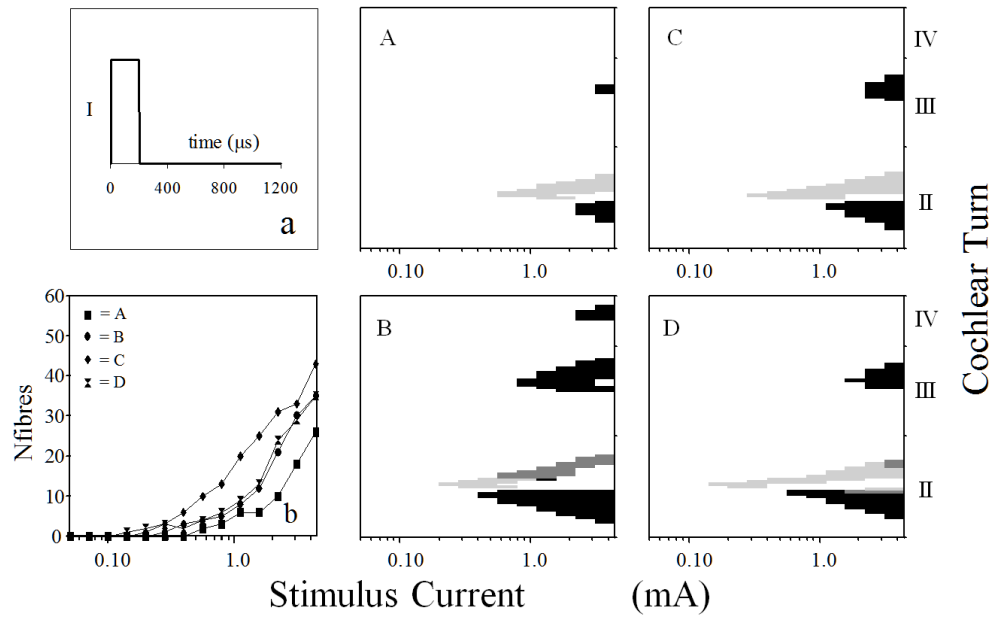


Fig. 4 The same as Fig. 3, now for the monophasic current pulse shown in (a) with the more apical electrode of the bipolar pair acting as the cathode.

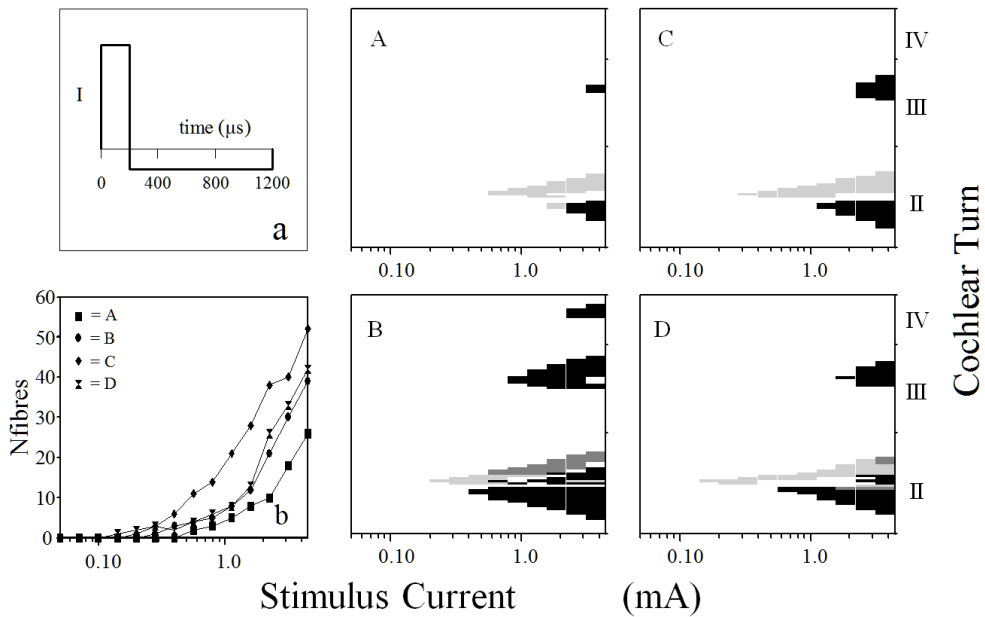


Fig. 5 The same as Fig. 3, now for the charge-balanced asymmetric biphasic pulse shown in (a) with the more apical electrode of the bipolar pair acting as the cathode during the first stimulus phase.

Although such monophasic stimuli apparently have favourable properties in terms of an improved spatial selectivity over symmetric biphasic pulses, they are not applicable for chronic stimulation *in vivo* as tissue damage will occur due to net charge injection (see Discussion). Comparison of Figs. 3 and 4 suggests that the application of charge-balanced asymmetric biphasic pulses (cf. Fig. 5<sup>a</sup>) is likely to result in a significant increase in spatial selectivity, comparable with the one obtained with monophasic pulses, while avoiding the risk of tissue damage. The concept behind this stimulus waveform is that the first stimulus phase will excite fibres near the electrode that acts as the cathode, while the second stimulus phase will reverse the charge injection with a (longer lasting) current pulse that is small enough to prevent excitation near the other electrode of the bipolar pair, which is the cathode during this stimulus phase. From Figs. 3 and 4 we inferred that a ratio of 5 (i.e. 14 dB) between the amplitude of the first and second stimulus phase would suffice to produce this effect for all four electrode sites. Fig. 5 displays the simulated I/O-curves and excitation profiles for all four electrode sites A - D with this stimulus waveform, while the third column in Table II lists the corresponding  $Q_{10\text{ dB}}$ -values. For ten of the twelve electrode configurations tested these  $Q_{10\text{ dB}}$ -values are identical to the ones for the corresponding monophasic stimuli, given in the second column of this table. The two exceptions are the 'bipolar' and 'bipolar+1' electrodes near the outer wall (site A), where the second stimulus phase was apparently yet so large that it caused some additional excitation near the basal electrode (see the corresponding excitation profile in Fig. 5). As indicated by the excitation profiles for the electrode sites C and D in Fig. 5 the use of asymmetric biphasic pulses instead of monophasic ones caused another side-effect as it counteracted the cathodal blocking effect in a number of instances. Generally speaking however, the simulation data presented here indicate that charge-balanced asymmetric biphasic current pulses improve the spatial selectivity of longitudinal electrode pairs indeed, especially for small inter-electrode separations.

#### *The effect of radial bipolar electrode configurations*

Another option to circumvent the occurrence of bimodal excitation patterns of the auditory nerve as occur in conventional bipolar stimulation with symmetric biphasic pulses (Fig. 3), is to apply bipolar electrodes that are radially rather than longitudinally oriented with respect to the scala tympani. As is illustrated in Fig. 6, this rotation of the dipole axis rotates the zero potential mid-plane between the electrodes also by 90 degrees. Therefore this zero potential plane does not cross the modiolus in the case of radially oriented dipoles, and the situation is avoided that nerve fibres cannot be stimulated due the fact that their entire course is in this equipotential plane.

To test to what extent the exact location of a radial dipole or the spacing of the constituting electrodes influences the predicted excitation profile of the auditory nerve and the spatial selectivity, we used the six dipoles shown in Fig. 1<sup>a</sup>. Dipoles 1, 2 and 3 are positioned immediately underneath the dendrites, while dipoles 4, 5 and 6 occupy more central positions in the scala tympani. Electrode

Table II The simulated  $Q_{10\text{ dB}}$ -values (as computed with Eq. 1) for symmetric biphasic current pulses (200  $\mu\text{s}/\text{phase}$ ), monophasic current pulses (200  $\mu\text{s}$ ) and charge-balanced asymmetric current pulses (200 and 1000  $\mu\text{s}/\text{phase}$  respectively) on longitudinal bipolar electrode pairs with different electrode spacing ('bipolar' = 375  $\mu\text{m}$ , 'bipolar+1' = 750  $\mu\text{m}$ , 'bipolar+2' = 1125  $\mu\text{m}$ ) in four electrode sites A - D (Fig. 1).

	<b>electrode</b>	<b>symmetric</b>	<b>mono-</b>	<b>asymmetric</b>
		<b>biphasic</b>	<b>phasic</b>	<b>biphasic</b>
<i>bipolar</i>				
	A	1.42	3.09	1.95
	B	1.95	4.33	4.33
	C	1.79	1.79	1.79
	D	2.40	10.85	10.85
	mean	1.89	5.02	4.73
<i>bipolar+1</i>				
	A	1.42	2.70	1.95
	B	1.52	1.95	1.95
	C	1.25	1.33	1.33
	D	1.95	4.33	4.33
	mean	1.54	2.58	2.39
<i>bipolar+2</i>				
	A	1.25	2.70	2.70
	B	1.25	1.42	1.42
	C	1.11	1.17	1.17
	D	1.52	1.79	1.79
	mean	1.28	1.77	1.77

pairs 1 and 4 have an inter-electrode distance of 375  $\mu\text{m}$  (i.e. identical to the 'bipolar' longitudinal configuration), the other four dipole spacings are half this value. If the innermost electrode of a dipole acts as the positive electrode we call the dipole anodic, while it is called cathodic if the negative electrode is closest to the modiolus.

Fig. 7<sup>b</sup> shows the simulated I/O-curves for the six radial dipoles for anodic monophasic pulses with a duration of 200  $\mu\text{s}$ . The corresponding excitation profiles are also reproduced in Fig. 7. Expectedly, the larger dipoles 1 and 4 yield lower excitation thresholds than the smaller ones located at the same level in the cochlea. However, excitation thresholds and the node of Ranvier that is depolarised initially depend on the exact site in the scala tympani. This is illustrated (Table III) by the fact that the threshold for the small dipole in position 2 is even slightly lower than the one for the large dipole in position 4.

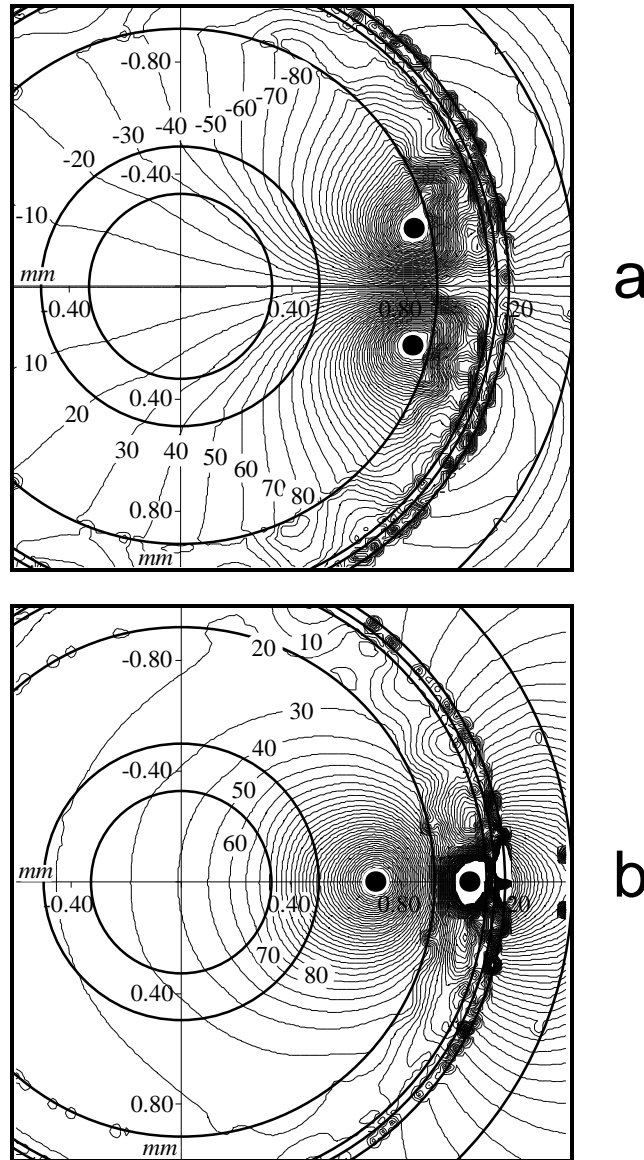


Fig. 6 a The potential distribution in a horizontal plane through the peripheral processes of the auditory nerve fibres (i.e. at 0.05 mm on the vertical axis in Fig. 1<sup>a</sup>) for the longitudinal 'bipolar' electrode configuration close to the dendrites (site D in Fig. 1<sup>a</sup>). The circles represent the boundaries between the various media (from the inside out: modiolar nerve tissue, osseous spiral lamina, dendritic nerve tissue, organ of Corti, scala media, stria vascularis, spiral ligament, outer wall bone). The numbers on the equipotential lines indicate the potential in millivolts due to the injection of a current of 1 mA. Note the existence of a zero potential plane running midway between the electrodes through the origin.

b The same as (a), now for the radial dipole pair 3 (Fig. 1<sup>a</sup>), which has the same electrode spacing as the longitudinal dipole used to compute (a).

An interesting observation in Fig. 7 and Table III is the fact that for both stimulus polarities electrodes 1, 2 and 3, which are located just below the dendrites, give rise to a higher spatial selectivity (average  $Q_{10\text{ dB}}$  4.6 vs. 1.5), a lower excitation threshold (by 8.2 dB on the average) and a 6 to 12 dB larger usable range of stimuli with respect to ectopic modiolar stimulation than the electrodes 4, 5 and 6 that are located more centrally in the scala tympani. The model results do not reveal any consistent relationship between the spacing of the electrodes and the sharpness of the simulated distribution of the excited fibres as expressed in the  $Q_{10\text{ dB}}$ .

A similar analysis was made for cathodic monophasic pulses of the same duration. The results are presented in Fig. 8 and Table III. For this stimulus polarity the model predicts excitation thresholds that are lower by a factor 2.6 on the average than those for the anodic monophasic pulses. As with anodic stimulation we find also for cathodic pulses the highest  $Q_{10\text{ dB}}$ -values for electrode positions just below the dendrites. For these electrode positions polarity reversal has much more impact on the  $Q_{10\text{ dB}}$  than for the electrodes located more centrally in the scala tympani. Polarity reversal lowers the simulated thresholds for the fibres from more apical turns more than those for the turn, where the electrodes are located. Especially for electrode positions 4, 5, and 6 this imposes a serious constraint on the predicted dynamic range (Fig. 8). As is readily seen in the simulated I/O-curves and excitation profiles of Fig. 8, the model predicts such a large influence of cathodal blocking, that the number of excited fibres even decreases for stimulus currents above 5 mA.

Table III The simulated excitation thresholds and  $Q_{10\text{ dB}}$ -values (as computed with Eq. 1) for monophasic current pulses (200  $\mu\text{s}$ ) and the six radial dipoles of Fig. 1<sup>a</sup>. The stimulus polarity is defined according to the polarity of medial electrode. The column *an/cath* lists the ratio between the threshold currents for anodic and cathodic dipoles.

electrode	anodic		cathodic		an/cath ratio
	threshold (mA)	$Q_{10\text{ dB}}$	threshold (mA)	$Q_{10\text{ dB}}$	
1	0.39	3.09	0.14	4.33	2.8
2	0.75	3.09	0.15	7.23	5.0
3	0.80	4.33	0.39	5.42	2.1
4	0.77	1.42	0.36	1.65	2.1
5	1.33	1.52	0.55	1.95	2.4
6	2.17	1.42	1.57	0.82	1.4

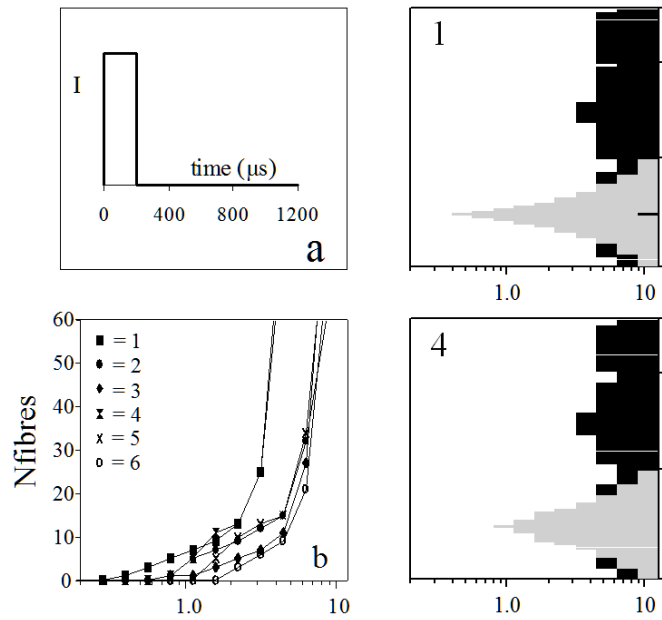


Fig. 7 The same as Fig. 3, now for the monophasic pulse shown in (a) and the six radially oriented current dipoles of Fig. 1<sup>a</sup>, with the electrode closest to the modiolus acting as the anode. The numbers (1 and 4 on this page, 2, 3, 5 and 6 on page 141) in the legends refer to the corresponding electrode configuration.

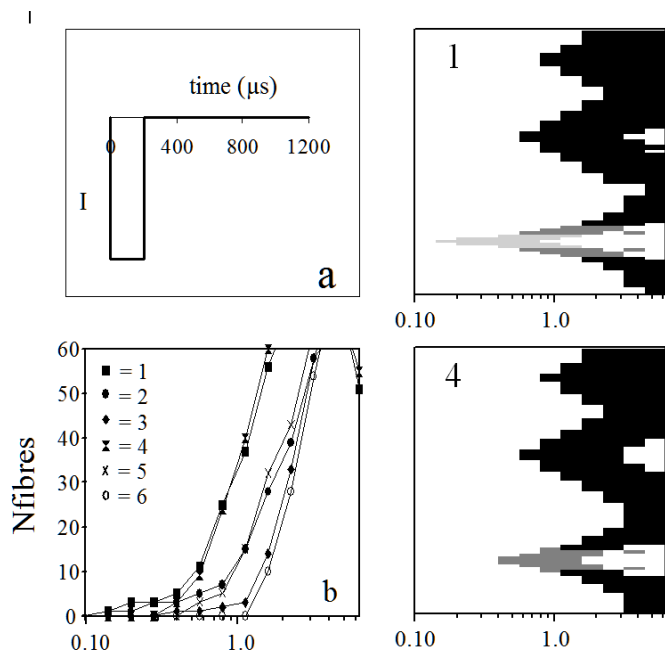
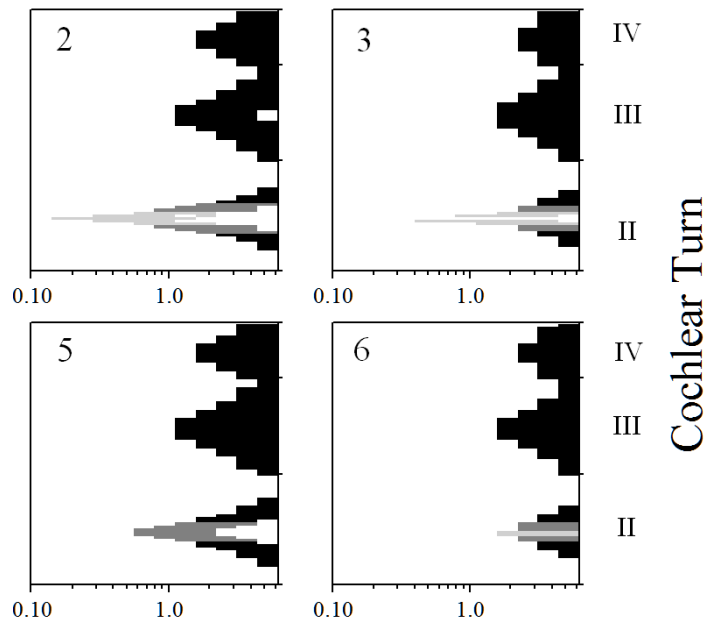
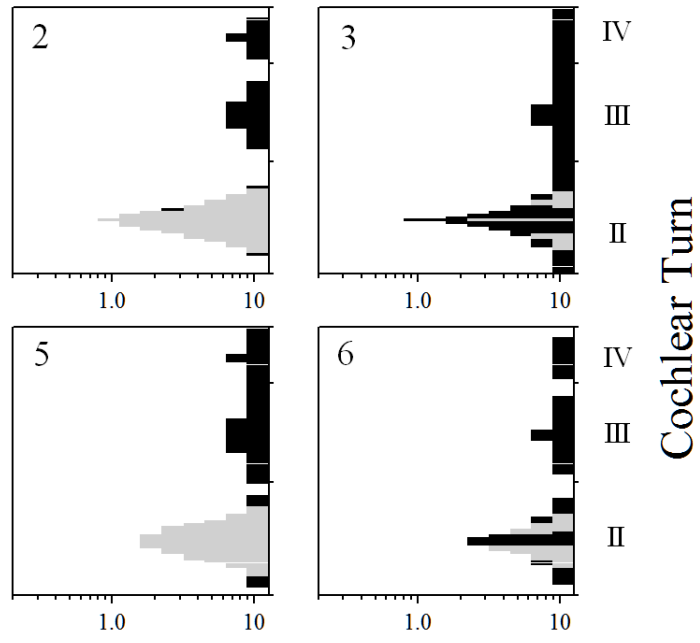


Fig. 8 As Fig. 7, now for monophasic current pulses of the opposite polarity, i.e. with the more medial electrode acting as the cathode.



*The influence of the peripheral processes*

There exists a considerable variability in the morphology of the auditory nerve fibres in a normal cochlea, especially in the diameter of the peripheral processes, which are also called dendrites (Gleich and Wilson, 1993). In the simulations presented in the previous sections, however, we used for all nerve fibres the standard morphology of an average HSR fibre, which has a relatively thick dendrite (3  $\mu\text{m}$ , Fig. 2). Since thinner nerve fibres are known to exhibit higher excitation thresholds (Gorman and Mortimer, 1983), the question arises to what extent the presence of LSR fibres (which are known to possess thinner dendrites, see Gleich and Wilson, 1993) influences the excitation pattern of the electrically stimulated auditory nerve. This is the more interesting, as the relative contribution of this fibre type to the total auditory fibre population is not exactly known, but estimates range from 25% to over 50% (Gleich and Wilson, 1993). Therefore, we performed simulations with a nerve fibre model that has a thinner dendrite (2  $\mu\text{m}$ ) and thus is more representative for LSR fibres. It turned out that the calculated excitation thresholds are approximately 2 dB higher for LSR fibres indeed (Table IV), and that these differences vary with the electrode spacing. As is illustrated by the  $Q_{10\text{dB}}$ -values in Table IV, also the spatial selectivity is only influenced marginally by the diameter of the peripheral processes (cf. Table II). Because of this, also the excitation profiles and I/O curves closely resemble the corresponding results for HSR fibres (Fig. 3). Therefore they are not reproduced here.

In profound deafness, loss of entire peripheral processes is often reported, and this situation may grow worse after the insertion of a scala tympani electrode (Linthicum et al., 1991; Schuknecht, 1993). To study the influence of this phenomenon on spatial selectivity, we performed simulations with nerve fibres

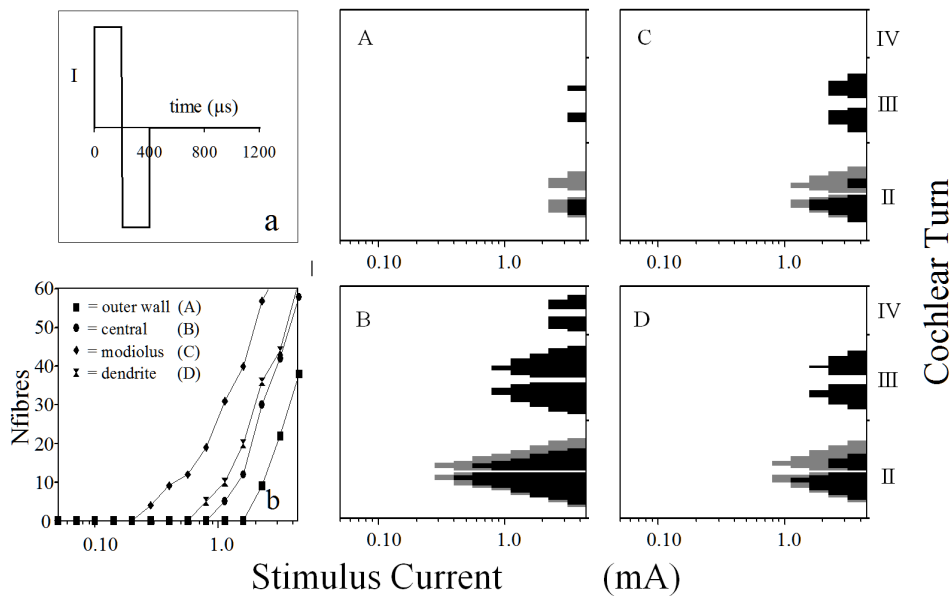


Fig. 9 As Fig. 3, now for the situation that all nerve fibres have lost their peripheral processes.

that did not extend beyond the cell body in the spiral ganglion. As is shown in Fig. 9, the absence of the peripheral dendrites has considerable influence on both the simulated excitation thresholds and the spatial selectivity of most electrode positions. An exception to this observation is formed by the electrode position close to the cell bodies (site C). For this site the excitation thresholds are increased by about 2 dB relative to the thresholds for HSR fibres, while the thresholds are elevated by approximately 15 dB for the other 'bipolar' electrode positions (Table IV). The threshold differences diminish slightly with increasing electrode separation, but, according to the model's predictions, ectopic stimulation in the modiolus will occur for stimuli that are just a few decibels above threshold for all electrode configurations tested ( Fig. 9).

## Discussion

This paper used the rotationally symmetric model of the electrically implanted cochlea we developed recently (Frijns et al., 1995a) to study the way stimulus

Table IV The influence of thinner (2  $\mu\text{m}$ , LSR) or absent (No Dendrite) peripheral processes of the auditory nerve fibres on the simulated excitation thresholds and  $Q_{10\text{ dB}}$ -values (as computed with Eq. 1) for symmetric biphasic pulses (200  $\mu\text{s}$ /phase). Threshold differences are given in decibels relative to the corresponding thresholds for non-degenerated HSR-fibres ( $d_{\text{dendrite}}=3\text{ }\mu\text{m}$ ).

electrode	LSR			No Dendrite		
	threshold (mA)	relative threshold (dB)	$Q_{10\text{ dB}}$	threshold (mA)	relative threshold (dB)	$Q_{10\text{ dB}}$
<i>bipolar</i>						
A	0.594	1.5	1.65	2.650	14.5	0.67
B	0.342	1.8	1.95	1.288	13.3	1.33
C	0.219	1.8	1.65	0.225	2.1	1.52
D	0.138	0.9	2.40	0.813	16.3	0.95
mean		1.5	1.91		11.6	1.12
<i>bipolar+1</i>						
A	0.369	2.7	1.42	1.463	14.7	0.64
B	0.261	3.1	1.42	0.794	12.7	0.70
C	0.189	2.9	1.11	0.170	2.0	1.11
D	0.099	0.9	1.95	0.434	13.8	0.90
mean		2.4	1.47		10.8	0.84
<i>bipolar+2</i>						
A	0.270	2.5	1.25	0.844	12.4	0.70
B	0.197	2.1	1.25	0.447	9.3	0.75
C	0.140	2.3	0.99	0.124	1.3	0.99
D	0.095	0.6	1.65	0.334	11.6	0.82
mean		1.9	1.28		8.6	0.82

and patient related parameters influence the spatial selectivity obtained with cochlear implants. For this purpose we computed neural excitation patterns and the corresponding input-output curves for various stimuli, electrode configurations and nerve fibre morphologies. As the spatial selectivity of a stimulus configuration is reflected in the sharpness of the peak around the electrodes in the computed excitation profiles, we measured this spatial selectivity in terms of a quality factor,  $Q_{10\text{ dB}}$  (Eq. 1), that resembles one used to quantify tuning in single fibre measurements in hearing animals (Pickles, 1988). In this respect it makes sense to compare the  $Q_{10\text{ dB}}$ -values in Tables II - IV to auditory single fibre data, which usually render  $Q_{10\text{ dB}}$ -values between 2 and 8 (Evans, 1975). There are, however, some fundamental differences. While a tuning curve represents the threshold of a single nerve fibre for a pure tone stimulus of varying frequency, the excitation profile in the case of electrical stimulation depicts the response of a region of nerve fibres to a single stimulus configuration with varying intensity. However, in the present rotationally symmetric model with uniformly distributed nerve fibres,  $Q_{10\text{ dB}}$  will obviously have the same value if it is computed either by measuring the width of the excitation profile 10 dB above threshold as done in this study, or by shifting the entire electrode configuration (with a stimulus strength of 10 dB above threshold) along the length of the basilar membrane while monitoring the response of a single nerve fibre.

Direct comparison of the simulated  $Q_{10\text{ dB}}$ s against experimental values can only be done in a restricted way, for single nerve fibre studies to electrical stimulation by similar electrode configurations are scarce. Van Den Honert and Stypulkowski (1987) performed such single fibre recordings for both electrical and acoustic stimuli in normally hearing cats. The relative dimensions of their longitudinal bipolar electrodes (500  $\mu\text{m}$  ball contacts with 2 mm distance) to the basal turn in the cat cochlea were comparable with our 'bipolar+1' (electrode spacing 0.75 mm) configuration in the simulated second turn of the guinea pig cochlea. For monophasic current pulses on these longitudinal dipoles they observed  $Q_{10\text{ dB}}$ -values ranging from 0.53 to 2.62 with a mean of 1.25, while the average simulated  $Q_{10\text{ dB}}$  for the four 'bipolar+1' electrode sites A - D is 2.58 (range 1.33 - 4.33, Table II). They reported lower and sharper minima in the distribution of the excitation thresholds when the apical electrode served as the cathode and explained this longitudinal polarity effect on the basis of the diminishing dimensions of the scala tympani from the round window to the apex. As the rotationally symmetric model does not account for this tapering, it is not surprising that the model does not exhibit any effect of a polarity reversal on longitudinal dipoles on the threshold or the spatial selectivity. The simulated thresholds for modiolar fibres coming from more apical turns of the cochlea are at least 12 to 20 dB above the ones in the turn where the electrodes are located, which is comparable with the minimum threshold difference of 14 dB for fibres differing at least one octave in characteristic frequency as reported by Van Den Honert and Stypulkowski (1987). As contrasted with their measurements the model does, however, not yield a uniform distribution of excitation thresholds for these 'distant' fibres ( Fig. 8). It is not clear whether this difference is caused by the fact that Van Den Honert and Stypulkowski

used normally hearing animals or by one or more invalid assumptions in our model.

The simulated excitation thresholds are comparable with the ones reported by Van Den Honert and Stypulkowski (1987)<sup>1</sup> or all (longitudinally and radially oriented) dipoles. Unlike these authors, however, we found the average threshold for radial electrodes to be 8.3 dB lower rather than higher if the cathode was placed medially (i.e. close to the neural elements) instead of laterally. Finley *et al.* (1990) arrived at a similar conclusion using the activating function (Rattay, 1989) to estimate neural responses in an unrolled cochlear volume conduction model.

The spatial selectivity of radially oriented dipoles does not seem to depend on the stimulus polarity in the measurements of Van Den Honert and Stypulkowski (1987). Regarding such electrode configurations these authors report higher  $Q_{10\text{ dB}}$ -values (mean 4.04, range 2.0 to 6.6) than for longitudinal electrode pairs. The corresponding simulation data exhibit a slightly larger variability with  $Q_{10\text{ dB}}$ s ranging from 0.8 to 7.2, while the average of 3.03 is not much larger than the average  $Q_{10\text{ dB}}$  for the 'bipolar+1' longitudinal electrode configuration. We found however, that the position in the scala tympani, for which Van Den Honert and Stypulkowski reported that they could not control experimentally, has a major influence on the spatial selectivity with radial electrode orientations: The  $Q_{10\text{ dB}}$ -values for both anodic and cathodic electrode configurations 1, 2, and 3 are at least twice (and up to 6.6 times) these values for the corresponding electrodes lower in the scala tympani (4, 5, and 6, respectively). In addition, polarity reversal does virtually not influence the computed  $Q_{10\text{ dB}}$  for electrodes 4, 5, and 6, while it does have influence on the spatial selectivity for radial electrodes high in the scala tympani (1, 2, and 3). From these observations we conclude that the widely accepted view that radially oriented electrode pairs have favourable properties in terms of spatial selectivity probably needs some nuance.

It is well known from functional electrical stimulation of the peripheral nervous system that the stimulus waveform can be used as a means to influence the neural recruitment characteristics (Gorman and Mortimer, 1983), especially when the nerve contains nerve fibres with clearly different diameters. In the case of electrical stimulation of the eighth nerve in the cochlea, however, the model predicts such an influence, even if all fibres would have the same morphology: Figs. 3 and 4 and Table II show that monophasic pulses result in a more circumscribed region of excited nerve fibres than symmetric biphasic ones in the case of longitudinal bipolar electrodes, especially for relatively small inter-electrode spacings. As Van Den Honert and Stypulkowski (1987) already inferred from their measurements, monophasic stimuli excite predominantly nerve fibres around the cathode, at least for stimuli that are less than 6 to 12 dB supra-threshold. This is in accordance with the fact that (real and modelled) nerve fibres react with four to eight times lower thresholds to stimulation by an extracellular cathode than to anodal stimulation (polarity selectivity ratio, Frijns *et al.*, 1994b). The simulation data in Fig. 5 indicate that

---

<sup>1</sup>

From comparison of their Table I and Fig. 4 with their Fig. 3 we concluded that the unit along the vertical axes in their Figs. 3, 5, and 6 should be mA rather than  $\mu\text{A}$ .

this more selective stimulation can also be achieved by applying charge-balanced asymmetric biphasic pulses. An important advantage of such charge-balanced asymmetric biphasic stimuli over monophasic pulses for neural prostheses is the fact that no net charge is injected into the tissue. This is generally considered an obligatory condition to avoid damage to the inner ear tissues (Donaldson and Donaldson, 1986; Brummer and Turner, 1977). We expect that the use of asymmetric rather than symmetric biphasic stimuli in cochlear implants will result in an increased perceptual difference between stimulating electrodes as their regions of excitation show less overlap. In other words, this strategy, which is applicable with any type of cochlear implant with longitudinal electrodes, is expected to give the patient more independent input channels. A possible limitation of this technique, e.g., when used in combination with the continuous interleaved strategy (Wilson et al., 1991), is caused by the fact that the duration of the charge-balancing second phase of an asymmetric biphasic pulse is prolonged by a factor equal to the amplitude ratio of the first and second phase. This can lead to overlap in time between current pulses on different electrode pairs with the possible consequence of broadened excitation patterns. The application of an exponentially decaying instead of a rectangular second stimulus phase (Gorman and Mortimer, 1983) might serve to overcome this problem. Future studies will have to clarify this issue.

Another aspect of the use of monophasic and asymmetric biphasic pulses that should be discussed in this context is the phenomenon of 'cathodal blocking' or 'anodal surround' (Ranck, 1975). This phenomenon occurs in the vicinity of any cathode at higher stimulus intensities: the stimulus elicits an action potential near the nerve fibre's terminal, but the stimulus itself prevents its propagation due to a strong hyperpolarisation of the more distant, modiolar part of the fibre. The model predicts that this phenomenon will have serious impact, e.g. in the case of a radial dipole with the cathode located medially, where the predicted number of excited nerve fibres even decreases with increasing stimulus intensity for stimulus strengths above 5 mA (Fig. 8<sup>b</sup>). This is in accordance with experimental findings for the amplitude of the electrically evoked compound action potential (Prijs (1980), Fig. 6). The simulation data indicate that this unwanted effect can be prevented by application of biphasic stimuli, as the polarity reversal in the second stimulus phase will eliminate the cathodal block. Since the  $Q_{10\text{ dB}}$ -values for radial dipoles do not notably depend on the stimulus polarity, symmetric biphasic pulses will suffice for this purpose. The simulation data regarding ectopic stimulation in the modiolus suggest, however, that an electrode configuration with the anode in the medial position will yield a larger dynamic range, and charge-balanced asymmetric biphasic pulses may come in useful to mimic this situation without the risk of damaging the cochlear tissues.

The simulations with auditory nerve fibres with thinner peripheral processes, which are the modelled counterparts of LSR fibres (Lieberman and Oliver, 1984; Gleich and Wilson, 1993), did - apart from a slight (circa 2 dB) increase in excitation - not reveal any significant differences with the simulations for HSR fibres, which possess thicker dendrites. This means that physiological

variations in size of the auditory nerve fibres ( Gleich and Wilson, 1993) are not expected to have significant influence on the performance of cochlear implant users. The situation with respect to the loss of peripheral dendrites following hair cell degeneration, however, is quite different: The model predicts that this will result in an increase in excitation threshold and as a consequence in a reduction of the dynamic range by approximately 10 dB. As is illustrated in Table IV, this threshold change is accompanied by a significant reduction of the spatial selectivity. An exception to these general observations is formed by electrodes close to the cell body (like site C) for which excitation occurs near the soma, even in the presence of a dendrite. Unfortunately, such electrode positions are among the less favourable ones in terms of spatial selectivity when there is no neural degeneration, and currently available pre-operative tests do not yield sufficient information regarding the number of intact auditory nerve fibres ( Estève-Fraysse et al., 1993 ).

We conclude that the rotationally symmetric, integrated neuron-field model of the implanted cochlea provides a valuable means to study the relative influence of various parameters on the spatial selectivity that can be achieved with a cochlear implant. Since the model includes active neural elements, we were able to include not only geometric factors such as electrode orientation and variations in nerve fibre morphology (including degeneration of the peripheral process) in the present study, but also the temporal waveform of the stimuli. This analysis led, amongst others, to the conclusion that the application of charge-balanced asymmetric biphasic current pulses is probably a way to realise the relatively localised excitation pattern produced by monophasic current pulses while complying with biological safety considerations. On the basis of our results, such charge-balanced asymmetric current pulses are expected to yield  $Q_{10\text{ dB}}$ -values for longitudinally directed bipolar electrode pairs that are comparable with those for radial dipoles, which means approximately a doubling of the number of non-overlapping loci of stimulation without the need to change the design of the longitudinal electrode arrays currently available. Therefore it will have to be the subject of further studies whether these stimuli indeed provide a good alternative for the - technically difficult to manufacture - radial electrode configuration that is generally considered to give the best spatial selectivity.

### **Acknowledgement**

The authors wish to express their thanks to R. Schoonhoven, PhD for his valuable advice and to prof. J.J. Grote, MD PhD for continuous support. They are also kindly obliged to the Heinsius-Houbolt Fund for their financial support.

## References

- Black, R.C. and Clark, G.M. (1980) Differential excitation of the auditory nerve. *J. Acoust. Soc. Am.* 67 (3), 868-874.
- Black, R.C., Clark, G.M. and Patrick (1981) Current distribution measurements within the human cochlea. *IEEE Trans. Biomed. Eng.* 28.
- Brebbia, C.A. and Dominguez, J. (1992) *Boundary elements - An introductory course.* Mc Graw-Hill, New York, 314 pp..
- Brummer, S.B. and Turner, M.J. (1977) Electrochemical considerations for safe electrical stimulation of the nervous system with platinum electrodes. *IEEE Trans. Biomed. Eng.* 24 (1), 59-62.
- Colombo, J. and Parkins, J.W. (1987) A model of electrical excitation of the mammalian auditory-nerve neuron. *Hear. Res.* 31, 287-312.
- Donaldson, N. de N. and Donaldson, P.E.K. (1986) When are actively balanced biphasic ('Lilly') stimulating pulses necessary in a neurological prosthesis? I Historical background; Pt resting potential; Q studies. *Med. & Biol. Eng. & Comput.* 24 (1), 41-49.
- Eddington, D.K., Dobelle, W.H., Brackman, D.E., Mladejovsky, M.G., and Parkin, J.L. (1978) Auditory prosthesis research with multiple channel intracochlear stimulation in man. *Ann. Otol. Rhinol. Laryngol.* 87, Suppl. 53, 1-39.
- Estève-Fraysse, M.J., Corvera, G., Deguine, O., Sans, A., Vincent, M., Laur, D. and Sonilhac, F. (1993) Significance of the promontory test: histological and electrical results. *Adv Otorhinolaryngol* 48, 97-102.
- Evans, E.F. (1975) Cochlear nerve and cochlear nucleus. In: W.D. Keidel and W.D. Neff (Eds), *Handbook of sensory physiology*, Vol. 5/2, Springer, Berlin, pp. 1-108.
- Favre, E. and Pelizzone, M. (1993) Channel interactions in patients using the Inneraid multichannel cochlear implant. *Hear. Res.* 66, 150-156.
- Finley, C.C., Wilson, B.S. and White, M.W. (1990) Models of neural responsiveness to electrical stimulation. In: J.M. Miller and F.A. Spelman (Eds.), *Cochlear implants: models of the electrically stimulated ear.* Springer-Verlag, New York, pp. 55-96.
- Frijns, J.H.M. and ten Kate, J.H. (1994a) A model of myelinated nerve fibres for electrical prosthesis design. *Med. Biol. Eng. Comput.* 32 (5).
- Frijns, J.H.M., Mooij, J. and ten Kate, J.H. (1994b) A quantitative approach to modelling mammalian myelinated nerve fibres for electrical prosthesis design. *IEEE Trans. Biomed. Eng.* 41 (6).
- Frijns, J.H.M. and Snoo, S.L. de. (1995) Improving the accuracy of the boundary element method by the use of second order interpolation functions. *submitted.*
- Frijns, J.H.M., Snoo, S.L. de, Schoonhoven, R. (1995) Potential distributions and neural excitation patterns in a rotationally symmetric model of the electrically stimulated cochlea. *submitted.*
- Frijns, J.H.M., Mooij, J. and Schoonhoven, R. (1995b) Have mammalian myelinated nerve fibres diameter dependent nodal properties? A model study. *submitted*
- Gantz, B.J. and Tyler, R.S. (1990) Evaluation of five different cochlear implant designs: audiologic assessment and predictors of performance. *Laryngoscope* 98, 1100-1106.
- Gleich, O. and Wilson, S. (1993) The diameters of guinea pig auditory nerve fibres: distribution and correlation with spontaneous rate. *Hear. Res.* 71, 69-79.
- Gorman, P.H. and Mortimer, J.Th. (1983) The effect of stimulus parameters on the recruitment characteristics of direct nerve stimulation. *IEEE Trans. Biomed. Eng.* 30, 407-414.

- Honert, C. van den and Stypulkowski, P.H. (1987) Single fiber mapping of spatial excitation patterns in the electrically stimulated auditory nerve. *Hear. Res.* 29, 195-206.
- Ifukube, T. and White, R.L. (1987) Current distributions produced inside and outside the cochlea from a scala tympani electrode array. *IEEE Trans. Biomed. Eng.* 34, 883-890.
- Johnsson, L.-G. (1988) Otopathological aspects of cochlear implants. *Acta Otolaryngol. (Stockh.)* 449, 65-66.
- Lieberman, M.C. and Oliver, M.E. (1984) Morphometry of Intracellularly Labeled Neurons of the Auditory-Nerve: Correlations with Functional Properties. *J. Comp. Neurol.* 223, 163-176.
- Linthicum, F.H., Jr., Fayad, J., Otto, S.R., Galey, F.R. and House, W.F. (1991) Cochlear implant histopathology. *Am. J. Otol.* 12, 245-311.
- Meijs, J., Weiers, O., Peters, M. and Oosterom, A van (1989) On the numerical accuracy of the boundary element method. *IEEE Trans. Biomed. Eng.* 36, 1038-1049.
- O'Leary, S.J., Black, R.C. and Clark, G.M. (1985) Current distributions in the cat cochlea: a modelling and electrophysiological study. *Hear. Res.* 18, 273-281.
- Oosterom, A. van (1991) Mathematical aspects of source modeling, *Acta Otolaryngol. (Stockh.) Suppl* 491, 70-79.
- Peeters, S., Offeciers, F.E., Joris, Ph. and Moeneclaey, L. (1993) The Laura cochlear implant programmed with the continuous interleaved and phase-locked continuous interleaved strategies. *Advances in Otorhinolaryngology* 48, 261-268.
- Pickles, J.O. (1992) An introduction to the physiology of hearing. Academic Press, London.
- Prijs, V.F. (1980) On peripheral auditory adaptation. II. Comparison of electrically and acoustically evoked action potentials in the guinea pig. *Acustica* 45, 35-13.
- Ranck, J.B. Jr. (1975) Which elements are excited in electrical stimulation of mammalian central nervous system: A review. *Brain Res.* 98, 417-440.
- Rattay, F. (1989) Analysis of models for extracellular fiber stimulation. *IEEE Trans. Biomed. Eng.* 36, 676-692.
- Schuknecht, H.F. (1993) *Pathology of the ear.* 2<sup>nd</sup> Ed. Philadelphia, Lea & Febiger.
- Schwarz, J.R. and Eikhof, G. (1987) Na currents and action potentials in rat myelinated nerve fibres at 20 and 37°C. *Pflügers Arch.* 409, 569-577.
- Shannon, R.V. (1983) Multichannel electrical stimulation of the auditory nerve in man. II. Channel interaction. *Hear. Res.* 12., 1-16.
- Shepherd, R.K., Hatsushika, S. and Clark, G.M. (1993) Electrical stimulation of the auditory nerve: the effect of electrode position on neural excitation. *Hear. Res.* 66, 108-120.
- Strelhoff, D. (1973) A computer simulation of the generation and distribution of cochlear potentials. *J. Acoust. Soc. Am.* 54, 620-629.
- Suesserman, M.F. (1992) Noninvasive microelectrode measurement technique for performing quantitative, in vivo measurements of inner ear tissue impedances. Ph.D. Thesis, University of Washington.
- Suesserman, M.F. and Spelman, F.A. (1993) Lumped-parameter model for in vivo cochlear stimulation. *IEEE Trans. Biomed. Eng.* 40, 237-245.
- Townsend, B., Cotter, N., Compennolle, D. van, and White, R.L. (1987) Pitch perception by cochlear implant subjects. *J. Acoust. Soc. Am.* 82 (1), 106-115.
- Townsend, B. and White, R.L. (1987) Reduction of electrical interaction in auditory prostheses. *IEEE Trans. Biomed. Eng.* 34 (11), 891-897.

- Warman, E.N., Grill, W.M. and Durand, D. (1992) Modeling the effects of electric fields on nerve fibers: determination of excitation thresholds. *IEEE Trans. Biomed. Eng.* 39, 1244-1254.
- Wilson, B.S., Finley, C.C., Lawson, D.T., Wolford, R.D., Eddington, D.K. and Rabinowitz, W.M. (1991) Better speech recognition with cochlear implants. *Nature* 352, 236-238.

# Chapter VII

---

## **A MULTI-CHANNEL SIMULTANEOUS DATA ACQUISITION AND WAVEFORM GENERATOR SYSTEM DESIGNED FOR MEDICAL APPLICATIONS**

*J.H.M. Frijns, A. van Wijngaarden and S. Peeters (1994)  
J. Med. Eng. & Techn. 18 (2), 54-60.*

## Abstract

To meet the needs of our research programmes on auditory prostheses for the totally deaf, a 15-channel data acquisition and waveform generator system with flexible triggering, pacing and linking was developed. It allows both synchronous and asynchronous operation at high speed. Each channel of the system, which is controlled by a simple personal computer, has an on-board microcontroller, a 512 kWord signal memory, a voltage input and both voltage and current outputs. The system includes a master pacer and trigger unit with elaborate hardware and software triggering options. This paper describes the system hardware and the software used to control it. Finally, some of its applications are demonstrated. The flexibility of the system makes it widely applicable in the field of biomedical engineering.

## Introduction

During the past decade many digital signal processing and waveform generators for use with a personal computer have become commercially available. Many of those devices provide for an optional multi-channel output by means of a multiplexer, which inevitably causes a diminished sampling rate per channel. For our research programmes on auditory prostheses for the totally deaf, however, we needed a multi-channel, non-multiplexed (synchronous) waveform generator with at least 5  $\mu$ s time resolution per channel and with voltage and current outputs to test new multi-polar stimulus patterns in laboratory animals. Additionally, the need was felt to be able to record simultaneously the output of all eight electrodes of the LAURA prosthesis [1] in an exact time relation to a standardized speech sample for the purpose of testing new speech processing strategies. It did not appear feasible to fulfill the speed and timing requirements with commercially available equipment, and so we decided to develop a flexible, multi-channel data acquisition and waveform generator system which allows both synchronous and asynchronous operation at high speed and which has copious memory for the storage of (speech) signals. In this paper we present the resulting system and some of its applications.

## Hardware

Figure 1 shows a functional overview of the system. It consists of up to 15 identical data acquisition and waveform generator (DAWG) cards and a pacer and master trigger unit that are connected to a bidirectional communication bus. This bus is controlled from a personal computer through a special-purpose PC controller card. To reduce power consumption all hardware was developed in CMOS technology.

### *The PC controller card and communication bus*

Any IBM<sup>®</sup> XT-compatible personal computer can be used to control the DAWG system. For this purpose a dedicated controller card was developed, which uses the prototype card address range in the PC (300H - 30FH) for I/O. The

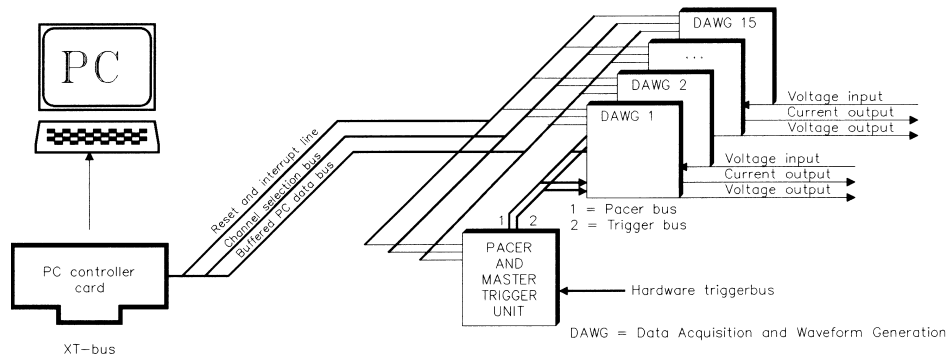


Figure 1. An overview of the data acquisition and waveform generator (DAWG) system which is controlled from a personal computer through a dedicated PC controller card. The system can contain up to 15 identical DAWG cards and a pacer and master trigger unit.

output of this controller card is the so-called communication bus, which consists of a 16-bit channel selection bus, an 8-bit buffered bidirectional PC data bus and a reset and interrupt line. This interrupt line generates an interrupt request on the PC (IRQ2, 3 or 4 depending on a jumper setting) when a DAWG card sends data or an error message to the host computer. The channel selection bus contains a single line for each card, allowing simultaneous communication of the PC with multiple DAWG cards, for example, to speed up communication when transferring the same waveform to different cards or to start conversion in multiple cards with a single soft trigger command. Similarly, a selected number of cards can be reset with a single command. If all cards must be reset simultaneously, the reset line is used.

*Data acquisition and waveform generator cards*

Each DAWG card allows one to generate a pre-programmed waveform while simultaneously recording any input signal. Both signal generation and recording are performed with a 12-bit resolution. The functional layout of the card is shown in figure 2. Its core is the so-called signal memory (512 kWord static RAM (random access memory)), which is accessed through a 16-bit bidirectional data bus and a 20-bit address counter. This address counter is under control of the clock select unit and can be programmed to count up or down, in order to enable sequential access to the signal memory during signal processing. Additionally, the address counter can be programmed to give cyclic access to a given address range. The clock select unit in turn allows selection of either an external pacer clock (e.g. from the pacer and master trigger unit) or signals from the microcontroller unit, which is described below. Depending upon the settings of this microcontroller unit there are three

---

\* An interrupt is a signal indicating that the PC should suspend its current task to serve a designated activity, e.g., process an error message.

conversion options available: these are analogue to digital conversion (ADC), digital to analogue conversion (DAC), and so-called alternating conversion, which means that the conversion mode switches between ADC and DAC after every sample. Applications of the alternating conversion mode include the programmable delay line function and impulse response recording.

To ensure high-speed operation data acquisition or waveform generation is initiated by a pacer clock without intervention of the microcontroller. As a consequence the maximum sampling rates are limited by the DAC (Analog Devices AD 667) and the ADC (Analog Devices AD 7870) to 300 kHz (full-scale sweep) and 100 kHz respectively. The signal-to-noise ratio is 72 dB for the voltage output and 68 dB for the voltage input. With future replacement of these convertors by faster - and, if desired, up to 16-bit - ones, sampling rates > 2 MHz are possible without the need to change other hardware components. In fact, with the existing DA convertor, smooth signals (e.g. sinusoids) with sampling rates of 1.3 MHz have been generated. For the purpose of patient security in future applications the DAWG cards will have an optional isolation area which includes the input amplifier and the output voltage and current sources. The current source has three software selectable output ranges (maximum positive and negative output current 100  $\mu$ A, 1 mA and 10 mA, respectively); the settling time constant for a full range current step is 6  $\mu$ s.

The 16-bit HPC 46003-based microcontroller unit of each DAWG card consists of the processor and its associated EPROM (erasable programmable read-only memory) and RAM (each 32 kB) and a timer module. This unit has two main tasks. The first one is to control the settings of the actual data acquisition and/or waveform generation process. An example of such a setting is done via the clock select unit to allow the selection of either an external pacer clock or a pacer clock that is derived (by division) from the 16 MHz crystal used to drive the HPC 46003 CPU. Alternatively, the processor itself can take control over the address counter of the signal memory by means of its read/write signals. Other settings performed by the microcontroller include the definition of the start and end address in the signal memory that will be used and -in the case of waveform generation-the number of cycles that will be produced. The microcontroller unit is also responsible for the pre- and post-triggering facilities available, and it generates variably delayed output triggers. The second main task of the microcontroller unit is the transfer of data between the personal computer and signal memory. The basic functions are programmed in the EPROM (see below). Downloading of new functions into the RAM (e.g., signal averaging routines) is one of these basic functions.

#### *Pacer and master trigger unit*

As shown in figure 3 the interface structure of the pacer and master trigger unit is identical to that in the DAWG cards. Again the microcontroller unit is primarily used to control the settings of the device. The pacer unit consists of 16 independent synchronous 32-bit modulo N counters driven by a single 33 MHz

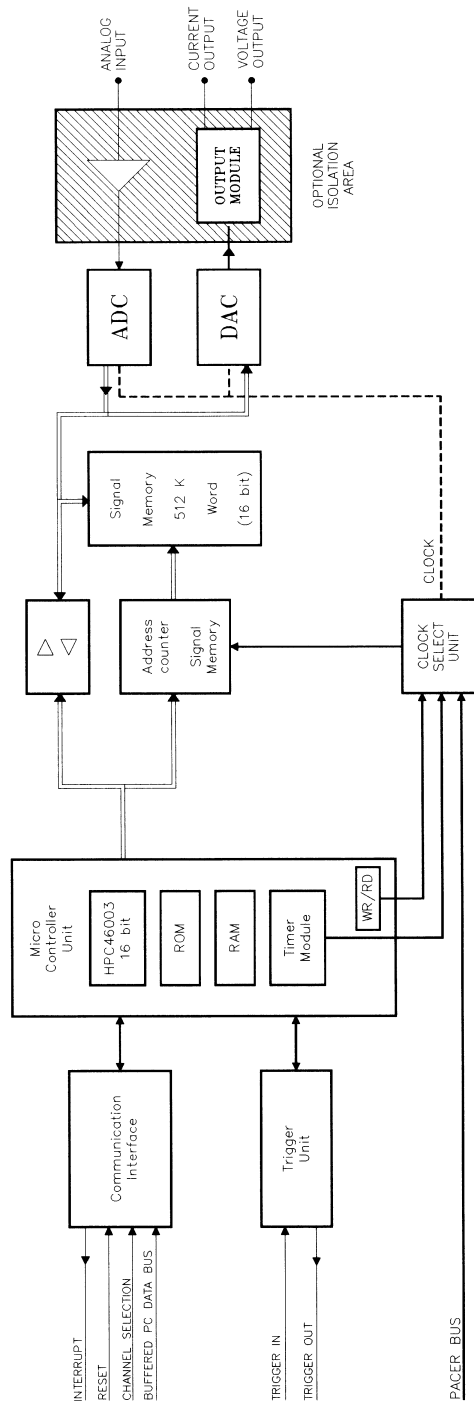


Figure 2. A functional overview of a single DAWG card. It is controlled by the PC through the communication interface and is connected to the master pacer and trigger unit by means of the pacer and trigger bus.

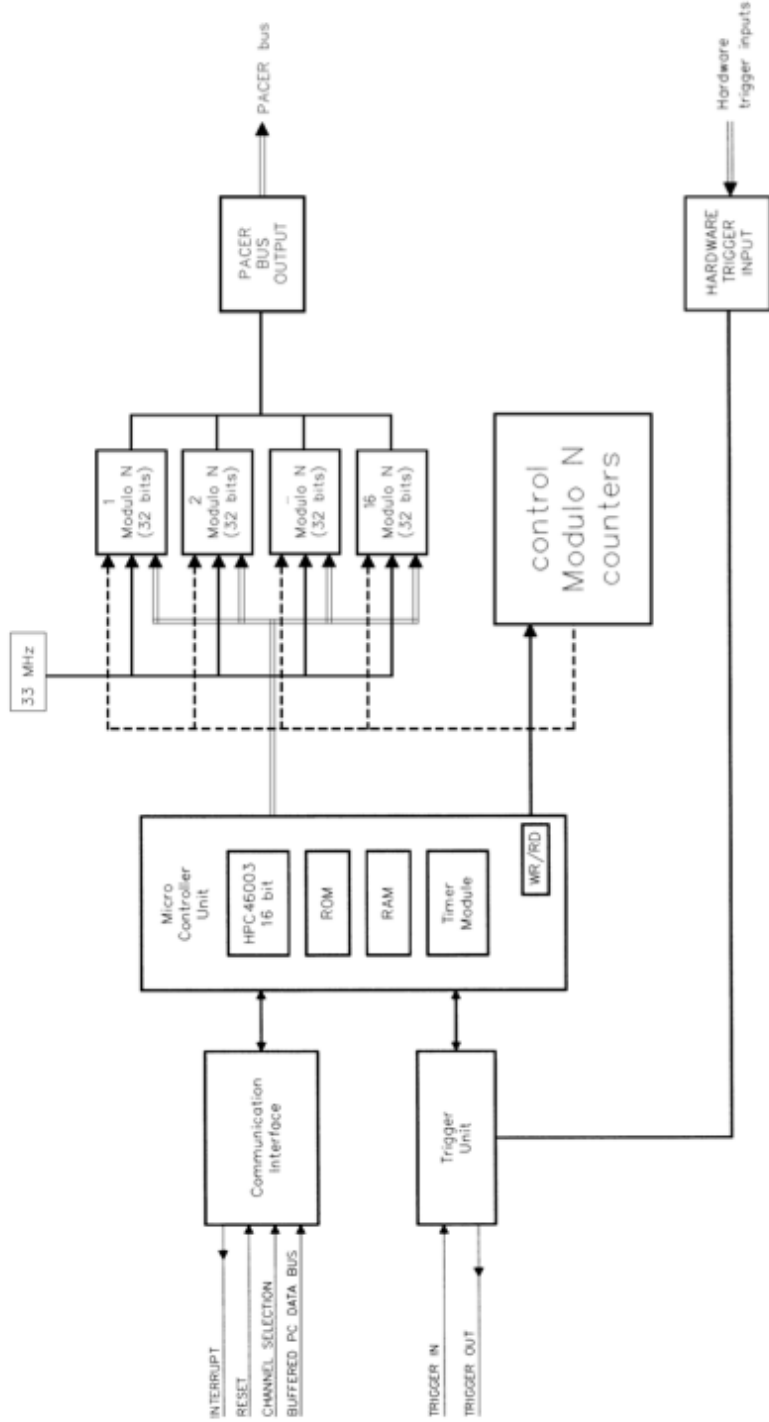


Figure 3. The pacer and master trigger unit, which generates 16 pacer clocks, independently derived from a single 33 MHz crystal by means of 32-bit synchronous modulo N counters. The trigger unit controls the trigger bus which is connected with the DAWG cards.

crystal. The division factor N is programmed for each counter separately and allows for pulse rates below 1 pulse/min, with a frequency resolution < 1% for rates < 330 kHz. This makes the unit applicable for both sweep triggering and the pacing of the conversion process in the DAWG cards. The high frequency resolution obtained is useful in, for example, eliminating the need to recompute the signal when performing a frequency sweep with a sinusoid. The various pacer clock signals are distributed to the DAWG card through the pacer bus (figure 1).

The device has 16 hardware trigger inputs that can be coupled to the trigger bus via the master trigger unit. In turn, this unit can also respond to soft trigger commands from the microcontroller unit or to (delayed) output triggers from DAWG cards. As a consequence the triggering facilities of the device are very flexible, also because the same trigger that is used to start the conversion process in one or multiple DAWG cards can be used to start one or more pacer clocks simultaneously. This ensures an exact synchrony between, for example, sensory stimulation and the recording of the physiological response. Since these pacer clocks are derived from a single source, the conversion processes in the individual DAWG cards have a constant time relation, even if they occur at different clock rates. If, on the other hand, truly asynchronous operation is required, one can make use of the CPU clock on the DAWG card (see above).

## **Software**

The 15 channel data acquisition and waveform generator system is controlled by the on-board software for the microcontroller in each card and a software driver in the personal computer.

### *On-board software in ROM*

The HPC 46003 microcontroller of the individual cards is used in the 16-bit mode. The software was written in assembly language and stored in the 32 kB EPROM available in each card.

On power-up a reset procedure is performed which initializes the system. Then the processor enters an infinite loop in which it monitors the state of four switches on the front panel (figure 4). These switches can be used to initiate test procedures such as testing the signal memory.

Commands issued from the personal computer give rise to a non-maskable interrupt, which forces the microcontroller to leave the infinite loop. After completion of the command it will return to this loop again and wait for another command. Each command can have 0 - 3 16-bit parameters which are sent to the microcontroller as consecutive data words. Two bits of the eight-bit command are used to encode the number of parameters, and another bit is used to tell whether a ROM or RAM routine should be executed. The remaining five bits serve to encode the command number, allowing for 32 pre-programmed ROM routines. The possibility of installing up to 32 additional command routines in the RAM further enhances the flexibility of the system. Table 1 gives a listing of the most important ROM commands. A detailed description of all commands is beyond the scope of this paper. Suffices it to state that most ROM commands cause the microcontroller to perform a basic

operation, such as loading the address counter of the signal memory (see figure 4) or setting the rate of the internal pacer clock, although some commands initiate a more complex process such as configuring the card as a digital delay line or as a storage oscilloscope. A special command is the so-called bit-command, which has one parameter. Each of the 16 bits of the parameter signals an action that must be performed. The bits are evaluated from low to high order and it is, for example, possible to enable the external pacer clock and the soft trigger and give the soft trigger impulse in a single action.

Some commands cause the microcontroller of a DAWG card to send data back to the personal computer. An interrupt request will signal the PC that the data word is available. In order to increase the speed of communication this interrupt is suppressed during the transfer of large blocks of data from a DAWG card to the PC. Similarly, the microcontroller will produce an interrupt when it sends an error code to the PC.

#### *Software for the personal computer*

It is, of course, possible to issue the basic commands of the microcontrollers as I/O instructions from a high-level programming language. For reasons of speed and memory usage we have written an assembly-language driver that performs all handshaking procedures when using the basic commands. Where it is feasible the driver allows one to send commands and/or data to multiple cards simultaneously. It also contains an interrupt handler to deal with error messages and a number of standard routines that combine several basic commands into a single action.

One such routine performs the initialization of the system. It detects which DAWG card numbers are physically present, waits until they have all finished their reset procedure and then tests the communication. It also installs the interrupt routine if this has not been done yet. An often-used routine allows the user to send a signal from a file on disk to a specified part of the signal memory of selected DAWG cards, and also perform the settings necessary to clock the signal out through the DA-converter. Other routines allow the transfer of additional RAM routines to selected microcontrollers or the transfer of data from the signal memory to a file on disk.

The driver is an executable file that is not linked into the application software but loaded below it in memory by means of a so-called application loader, which also makes the memory address of the driver software available to the application software. After completion of the application it removes both the application and the driver from memory. The driver can be used with application programs written in any high-level programming language provided that the correct assembly language interface is used. At present, such an interface is available for ASYST<sup>®</sup> (version 2.00 or higher) and Turbo Pascal<sup>®</sup> (version 4.0 or higher).

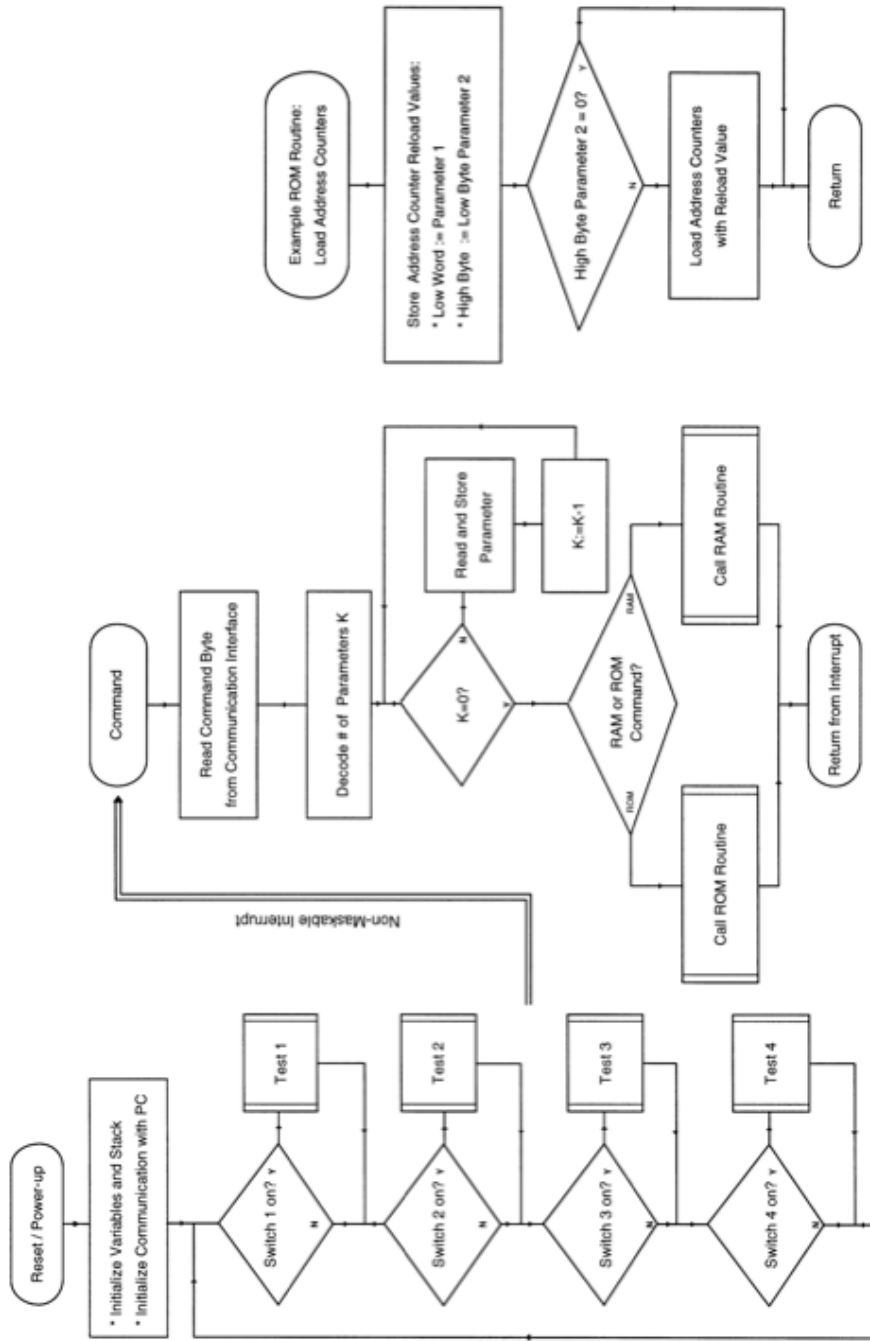


Figure 4. Flowcharts of core parts of the software built into the ROM in each DAWG card. The software used to load the address counter is included as an example of a ROM command routine.

Table 1 Brief description of some important ROM commands built into each DAWG card.

<b>Command name</b>	<b>No. of parameters</b>	<b>Brief description</b>
ModeLatch	1	Change the contents of the registers that determine the mode of conversion (ADC, DAC, or alternating) and the counting of the address counter
Receive	3	Receive a number of data words from the PC and store these into the signal memory
Send	3	Read data from the signal memory and send these data to the PC
AddressCounter	2	Set the reload value of the address counter and optionally load this value into the counter immediately
PrePostTrig	3	Activate the pre-triggering or post-triggering function
DelayTime	1	Change the delay between input trigger and output trigger
Fclock	1	Set the frequency of the on-board pacer clock
Ncycles	2	Set the number of waveform cycles to be produced
Nsamples	2	Set the number of samples in a cycle
loutMax	1	Select the current output range
DelayLine	3	Set the DAWG card to function as a delay line for analogue signals
StorScope	3	Set the DAWG card to function as a storage oscilloscope
BitCommand	1	Perform an action depending on each bit set in the parameter word (see text)

## **Applications**

The development of the multi-channel data-acquisition and waveform generator system was necessary for the cochlear implant projects at both universities, where it is a critical research tool in the development of new speech-encoding strategies since it offers the possibility of simultaneous and synchronized recording and stimulation. The ultimate goal of a cochlear implant is to restore speech understanding in deaf persons by stimulating nerve fibres of the auditory nerve by means of injected current pulses. Such an implant usually consists of an external part and an internal one. Both communicate with each other through a RF (radio frequency) link for both data transport and power supply. The external part is called the speech processor. It is responsible for the transformation of the speech signal into meaningful pulse sequences on different electrodes in the internal part. These pulse sequences are designed to allow electrical stimulation of different discrete groups of auditory nerve fibres, in order to produce as many different sound percepts as possible. In fact, one of the important research topics is to find out which is the best way to encode speech into electrical pulse patterns stimulating the fibres of the auditory nerve.

This research is focussed on the time structure of the stimulating wave form patterns, as well as on the frequency domain analysis of the speech signal. One of the applications of the DAWG system is to test whether a new speech-encoding strategy is correctly implemented in the speech processor. To do this, standard sentences are loaded in one of the DAWG cards. The output of this card is connected to the speech processor input, while the outputs of the electrode contacts of the implant are connected to the input ports of other DAWG cards. While the first DAWG board generates the standard sentences, the latter ones simultaneously and synchronously capture the pulse patterns that would be delivered to the multichannel microelectrode of the cochlear implant. Afterwards the storage scope function allows one to display the stored responses on a standard oscilloscope, while the window and zooming functions allow detailed analysis of the multichannel responses. Once an interesting part of the signal has been isolated the windowed signal can be sent to a file or printed on a laser printer for further analysis. In addition, the stored data of the output channels can be manipulated in the personal computer. The adapted pulse patterns can then be sent back to the DAWG to stimulate a patient or an experimental animal with an implanted electrode, to test the modified speech-processing strategy.

Figures 5 and 6 show examples of such an analysis of two different, though related, processing techniques, the so-called continuous interleaved (CIS) and phase-locked continuous interleaved strategy respectively. The input signal (the word /so/) is displayed on top of the time traces of the eight output channel responses. For both algorithms the speech signal is sent through eight bandpass filters to generate biphasic output current pulses with amplitudes that follow the envelope of the bandpass filter output signals. These current pulses are used to stimulate the electrodes in a sequential manner. In the case of the phase-locked CIS (figure 6) the biphasic pulses for channels 1 and 2 are generated with a fixed phase relation to the bandpass filter output. These

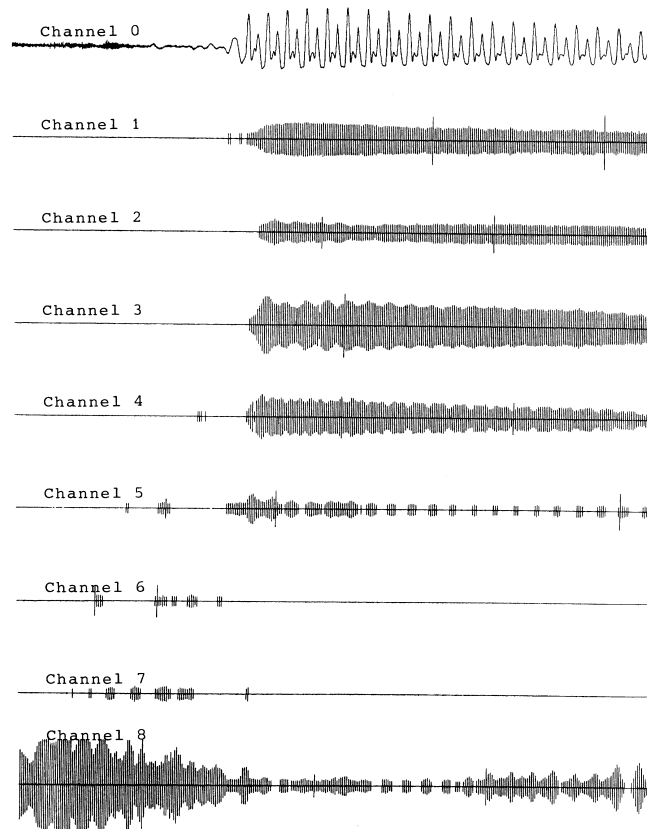


Figure 5. Nine channels of the DAWG system used to test the continuous interleaved strategy for speech processing in the LAURA cochlear implant. Channel 0 is used to generate the word /so/ at the input of the LAURA speech processor. Channels 1 - 8 are used to record the speech processor output signals simultaneously and synchronously.

channels correspond with low-frequency information, where in the physiological situation phase locking of the neural response with the input signal is observed. With the latter algorithm significantly better open set speech recognition was achieved than with conventional methods [2].

In the ENT Department of the Leiden University Hospital the DAWG system is used as an electro-stimulator in cochlear implants research and for the generation of the stimuli while simultaneously recording the patient's and laboratory animal's responses in auditory brainstem response (ABR) measurement [3] and electrocochleography [4,5]. Another audiological application is the measurement of distortion product otoacoustic emissions [6], which requires the generation of two sinusoids with varying frequency, while sampling the sounds coming from the ear. Several other applications of the device are conceivable, e.g. in neurophysiology, to accomplish spike-triggered averaging in single-fibre EMG (electromyography), [7], or to perform brain electrical activity mapping (BEAM) [8]. Since the device is equipped with

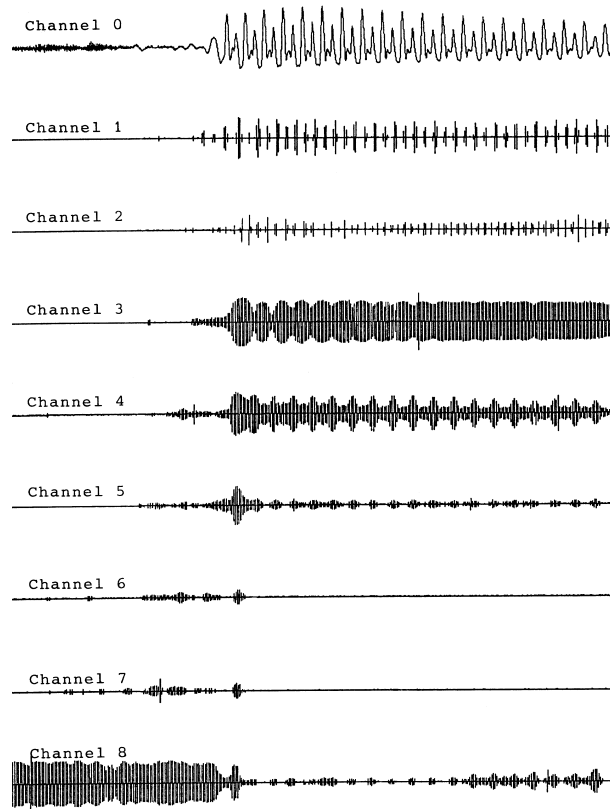


Figure 6. The same as figure 5, now for the phase-locked continuous interleaved strategy, in which channels 1 and 2 are phase-locked to the input signal.

current outputs it can also be used as an electrostimulator in order to test new modes of electrical nerve stimulation, not only in cochlear implants but also in other applications of functional electrical stimulation (FES) [9].

To conclude, it can be stated that the DAWG system presented here greatly enhances the flexibility and speed in the evaluation of different speech processing strategies for cochlear implants. Its applicability however, is not limited to this area and the system can be used anywhere in the field of biomedical engineering.

### Acknowledgement

The authors wish to express their thanks to the Heinsius-Houbolt fund for the financial support of this work.

## References

- [1] PEETERS, S., MARQUET, J., OFFECIERS, F. E., BOSIERS, W., KINSBERGEN, J., and VAN DURME, M. (1989) Cochlear implants: the Laura prosthesis. *Journal of Medical Engineering and Technology*, **13**, 76-80.
- [2] PEETERS, S., OFFECIERS, F. E., JORIS, PH. AND MOENECLAAY, L. (1993) The Laura cochlear implant programmed with the continuous interleaved phase-locked continuous interleaved strategies. In *Cochlear Implants: New Perspectives*, edited by B. Fraysse and O. Deguine, (Karger, Basel), and *Advances in Otorhinolaryngology*, **48**, 261-268.
- [3] EGGERMONT, J. J. AND SCHMIDT, P. H. (1990) The auditory brainstem response. In *Evoked Potential Manual*, edited by E. J. Colon and S. L. Visser (Kluwer, Dordrecht), pp. 41-77.
- [4] EGGERMONT, J. J., ODENTHAL, D. W., SCHMIDT, P. H. and SPOOR, A. (1974) Electrocochleography-basic principles and clinical application. *Acta Otolaryngologica Scandinavica*, **316** (Suppl.), 1-84.
- [5] RUTTEN, W. L. C. and KUPER, P. (1982) AP unmasking and AP tuning in normal and pathological human ears. *Hearing Research*, **8**, 157-178.
- [6] PROBST, R. (1991) A review of otoacoustic emissions. *Journal of the Acoustic Society of America*, **89** (5), 2027-2067.
- [7] STÅLBERG, E. V. (1986) Single fiber EMG, macro EMG and scanning EMG. New ways of looking at the motor unit. *CRC Critical Reviews in Clinical Neurobiology*, **2**, 125-167.
- [8] DUFFY, F. H. (1982) Topographic display of evoked potentials: clinical applications of brain electrical activity mapping (BEAM). In *Evoked Potentials*, edited by I. B. Wollner (New York, *Annals of the New York Academy of Sciences*), pp. 183-196.
- [9] MEIER, J. H., RUTTEN, W. L. C., ZOUTMAN, A. E., BOOM, H. B. K. and BERGVELD, P. (1992) Simulation of multipolar fibre selective neural stimulation using intrafascicular electrodes. *IEEE Transactions in Biomedical Engineering*, **39**, 122-134.

# *Chapter VIII*

---

## **GENERAL DISCUSSION**

In this chapter, the results of the individual studies described in this thesis will be discussed and placed in a broader perspective. The model of the electrically stimulated guinea pig cochlea that is presented in this thesis consist of two sub-models. The first sub-model is a non-linear cable model of auditory nerve fibres. In chapters II, III and IV it is explained how this model is constructed from voltage-clamp data in large motor fibres. In fact, the resulting auditory nerve fibre model is a special case of a more generally applicable neural model. It is shown that this model gives a good description of many relevant aspects of the behaviour of mammalian myelinated nerve fibres of all diameters, a.o. the shape and duration of the action potential, the spike conduction velocity and the frequency following behaviour.

The auditory nerve fibre model receives its input from the other sub-model that calculates the potential distribution in the cochlea due to the stimulating current sources. A rotationally symmetric model representation of the cochlea is used, that was created by rotating a cross-section from the base of the second turn of a guinea pig cochlea around the mid-modiolar axis. In this volume conductor the potential distribution is computed at sites representing the locations of the nodes of Ranvier of auditory nerve fibres from three successive cochlear turns. The integrated model is applicable to predict the number, distribution and firing patterns of excited auditory nerve fibres due various intra- and extracochlear electrode configurations and stimulus waveforms. One of the model predictions is that the excitation profile of the auditory nerve due to biphasic pulses on longitudinally directed bipolar intracochlear electrodes depends on the inter-electrode spacing and the exact location of the electrodes in the scala tympani. This prediction was found to be in good agreement with experimental EABR data in the cat (chapter V). In chapter VI the model is applied to investigate the influence of temporal stimulus parameters and electrode configurations on the spatial selectivity that is attainable with cochlear implants. An important conclusion in this chapter is that the use of charge-balanced asymmetric rather than symmetric biphasic current pulses approximately doubles the number of independent channels that can be applied in current cochlear implant designs, like a configuration with radial electrode pairs would also do.

This discussion will consist of three parts, the first considering the computational modelling of mammalian myelinated nerve fibres for functional electrical stimulation. The second part will discuss the implementation of the Boundary Element Method we used to solve the volume conduction problem in the cochlea, while in the third part some suggestions for further research on the basis of this study will be formulated.

## **Modelling mammalian myelinated nerve fibres**

Chapters II - IV of this thesis deal with the development of a cable model of mammalian myelinated nerve fibres with multiple non-linear nodes. It is shown, how models based on either amphibian (MSENN) or mammalian (SEF) voltage-clamp data can give an adequate description of many aspects of the behaviour of mammalian myelinated nerve fibres that are relevant for the design of functional electrical stimulation devices. To our knowledge, such voltage-clamp data are only available for neural elements with diameters above 10  $\mu\text{m}$  and therefore there is no unequivocal explanation for the fact that the duration of action potentials increases with decreasing fibre diameter (Paintal, 1966). As this is associated with an increased duration of the refractory period and, as a consequence, lower maximum steady-state firing rates (Paintal, 1978), this phenomenon is important in the light of modelling nerve fibres for electrical prosthesis design. In this thesis it is shown how Paintal's data on mammalian myelinated fibres can be matched by the SEF model on the basis of an adapted version of a hypothesis Jack (1975) formulated for amphibian unmyelinated nerve fibres. This makes the generalised SEF model not only applicable for simulating the responses of auditory nerve fibres as it is done in this thesis, but also for studying the recruitment characteristics of extraneural and intrafascicular electrodes used in the field of functional electrical stimulation (Veltink et al., 1988; Rijkhoff et al., 1994). Traditionally, researchers in this field make use of neural models that - like the SEF model - treat the internodal myelin as a perfect insulator. Rubinstein (1991) argued from analysis of a passive cable model that this assumption, which was first introduced by McNeal (1976), will lead to an underestimation of the strength/duration time constant. Simulations with a version the SEF model that incorporated a physiologically based internodal time constant, revealed however, that this effect is limited. On the other hand, the introduction of an internodal time constant has serious impact on both the spike shape and spike conduction properties (see chapter III). This conclusion also holds for more sophisticated computational models that take into account many anatomical and physiological details, including active ion channels under the myelin sheath (Halter and Clark, 1991). To explain this discrepancy and other phenomena regarding the initiation and propagation of action potentials in mammalian myelinated nerve fibres that are not yet fully understood (Rubinstein, 1991) further experimental effort is needed. To test the hypothesis formulated in chapter IV of this thesis, it would be very interesting if voltage-clamp measurements in thinner nerve fibres would be performed.

Several other extensions of the generalised SEF model are conceivable, e.g. the introduction of stochastic parameters to simulate membrane noise (Ball and Rice, 1992) or the introduction of slow-gated potassium channels (Halter and Clark, 1991) in the nodal membrane. The latter extension may be necessary if prolonged changes in the excitability of the auditory nerve after electrostimulation (Kilian, 1994) are to be described by the model.

## **The boundary element method with second order interpolation functions**

For the computation of the potential field in the cochlea due to the stimulating electrodes the Boundary Element Method (BEM) was used in chapters V en VI. As discussed there, a major advantage of the BEM over the finite element method as applied by Finley and Wilson (1990) is the relative ease of mesh generation, as this involves only the boundaries between media of different conductivity (Brebbia and Dominguez, 1992). Quadratic interpolation functions were used both to define the curved mesh elements and for interpolating the potential on these elements. This was done to ensure maximum accuracy with a minimum number of mesh points, especially with respect to the second order derivative of the potential to the place, as this is closely related to the excitation of myelinated nerve fibres (activating function; Rattay, 1989). Calculations on cylindrical test configurations for which an analytical solution could be derived (Gootzen et al., 1989) showed that this method is indeed superior in this respect to methods that use constant potentials on plain triangles (Meijs et al., 1989) or linear interpolation on plain triangles (De Munck, 1992). We have also tested the method on the problem of four concentric spheres, which is a commonly used, simplified model of the head in EEG studies. For this problem an analytic solution for the potential on the outer surface due to a dipole source in the inner sphere is available (Cuffin and Cohen, 1979). Whereas previous implementations of the BEM tended to predict potentials that are systematically too high by a factor 3 or more (Meijs et al., 1989), we found the method to be superior again, as it yields - when applied to the same number of mesh points - potentials that do not deviate systematically from the analytic solution by more than a few percent (Frijns et al., 1995).

Whereas the BEM as used in this thesis encompasses solely volumes with an isotropic conductivity, it is possible to expand its use to situations with anisotropic media by means of a co-ordinate transformation (Van Der Weiden and De Hoop, 1989; Zhou, 1994). This results in an extra equation with an extra unknown variable for each mesh point on the boundary of an anisotropic medium, for not only the potential on this boundary but also the current flow through this boundary enters the set of equations defining the BEM formulation of the problem. We have implemented and tested this extension in combination with the use of second order interpolation functions on the above-mentioned configuration with three co-axial cylinders. From comparison with the analytic solution we arrived again at the conclusion that the use of second order interpolation functions reduces the computational error significantly. This result is not only applicable to model the anisotropy that is present in the modiolus of the cochlea, as suggested in chapter V, but also in other fields of functional electrical stimulation where a limited number of anisotropy axes is present, e.g. in epidural spinal cord stimulation (Struijk et al., 1992).

## **Suggestions for further research**

In the modelling work presented here several simplifying assumptions were made. One of the most evident simplifications is the use of a rotationally

symmetric cochlea model rather than a full three-dimensional spiral. Although this model enables us to study a wide variety of patient and device related issues as demonstrated in chapter VI, simultaneous stimulation of electrodes located in or over different cochlear turns cannot be addressed adequately. The generation of a full spiralling mesh or, which is less difficult to accomplish, the use of multiple rotationally symmetric cochlear turns on top of one another, would enhance the model in this respect.

Another simplification, that will certainly have its influence on the model predictions is the use of point sources instead of macro-electrodes, as was illustrated previously in a two-dimensional model (Finley et al., 1987). Future versions of the model will therefore have to include large surface area electrodes, while also the insulator that usually serves as the electrode carrier will have to be incorporated in the model.

A quasi-static approach was used to solve the volume conduction problem. In this approximation the fields and potentials at any given instant in time are determined by the properties of the sources at that same instant only. This means that the electrical conductivity of all cochlear tissues is considered to be frequency independent (Van Oosterom, 1991). As a consequence, the capacitive influence of e.g., the thin membranes surrounding the scala media is neglected. Spelman et al. (1982) showed that this assumption holds up to approximately 12 kHz, while the signals typically applied in cochlear implants contain components close to this frequency. Therefore, a future extension of the model that allows for complex impedances will probably give a better description of the *in vivo* situation. The price that will have to be paid for this refinement is a significant increase in computational effort, especially when computing the neural responses to various temporal waveforms, since the transfer function for each electrode to each individual node of Ranvier will be frequency dependent in a different way.

The proof of the pudding is in the eating. In this context this means that the model predictions should be verified experimentally. These experiments are currently going on in our laboratory, using the guinea pig as the experimental animal. An important topic of interest in these experiments, both from the viewpoint of modelling and from its clinical interest, is to test the model's prediction that the number of independent channels in a cochlear implant with longitudinal electrodes can be doubled by the application of asymmetric biphasic pulses. Such experiments should also be performed in patients implanted with a cochlear implant, using both electrophysiological (EABR) and psychophysical methods.

The latter experiments are essential, for, even if the model's predictions of neural excitation in the guinea pig would be perfect, there is still an important question to be answered: To what extent can simulation and experimental data obtained from a (hearing or deafened) laboratory animal be extrapolated to the situation in deaf patients? Of course there is no general answer to this question. Pfingst (1988) addressed this question before. He concluded that animal models, at least nonhuman primates, probably provide a close match to humans, although neurophysiological studies invariably indicate higher thresholds to electrical stimulation than psychophysical ones. A few additional

remarks, specific to our situation, can be made. First, there are gross anatomic differences between the guinea pig and primates. The dimensions of the guinea pig inner, middle and outer ear are much smaller than the human one, and the human cochlea is deeply embedded in the petrous bone instead of projecting into an air containing bulla. Moreover, there is electronmicroscopic evidence that approximately 2 percent or less of human spiral ganglion cell bodies is myelinated, while this is the case for over 90 percent of such cell in other species, including guinea pigs and monkeys (Arnold,1987). Apart from this, there exist several other differences among species in the organ of Corti and the cochlear innervation pattern (Nadol, 1988). These and possibly other unknown differences will probably have their impact on the clinical outcome of stimulating the auditory nerve by cochlear implants. Computational models that take into account the known differences may help to understand the differences encountered between animal experiments and clinical results.

Then, as anywhere in (bio-)physics, models like the one presented in this thesis will permit specification of more rigorous experimental questions, organised within a theoretical framework, and provide a plan which will guide the development of knowledge and technology in the field.

## References

- Arnold, W. (1987) Myelination of the human spiral ganglion. *Acta Otolaryngol (Stockh) Suppl.* **436**, 76-84.
- Ball, F.G. and Rice, J.A. (1992) Stochastic models for ion channels: Introduction and bibliography. *Math Biosc* **112**, 189-206.
- Brebbia, C.A. and Dominguez, J. (1992) Boundary elements - An introductory course, Mc Graw-Hill, New York, 314 pp.
- Cuffin, B.N. and Cohen, D. (1979) Comparison of the magnetoencephalogram and the electroencephalogram. *Electroencephalogr Clin Neurophysiol* **47**, 132-146.
- Finley, C.C., Wilson, B.S. and White, M.W. (1987) A finite element model of bipolar field patterns in the electrically stimulated cochlea - A two-dimensional approximation. *Proc Ninth Ann Conf IEEE EMBS* **4**, 1901-1903.
- Finley, C.C., Wilson, B.S. and White, M.W. (1990) Models of Neural Responsiveness to Electrical Stimulation. In: J.M. Miller and F.A. Spelman (Eds.) *Cochlear Implants: Models of the Electrically Stimulated Ear*. Springer-Verlag, New York, pp 55-96.
- Frijns, J.H.M., Snoo, S.L. de, and Schoonhoven, R. (1995) Improving the accuracy of the boundary element method by the use of second order interpolation functions. *submitted*.
- Gootzen, T.H.J.M., Stegeman, D.F. and Heringa, A. (1989) On the numerical problems in analytical calculations of extracellular fields in bounded volume conductors. *J Appl Phys* **66**, 4504-4508.
- Halter, J.A. and Clark, J.W, Jr. (1991) A distributed-parameter model of the myelinated nerve fibre. *J Theor Biol* **148**, 345-382.
- Jack, J.J.B. (1975) Physiology of peripheral nerve fibres in relation to their size. *Br J Anaesth* **47**; 173-182.
- Kilian, M.J.P. (1994) Excitability of the electrically stimulated auditory nerve. Ph.D. Thesis, Utrecht University.
- McNeal, D.R. (1976) Analysis of a model for excitation of myelinated nerve. *IEEE Trans Biomed Eng* **23**, 329-337.
- Meijs, J., Weiers, O., Peters, M. and Oosterom, A van (1989) On the numerical accuracy of the boundary element method. *IEEE Trans Biomed Eng* **36**, 1038-1049.
- Munck, J.C. de (1992) A linear discretization of the volume conductor boundary integral equation using analytically integrated elements. *IEEE Trans Biomed Eng* **39**, 986-990.
- Nadol, J.B. Jr. (1988) Comparative anatomy of the cochlea and auditory nerve in mammals. *Hear Res* **34**, 253-266.
- Oosterom, A. van (1991) Mathematical aspects of source modeling. *Acta Otolaryngol (Stockh) Suppl* **491**, 70-79.
- Paintal, A.S. (1966) The influence of diameter of medullated nerve fibers of cat on the rising and falling phases of the spike and its recovery. *J Physiol (London)* **184**, 791-811.
- Paintal, A.S. (1978) Conduction properties of normal peripheral mammalian axons. In: S.G. Waxman (Ed.) *Physiology and pathobiology of axons*. Raven Press, New York, 131-144.
- Pfingst, B.E. (1988) Comparisons of psychophysical and neurophysiological studies of cochlear implants. *Hear Res* **34**, 243-252.
- Rattay, F. (1989) Analysis of Models for Extracellular Fiber Stimulation. *IEEE Trans Biomed Eng* **36**, 676-692.

- Rijkhoff, N.J.M., Holsheimer, J., Koldewijn, E.L., Struijk, J.J., Kerrebroeck, P.E.V. van, Debruyne, F.M.J. and Wijkstra, H. (1994) Selective stimulation of sacral nerve roots for bladder control: A study by computer modeling. *IEEE Trans Biomed Eng* **41**, 413-424.
- Rubinstein, J.T. (1991) Analytical theory for extracellular electrical stimulation of nerve with focal electrodes: II. Passive myelinated axon. *Biophys J* **60**, 538-555.
- Spelman, F.A., Clopton, B.M. and Pfingst, B.E. (1982) Tissue impedance and current flow in the implanted ear. Implications for the cochlear prosthesis. *Ann Otol Rhinol Laryngol Suppl.* 98, **91**, 3-8.
- Struijk, J.J., Holsheimer, J., Heide, G.G. van der and Boom, H.B.K. (1992) Recruitment of dorsal column fibers in spinal cord stimulation: Influence of collateral branching. *IEEE Trans Biomed Eng* **39**, 903-912.
- Veltink, P.H., Alsté, J.A. van and Boom, H.B.K. (1988) Influences of stimulation conditions on recruitment of myelinated nerve fibres: A model study. *IEEE Trans Biomed Eng* **35**, 917-924.
- Weiden, R.M. van der, and Hoop, A.T. de (1989) Boundary integral equations for the computational modeling of three-dimensional groundwater flow problems. *Computational Mechanics* **4**, 283-291.
- Zhou, H. (1994) Anisotropic volume conduction in biological media, Ph.D. Thesis, University of Nijmegen, 94 pp..

# *Summary*

---

**COCHLEAR IMPLANTS  
A MODELLING APPROACH**

Cochlear implants are electronic devices intended to restore the sense of hearing in people with profound sensorineural hearing loss. They work by electrically stimulating the spiral ganglion cells that are still present in the deaf inner ear. Despite many promising results with patients that gained open-set speech understanding without the help of lip-reading, the clinical outcome in an individual patient is hardly to predict. It seems to depend on the complex interplay of various patient and device related factors that are not yet fully understood. The work presented in this thesis aims at getting a better understanding of the fundamental processes that are involved in the process of electrically stimulating the inner ear. It is part of the Leiden University cochlear implant research program that is outlined in **chapter i** of this thesis.

In that chapter a short review of relevant topics regarding cochlear implants is given, using a scheme that classifies the different cochlear implant designs on the basis of the number and location of the stimulating electrodes. It is explained that there exist some fundamentally different ways to process the sound signal into electrical stimuli and that it is not yet clear which way is the best. In this introductory chapter also the advantages and disadvantages of extracochlear electrodes relative to intracochlear ones are discussed. The last part of **chapter i** presents an overview the main questions addressed in this thesis.

The main topic of this thesis is the development of a computational model of the electrically stimulated cochlea. It consists of two sub-models, the first one calculating the potential distribution in the neural compartment of the inner ear. This potential field, in turn, is used as the input signal for the second sub-model, which is an active, non-linear model of the auditory nerve fibres.

**Chapter ii** draws attention to the fact that previous neural models provide a good qualitative description of many aspects of neural behaviour, but that they fall short quantitatively in several respects when stimulation of mammalian nerve fibres is considered. It is shown that a good fit is obtained between the shape, duration and conduction velocity of simulated and *in vivo* action potentials in mammalian motor neurons, if the effects of temperature are incorporated in an existing amphibian-based nerve fibre model and a realistic nerve fibre morphology is introduced. The resulting MSEN model also correctly describes the refractory behaviour of real nerve fibres. The simulation data lead to the conclusion that single-node models cannot replace a multiple non-linear node model as the maximum steady-state firing rates are limited by impulse conduction properties rather than by the frequency following behaviour of a single node.

In the last decades, there was growing evidence that mammalian nerve fibre kinetics is governed by rules that differ from those describing amphibian fibres. Essentially, the difference is that mammalian fibres have far less active potassium channels in the nodal area and that, as a consequence of this, the repolarisation of the nerve fibre's membrane in the falling phase of the action potential occurs mainly due to a relatively large leak conductance. The non-linear node SEF nerve fibre model described in **chapter iii** of this thesis contains nodal kinetics based upon voltage-clamp measurements in large rat and cat motor fibres at 37°C. The resulting spike shape, conduction velocity,

strength/duration behaviour and absolute and relative refractory period are in good quantitative agreement with published experimental data from large mammalian fibres (with axon diameters above 10  $\mu\text{m}$ ) at normal body temperature and at 20°C. In addition, the model generates realistic abortive spikes towards the end of the absolute refractory period and it can describe the consequences of repetitive firing adequately.

For the purpose of our cochlear implant project we were interested in a model of primary auditory nerve fibres, which have axon diameters between 2 and 3  $\mu\text{m}$ . Unfortunately, no voltage-clamp data are currently available for such thin fibres. If the MSEN and SEF model are scaled down geometrically, the simulated spike conduction velocity varies linearly with fibre diameter, which is acceptable in view of the available experimental data, but the shape of the action potential does not change with fibre diameter. However, it is known from literature that the action potentials of thinner nerve fibres last longer and that these increased spike durations are associated with prolonged refractory periods. In **chapter iv** of this thesis it is hypothesised that this phenomenon results from the fact that the specific nodal properties vary with fibre diameter. It is demonstrated how the SEF model can be generalised to include fibres of different diameter on the basis of this hypothesis. The resulting model, of which the parameters were obtained by fitting the duration of the falling phase of the simulated action potential to experimental data, is shown to have also a rise time of the action potential that is within physiological ranges for all fibre diameters. Moreover, the model exhibits a non-linear, sigmoidal, relationship between the spike conduction velocity and fibre diameter, while such a non-linear relationship was inferred previously from electromyographic data.

With this generalised form of the SEF model we constructed an anatomically-based model of an auditory nerve fibre. It produces realistic spike shapes and - what is more important for the desired application - its maximum firing rates are in good correspondence with experimental observations.

This model is applied in **chapter v** of this thesis to simulate the neural response to the electrical field due to intracochlear electrodes. This potential field is calculated with an implementation of the boundary element method that - unlike previous studies in the field of biomedical engineering - uses quadratically curved triangular elements to represent the boundaries between media with different conductivities. The application of curved elements ensures a better approximation of the contours of the cross-section of a guinea pig cochlea that was used to construct the mesh of the model. The fact that the potential is interpolated quadratically on these surface elements further improves the accuracy of the solution. Whereas previous volume conduction models of the cochlea consist of lumped circuits or use an unrolled cochlear duct, the present field model is rotation symmetric about a common mid-modiolar axis. Also the fact that the model incorporates three arrays of actively modelled spiral ganglion cells extends the model beyond the previously published modelling work. The resultant model predicts that the exact location in the scala tympani of intracochlear electrodes has a strong influence on both the excitation thresholds and selectivity of stimulation. These model results are shown to be in good agreement with published experimental electrical auditory

brainstem response data. It is also demonstrated that the use of actively modelled nerve fibres is essential to obtain correct predictions for the biphasic stimuli typically used in cochlear implants and that unrolling the cochlear duct has serious consequences for the predictions regarding modiolar stimulation. In **chapter vi** the rotation symmetric model is applied to study the influence of temporal stimulus parameters and electrode configurations on the spatial selectivity obtained with cochlear implants. To quantify this spatial selectivity a  $Q_{10\text{ dB}}$  is defined, which measures the sharpness of the peak in the excitation profile of the auditory nerve. The simulated excitation profiles are compared to auditory single fibre data from literature. The results presented in this chapter indicate that the use of charge-balanced asymmetric rather than symmetric biphasic pulses approximately doubles the number of independent channels that can be applied in a cochlear implant, like a configuration with radial electrode pairs using symmetric biphasic pulse stimulation would also do. The influence on selectivity of the actual variation in diameter of the cochlear nerve fibres and by a possible loss of their peripheral processes is also studied. The next step in our research project is formed by the experimental verification of the model predictions by performing electrophysiological measurements in guinea pigs that have been chronically implanted with extracochlear electrodes. For these measurements a multichannel synchronous data acquisition and waveform generator (DAWG) system with voltage inputs and voltage and current outputs was developed. This system is described in **chapter vii** of this thesis. It consists of up to 16 independent DAWG cards which each have their own microcontroller, signal memory and high-speed analog-to-digital and digital-to-analog converter. The device is controlled from a personal computer and includes elaborate hardware and software triggering options. The flexibility of the system makes it widely applicable in the field of biomedical engineering. **Chapter viii** summarises the most important results of this thesis and discusses them in a more general context. Attention is paid to the implications and possible areas of application of the neural modelling work and also to the boundary element method with second order interpolation functions as it was developed alongside with this project. Finally, it comes to the formulation of suggestions for further modelling, animal, and clinical research with this thesis as a starting point.

# *Samenvatting*

---

**COCHLEAR IMPLANTS  
A MODELLING APPROACH**

Electrische binnenoorprothesen (cochlear implants) zijn elektronische hulpmiddelen, waarmee aan doven een gehoorsensatie kan worden gegeven door de spirale ganglioncellen die nog aanwezig zijn in het beschadigde binnenoor elektrisch te prikkelen. Ondanks veelbelovende resultaten bij patiënten die hiermee in staat blijken een gesprek te kunnen voeren zonder gebruikmaking van spraakafzien, is het klinische resultaat in een individuele patiënt nauwelijks voorspelbaar. Dit blijkt namelijk afhankelijk te zijn van het complexe samenspel van diverse, nog niet geheel begrepen factoren, die zowel met de patiënt als met het implantaat samenhangen. Het onderzoek dat in dit proefschrift beschreven wordt, poogt te komen tot een beter begrip van de fundamentele processen die betrokken zijn bij het elektrisch stimuleren van het binnenoor. Het maakt deel uit van het onderzoeksprogramma elektrische binnenoorprothesen van de Leidse Universiteit, zoals dat uiteengezet wordt in **hoofdstuk 1** van dit proefschrift.

In dat hoofdstuk wordt een kort overzicht over een aantal relevante zaken met betrekking tot elektrische binnenoorprothesen gegeven aan de hand van een schema dat de verschillende cochlear implants classificeert op basis van het aantal en de plaats van de elektroden. Vervolgens wordt uitgelegd dat er een aantal principieel verschillende manieren zijn om het geluidssignaal te vertalen in elektrische signalen en dat het nog niet duidelijk is welke methode het beste is. In dit inleidende hoofdstuk wordt ook ingegaan op de voor- en nadelen van extracochleaire elektroden ten opzichte van intracochleaire. Het slot van **hoofdstuk I** geeft een overzicht over de belangrijkste vragen die in dit proefschrift aan de orde komen.

Het hoofdonderwerp van dit proefschrift is de ontwikkeling van een computermodel van de cochlea onder elektrische stimulatie. Het bestaat uit twee sub-modellen, waarvan het eerste de potentiaalverdeling uitrekent ter plaatse van de zenuwvezels in de cochlea. Op zijn beurt is deze potentiaalverdeling weer het invoersignaal voor het tweede sub-model, een actief, niet-lineair model van de vezels van de gehoorzenuw.

**Hoofdstuk II** vestigt de aandacht op het feit dat bestaande zenuwmodellen weliswaar een goede kwalitatieve beschrijving van verscheidene aspecten van het gedrag van zenuwvezels geven, maar dat deze modellen niet bruikbaar zijn om elektrische stimulatie van zenuwvezels in zoogdieren kwantitatief te beschrijven. Hier wordt aangetoond, dat uitgaand van een bestaand model van amfibie-neuronen, een goede overeenstemming bereikt wordt tussen de vorm, duur en voortgeleidingssnelheid van gesimuleerde en echte actiepotentialen in zoogdierzenuwvezels, als temperatuureffecten meegenomen worden en een realistische vezelmorfologie wordt geïntroduceerd. Het resulterende MSEN model beschrijft tevens het refractaire gedrag van echte zenuwvezels op realistische wijze. De simulatieresultaten laten zien dat modellen, bestaande uit één knoop van Ranvier, kabelmodellen met een aantal niet-lineaire knopen niet kunnen vervangen, omdat de maximale vuurfrequenties niet alleen bepaald worden door het frequentie-volgedrag van de afzonderlijke knopen maar ook door de impulsgeleidingseigenschappen van de vezel.

De laatste tientallen jaren werd het meer en meer duidelijk dat de kinetiek van zoogdierzenuwvezels wordt beheerst door andere regels dan die van amfibie-

neuronen. Het belangrijkste verschil is dat zoogdiervezels veel minder actieve kaliumkanalen hebben in de knoop van Ranvier en dat als gevolg daarvan de repolarisatie van het celmembraan tijdens de dalende fase van de actiepotentiaal voornamelijk berust op een relatief grote lekgeleidbaarheid. In het niet-lineaire SEF zenuwvezelmodel dat beschreven wordt in **hoofdstuk iii** van dit proefschrift wordt dan ook een kinetiek toegepast die gebaseerd is op zogenaamde voltage-clamp metingen aan dikke ratte- en kattenmotorvezels bij 37°C. De vorm en geleidingsnelheid, de sterkte/duurrelatie en de absolute en relatieve refractaire periode van dit model zijn in goede, kwantitatieve overeenstemming met gepubliceerde gegevens over dikke zoogdier zenuwvezels (met axon diameters boven 10 µm), zowel bij normale lichaamstemperatuur als bij 20°C. Bovendien genereert het model realistische, niet voortgeleide actiepotentialen tegen het einde van de absoluut refractaire periode en kan het de gevolgen van herhaalde stimulatie adequaat beschrijven.

Voor toepassing binnen ons cochlear implant project waren we geïnteresseerd in een model van primaire auditieve zenuwvezels, die een axondiameter hebben tussen 2 en 3 µm. Helaas zijn op dit moment geen voltage-clamp metingen beschikbaar voor zulke dunne vezels. Als het MSEN en SEF model geometrisch verkleind worden verandert de actiepotentiaal geleidingsnelheid recht evenredig met de vezeldiameter, wat acceptabel is gezien de beschikbare experimentele gegevens, maar de vorm van de actiepotentiaal hangt niet van de diameter af. Het is echter uit de literatuur bekend, dat de actiepotentialen van dunnere vezels langer duren en dat deze langere actiepotentialen gepaard gaan met langere refractaire perioden. In **hoofdstuk iv** van dit proefschrift wordt de hypothese geformuleerd, dat dit fenomeen het gevolg is van het feit dat de nodale eigenschappen per eenheid van oppervlak variëren met de vezeldiameter. Het wordt gedemonstreerd hoe het SEF model op basis van deze hypothese gegeneraliseerd kan worden, zodat het vezels van uiteenlopende diameter kan beschrijven. Het resulterende model, waarvan de parameters verkregen werden door de duur van de dalende flank van de actiepotentiaal te schalen aan de hand van experimentele gegevens, blijkt ook voor alle vezeldiameters een stijgtijd van de actiepotentiaal te hebben die binnen fysiologische grenzen valt. Bovendien vertoont dit model een niet-lineair, S-vormig verband tussen de actiepotentiaalgeleidingsnelheid en de vezeldiameter, wat voorheen al afgeleid was uit electromyografische metingen. Met deze gegeneraliseerde vorm van het SEF model hebben we aan de hand van anatomische gegevens een model van een auditieve zenuwvezel geconstrueerd. Het produceert realistische actiepotentiaalvormen en - wat belangrijker is voor de beoogde toepassing - de maximale vuurfrequenties zijn in goede overeenstemming met experimentele waarnemingen.

Dit model wordt in **hoofdstuk v** van dit proefschrift toegepast om de neurale responsies op het elektrische veld ten gevolge van intracochleaire elektroden te simuleren. Deze potentiaalverdeling wordt berekend met de oppervlakte integraalmethode. De gekozen implementatie maakt - in tegenstelling tot eerdere onderzoeken op biomedisch terrein - gebruik van kwadratisch gekromde driehoekselementen om de grenslagen tussen media met

verschillende geleidbaarheid te beleggen. Door de toepassing van gekromde elementen wordt een betere benadering verkregen van de contouren van de doorsnede door een cavia-cochlea, die gebruikt is om het volumegeleidingsmodel te bouwen. Het feit dat de potentiaal kwadratisch geïnterpoleerd wordt op deze oppervlakte-elementen komt de nauwkeurigheid van de oplossing verder ten goede. Waar eerdere volumegeleidingsmodellen van de cochlea bestaan uit samengestelde, discrete elektrische componenten of een ontronde ductus cochlearis gebruiken, is het hier gepresenteerde model rotatiesymmetrisch om een as door het centrum van de modiulus. Ook het feit dat het model drie rijen actief gemodelleerde spirale ganglioncellen bevat, is een uitbreiding ten opzichte van eerder gepubliceerd modelwerk. Het resulterende model voorspelt dat de exacte positie in de scala tympani van intracochleaire elektroden een sterke invloed heeft op zowel de excitatiedrempels als de selectiviteit van stimulatie. Deze modelresultaten blijken goed in overeenstemming te zijn met uit de literatuur bekende experimentele gegevens van elektrisch opgewekte auditieve hersenstam potentialen. Verder blijkt het gebruik van actief gemodelleerde zenuwvezels essentieel te zijn om goede voorspellingen te verkrijgen voor de bifasische pulsen die in het algemeen gebruikt worden bij cochlear implants, terwijl het ontrollen van de cochlea een sterke invloed heeft op de voorspellingen met betrekking tot stimulatie van vezels in de modiulus.

In **hoofdstuk vi** wordt het rotatie-symmetrisch model toegepast om de invloed te bestuderen van temporele stimulusparameters en van de electrode configuratie op de spatiële selectiviteit die met cochlear implants bereikt kan worden. Om deze spatiële selectiviteit te kwantificeren wordt een  $Q_{10\text{ dB}}$ -waarde gedefinieerd, die een maat is voor de breedte van de piek in het excitatieprofiel van de gehoorzenuw. De gesimuleerde excitatieprofielen worden vergeleken met enkele-vezelmetingen uit de literatuur. De resultaten uit dit hoofdstuk geven aan, dat het gebruik van ladingsgebalanceerde, asymmetrische bifasische pulsen in plaats van de gebruikelijke symmetrische, het aantal onafhankelijke kanalen dat toegepast kan worden in een elektrische binnenoorprothese ongeveer verdubbelt, net zoals het geval is bij gebruik van symmetrische bifasische pulsen op radiaire electrodeparen. Verder wordt de invloed die de bestaande variatie in diameter tussen de vezels van de gehoorzenuw heeft op de selectiviteit bestudeerd, alsmede de invloed hierop van een eventueel verlies van de perifere uitloper van deze vezel.

De volgende stap in ons onderzoeksproject wordt gevormd door de experimentele verificatie van de modelvoorspellingen door middel van electrofysiologische metingen in cavia's met chronisch geïmplanteerde extracochleaire elektroden. Voor deze metingen werd een meerkanaals, synchroon signaalacquisitie en -generatorsysteem (S.A.G.) ontwikkeld met spanningsingangen en spannings- en stroomuitgangen. Dit systeem wordt beschreven in **hoofdstuk vii** van dit proefschrift. Het bestaat uit maximaal 16 onafhankelijke S.A.G.-kaarten die elk hun eigen microprocessor eenheid, geheugen voor signaalopslag en snelle analoog naar digitaal en digitaal naar analoog converter hebben. Het apparaat wordt bestuurd vanuit een personal computer en heeft uitgebreide hardware en software triggermogelijkheden. De

flexibiliteit van het systeem maakt het breed inzetbaar op het gebied van biomedisch onderzoek.

**Hoofdstuk** viii zet de belangrijkste resultaten uit dit proefschrift op een rijtje en bediscussieert ze in een ruimer kader. Daarbij wordt ingegaan op de implicaties en mogelijke toepassingen van het aan zenuwvezels verrichte modelwerk en de ruimere toepasbaarheid van de in het kader van dit onderzoek ontwikkelde oppervlakte integraalmethode met tweede orde interpolatiefuncties. Tenslotte worden suggesties voor verder modelmatig, dierexperimenteel en patiëntgebonden onderzoek op basis van de hier verkregen gegevens geformuleerd.



# *Curriculum Vitae*

---

***J.H.M. FRIJNS***

The author of this thesis was born on May 29, 1961 in The Hague, The Netherlands. In the year 1979 he passed cum laude the Gymnasium- $\beta$  examination at the 'Scholengemeenschap Caland' in Rotterdam and he commenced the study Applied Physics at the Delft University of Technology. In July 1981 he received the certificate Reading Ability Scientific Russian Language from this institute, while he was awarded cum laude the B.Sc. degree in Applied Physics in July 1982. In September of that year he concurrently started to study Medicine at the Leiden University, where he passed the pre-medical examination (cum laude) in August 1983. In November 1983 he graduated cum laude in Applied Physics on a Master's thesis entitled 'Development of non-periodic stimuli for and investigation of the Binaural Edge Pitch'. This work was performed in the Acoustical Perception Group (the late Prof. G. van den Brink, Ph.D. and Prof. F.A. Bilsen, M.Sc. Ph.D.). In December 1986 he passed the Medical 'doctoraalexamen' (cum laude) in the Leiden University, where he was cum laude awarded the M.D. degree in July 1988. In September that year he started the cochlear implant project at the E.N.T. department of the Leiden University Hospital (Head: Prof. P.H. Schmidt, M.D. Ph.D.) under the guidance of Prof. J.J. Grote, M.D. Ph.D., which has resulted in the work presented in this thesis. From October 1989 to October 1994 he worked as a resident in Otorhinolaryngology at this department. Since he was certified as an Otorhinolaryngologist in October 1994, he is a staff-member at the department of Otorhinolaryngology of the Leiden University Hospital (Head: Prof. J.J. Grote, M.D., Ph.D.).